This is to certify that the
dissertation entitled

INVESTIGATION OF MICROWAVE CAVITY APPLICATORS FOR PLASMA ASSISTED CVD DIAMOND SYNTHESIS AND PLASMA ASSISTED COMBUSTION

presented by

Kadek Wardika Hemawan

has been accepted towards fulfillment
of the requirements for the

Ph.D. degree in Electrical Engineering

Major Professor's Signature

5/6/10

Date

INVESTIGATION OF MICROWAVE CAVITY APPLICATORS FOR PLASMA ASSISTED CVD DIAMOND SYNTHESIS AND PLASMA ASSISTED COMBUSTION

By

Kadek Wardika Hemawan

A DISSERTATION

Submitted to
Michigan State University
in partial fulfillment of the requirements
for the degree of

DOCTOR OF PHILOSOPHY

Electrical Engineering

2010

ABSTRACT

INVESTIGATION OF MICROWAVE CAVITY APPLICATORS FOR PLASMA ASSISTED CVD DIAMOND SYNTHESIS AND PLASMA ASSISTED COMBUSTION

By

Kadek Wardika Hemawan

The objective of this research was to design, build, optimize, and experimentally evaluate microwave applicators that operate at high pressures for two specific applications: (a) microwave plasma assisted chemical vapor deposition (MPACVD) and (b) microwave plasma assisted combustion (MPAC).

Microwave plasma assisted chemical vapor deposition was experimentally investigated using a cylindrical plasma source, high purity, 2-5% H_2/CH_4 input gas chemistries and operating at high pressures of 180-250 Torr for diamond synthesis. A microwave cavity plasma reactor was specifically modified to be experimentally adaptable and tunable in order to enable operation with high input microwave plasma absorbed power densities within this higher pressure regime. Uniform polycrystalline diamond films were synthesized on 2.54 cm diameter silicon substrates and single crystal diamonds were deposited on HPHT diamond seeds at substrate temperatures of 950-1282 °C. The polycrystalline growth rates ranged from 3 to 21 μm/hr at 2-5% CH_4/H_2 while single crystal diamond growth rate varied from 8 to 36 μm/hr at 3-5% CH_4/H_2. Higher operating pressures, absorbed power densities, and methane concentrations resulted in higher

diamond growth rates. FTIR transmission and Raman measurements indicated the synthesized diamond at these high pressures was of excellent quality.

Microwave plasma assisted combustion was also investigated using cylindrical and coaxial microwave cavity applicators using premixed gas chemistries of O_2/CH_4. These applicators were developed to enable the efficient coupling of microwave energy into gases/plasmas/flames at pressures of one atmosphere. The mechanical tuning of the applicators allowed for the efficient matching of microwave power into the flame and also allowed the optimal positioning of the flame with respect to the impressed electric field. The addition of a few Watts of microwave power to a combustion flame with a flame power of 10-40 W served to extend the flammability limits under fuel rich and fuel lean conditions, increased the flame length and intensity, and also increased the number density and mixture of excited radical species in the flame vicinity. Optical emission spectroscopy measurements showed gas rotational temperatures in the range of 2300 - 3600 K.

This thesis research has led to two experimental applicator designs and associated systems that allow experimental investigation of microwave energy interaction with combustion flame and a microwave applicator that enables MPACVD diamond synthesis at 180-250 Torr pressure regime. This MSU MPACVD reactor design has recently been commercialized.

ACKNOWLEDGEMENTS

I would like to express my sincere gratitude to my major advisor, Dr. Jes Asmussen, for providing opportunity, guidance, editorial, technical suggestions, and mentorship during the course of this research. Along with my advisor, I would like to thank Dr. Timothy A. Grotjohn, Dr. Donnie K. Reinhard and Dr. Greg Swain for serving on my advisory committee.

Next I would like to thank Dr. Thomas Schuelke and the Fraunhofer USA CCL personnel's in providing assistance with the laboratory equipments. I also would like to thank Dr. Indrek Wichman and Chandra Romel from the Mechanical engineering department as a collaborator in the plasma assisted combustion study.

Sincere appreciation for Matt Swope with the Raman spectroscopy instruments set up, Roxanne Peacock, and Brian Wright with their ECE machine shop technical support. Additional thanks are given to fellow graduate students for their friendship and valuable assistance during the course of this work.

Finally, special thanks to my family for their great understanding, moral support, and encouragement in completing this degree.

This work was supported by Fraunhofer USA, Center for Coatings and Laser Applications and The Richard M. Hong Chaired Professorship.

TABLE OF CONTENTS

LIST OF TABLES

LIST OF FIGURES

Images in this dissertation are presented in color

CHAPTER 1

INTRODUCTION

1.1 Research motivation

A major motivation of this thesis research was to develop microwave applicator technologies that efficiently create and maintain microwave discharges at pressure regimes of 180 Torr and above. Thus, this thesis research was devoted to exploring microwave discharge coupling behavior at high pressures and developing the associated microwave plasma cavity applicator technologies.

The approach which was primarily experimental initially extends the limit of the existing microwave reactor technologies from 180 to 250 Torr. This was done by a redesign of a specific reactor in order to enable it to operate robustly and optimally in the 180-250 Torr pressure regime. Other experiments were performed at one atmosphere where small, efficient microwave applicators sustain a microwave discharge in argon and molecular gases such as CH_4, O_2 and N_2.

The reliability and efficiency of the applicator designs was then evaluated in the specific high pressure microwave discharge applications. In particular, applicator designs were experimentally investigated in two applications: (1) MPACVD synthesis of diamond and (2) microwave plasma assisted combustion (MPAC). Each application is briefly described in section 1.1.1 and 1.1.2 below:

1.1.1 Microwave plasma assisted CVD diamond synthesis

Early investigations of chemical vapor deposition of diamond employed low power density microwave discharges/reactors (< 5 W/cm^3) that were operated within the low pressure, 20-100 Torr, regime and used input CH_4/H_2 gas mixtures that varied between 1-5% [1, 2]. Both polycrystalline and single crystalline films were synthesized with deposition rates that increased from less than a one μm/h at very low methane concentrations (< 1%) to a maximum of a few μm/h as methane concentrations were increased to 5%. However, high-quality films could only be produced under low methane input conditions (< 1%) and as a result, diamond growth rates were very low; i.e < ~1 μm/h. Attempts to increase the growth rate by increasing the input methane concentrations led to the formation of defects such as secondary nucleation and unepitaxial crystallites. While these results were of scientific interest [2] the very low growth rates limited the commercial potential of microwave plasma assisted CVD synthesis of diamond. Thus, in the mid 1990's an important scientific and engineering challenge and opportunity that remained unsolved was to discover and develop diamond synthesis methods that dramatically increase the deposition rates while still producing excellent crystalline quality.

During the mid 1990's and early 2000's several research groups [3-8] searched for improved diamond synthesis methods. Their experiments, which synthesized both polycrystalline and single crystalline materials, utilized high power density (50-100 W/cm^3) microwave discharges operating at moderate

pressures between 100-180 Torr. They found that (1) synthesis rates for both polycrystalline (PCD) and single crystalline diamond (SCD) were greatly increased and (2) the diamond quality was improved as the microwave discharge power density and process pressure were increased. In particular, good quality PCD was deposited at 4-10 μm/h [7-8] and SCD was produced at rates of 50-100 μm/h [3, 5]. These growth rates were higher by a factor of 5 to 100 times than the growth rates for good quality CVD synthesized diamond that was obtained in the early 1990's using low pressure microwave discharges.

The research activities in this thesis were directed towards the development of new microwave reactor technologies that enable the experimental exploration of CVD diamond synthesis at operating pressures above 180 Torr. A motivation of the research was to grow diamond at high rates and high quality. The results of this investigation have been submitted for publication in Diamond Related Materials and also have been commercialized by Lambda Technologies.

1.1.2 Microwave plasma assisted combustion

Diamond can also be synthesized using combustion CVD. The first experiments were conducted by Hirose and Kondo [8] using acetylene flames and later confirmed by Naval Research laboratory [10]. Combustion CVD is a potential technique for diamond synthesis because of its simplicity of the

experimental systems, it is scalable technique, and has lower capital costs as compared to other plasma assisted CVD [11].

As of late, an emerging topic that combines both plasma and combustion fields commonly referred to plasma assisted combustion, has gained attention among the plasma and combustion scientific community. Many researchers have investigated techniques that combine electrical energy with a flame. They demonstrated the potential to modify the combustion process with the addition of electric energy. Various discharges such as DC and AC, dielectric barrier, RF, pulsed corona, and microwave discharges were experimentally investigated for their ability to interact with, and to modify premixed and diffusion flames. Microwave plasma-assisted hydrocarbon treatment was initially investigated for internal-combustion engine improvement [13-17] and for the conversion of hydrocarbons into methane and acetylene gases [18]. More recently the conversion of hydrocarbons into hydrogen fuels has been also investigated [19].

By investigating microwave plasma assisted combustion, it was desired to understand any macroscopic changes in the plasma behavior when the combustion flame is subjected to microwave energy. Thus, the thesis research developed and experimentally evaluated two microwave applicator designs that were able to gradually and efficiently couple microwave energy into a flame. Some of the investigation results have been published in the Applied Physics Letters, 89, 141501 (2006) and the Review of Scientific Instruments, 80, 053507 (2009). These reactors are now available as experimental test facilities that enable further investigation of microwave energy interaction with combustion

flames and also may lead to new MPACVD reactor designs that at high pressure combine combustion and microwave plasma i.e., a hybrid MPACVD combustion flame reactor for CVD diamond synthesis.

1.2 Research objectives and approach

The objective of this research was to design, develop, optimize, and experimentally evaluate microwave applicators that operate at high pressures (> 180 Torr - 1 atmosphere) for two specific applications: (a) microwave plasma assisted chemical vapor deposition (MPACVD) and (b) microwave plasma assisted combustion (MPAC).

The specific goal of the microwave plasma assisted CVD research was to extend the operation of an existing MSU reactor technology to higher pressures. When increasing the operating pressure, it is expected that the diamond growth rate and quality will increase. The high pressure plasma reactors and experimental methods described in this thesis allow the spatial positioning and shaping of the resulting discharge in a high pressure, thermally inhomogeneous, high power microwave density discharge, and thereby enable the synthesis of polycrystalline and single crystal diamonds at high pressures between 180 to 250 Torr.

The specific goal of the microwave plasma assisted combustion research was to build and modify microwave cavity applicators that enable the investigation of the underlying microwave coupling mechanism, the macroscopic

changes that occur when electromagnetic energy was added into the combustion flame, and study the hybrid plasma flame discharge characteristics at 760 Torr.

The research approach and specific tasks conducted during the investigation are outlined below:

1. Modify the existing microwave plasma assisted CVD reactor design and test the new applicator for diamond synthesis at higher pressure
    a. Modify the reactor to enable the excitation of a hybrid (TM013 + TEM001) mode and provide additional length tuning for the coaxial section of the reactor.
    b. Design and build a water cooled stage and substrate holders for high pressure polycrystalline CVD diamond synthesis.
    c. Experimentally synthesize polycrystalline diamond at 180-240 Torr.
    d. Design and build a water cooled stage and substrate holders for single crystal diamond synthesis.
    e. Experimentally synthesize single crystal diamond (without nitrogen) at 180-250 Torr.

2. Develop microwave plasma applicators at one atmosphere for plasma assisted combustion
    a. Experimentally evaluate a premixed combustion flame at 760 Torr pressure using a miniature coaxial plasma torch burner (new applicator design).

b. Improve microwave coupling of the coaxial plasma torch burner by placing it inside a tunable cylindrical seven inch cavity (new applicator design).

c. Modify the microwave coaxial re-entrant plasma cavity applicator for efficient and optimum coupling between the microwave energy and combustion flame (applicator design improvement).

1.3 Dissertation outline

The thesis research activities have two major research components: (1) MPACVD for diamond synthesis at operating pressures of 180-250 Torr and (2) microwave plasma assisted combustion at operating pressure of 760 Torr. These are described respectively in Chapter 2 to Chapter 5 and Chapter 6 to Chapter 9. In Chapter 2, the theoretical background and literature review of microwave plasma assisted chemical vapor deposition is presented. In Chapter 3, the MPACVD diamond reactor design is described. The chapter begins with a brief review of MSU generic reactor technology followed by the description of the existing or reference reactor. Detail designs of the modified or hybrid reactor is also presented. This includes a new water cooling stage and substrate holder designs. General background of circular and coaxial waveguides/cavities such as mode charts and field patterns is also presented. Chapter 4 begins with the description of the overall experimental system setup. The description of the CVD diamond synthesis experimental multivariable space and experimental

procedures are discussed. Presentation of experimental results such as the reactor's performance, optimization, and microwave plasma discharge characteristics are presented in Chapter 5. Here the diamond growth rates, diamond uniformity, diamond surface morphology, and diamond quality for both polycrystalline and single crystal diamonds are discussed.

Chapter 6 presents the background and literature review of plasma assisted combustion. In Chapter 7, the microwave plasma assisted combustion experimental systems and procedures are described. This includes, microwave system networks, optical emission spectroscopy set up, and rotational temperature calculation procedures for both N_2 and CH. Chapter 8 covers the microwave plasma assisted combustion applicator #1, i.e., hybrid cavity plasma flame burner system which consists of miniature plasma torch combined with the seven-inch cavity applicator. The experimental results such as influence of microwave coupling on the flame structure, flammability limits, and gas temperature are also presented. Chapter 9 covers the microwave plasma assisted combustion applicator #2, i.e., compact re-entrant cavity plasma flame burner and the experimental results drawn from the experimental measurements. Chapter 10 concludes the dissertation with a summary of the work on the microwave plasma assisted combustion and microwave plasma assisted CVD diamond synthesis. Recommendations for future research are also presented.

CHAPTER 2

MICROWAVE PLASMA ASSISTED CVD DIAMOND

BACKGROUND

2.1 Introduction

This chapter presents general background and literature review of CVD diamond synthesis at high pressure (≤ 120 Torr and above). It begins with basic properties of diamond and its potential use in various technical applications. Then, the comparison between microwave plasma CVD versus combustion CVD for diamond deposition technique is presented. The general growth process and surface kinetics chemistry of CVD diamond is also described. A literature review of polycrystalline and single crystal diamond deposition at high pressure concludes the chapter.

2.2 Diamond structure, properties and its applications

Diamond has a crystal structure of face-centered cubic (FCC) lattice with a basis of two identical carbon atoms or lattice points primitive unit cell, one at (0, 0, 0) and the other at (1/4, 1/4, 1/4). It can be viewed as the superposition of two FCC lattices one displaced relative to the other along the body diagonal by one quarter of lattice parameter from the origin. At room temperature, the unit cell is cubic with a side length approximately equal to 3.567 Angstrom. Every carbon atom in the lattice is bonded with four other carbon atoms to form a tetrahedral structure. Four valence electrons in each carbon atom form strong covalent bonds by sp^3 hybridization with nearest neighbor distance of 1.54 Angstrom. Figure 2.1 shows the cubic crystal structure of diamond.

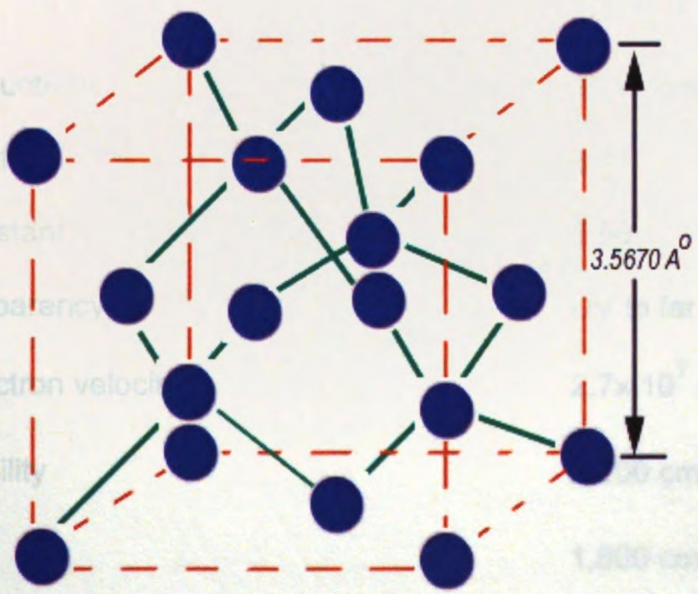

Figure 2.1 – Diamond cubic crystal structure

Diamond has unique and superior properties as compared to other materials. Among other properties, diamond is the hardest known solid material, has a very high bulk modulus. It has highest thermal conductivity at room temperature, it has a broad optical transparency from the deep ultraviolet to the far infrared, it has the highest sound propagation velocity, it is a very good electrical insulator, it can be doped to become a semiconductor, it is a biologically compatible material, and it is very resistant to chemical corrosion since it is inert to most chemical reagents. Listed below are the mechanical, thermal, optical an electrical properties of diamond [20-23].

- Hardness — 10,000 kg/mm^2
- Strength, Tensile — > 1.2 GPa
- Sound velocity — 17,500 m/s
- Young's modulus — 1140 GPa
- Atom density — $1.77x10^{23}$ $1/cm^3$
- Thermal conductivity — 20 W/cm K
- Refractive index — 2.41
- Dielectric constant — 5.68
- Optical transparency — UV to far IR
- Saturated electron velocity — $2.7x\ 10^7$ cm/s
- Electron mobility — 2,200 cm^2/Vs
- Hole mobility — 1,600 cm^2/Vs
- Band gap — 5.45 eV
- Resistivity — 10^{13}-10^{16} Ωcm

These highly attractive properties make diamond a very promising material for various technical applications ranging from space, defense, semiconductor, computers, tribological, and commercial technologies. Due to great hardness, wear resistance, high strength, rigidity, and chemical inertness, diamond can be used in grinding or cutting tools. For example, industrial knives, oil drilling tools, surgical scalpels, saws, circuit board drills, ball bearings, jet nozzle coatings, and abrasive pump seals.

Because of the high thermal conductivity and electron carrier mobility, saturated carrier velocity and high frequency performance, diamond has the potential to be used in semiconductor devices and thermal management. Examples of applications are heat sink diodes and PC boards, field-effect transistors, photovoltaic elements, and high power microwaves.

Due to good radiation resistance and transparency from UV to IR, diamond can be used as an optical coating or an optical material for many applications such as X-ray windows, fiber optics, UV to IR windows, laser protection and UV sensors. Also diamond can be used as inert conducting electrode for a variety of electro chemical applications and in the harsh environment found in internal-combustion and jet engines.

2.3 Plasma-assisted CVD vs. combustion CVD diamond synthesis

There are a number of methods that are commonly used to synthesize diamond; namely, hot filament CVD [24-25], DC plasma CVD [26-27], RF plasma CVD [28], combustion CVD [9,10,30] and laser assisted CVD [31]. Since the topic of this research is microwave plasma assisted CVD and microwave plasma assisted combustion, only microwave plasma assisted CVD (MPACVD) and combustion CVD (CACVD) are being compared. Shown in Table 2.1 is the comparison between microwave CVD and combustion CVD techniques. The advantages and disadvantages of each technique along with typical characteristics are listed. The several factors that make the microwave plasma assisted CVD technique popular or commonly used for diamond synthesis are: (1) high plasma density and low sheath potential which result in high energy efficiency, (2) high gas temperature as needed for H production, (3) stability and reproducibility which allows for continuous and long hours of deposition, (4) potential to scale up the process for larger substrate area, and (5) high purity deposition environment. The main challenge of this technique still however has to do with the deposition growth rates and process control (over heating of reactor walls) when operated at high pressure. As of late, great progress has been made in increasing the diamond growth rates using MPACVD technique.

Combustion flame diamond deposition at atmospheric pressure was first reported by Hirose *et.al.* [9] and then followed by Hanssen *et.al.* [10]. In a flame CVD process, a premixed combustion flame is used to synthesize the diamond. Diamond is formed on the deposition substrate positioned at the reducing part of

the flame at substrate temperature of 800-1100 °C and a gas temperature of about 2000 °C. The atmospheric flame deposition is simpler in design, easy to use and shows great promise for high growth rates. The main challenge of this method is that the deposition area is still relatively small and uniformity of the grown diamond is still not at its optimum. Also, it has been reported that by employing this method, the consumable costs are too high due to large amounts of acetylene and oxygen required during deposition.

Table 2.1 - Characteristics of diamond CVD synthesis technique for plasma assisted CVD and combustion CVD

Method	Gas composition	Pressure (Torr)	Gas flow rate (sccm)	Substrate material	Growth rate (μm/h)	Advantage	Disadvantage	Ref.
Microwave plasma CVD	0.2-20% CH_4 in H_2	10-340	20-1000	Si, Mo, WC, HPHT	1-160	Quality, area, scale up	Growth rate, walls heating	[32, 33, 34, 35, 36, 37]
Combustion CVD	0.44 C_2H_2 0.19 H_2 0.37 O_2 0.75 CH_4	Up to 760	1000-10000	Si, Mo, WC, Al_2O_3, TiN	30-500	Growth rate, simpler system	Uniformity, stability, area	[11, 12, 38, 39, 40]

2.4 Diamond growth

Figure 2.2 illustrates the linear growth rate (μm/hr) for various diamond CVD methods versus gas temperature in their activation zone. It can be seen that the linear growth rate between ~ 0.01 μm/hr to ~ 1000 μm/hr could be obtained depending on the deposition techniques employed. The lowest growth rates are obtained with the simple thermal decomposition. Then, using the low pressure DC or RF glow discharges, it induce some gas heating which helped increase the diamond growth rate at around 0.1 μm/hr. The low pressure microwave and hot filament CVD methods have gas temperature between 2000-2500 °C and their growth rate varies from 1 to 10 μm/hr. Using the oxyacetylene method with gas temperature between 5000-7000 °C resulted in growth rate over 100 μm/hr. High gas temperatures lead to the highest linear growth rates due to atomic hydrogen generation and appropriate neutral carbon containing radicals by collisions [9].

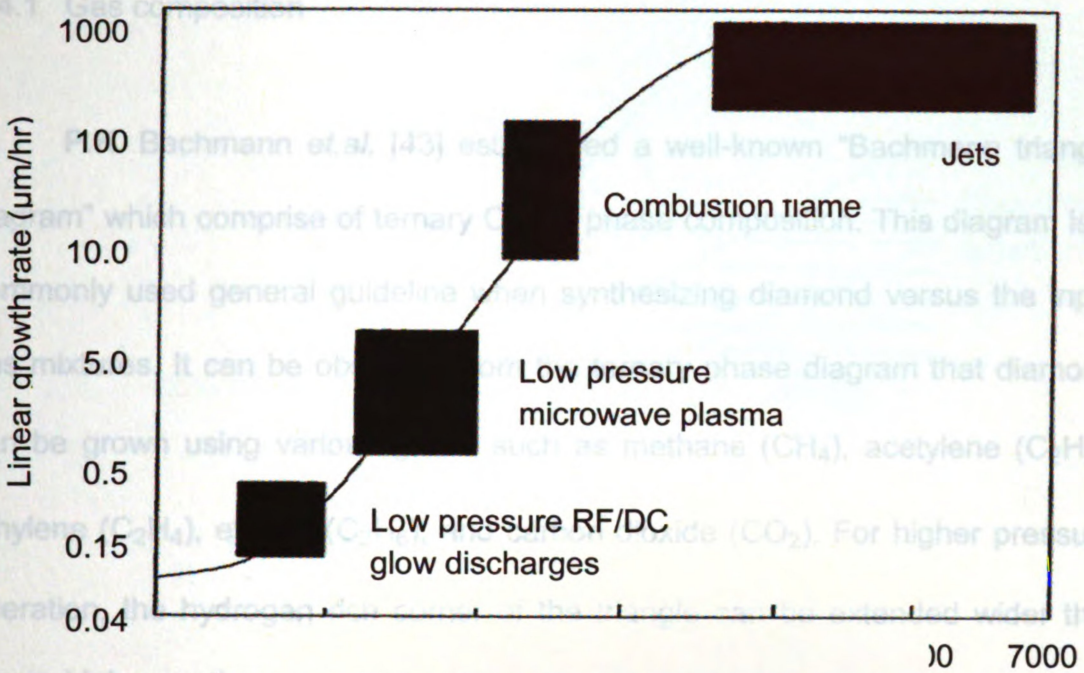

Figure 2.2 – Linear growth of various diamond CVD methods versus gas phase temperature in their activation zone [32].

Goodwin *et.al.* [41] and Silva *et.al.* [42] proposed a theoretical formulation on the influence of CH_3 methyl radical and H atomic hydrogen during diamond growth. Simulation results by Silva *et.al.* suggested that higher CH_3 and H resulted in higher growth rates and lower defect density. Likewise, as the operating pressure and methane concentration increase, diamond growth rate dramatically increases. The atomic hydrogen concentration at the surface increases by three orders of magnitude while the CH_3 concentration is multiplied by factor of ten. This leads to an increase in growth rate that is greater than10 μm/hr at 300 mbar. Also, since the atomic hydrogen density is very high, it is possible to increase methane concentration at high pressure for high growth rate without sacrificing the grown diamond quality.

2.4.1 Gas composition

P.K. Bachmann *et.al.* [43] established a well-known "Bachmann triangle diagram" which comprise of ternary C-H-O phase composition. This diagram is a commonly used general guideline when synthesizing diamond versus the input gas mixtures. It can be observed from the ternary phase diagram that diamond can be grown using various gases such as methane (CH_4), acetylene (C_2H_2), ethylene (C_2H_4), ethane (C_2H_6), and carbon dioxide (CO_2). For higher pressure operation, the hydrogen rich corner of the triangle can be extended wider that allows higher methane concentration to be added into the gas mixture as shown in Figure 2.3.

For each point within the triangle, a set of three characteristic coordinates can be calculated. For example:

$$X_H = \frac{H}{(H+C)} \qquad X_O = \frac{O}{(O+H)} \qquad X_C = \frac{C}{(C+O)}$$

Where H, O, and C are the total number of H, O, or C atoms in the molecules of the used gas mixture. It has been observed that diamond only grows when the gas composition is in the thin region close to and just above the CO tie-line regardless of the deposition system method employed. Below the CO line tie-line, no film growth will be achieved. Above the CO tie-line, non diamond carbon will be deposited, with the exception of a very narrow window close to the tie-line which produces diamond films.

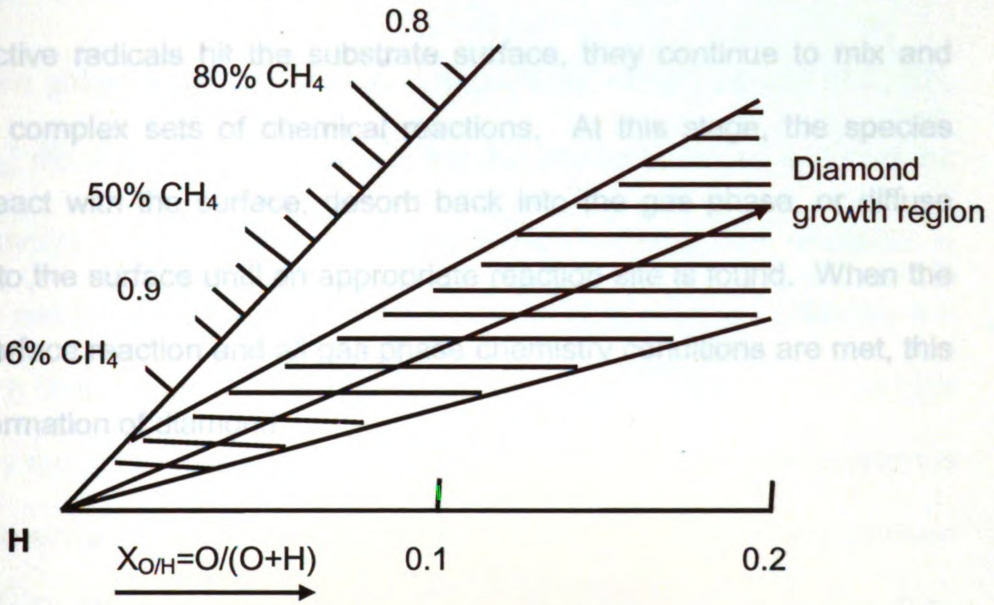

Figure 2.3 – Magnification of the hydrogen rich corner of the Bachmann diagram for higher pressure operation [44].

2.4.2 Physical growth process

The CVD diamond growth process is quite complex. A general simplified growth diamond CVD process is shown in Figure 2.4 and can be summarized as follows: Initially the process gases first mix in the discharge chamber before diffusing through the plasma and onto the substrate surface. As the species pass through the plasma discharge activation region they can be ionized and dissociated. In particular the hydrogen and hydrocarbon precursor molecules dissociate in the discharge and create an equilibrium concentration of gas-phase hydrogen atoms. More specifically, this activation results in breaking down of the molecules into reactive radicals and atoms, creates ions and electrons, and

heats the gas to a high temperature of the order of a couple thousands Kelvin. As these reactive radicals hit the substrate surface, they continue to mix and undergo very complex sets of chemical reactions. At this stage, the species adsorb and react with the surface, desorb back into the gas phase, or diffuse around close to the surface until an appropriate reaction site is found. When the appropriate surface reaction and all gas phase chemistry conditions are met, this leads to the formation of diamond.

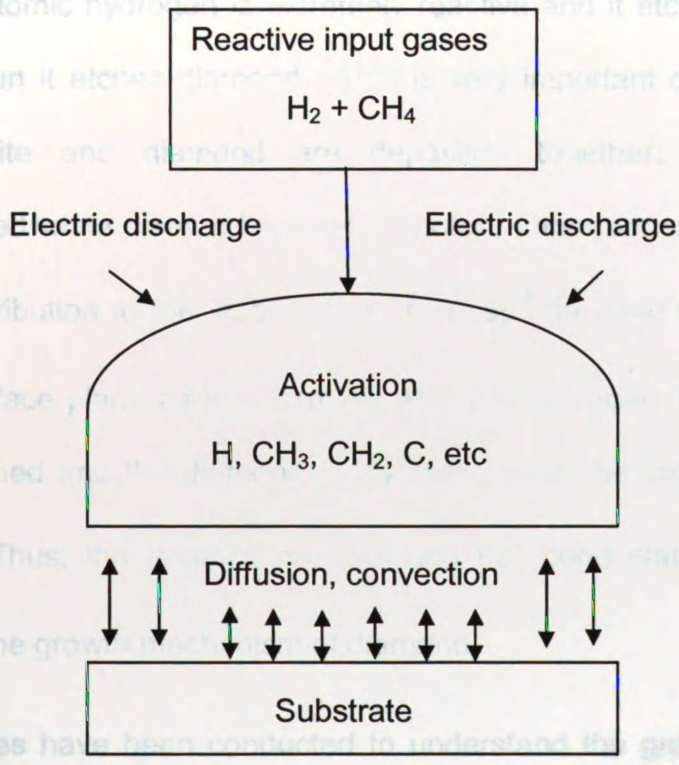

Figure 2.4 – General diamond CVD growth process

2.4.3 Surface kinetics

The main growth species in diamond depositions usually consist of C, CH, C_2, C_2H_2, CH_3, etc. It is believed however, that the atomic hydrogen is one of the critical components in the gas phase mixture. A high concentration of atomic H plays a major role for a number of processes. In the normal state, hydrogen is a molecule which dissociates at a very high temperature above 2000 °C or in high current density arc to produce atomic hydrogen. The rate of the recombination is also very rapid since the mean free path dependent half life of atomic hydrogen is very short [45]. Atomic hydrogen is extremely reactive and it etches graphite much faster rate than it etches diamond. This is very important characteristic since when graphite and diamond are deposited together; graphite is preferentially removed while diamond remains. Another important role of atomic hydrogen is its contribution to the stabilization of the sp^3 dangling bonds found on the diamond surface plane as it is formed. Without hydrogen, these bonds may not be maintained and the diamond {111} plane would be collapse to the graphite structure. Thus, the graphite removal and sp^3 bond stabilization are essential factors in the growth mechanism of diamond.

Several studies have been conducted to understand the growth species and surface kinetic chemistry of diamond growth [41, 46]. During diamond growth typically the diamond surface is saturated with hydrogen atoms. An atomic H abstracts a surface H to form H_2 leaving behind a reactive surface site. This open surface site can react with another nearby H atom, which resulted in

stable form as its previous situation. However, there are probabilities that a gas phase CH_3 radical may collide and react with the surface site, adding carbon to the lattice. This process of H abstraction and methyl addition may then occur on a site adjacent to the attached methyl. A further H abstraction process on one of the chemisorbed groups creates a radical, which hit the other nearby carbon group to complete the ring structure, locking the two carbons into the diamond lattice. Recent publications by various diamond researchers seemed to indicate the consensus that diamond growth occurs mainly from primary species such as methyl radicals (CH_3) and acetylene (C_2H_2). Butler *et.al.* [46] simulated a diamond growth model based on hydrocarbon radical such as C_2H_2 and CH_3 on the {110} and {111} oriented diamond films under typical chemical vapor depositions. The growth on a flat {110} surface is initiated by H abstraction from and CH_3 chemisorption onto the diamond surface, H abstraction from and CH_3 addition to the chemisorbed CH_3 molecule, H abstraction from the second CH_3 molecule and from an adjacent site on the diamond surface, and bonding between the C_2H_4 radical and the film. Table 2.2 shows the reaction rate constants that describe each reaction transition for each step.

Table 2.2 – Reaction rate constants at 1100 K. The notation C_d represents a surface diamond carbon atom, f and r denotes forward and reverse rate respectively. The * indicates a surface biradical [46].

Reaction	K_f	K_r
1. $C_dH+H \leftrightarrow C_d+H_2$	$1.83x10^{12}$	$3.63 x10^{9}$
3. $C_d+ CH_3 \leftrightarrow C_dCH_3$	$2.06 x10^{12}$	$1.13 x10^{5}$
5. $C_dC_xH_y \leftrightarrow C_dC_xH_y$-1+ H_2	$1.83 x10^{12}$	$4.76 x10^{9}$
7. $C_dCH_y+CH3 \leftrightarrow C_dC2H_y+3$	$2.06 x10^{12}$	$1.13 x10^{5}$
9. $C_d+*+C_dC_xH_y \leftrightarrow C_d+C_dC_x$-$1H_y+C_d$	$3.57 x10^{11}$	N/A

Goodwin *et.al.* [41] proposed a diamond growth model based on surface reactions where atomic hydrogen is bonded to almost the entire surface. It was postulated that the primary mechanism that opens sites on the surface is by abstraction of surface-terminating hydrogen by atomic hydrogen. The reaction and associated rate, $R_{abs\text{-}H}$, is given by [41, 47]:

$$CdH + H \rightarrow Cd^{*} + H_2$$
$$R_{abs-H} = k_1[H]$$

where k_1 is the reaction rate constant and [H] is the atomic hydrogen concentration (flux) at the surface. The abstraction results in an open site on the

diamond surface, which can be filled by either a carbon radical species such as CH_3 or the adsorption of atomic hydrogen. The reaction and associated rate, R_{adH}, of hydrogen adsorption onto an open site, C_d^*, is

$$C_d^* + H \rightarrow C_d H$$
$$R_{adH} = k_2[H]$$

A growth species can also be adsorbed on to the surface with the reaction and associated rate for an open surface site given by:

$$C_d^* + CH_3 \rightarrow C_d CH_3$$
$$R_{adC} = k_3[CH_x]$$

Once the growth species is on the surface it can then continue along one of two primary paths. The first path is thermal desorption from the surface leading to an open site on the surface again. The reaction and associated rate for a given adsorbed site is

$$C_d CH_3 \rightarrow C_d^* + CH_3$$
$$R_{des} = k_4$$

The other pathway is the incorporation of the adsorbed carbon species into the diamond structure. The general event that begins this mechanism in growth models is an abstraction of hydrogen from the adsorbed carbon species.

$$C_dCH_3 + H \rightarrow C_dCH_2 + H_2$$
$$R_{abs-CHx} = k_5[H]$$

In steady state conditions this set of reactions can be combined to give a growth rate G given by [41]:

$$G = k_3 \frac{n_s}{n_d}\left(\frac{k_1}{k_1 + k_2}\right)\frac{[CH_3][H]}{\frac{k_4}{k_5} + [H]}$$

where n_s is the surface site density (2.61×10^{-9} mole/cm^{2}on (100) surfaces), n_d is the molar density of diamond (0.2939 mole/cm^3), k1, k2, k3, k4, and k5 is the reaction rate constant respectively. It was noted that in order to obtain a good quality diamonds with low defects, the carbon species concentration in the input gas flow (CH_4/H_2) should be low.

Mankelevich *et.al.* [48] described a more detail numerical model of the plasma and the plasma surface chemistry and the growth mechanism of single crystal diamond in microwave plasma CVD at operating pressure ranges from 100-180 Torr. The 2D model assumed that the CVD reactor has cylindrical symmetry with coordinate system r in the radial distance from the center line of the chamber, and z, the axial (vertical) height above the substrate surface. Also with the assumption that the plasma electron temperature, T_e ~ 1.5 eV, plasma volume, V_p ~ 5 cm^3, and microwave absorbed power density ~ 120 W/cm^3.

Shown in Figure 2.5(a) is the temperature distribution across the center of the plasma with average value of ~3300 K across the plasma discharge. The gas temperature drops significantly in the gap of a few mm between the plasma ball and the substrate surface. Based on their calculation the substrate temperature is at around 1600 K. Figure 2.5(b) shows the H atom mole fraction expressed as a percentage and H atom is a maximum in the hottest region at the center of the plasma ball but decays at the substrate surface. They concluded that there are a significant number of H atoms striking the surface that can initiate abstraction reactions and create the radical sites necessary for diamond growth.

Figure 2.6 shows the mole fraction profiles for (a) $C_2(a)$ and (b) CH_3. The $C_2(a)$ concentration was much localized in the hot center of the plasma ball where it was created, but outside of this region including near the substrate surface, the concentration rapidly falls to negligible levels. It was postulated that for CH_4/H_2 plasmas, emission from the Swan band of excited C_2 occurs over most of the visible region that produces most of the light which gives the plasma its apparent visual size as shown in Figure 2.6(a). Since the CH_3 maximizes around the periphery of the hot gas region, and thus it was these regions that will be important for diamond growth.

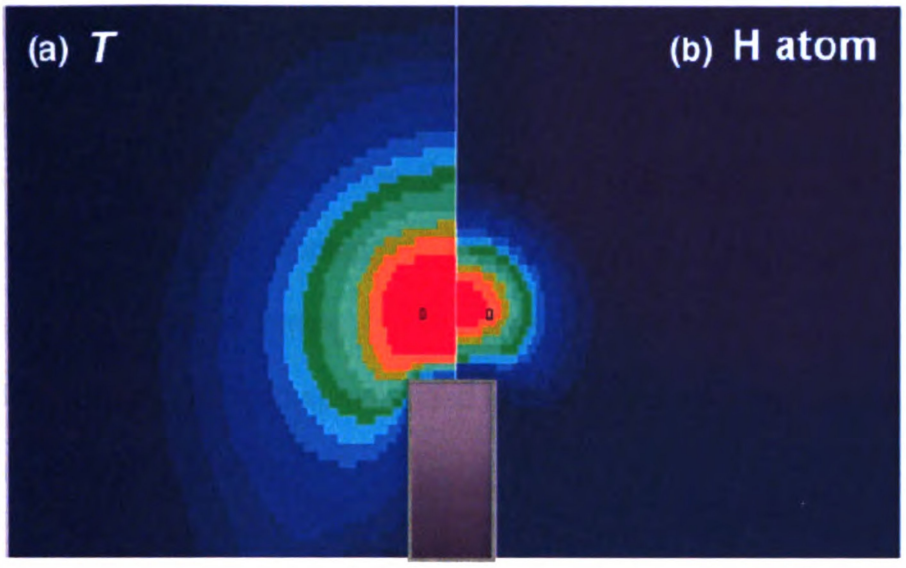

Figure 2.5 - 2D plots of the calculated (a) gas temperature, T, in Kelvin and (b) H atom mole fraction for substrate holder diameter D_{sh}= 9 mm and power density ~120W/cm^3 [48].

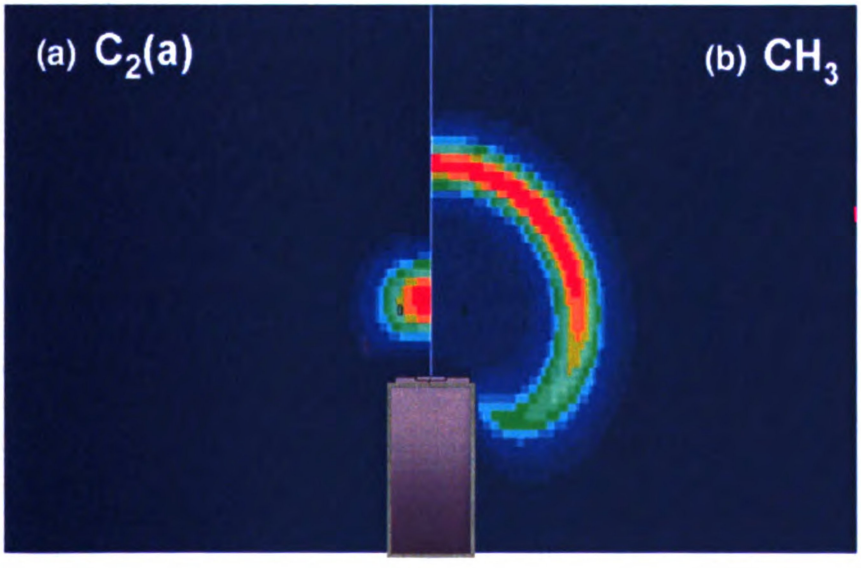

Figure 2.6 - 2D plots of the calculated (a) $C_2(a)$ and (b) CH_3 mole fraction for substrate holder diameter D_{sh}= 9 mm and power density ~120 W/cm^3 [48].

2.5 Microwave plasma CVD diamond synthesis literature review

The microwave plasma CVD diamond synthesis at high pressure literature review in this section is divided into two parts: (1) polycrystalline and (2) single crystal diamond. Reactor configurations, operating conditions, and deposition results are summarized below. Lower pressure MPACVD for polycrystalline diamond synthesis has been summarized in previous research thesis at Michigan State University [7, 8, and 49].

2.5.1 Polycrystalline diamond

Lately, polycrystalline diamond via microwave plasma assisted chemical vapor deposition is synthesized at an increasing pressure i.e., 100 Torr and above. Presented below is literature review of polycrystalline diamond synthesis via microwave plasma assisted CVD operated above 120 Torr using 2.45 GHz excitation.

Chein *et.al.* [44] in 1999 investigated the effect of using high power density microwave plasma with elevated substrate temperature and oxygen addition into their methane/hydrogen gas mixture. Diamond growth rate of 30 μm/hr was achieved with operating pressure of 150 Torr, substrate temperature up to 1620 °C, methane concentration of 1-50%, and input microwave power between 1400-1750 kW. The reactor used was microwave plasma CVD with magnetron output power up to 6 kW as shown in Figure 2.7. A quartz window of 0.25 inch thick was

used to separate the discharge chamber and the rectangular waveguide. The diamond growth rate increases as the substrate temperature and methane concentrations increases. It was found that the higher substrate temperature resulted in a higher growth rate. However, graphite was usually deposited at substrate temperature above 1200 °C when using lower pressure low power density microwave plasma. By using high power density microwave plasma, diamond can grow at substrate temperature of 1500 °C with 1% methane mixed into the hydrogen.

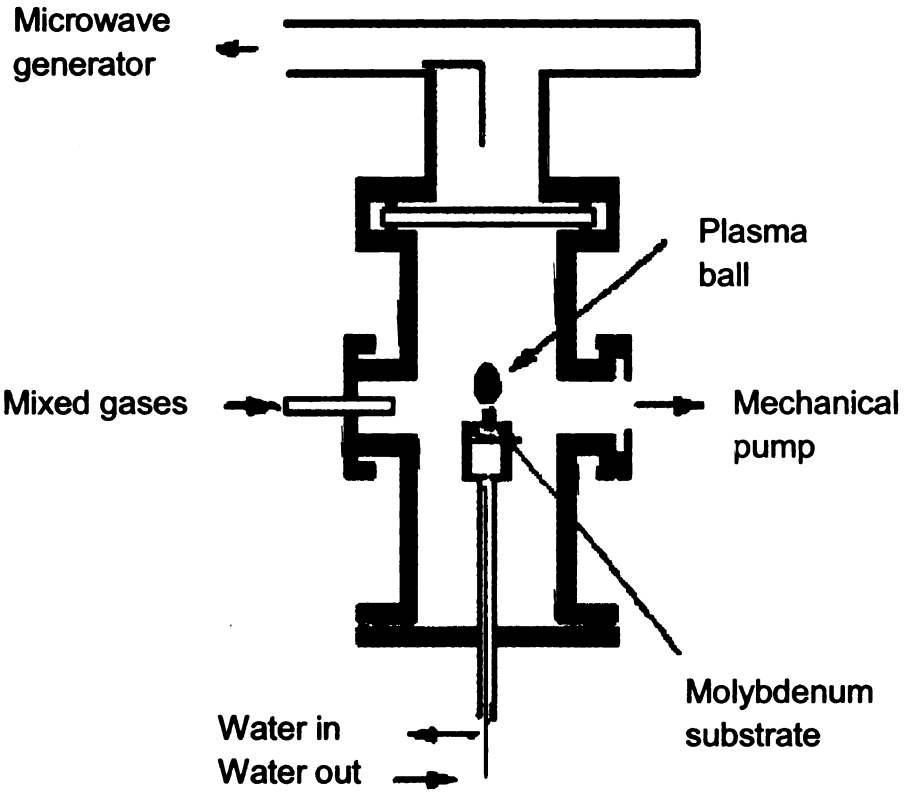

Figure 2.7 - Microwave plasma assisted CVD reactor used at Auburn University [44].

Mortet *et.al.* [4] in 2004 investigated polycrystalline diamond growth rate at high pressure up to 250 mbar (~ 187 Torr) using high power microwave plasma CVD rotational ellipsoidal reactor. The substrate was 5 mm thick (100) silicon with diameter of 2 inches and mechanically seeded with diamond powder. Growth rates up to 4.5 μm/hr were obtained using hydrogen methane gas mixture in the range of 0.5-3% of CH_4 in hydrogen. Shown in Figure 2.8 is the microwave ellipsoidal reactor which consists of waveguide system with an axial antenna, ellipsoid cavity, and quartz bell jar that contains the deposition chamber. It is a 2.45 GHz operating frequency with 6 kW of magnetron power. It was found that the growth rate increases linearly with methane concentration up to 1% followed by saturation, nearly linear increase in growth rate with total pressure at methane concentration of 0.5%. Also, the growth rate increases with higher substrate temperature.

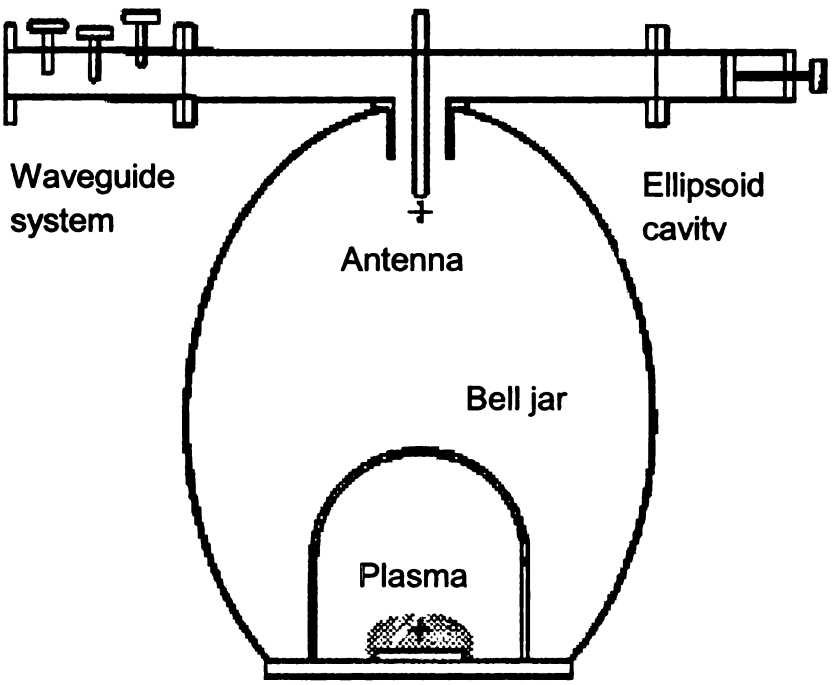

Figure 2.8 – Ellipsoidal high pressure microwave plasma assisted CVD reactor [50].

Kuo *et.al.* [6] and Kahler [7] in 1997 and investigated polycrystalline diamond uniformity and quality of freestanding film using 2.45 GHz microwave cavity applicator as shown in Figure 2.9. They initially explored the synthesis of diamond film at high pressure using this microwave plasma cavity reactor and studied the growth rate versus methane concentration and substrate temperature. Zuo *et.al.* [49] then optimized the reactor to enable larger substrate deposition, better cooling, and better uniformity of the grown polycrystalline diamond. The substrate diameter deposited was up to 75 mm on silicon wafers. The growth rate achieved was in the range of 0.5 to 6 μm/hr. The operating conditions were 80 to 160 Torr deposition pressure, 3.0 to 4.5 kW of microwave input power, and up to 8% of methane concentration.

The maximum growth rate achieved was 8 μm/hr while the minimum growth rate was 0.1 μm/hr with methane concentration varied between 1-8% and substrate temperature varied between 700-1100 °C [7].

The variation of grown freestanding diamond uniformity on 50 mm diameter substrate with 75 μm thick was ± 4.7% and ± 4.0% in the radial and circumferential directions. This indicates an excellent uniformity of the grown freestanding diamond. An additional of argon gas into the gas deposition chemistry was found to be useful in maintaining the plasma discharge coverage of larger diameter substrate and hence produced a good uniformity [49].

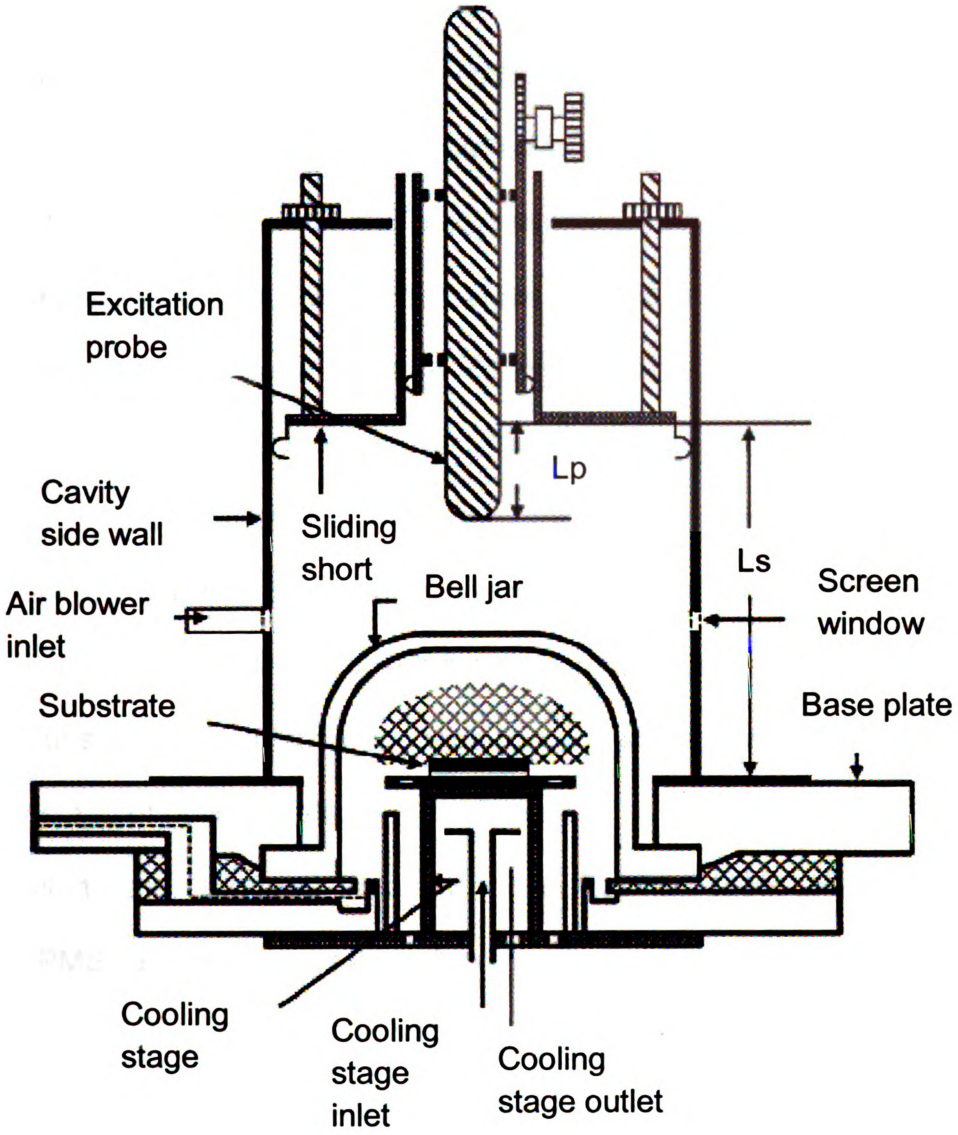

Figure 2.9 - MSU high pressure microwave plasma assisted CVD reactor [7, 8, 49].

Bachmann *et.al.* [43] in 1991 investigated diamond deposition at high pressure by improving the earlier generation of ASTeX bell jar design reactor. The high pressure microwave source (HPMS) operated up to 140 Torr is shown in Figure 2.10. The magnetron and power supply was increased up to 8 kW, the bell jar was replaced with a silica microwave window, and the substrate position could be adjusted to optimize substrate-discharge interaction and grown diamond film uniformity. The growh rates achieved using this reactor is reported between 4-14 μm/hr. The main drawback of this reactor has been reported that when the input power is too low or pressure is too high, the plasma can not be sustained. Also when the power level is too high for a given pressure, the plasma discharge becomes unstable. The discharge tends to jump into the reactor silica vacuum window instead of hovering above the substrate.

Mollart *et.al.* [51] and Ralchenko *et.al.* [52] in 1999 utilized the 5 kW ASTeX HPMS reactor to grow free standing diamond wafer on 50 mm polished tungsten at operating pressure up 140 Torr. The uniformity of the grown diamond was found to be increasingly non-linear above 80 Torr and 3 kW. The limit of the uniform deposition for 25 mm diameter wafer was at 140 Torr with 4.5 kW microwave power.

Ando *et.al.* [53] in 2001 also utilized the 5 kW ASTeX reactor to grow polycrystalline diamond at high pressure of 100-120 Torr. The substrate was a one inch silicon wafer with gas chemistry of CH_4-H_2-O_2 mixture. The maximum growth rate achieved was 9.3 μm/hr when the CH_4 concentration was 2 to 4%, a microwave power of 4.5 kW and gas pressure of 120 Torr.

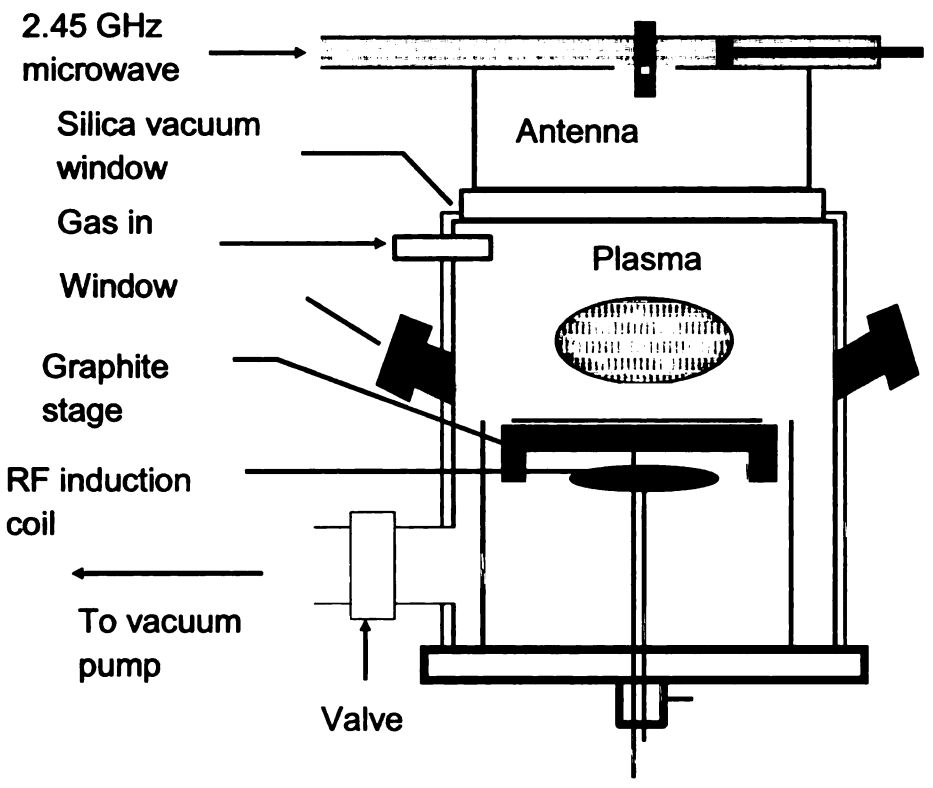

Figure 2.10 - ASTeX 2.45 GHz high pressure microwave source diamond CVD reactor [43].

2.5.2 Brief history of single crystal diamond synthesis

Kamo *et.al.* [1] in 1988 was the first to report homoepitaxial chemical vapor assisted diamond film synthesis. Since then, especially during the 1990's, homoepitaxial diamond synthesis by microwave plasma assisted chemical vapor deposition (MPACVD) has been extensively investigated in Japan, Europe and the U.S. A 2006 review article by T. Teraji [2] summarizes these early investigations. In particular, these early investigations employed low power density microwave discharges/reactors (< 5 W/cm^3) operating within the 20-100 Torr pressure regime with input CH_4/H_2 gas mixtures varying between 5% to much less than 1%. MPACVD was chosen as the method of synthesis because of the deficiencies with the other competing methods. For example the hot filament reactor suffers from filament contamination issues and the combustion flame suffers from film nonuniformity and ambient gas contamination problems. Good high-quality single crystal diamond (SCD) films were synthesized using MPACVD. However high-quality SCD films were only produced under low methane input conditions (< 1%) and as a result diamond growth rates were very low; i.e < ~1 micron/h. Attempts to increase the growth rate by increasing the input methane concentration led to formation of defects such as secondary nucleation and unepitaxial crystallites. While these results [2] were of scientific interest the very low growth rates limited the commercial potential/interest in the plasma assisted CVD synthesis of SCD. The challenge that remained was to find

synthesis methods that dramatically increase the deposition rate while maintaining crystalline quality.

However, recently the interest in MPACVD SCD synthesis has dramatically increased due to the results from a number of very promising experiments that employ high microwave power density and high pressure (100-200 Torr) microwave plasma reactor technology. SCD synthesis rates of 50-100 micron/h have been demonstrated. The initial communications [3, 5] that suggested the potential feasibility of high growth rate homoepitaxial synthesis of SCD by high power density and high pressure, MPACVD were reported in the late 90s and early 2000's. Since then these results have been confirmed and extended by others [6, 54-56] around the world and now most research activities concerned with the synthesis of SCD are focused on the development of high power density, high pressure MPACVD reactors and the associated processes methods that take place within this new process/pressure (100 -200 Torr) regime.

It is now commonly understood that we are in the beginning of a major revolution in the science and technology of diamond. High quality SCD blocks and plates have already been produced by employing high power density, high pressure MPACVD and significant process improvements, i.e. interns of increased synthesis rates, improved diamond quality, and large synthesized diamond crystal size, appear possible with the design of optimized high-power MPACVD reactors and the associated development and refinement of high pressure high power CVD processes.

2.5.3 Single crystal diamond

Described below is the summary of single crystal diamond deposition reported by various research groups. This includes reactor type, substrate holder, substrate seed type and size, gas chemistry, substrate temperature and the evaluation or characterization measurement method. Also, pre-treatment and post-treatment procedures and grown diamond material quality are presented.

Hemley *et al.* [5, 37, 57-62, 52C] success in growing synthetic high quality single crystal diamond with extremely high growth rates has renewed the interest of single crystal diamond synthesis research. High quality single crystal diamond was synthesized. The SCD has smooth, transparent surfaces and other characteristics identical to those of high-pressure high temperature synthetic diamond. It was suggested that the production of high quality single crystal diamond greatly depends on the substrate holder design, methane concentration and the ability to control the substrate temperature. Furthermore, when the reactor pressure is increased from 60 to 200 Torr, the diamond growth rate increases (approximately five-fold) while penetration twins decreases. The experimental operating parameters and growth conditions are described below.

Reactor:

The reactor was a 6 kW, 2.45 GHz microwave plasma consisting of a cylindrical stainless steel vacuum chamber with volume of 5000 cm^3. The original microwave applicator was made by Wavemat Inc. which is a variation of reactor

shown in Figure 2.9. The amount of microwave power applied during deposition was between 1 to 2 kW. The MPACVD system contained a quartz bell jar that acts as a chamber seal. The plasma discharge is generated within the chamber above the holder assembly inside the vacuum chamber. Other reactor utilized for SCD growth was ASTeX/Seki 5400 2.45 GHz 5kW reactor which is a variation of reactor shown in Figure 2.10.

Substrate holder and stage:

The holder assembly consists of a stage, set rings, collets and sheath or substrate holder [61-62]. The diameter of the stage and the sheath was 10.1 cm and 2.5 cm respectively. The stage was enclosed by a quartz bell jar dome and connected to the base plate. This holder assembly and the bell jar were located inside the cavity reactor system. During the diamond deposition process, the stage was water-cooled and it is attached to the base plate by bolts. The substrate holder holds the diamond in a stationary position and acts as a heat sink, which prevents the formation of twins or polycrystalline diamond along the edges of the growth surface of the diamond. The diamond was mounted on a diamond actuator within the sheath of the specimen holder assembly. The stage, set rings, and sheath were made of molybdenum since these materials have a high thermal conductivity and high melting point, which is 2617 °C. During the diamond deposition, the growth process was periodically halted so that the position of the diamond can be adjusted downward with respect to the substrate holder to reduce the distance D, and height H, adjustments. This repositioning

allows the diamond growth on the surface of the holder to occur within the desired region of resonant microwave plasma discharge.

Substrate type and size:

The substrates were 3.5 x 3.5 x 1.6 mm^3 HPHT synthetic type Ib or type IIa diamonds with deposition surface within 2° of the {100} top surface.

Pre-treatments procedure:

The substrates were cleaned ultrasonically with acetone

Gas pressure and chemistry:

The gas pressure during the diamond growth ranges from 120 to 220 Torr. The gas concentration is N_2/CH_4 = 0.2–5.0%, CH_4/H_2 = 12–20%. For example: 500 sccm of H_2, 60 sccm of CH_4, and 1.8 sccm of N_2. A small amount of oxygen is sometimes added 0.2-2% O_2/CH_4 to lower growth temperature, which can remove the nitrogen-related impurities and reduce the silicon and hydrogen impurity levels.

Temperature reading:

The deposition temperature was measured by a two-color infrared thermometer. The thermal emission was focused through a quartz window at an incident angle of 65°on the target, with a 2-mm diameter minimum target size. The substrate temperature reading ranged from 900 to 1500 °C during the diamond growth process. It was found that there was a strong dependence on

temperature versus the morphology and quality of the synthesized diamond. For example, when the temperature range is < 1000 °C, the type of diamond produced is spherical, black diamond like carbon, 1000-1100 °C produced smooth dark brown, 1100-1200 °C produced brown diamond, 1200-1220 °C produced smooth yellow tinted diamond, 1220-1400 °C produced step flow type pyramid like octahedron tinted yellow, and temperature range > 1300 °C produced twinned or polycrystalline diamond [61].

Post treatments procedure:

The yellow or brown diamond was annealed under HPHT at pressure of 5-7 GPa (37.5-52.5 Mega Torr) and temperatures of 1,500-2000 °C for a few minutes to several hours which then transformed the CVD diamond into transparent colorless material, and lightening the tint of the type Ib seed crystals. To enhance the optical properties of the grown SCD diamond, low pressure high temperature annealing were performed at operating pressure of less than 300 Torr and temperature up to 2200 °C [63].

Grown diamonds quality:

Figure 2.11 shows the UV-visible absorption coefficient of the grown single crystal diamonds [37]. The higher the nitrogen content in the synthesis gas results in a higher ultra violet-visible absorption. It was observed that the intensities of nitrogen related bands decrease with lower nitrogen concentration in the gas chemistry. They suggested that the SCD-3 has higher absorption

coefficient compared to the natural type IIa natural diamond was probably due to nitrogen impurities within the methane process gas.

Figure 2.12 shows the infrared-absorption spectra of light brown and colorless single-crystal CVD diamond [34]. The results show typical absorption for CVD diamond with strong peaks near the infrared at various wavenumber which corresponds to hydrogen impurities. The broad band at 2930 cm^{-1} was suggested that it was attributed to hydrogenated amorphous carbon. The strong absorption in the near infra red region at 7358, 7234, 6857, and 6427 for the brown single crystal CVD was concluded due to hydrogen impurities. When the spectrum of the two samples was compared, the colorless single-crystal CVD diamond was smoother and free of spikes within the same region.

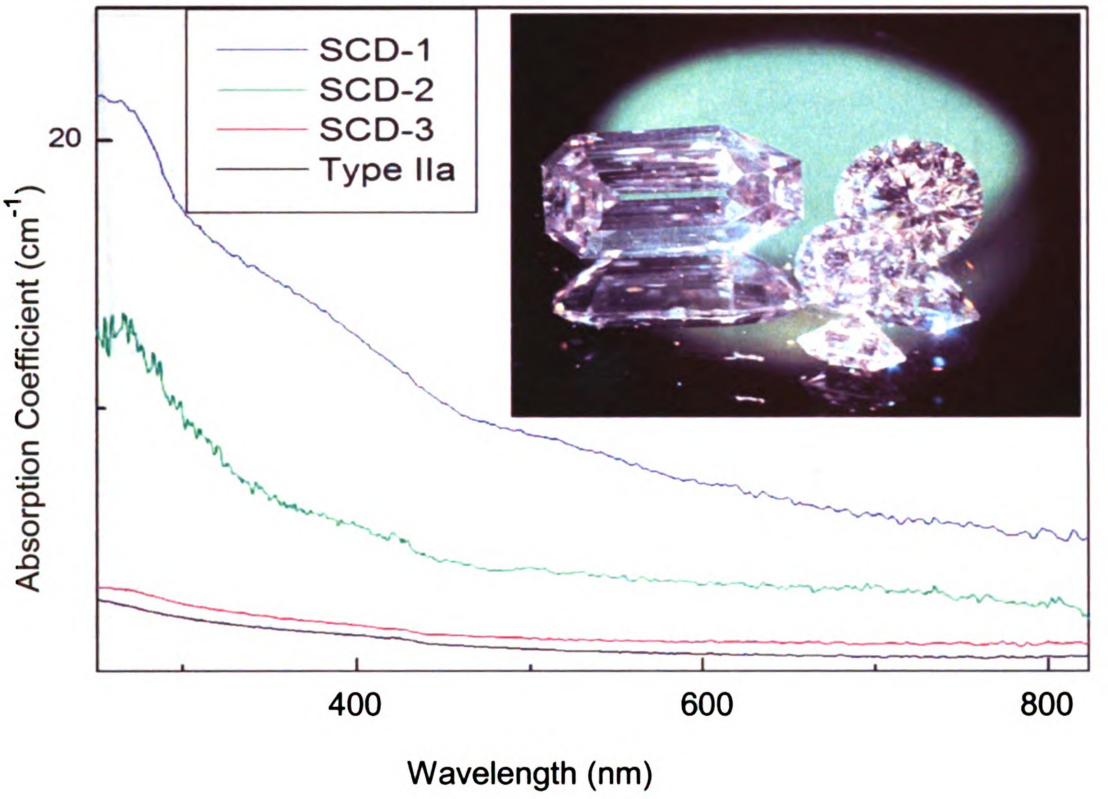

Figure 2.11 - UV–Visible absorption coefficient of single-crystal CVD diamond samples and natural type IIa diamond. The inset shows examples of three single crystal diamonds [37].

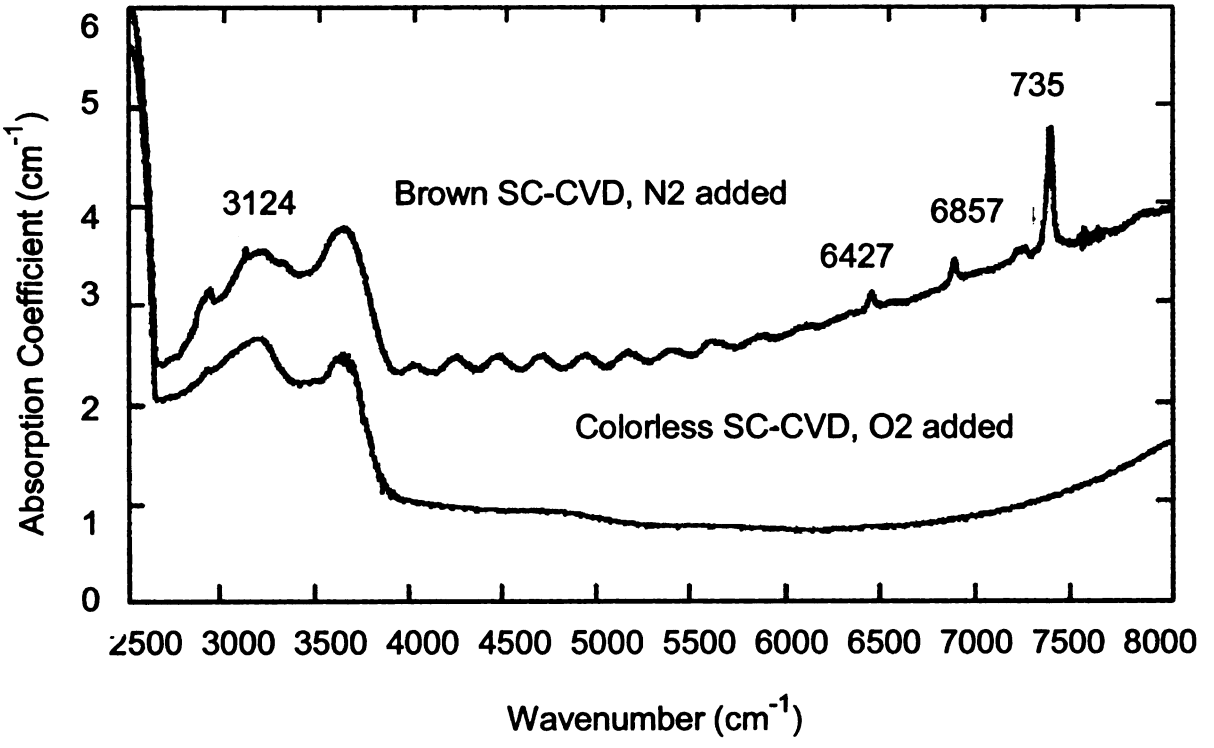

Figure 2.12 - Infrared absorption spectra of near colorless and light brown single-crystal CVD diamond [34].

Yamada *et.al.* [54, 64-69] synthesized single crystal diamond growth by a repetition steps method, which had nitrogen gas added to the gas phase. A repetition growth method was employed because during the deposition, as the amount of the polycrystalline diamonds increase on the holder, the films sometimes peeled off the holder or overheated and then were incorporated into single crystal material. Sometimes these polycrystalline diamonds also disturbed the growth temperature measurement. In order to avoid these problems, it was necessary to interrupt the diamond growth periodically and clean the substrate holder. The addition of nitrogen enabled long-term growth conditions that are required to produce large crystals. It was suggested that the holder diameter, nitrogen methane ratio and the reactor pressure have strong influence on the growth rate and the diamond quality. The growth rates achieved ranged from 30 - 120 μm/h, depending on the growth conditions.

Reactor:

The microwave plasma CVD system was a 5-kW, 2.45 GHz Seki Technotron AX-5250. The applied microwave input power ranged from 1.2 to 3.6 kW. Figure 2.13 shows the cross section of the reactor. A rectangular waveguide is connected to the cylindrical cavity with antenna probe located at the center and top sections of the cavity applicator. The inner diameter of the cylinder is 14 cm. A quartz plate separates the cavity atmospheric region from the vacuum plasma discharge region. The cooling stage and substrate holder that contains a diamond seed was placed at the bottom floor of the vacuum chamber.

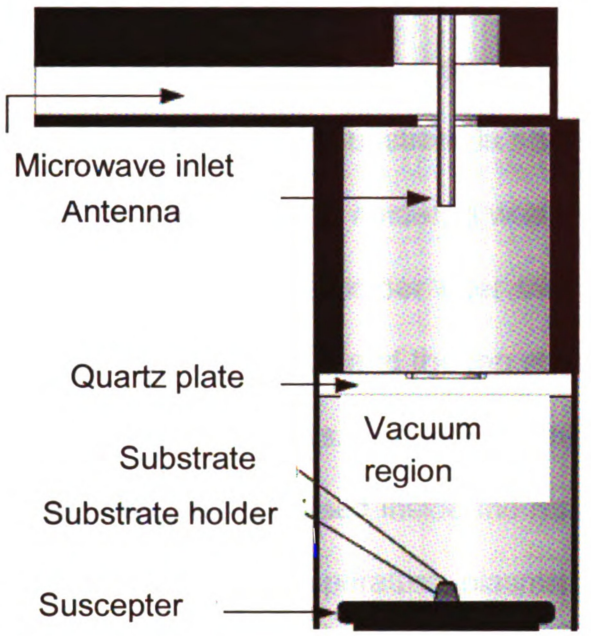

Figure 2.13 - Schematic of the reactor based on plasma model analysis [64].

Substrate type and size:

The substrate type was Ib HPHT synthetic single crystal diamond seed from Sumitomo with (100) orientation. The size of the substrates was either 3 x 3 x 0.5 mm^3 or 5 x 5 x 0.7 mm^3 or 27-37 mm^2.

Substrate holder:

Figure 2.14 shows schematic drawings of the two types of substrate holders; i.e., the open and enclosed type substrate holder. The enclosed type holder supports a substrate inside a drilled hole in the Molybdenum rod, in which

the surface of the diamond seed is beneath the top surface of the substrate holder. In contrast, the open type holder supports a substrate on the Molybdenum rod where the surface of the substrate is above the top surface of the substrate holder. For the enclosed type holder, d was defined as final depth of diamond relative to top surface of the holder after the growth. Both of the holders have a conical shape with a flat top and the top surfaces have a smaller diameter than the ASTeX's original holders. Figure 2.15 displays the placement of the substrate holder and the diamond seed inside the reactor. This schematic drawing was used for the simulation of temperature, plasma density and gas flow distributions analysis.

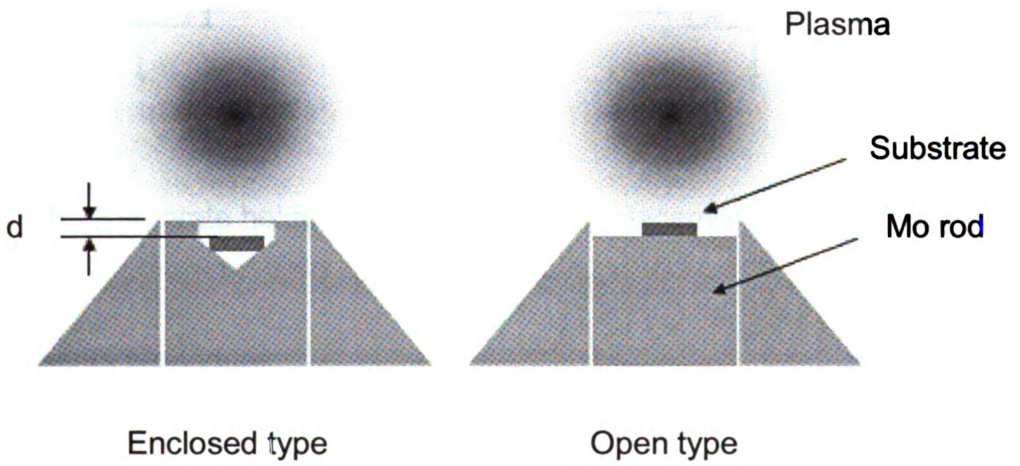

Figure 2.14 - Schematic illustration of enclosed type and open type holders [54].

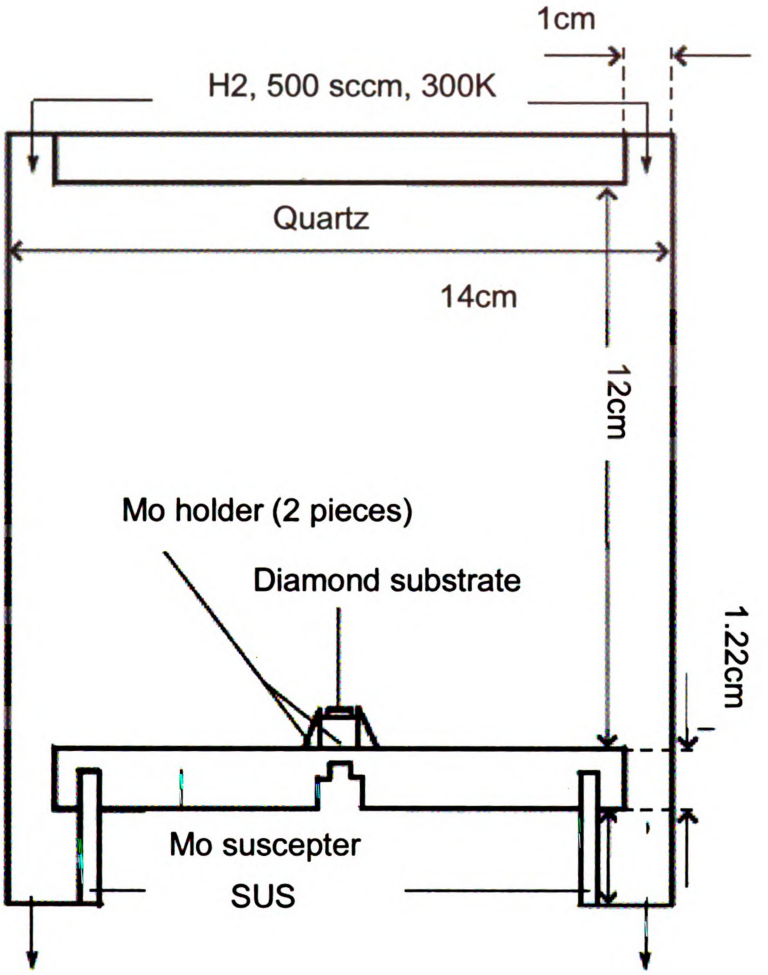

Figure 2.15 - Substrate holder and diamond seed placement in the reactor [69].

Pre-treatments procedure:

The substrate was cleaned with isopropanol in an ultrasonic bath before placed on substrate holder and put into the reactor. Igniting the discharge at low pressure, the H_2 gas was brought up to the operating pressure. When the growth pressure (128-218 Torr) and substrate temperature (1100–1200 °C) were reached, a 1.8 sccm amount of nitrogen was then added to the H_2 flow (3%

N_2/CH_4 and 12% CH_4/H_2). The typical etching depth is estimated to be 1.4 μm. After the 30 minutes etching, methane gas is introduced to the chamber to start the diamond growth deposition.

Gas pressure and chemistry:

The pressure of the reactor during the etching and the growth was 17-29 kPa (128 -218 Torr) and the gas flow rate was 60 sccm for CH_4, 500 sccm for H_2, and 0.6-1.8 sccm for N_2 (3% N_2/CH_4 and 12% CH_4/H_2). The process gas used has a high purity grade (6 N) hydrogen, (6 N) methane, and (4 N) nitrogen.

Temperature reading:

The growth temperature was measured by an optical pyrometer and monitored by a 2-color infrared radiation thermometer observed through a quartz viewing port. The substrate temperature reading for the open type holder range was 1130 - 1220 °C and 1155 - 1180 °C for the enclosed type holder. The color of diamond films grown at substrate temperature higher than 1100 °C was similar to the color of Ib seed crystal. The color becomes dark for the film grown at 1060 °C.

Grown diamonds quality:

The films grown by the open type holder indicated the promotion of edge growth. On the contrary, the films grown by the enclosed type holder produce flat surface morphology without growth at the rim. Figure 2.16 shows the optical microscope images of grown diamond after first growth (left) and repetition of

growth (right) for the open and enclosed type holder. In the case of the open type holder, a crack appeared in the center part after the second growth and additional growth steps. In contrast, by using the enclosed type holder, the surface morphology is much smoother and flatter without growth hillocks or non-epitaxial crystallites even after the 5th growth. The average time for each growth step is 7 to 8 hours.

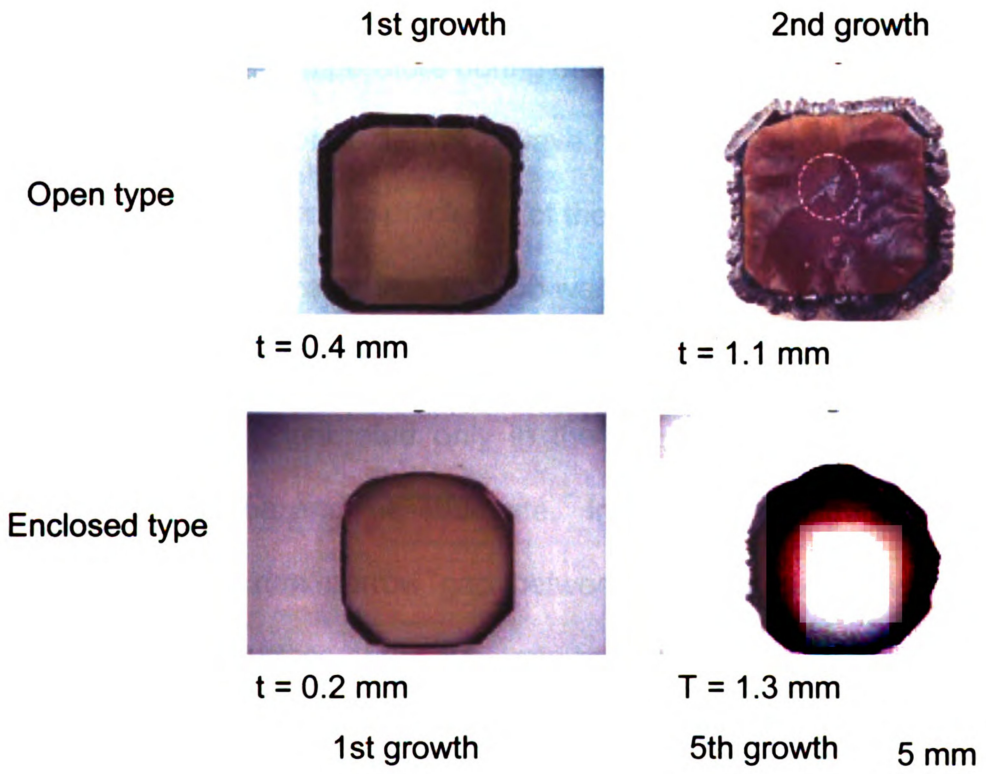

Figure 2.16 - Optical microscope images of grown diamond after 1st growth (left) and repetition of growth (right) for the open and enclosed type holder [64].

Yamada *et.al.* [70] further modified the reactor in order to produce high power density plasma to obtain higher diamond growth rates. Figure 2.17(a) shows the schematic cross-sectional view of the conventional reactor, which is the AX6500 produced by SEKI Technotron Corp. The microwave energy enters from the bottom of the discharge chamber and focused above the substrate holder on the stage. The distance from the top wall to the substrate holder is around one wavelength ~ 12 cm. The top wall has ports which are used to measure the substrate temperature during diamond deposition.

A modified variation of the microwave plasma CVD reactor was proposed in order to enhance the power-efficiency of the growth. This was done by altering the conventional structure, where the top-wall of the chamber was replaced by cylindrical conductor made by Cu. This acts as an antenna, and expected that the plasma could be generated only in the narrow gap between the bottom surface of the antenna and the substrate. In the new configuration plasma is generated in a ~10 mm narrow gap between the bottom surface of the Cu cylinder and the top surface of the substrate holder as shown in Figure 2.17(b).

The radial profile of the power density for the conventional configuration homogeneity was maintained up to 110 Torr. However, for 180 Torr, the power density decreases 25% of its maximum at 1/2 inches in radius. The profile has its maximum value at the central position and monotonically decreases as a function of radius in this case. On the other hand, for the case of the new configuration, the power-density is relatively high at the edge-region. Even for such high pressure, variation in radial direction is almost 10%.

In terms of growth rates, for the conventional configuration, growth rate was smaller in the edge region than that of central region and gradient of the power density was more intense for higher pressure. The growth rate reaches 40–50 μm/hr for 110 Torr, and 15–30 μm/hr for 80 Torr.

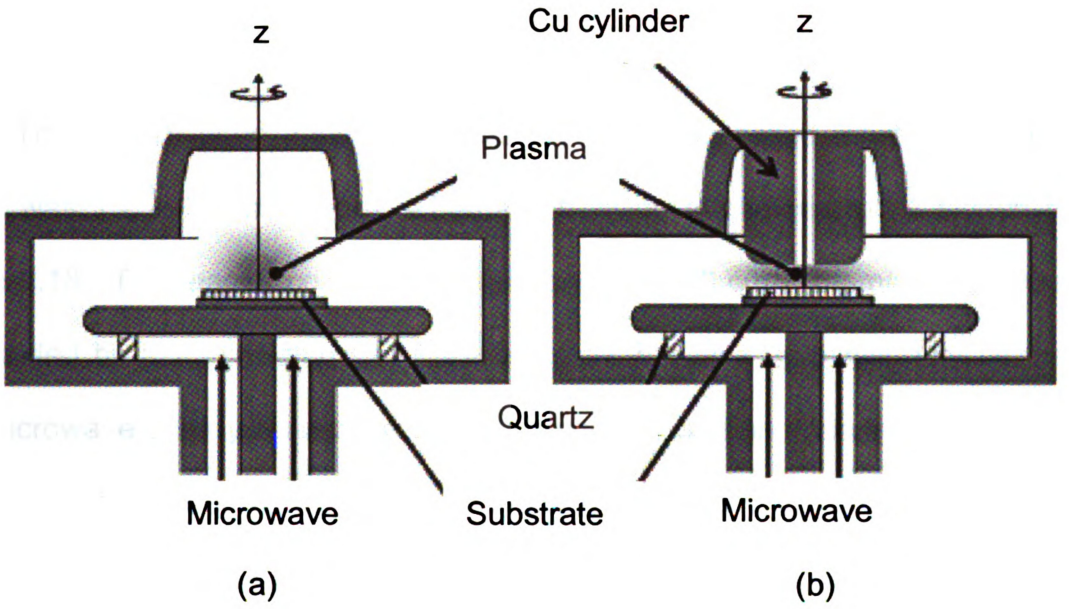

Figure 2.17 - Cross sectional view of the reactor configurations for high power density plasma a) conventional configuration, b) new configuration [70].

Gicquel *et al.* [55, 71-74] at the University of Paris with the collaboration of King's College London and the University Warwick, United Kingdom synthesized single crystal diamond deposition using MPACVD. High absorbed microwave plasma power densities of about 95 W/cm^3 were measured during the deposition. A 520 μm thick single-crystal was synthesized with growth rate at 6 μm/h.

Reactor:

The reactor used 2.45 GHz excitation and the applied input microwave power was 1.2 – 3.1 kW. The schematic drawing of the reactor is shown in Figure 2.18. The reactor consists of a quartz bell jar 10 cm in diameter that was surrounded by a 25 cm diameter Faraday cage that acts as a resonant cavity. The microwave energy was coupled via a waveguide and antenna into the cavity. The substrate holder can be adjusted axially to obtain a maximum plasma discharge interaction with the diamond substrate, which leads to deposition uniformity.

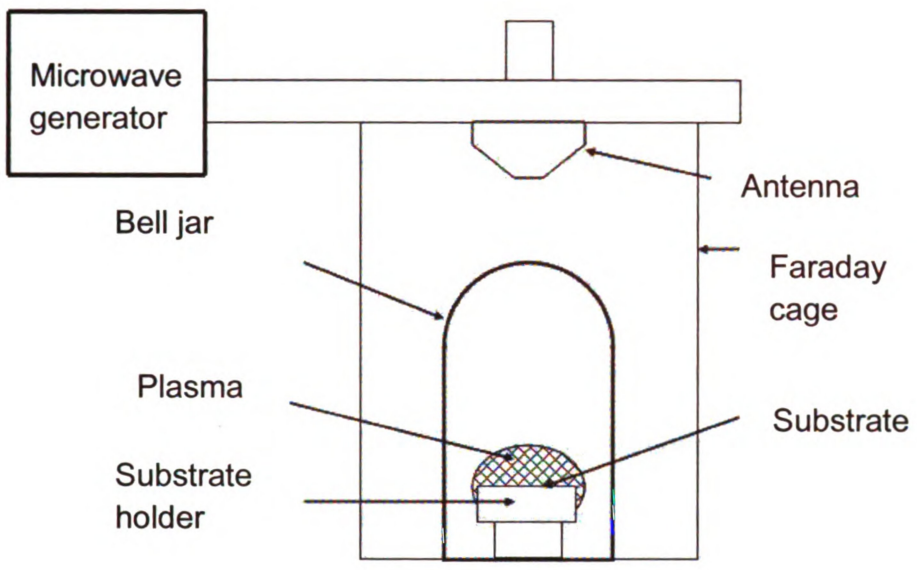

Figure 2.18 - LIMHP France MPCVD reactor [71].

Substrate type and size:

The diamond substrate was type Ib commercial HPHT (100) with dimensions of 3 x 3 x 1.5 mm^3 and natural type IIa diamond single crystal seed with 2 x 2 x 0.25 mm^3.

Pre-treatment procedures:

The diamond seeds were first cleaned in boiling sulfochromic acid followed by cleansing with HCl/HNO_3 mixture in order to remove any metallic, graphite or organic contamination. The samples were then brazed under high vacuum on a molybdenum plate using gold as a brazing metal in order to improve the thermal contact between the sample and the cooled substrate

holder. Plasma etching of the samples was performed for different etching times ranging from 1 hour to 4 hours using gas mixture of 2% O_2, 10% Argon and 88% H_2, or gas mixture of 2% O_2 and 98% H_2.

Gas pressure and chemistry:

During the actual diamond growth, the total pressure inside the chamber was maintained at 220 mbar (~ 165 Torr). The methane concentration was varied from 2% to 7% in a total flow of 500 sccm. For some samples, 6 to 20 parts per million (ppm) of pure nitrogen was also introduced in the total gas flow corresponding to N_2/CH_4 ratio in the range 150 to 280 ppm.

Temperature reading:

The substrate temperature was varied in the range 750 – 1000 °C and maintained close to 800-850 °C.

Grown diamonds quality:

Figure 2.19 shows the differential interference contrast microscopy (DICM) images of the CVD diamond films grown at 850 °C with 2%, 4%, 6% and 7% of methane concentration. With 2% of CH_4, the growth rate was 2 μm/h, and the film surface was very rough, exhibiting a large number of pits. They suggested that this could be a consequence of a high etch rate by atomic hydrogen during growth enhanced at such high microwave power. When the concentration of CH_4 was increased, the growth rate was considerably increased, and the surface

morphology was improved. With 4% of methane, the growth rate was 6 μm/h and the crystal surface was very smooth. For the films grown with 6% and 7% of methane, the growth rates were 11 and 15 μm/h, respectively. The films were also of good quality with no un-epitaxial crystallites, but step bunching occurred in some parts of the samples as can be observed in Figure 2.19(c) and 2.19(d).

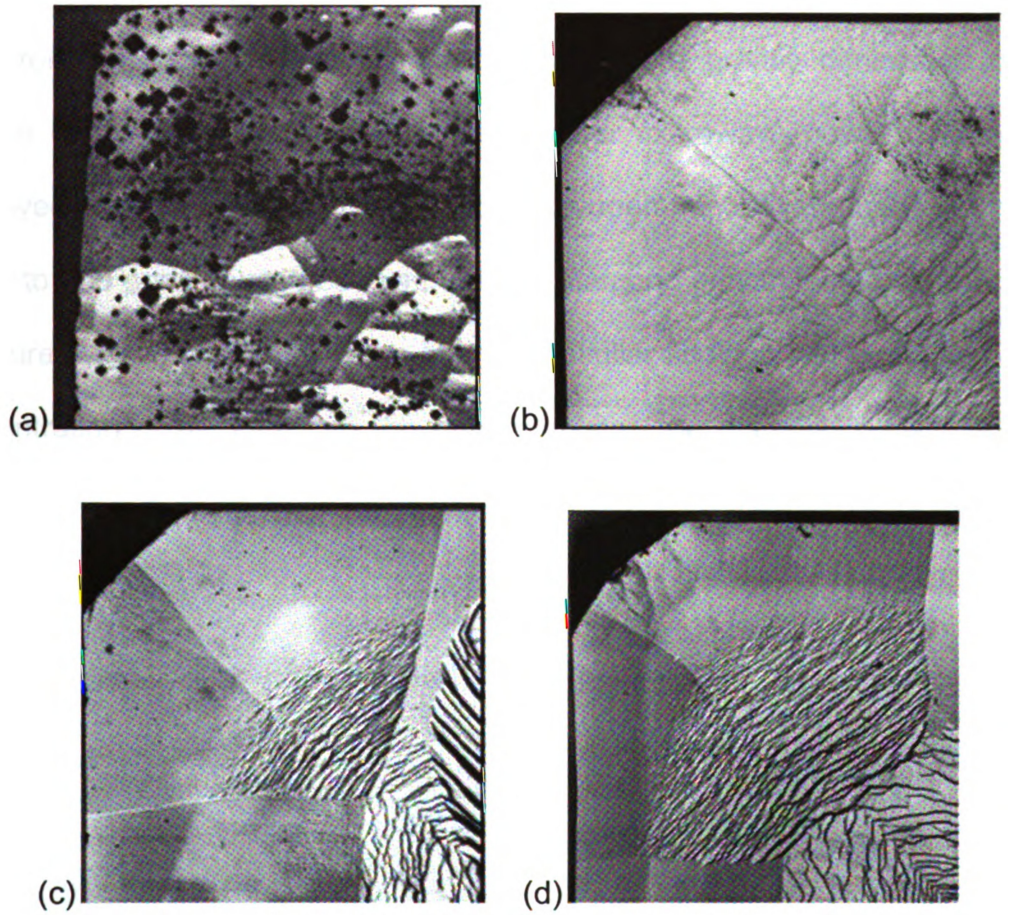

Figure 2.19 - DICM images of the diamond films grown at 850 °C with (a) 2% CH_4, (b) 4% CH_4, (c) 6% CH_4 and (d) 8% CH_4 [55].

Achard *et.al.* [42, 75] investigated the effect of using higher microwave power density discharge during the diamond growth. They performed a modeling of the plasma power density with respect to the distance of the substrate. The maximum CH_3 methyl radicals were closer to the surface when microwave power density increases. They suggested that when the gas temperature increases the CH_3 production zone will be closer to the surface and resulted in higher growth kinetics and a more efficient dissociation of the gas species. The appearances of large round hillocks on the diamond surface were greatly diminished or the surface becomes much smoother when higher microwave power density was employed during the deposition. By adding nitrogen from several parts per million (ppm) to 200 ppm, it was observed that the diamond growth increases as shown in Figure 2.20. Other researchers observed similar findings that by adding a few concentration of nitrogen into the gas chemistry, the diamond growth rate will increase.

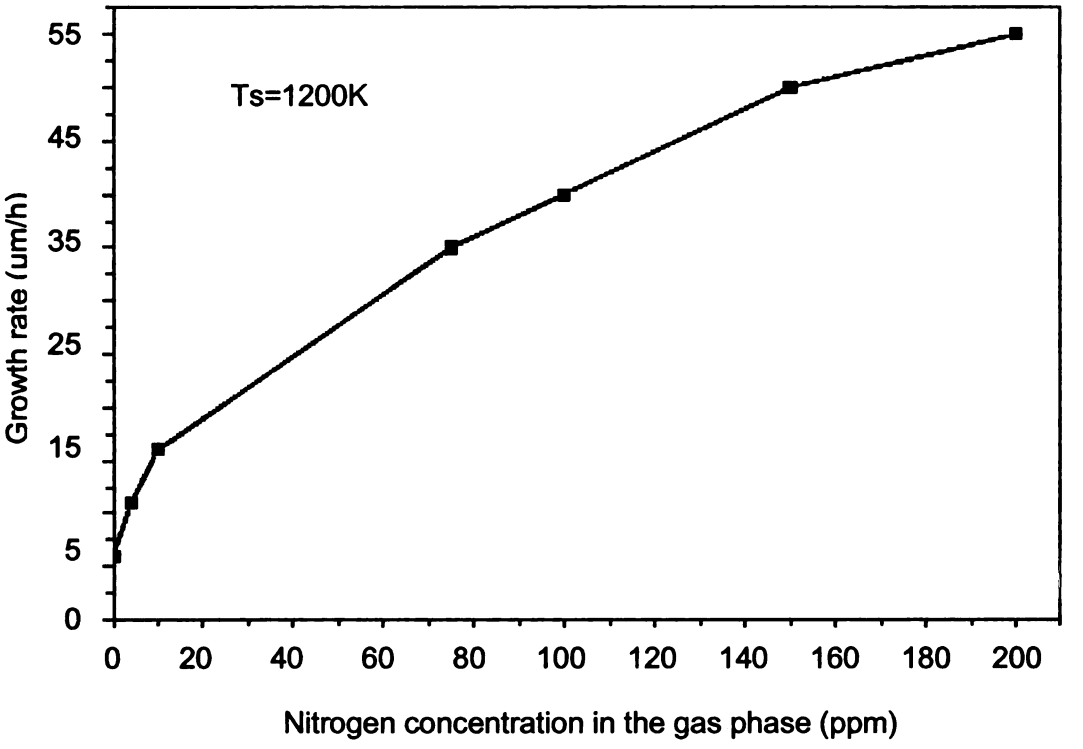

Figure 2.20 - Experimental growth rate as a function of nitrogen content in the gas phase with 4% of CH_4 and a microwave power density of 100 W/cm^3 [42].

Asmussen *et.al.* [76-82] grown single crystal diamond by employing two different types of diamond machines namely the 2.4 GHz and 915 MHz reactors. The gas chemistry consists of hydrogen-methane with and without addition of nitrogen and diborane. The SCD deposition was synthesized at operating pressure of 110-135 Torr on the 915 MHz and 160-260 Torr on the 2.45 GHz reactor. The 915 MHz reactor is a scale up of the 2.45 GHz and this reactor can accommodate multiple substrates deposition.

Shown in Figure 2.21 is the cross sectional view of the microwave reactor used for the multiple substrate SCD deposition i.e., up to eighty eight 3.5 x 3.5 mm^2 HPHT single crystal diamond seeds. The cylindrical cavity utilizes internal tuning that selects the electromagnetic excitation similar to the 2.45 GHz. This reactor can provide plasma-assisted deposition over 6-8 inch surface areas.

Figure 2.22 shows an optical micrograph top surface view of 70 grown single crystal diamonds. The growth conditions reported were as follows: pressure of 125 Torr, input microwave power of 11.5 kW, 7% CH_4/H_2 gas chemistry with addition of nitrogen of 150 ppm, and deposition time of 38 hours. The achieved average growth rate per seed was approximately 18 μm/hr. No major surface defects were reported on the grown diamonds.

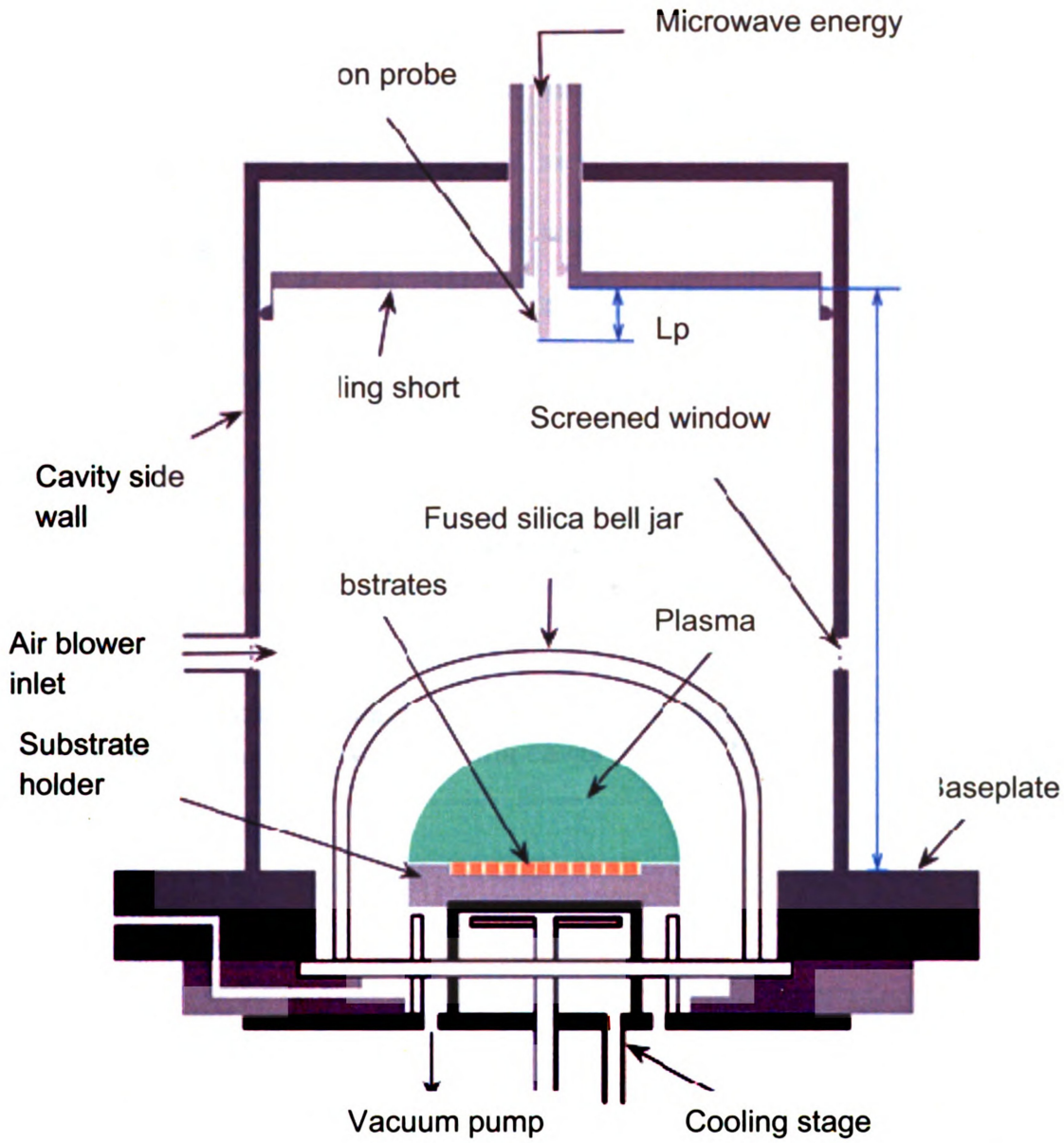

Figure 2.21 – MSU microwave plasma cavity reactor for multiple substrates single crystal diamond deposition [76].

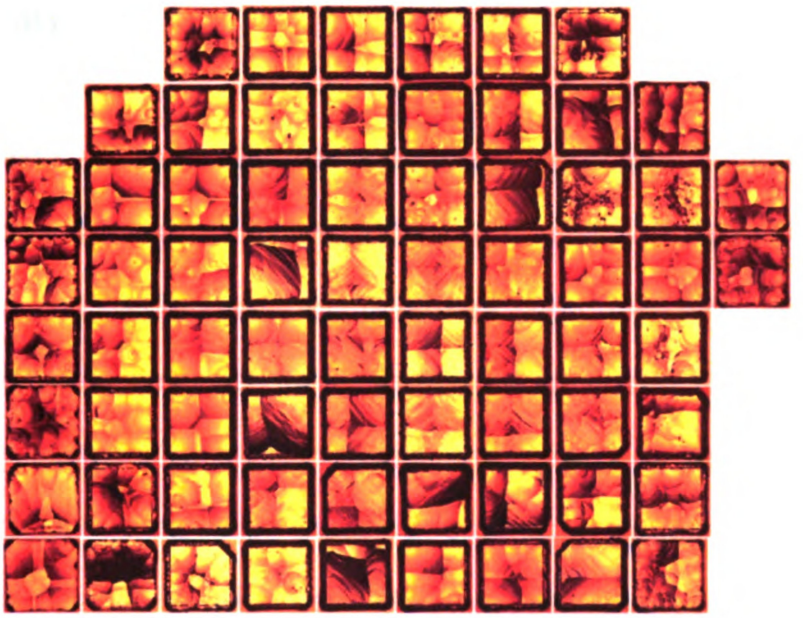

Figure 2.22 – Optical micrograph of the grown multiple substrates single crystal diamond using MSU microwave plasma cavity reactor [76].

2.6 Summary

Diamond CVD properties, general growth mechanisms, and synthesis via microwave plasma assisted chemical vapor deposition (MPACVD) for both polycrystalline and single crystal diamond has been reviewed. High pressure operation was mostly employed for single crystal diamond synthesis compared to polycrystalline diamond deposition. Since the size of the plasma discharge becomes smaller during high pressure operation, synthesizing large area polycrystalline diamond is still rather difficult. At this high pressure regime, there is still a limitation in the substrate coverage considering that polycrystalline substrate has been grown up several inches in diameter. The smaller size of the plasma discharge at higher pressure allows for single crystal diamond to be synthesized without worrying too much about maximum substrate coverage and uniformity. The single crystal diamond substrate seed at present is still fairly small surface area compared to polycrystalline substrate. Although single crystal diamond deposition currently requires less plasma discharge size, microwave absorbed power density and substrate holder configuration must be carefully considered in order to achieve optimum growth rate and quality.

CHAPTER 3

MICROWAVE PLASMA ASSISTED CVD DIAMOND REACTOR DESIGN

3.1 Introduction

This chapter describes the microwave plasma assisted chemical vapor deposition (MPACVD) diamond reactor design that enable the operation of higher pressure from 180-260 Torr.

It is now widely recognized [54-56, 65, 70] that growth rates can be increased by carrying out the deposition process above 100 Torr and by using high power density microwave discharges. It is now further speculated that by increasing the deposition pressure beyond 180 Torr and by increasing the discharge power density that the diamond growth rates can be increased considerably further while yielding good quality diamond. Thus, research groups around the world [65, 67, 69-70, 76, 83] are exploring new designs for higher pressure (> 180 Torr) and higher power density (> 150 W/cm^3) MPACVD machines. In addition in this high pressure regime, new process methods are being developed with the goal to develop high deposition rate CVD diamond deposition processes that enable high quality diamond synthesis.

At high pressures and high power densities, microwave discharges in hydrogen gas have neutral gas temperatures in excess of 2500 K, contract and separate from the surrounding discharge chamber walls and they become a very non-uniform, intense and "arc like" discharge. As pressure is increased, the gas

temperature and discharge power density increase resulting in a floating discharge with increased active radical plasma species that have the potential for increased growth rates. The formation of contracted and floating microwave discharges "microwave arcs" at high pressures has been observed and studied in many experiments [7-8, 49, 84-87]. The microwave arc, like lower frequency arcs, is a thermally inhomogeneous discharge. It has a hot central core and sharp thermal gradients exist between the discharge center and the surrounding walls. Microwave energy is readily coupled into the electron gas in the hot discharge center because of its reduced gas density, and neutral gas species are also readily ionized, dissociated and excited in the hot central discharge core. These High pressure microwave discharges have been applied as discharges in electro-thermal thruster space engines [88-91] and as high pressure high power microwave discharge light sources [92].

Thus, high pressure microwave discharges behave very differently from the typical low pressure discharges and require new methods of discharge control and microwave applicator and plasma reactor design that take into account the distinctly unique nature of the high pressure microwave plasma. The goal in a CVD application is to control the size, the spatial location and the shape of this very hot, non-uniform and potentially explosive discharge in such a manner to enable optimal CVD diamond synthesis. This is a formidable engineering challenge. The high pressure plasma reactors and experimental methods described here allow the spatial positioning and shaping of this

thermally inhomogeneous, hot microwave discharge and there by enable the optimization of the diamond CVD process at high pressure.

The experiments reported in this thesis employ specific generic reactor geometry [7-8, 84] discussed in section 3.2. As was reported earlier [49, 85], when operated in the 100-160 Torr pressure regime this reactor which is referred to as the "reference reactor" throughout this dissertation has synthesized high quality and high growth rate CVD polycrystalline diamond material. In this investigation, the reference reactor is first redesigned to operate with high power densities and high pressures, and then the performance of this modified reactor is experimentally explored over the 180-260 Torr pressure regime by synthesizing polycrystalline diamond (PCD) and single crystal diamond (SCD).

The chapter begins with general over view of the generic reactor followed by description of the reference reactor and then the discussion of hybrid reactor. The hybrid reactor design modification was done by reducing the substrate holder radius from 5.08 cm to 3.24 cm and the coaxial cavity inner conductor radius from 4.13 cm to 1.91 cm. Furthermore, the hybrid reactor is a combination of both a cylindrical and coaxial cavities that support a hybrid mode excitation namely TM_{013} and TEM_{001} mode. The coaxial section of this reactor is tunable allowing the variation of discharge size and position. This improves discharge stability and enables process optimization during high pressure operation. Detailed design of hybrid reactor such as water cooling stage inner conductor, substrate holder for both polycrystalline and single crystal diamond, and shims configurations are described. Brief review of circular and coaxial cavity

waveguide theory, mode charts and electromagnetic field patterns inside cavity applicator are also presented in the hybrid reactor section.

3.2 Generic Reactor

A cross sectional view of a generic version of the MPCR is displayed in Figure 3.1. It has a cylindrical structure that is axially aligned along the z-axis and the applicator geometry is phi symmetric about the z axis. Microwave energy is introduced into the applicator via the length variable coaxial coupling probe that is located in the center of the length variable, "sliding short" top plate of the applicator. The applicator consists of two coupled cavities, i.e. a cylindrical cavity section ($z > 0$) and a coaxial cavity section ($z < 0$). The two cavities are coupled at the $z = 0$ plane which is also the cylindrical cavity bottom plane. The important dimensions and coordinates of the applicator are shown in Figure 3.1. They are the cylindrical cavity length, L_s, the cylindrical cavity radius, R1, the coupling probe depth, L_p, and the coaxial cavity radii R2 and R3, the molybdenum substrate holder radius R4, and the coaxial cavity lengths L1, and L2. The substrate itself is located approximately at the $z = 0$ plane on top of the open end of the coaxial cavity on the molybdenum holder. Thus, the end of the center conductor of the coaxial cavity also serves as the substrate holder. The center conductor is either water cooled or heated to control the substrate temperature. A silicon substrate is placed upon the molybdenum holder that is located on the top of the coaxial center conductor. The difference between L1 and L2 i.e., (L1-L2),

is identified as ΔZ and is the distance that the substrate surface is above or below the cavity bottom plane z = 0.

A specific design of reactor shown in Figure 3.1 is a function of the following geometric variables L_s, L_p, L1, L2, R1, R2, R3, and R4. In general, when these geometric length variables are changed the electromagnetic fields and the electromagnetic focus in the local region above and around the z = 0 plane are controlled and altered. Similarly, when a microwave discharge or plasma is present, the discharge power density, the plasma shape and position can be altered by varying one or more of the geometric variables. Thus, the diamond synthesis process can also be changed, controlled and optimized by changes in the reactor geometry.

If the size and shape of the MPCR is varied, for example by changing the various reactor radii or lengths, the reactor can be optimized for a deposition process. In practice R1 is determined primarily by the choice of the excitation frequency, and R1 and R2 are then determined by the specific process application, i.e., desired substrate size and operating pressure regime. For example, for low pressure, large area operation and low discharge power density R2 and R3 take on lengths that are slightly smaller than R1. Typical reactor designs fix the applicator radii, and then during process optimization the electromagnetic field patterns and associated microwave discharge are modified by varying L1, L2, L_s and L_p as well as pressure and input microwave power. This is a multivariable optimization procedure that is initially performed by the operator during process development and after some experience it can also be

performed automatically via preprogrammed recipe. Since there are many variables, there are many possible shapes, positions, and intensities that the discharge can assume in the vicinity of the z = 0 plane. All of these are available for process optimization.

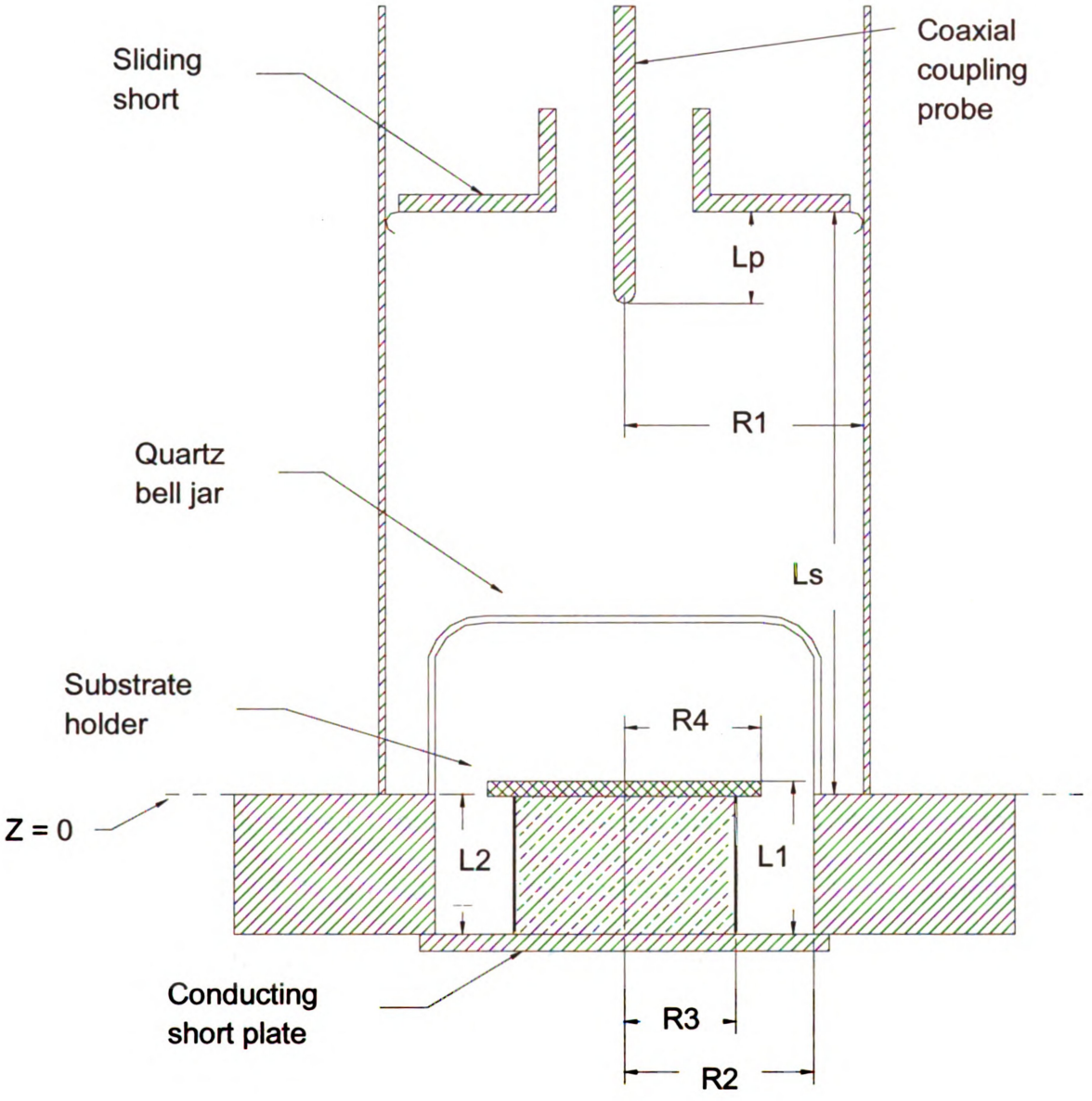

Figure 3.1 - Generic microwave plasma applicator cross section.

3.3 Reference reactor

Historically, the first experimental investigations that used a microwave plasma cavity reactor employed a specific 2.45 GHz design identified here as the reference reactor and explored CVD diamond synthesis over the low to moderate 60-160 Torr synthesis pressure regime. These results have been reported in several publications [7-8, 49, 84-85]. The cross section of the reference microwave plasma applicator and the associated tuning adjustments variables are shown in Figure 3.2. The diameter of the microwave cavity is 17.8 cm. The important dimensions and coordinates of the applicator are the coupling probe depth, L_p, the cylindrical cavity length, L_s, the cylindrical cavity radius, R1, the coaxial cavity radii R2 and R3, the molybdenum substrate holder radius R4, and the coaxial cavity lengths L1, and L2. The specific dimensions of this reactor are R1 = 8.89 cm, R2 = 7.04 cm, R3 = 4.13 cm and R4 = 5.08 cm. These dimensions were chosen to enable diamond synthesis over 2 to 4 inch substrate areas while operating in the low to moderate pressure regime, i.e. this design was especially designed for operation in low to moderate pressures (20-160 Torr) and to deposit diamond over modest to large area substrates.

The cavity walls have observation windows (not shown in Figure 3.2) that allow for temperature and photographic measurements. The discharge chamber is located at the base of the cavity applicator and is enclosed by stainless steel base plates and a quartz bell jar dome. The quartz dome bell jar that contains the plasma discharge sits on top of the circular base plate. The base plate is

internally water cooled to prevent over heating during the diamond deposition. The deposition substrate is placed on the molybdenum substrate holder. The molybdenum substrate holder is supported by a quartz tube and water-cooling stage. The cooling stage is used to cool and control the substrate temperature at a desired temperature range. The premixed input gases are fed into the gas inlet of the base plate assembly. The bell jar has the dimension of 12.98 cm inside diameter and height of 8.66 cm. The bell jar has an extended flange length of 3.14 cm around the base with thickness of 0.895 cm. The size and shape of the quartz bell jar, stainless steel base plate, substrate holder, and placement of the substrate holder greatly influence the plasma discharge location, size and shape.

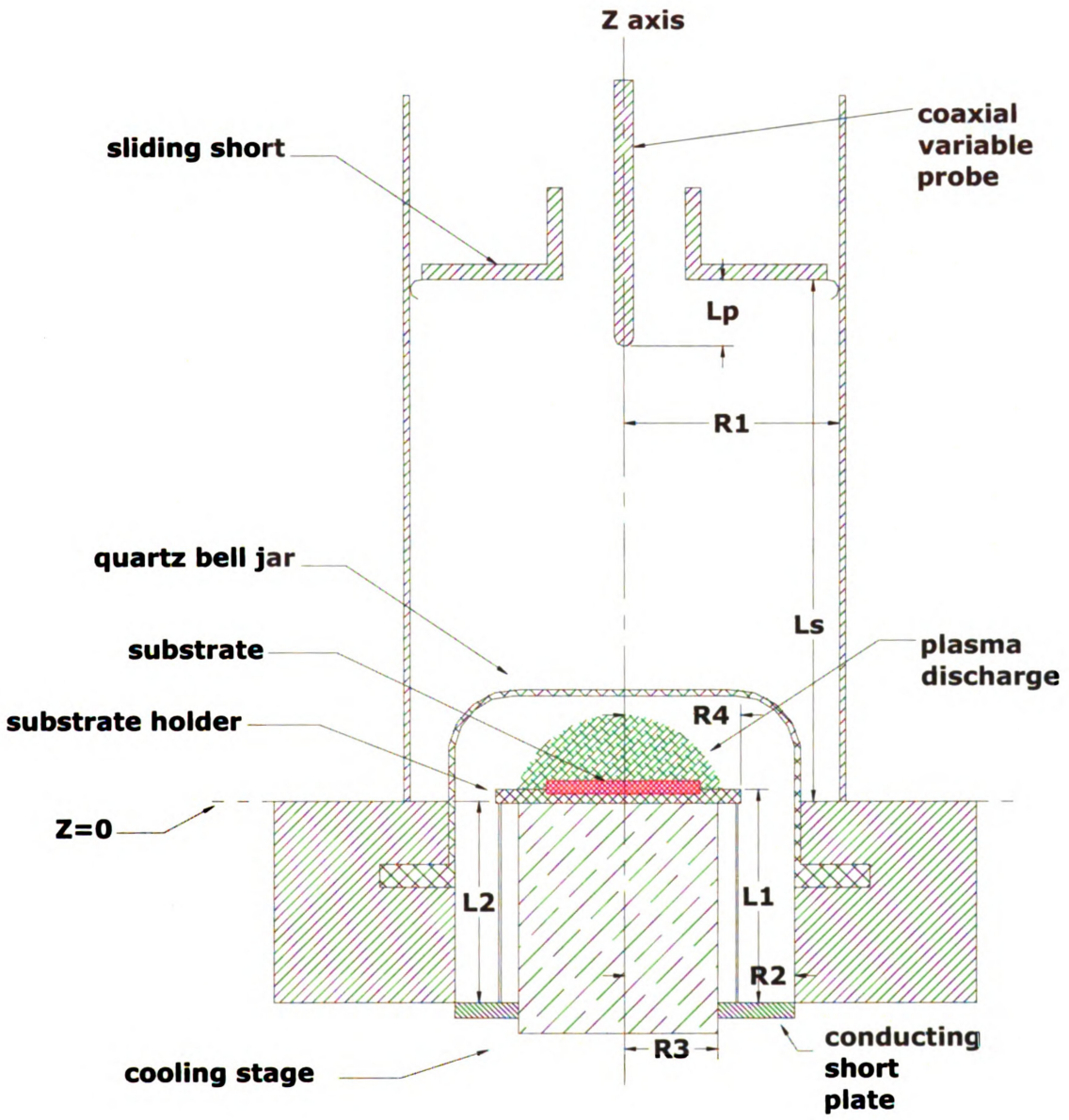

Figure 3.2 - Reference microwave plasma applicator cross section.

3.4 Hybrid reactor

This section describes the modifications made to the reference reactor that enabled optimized operation of the reactor at 180-260 Torr. Shown in Figure 3.3 is the comparison between the existing/reference and modified hybrid reactor. As can be seen from the cross section drawings, main modifications are the redesign of the substrate holder and inner conductor stage water cooling stage. In particular the R1 and R2 were held constants and R3 and R4 were reduced in size. Additionally, the L1 and L2 were variable enabling the adjustments of ΔZ. Specific details of the redesign are discussed in section 3.43 – 3.44.

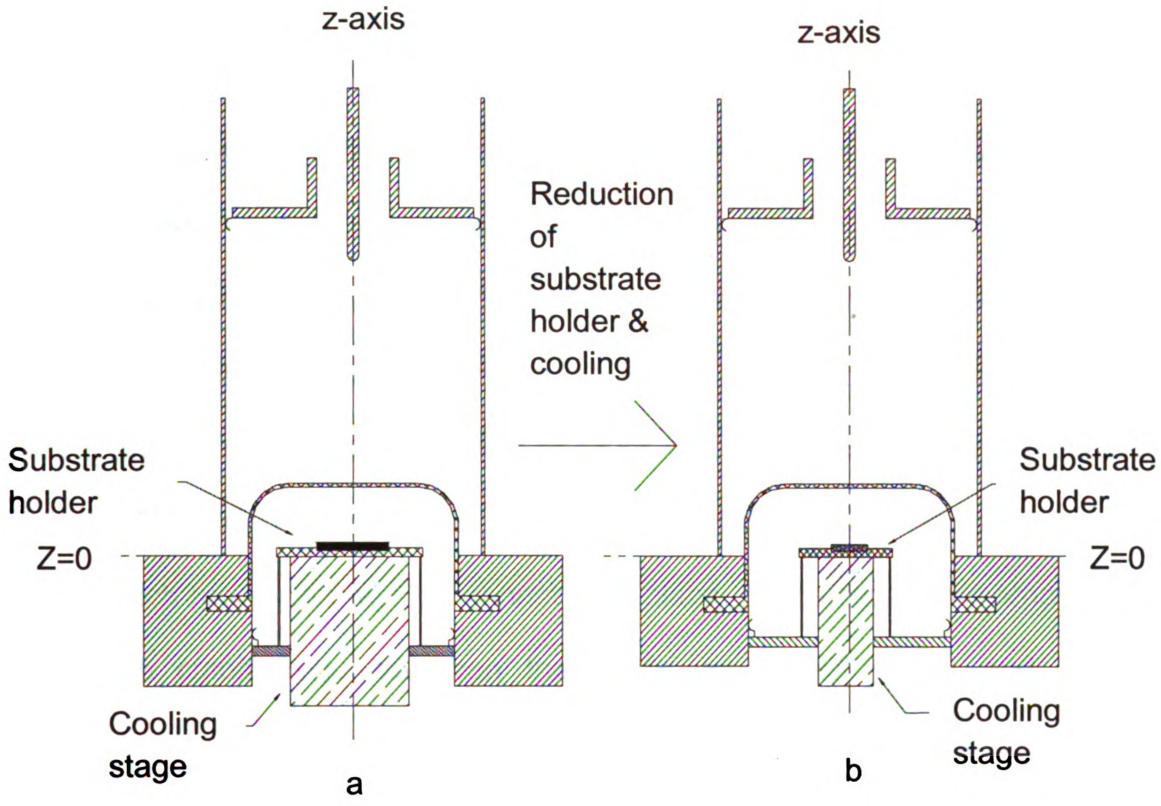

Figure 3.3 - Microwave applicator modification from (a) reference to (b) modified reactor. Major modifications as shown are the substrate holder and inner conductor water cooling stage.

3.4.1 General cylindrical waveguide/cavity background

The general electromagnetic propagating waves along a straight, uniform cross section, guiding tubes can be divided into three types of waves: (1) transverse electromagnetic (TEM), (2) transverse magnetic (TM), and (3) transverse electric (TE) waves. However, for the circular cavity applicator, only the TM and TE waves can propagate because it is a single conductor waveguide. Both the TM and TE modes have characteristic cutoff frequencies, i.e. frequency below which mode propagation cannot take place. If the mode frequencies are below the cutoff frequency then the mode waves will decay and cannot propagate along the cavity axis. Conversely, if the wave frequencies are above the cut off frequencies then the electromagnetic mode will propagate and the power will be transmitted along the waveguide axis.

The guided wavelength, λ_g is defined as the wave-propagating wavelength inside the cylindrical waveguide which is governed by the following equations [93-94]:

$$\lambda g = \frac{\lambda}{\sqrt{1-(f_c / f)^2}} \tag{3.1}$$

Where f_c is the cut off frequency of the cylindrical resonator for TM and TE modes with radius of b and given by:

TM_{np} mode

$$fc = \frac{Xnp}{b2\pi\sqrt{\mu\varepsilon}} \tag{3.2}$$

TE_{np} mode

$$fc = \frac{X'np}{b2\pi\sqrt{\mu\varepsilon}} \tag{3.3}$$

λ is the free space wavelength, μ is the permeability, ε is the permittivity, and X_{np} and X_{np}' correspond to the p_{th} zeros of the Bessel functions J_n and J'_n respectively.

If one end of the waveguide is enclosed with a conducting end plate and there was incoming microwave energy travels towards this end plate, then, the incident wave will be reflected and travels in the opposite direction. A standing wave will be produced in front of the end plate by the interference of incident and reflected wave. If both ends of the waveguide are enclosed by conducting end plates and the length of the waveguide is some integer multiple of $\lambda_g/2$, where λ_g is the guide wavelength, then a standing wave cavity can be formed.

A microwave cavity applicator is essentially an enclosed conducting segment of a waveguide with closed end faces. The termination at each end of the waveguide causes the incident waves to bounce back and forth along its length repeatedly. This type of waveguide structure is commonly known as a cavity resonator as shown in Figure 3.4.

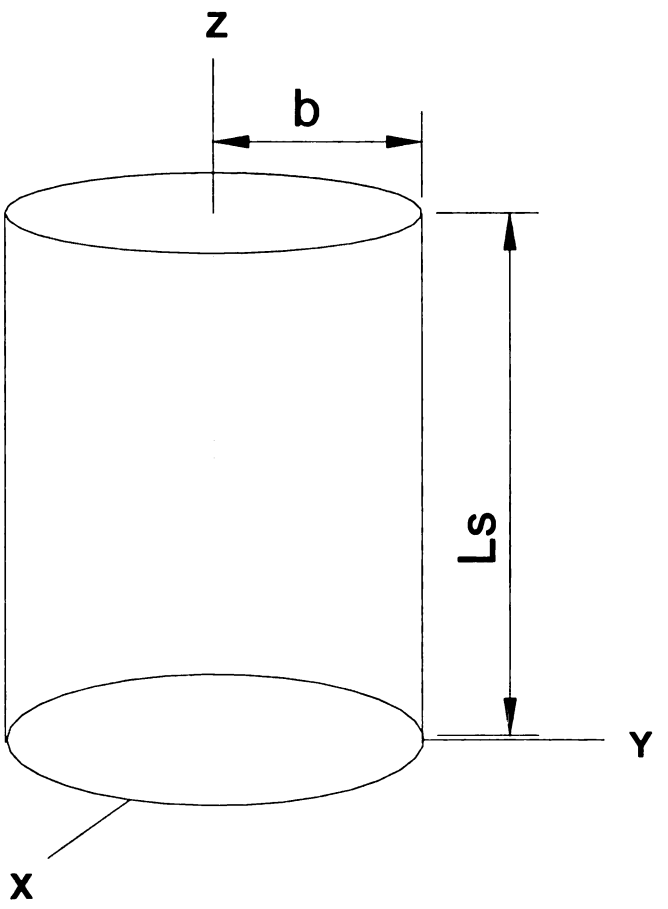

Figure 3.4 - Circular cylindrical cavity resonator and its variables b, cavity radius and Ls, cavity length.

Each of these modes has a set of infinite natural eigenfrequencies that can exist in the cavity. These natural eigenfrequencies are sinusoidal steady-state solutions of Maxwell's equations that exist at a certain frequency, which is also commonly known as the resonant frequency. For empty, perfectly conducting, cylindrical cavity applicators, the natural eigenfrequencies are governed by the following equations [95-96]:

$$f_c(TM_{npq}) = \frac{c}{2\pi b}\sqrt{\left((X_{np})\right)^2 + \left(\frac{q\pi b}{L_s}\right)^2} \qquad (3.4)$$

$$f_c(TE_{npq}) = \frac{c}{2\pi b}\sqrt{\left((X_{np}')\right)^2 + \left(\frac{q\pi b}{L_s}\right)^2}$$

where b and L_s are the radius and height/length of the cylindrical cavity, X_{np} and X_{np}' correspond to the p_{th} zeros of the Bessel functions J_n and J'_n respectively. For TM modes, the indices n, p and q may be any integer value and only n and q are allowed to be zero. The indices n, p, and q for TE modes may be any integer value but only n is allowed to be zero.

Table 3.1 - Selected roots of the Bessel function

Roots of Jn (X)	Roots of J'n (X)
$X_{01} = 2.405$	$X'_{01} = 3.832$
$X_{02} = 5.520$	$X'_{02} = 7.016$
$X_{11} = 3.832$	$X'_{11} = 1.814$
$X_{12} = 7.016$	$X'_{12} = 5.331$

Equations 3.4 show that the resonance frequency for an electromagnetic mode depends on the cavity radius, b, and cavity height/length, L_s. Given a specific excitation frequency and if the cavity height is adjustable then the cavity height can be physically varied so that the eigenfrequency is equal to excitation frequency.

Shown in Figure 3.5 is the mode chart for a seven inch cavity i.e., 2b = 17.78 cm. This chart was created by plotting the TE and TM mode resonant frequencies given by equations 3.4 for a fixed cylindrical cavity of radius (b), versus cavity height (L_s). Mode chart such as shown in Figure 3.5 is used to understand the behavior of specific reactor designs. In particular, the mode chart is useful in determining the frequency range the reactor can be tuned without interference from other modes. The resonant frequencies in this chart were calculated for the cavity height within the range of 10 cm to 26 cm. The resonant frequency range was swept from 1.8 to 3.2 GHz to observe possible eigenmodes that exist in the empty cavity. The horizontal line shown in Figure 3.5 represents the excitation frequency at 2.45 GHz while the vertical line denotes a specific TM_{013} mode theoretical cavity height at 21.6 cm. As can be seen from the mode diagram, TE_{211}, TM_{111} and TE_{011} (degenerate mode), TE_{112}, TM_{012}, TE_{311}, TE_{212}, TE_{113}, TM_{012} and TM_{013} modes can be excited for the 17.78 cm cavity resonator when operating at 2.45 GHz. Hence, the cavity resonator can be tuned to one of these resonant modes by adjusting the cavity height/length, L_s.

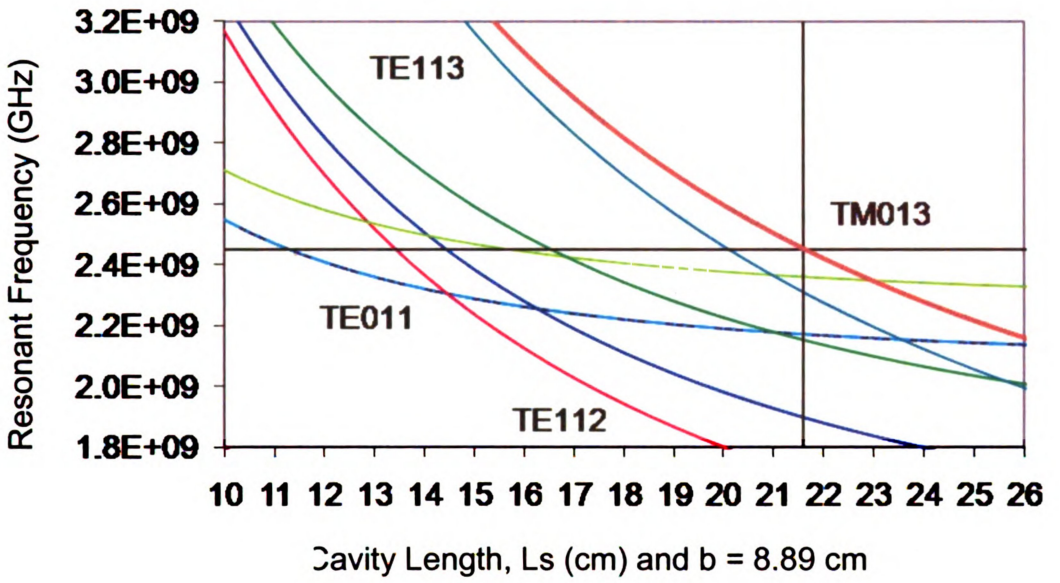

Figure 3.5 - Resonant mode chart for 2b = 17.78 cm cylindrical cavity. The plot is in function of resonant frequency in GHz and cavity length in cm.

The electromagnetic field distributions for each mode within a cylindrical circular perfectly conducting cavity applicator are governed by equations 3.5 and 3.6 listed below [94-97]. The tangential component of the electric field is equal to zero at the conducting wall boundaries. For the TM modes, the transverse magnetic waves do not have a component of the magnetic field in the direction of propagation, i.e. $H_z = 0$, but have axial electric fields, i.e. $E_z \neq 0$. Likewise for TE mode, the transverse electric waves do not have a component of the electric field in the direction of propagation, $E_z = 0$, but have axial magnetic fields, $H_z \neq 0$.

TM mode,
$$Ez = EozJn\left(\frac{Xnp}{b}r\right)\cos(n\phi)\cos\left(\frac{q\pi}{Ls}z\right) \qquad (3.5)$$

Where E_z = amplitude of the electric field

J_n = Bessel function of the first kind

X_{np} = pth x value at which $J_n(x) = 0$

n = number of periodicity in ϕ direction (n=0,1,2,...)

p = number of zero fields in radial direction (p=1,2,3...)

q = number of half waves in axial direction (q = 0,1,2,...)

TE mode,

$$Hz = HozJn\left(\frac{X'np}{b}r\right)\cos(n\phi)\sin\left(\frac{q\pi}{Ls}z\right) \qquad (3.6)$$

Where

Hz = amplitude of the magnetic field

J_n = Bessel function of the first kind

X'_{np} = p_{th} x value at which $J_n'(x) = 0$

n = number of periodicity in ϕ direction (n=0,1,2,...)

p = number of zero fields in radial direction (p=1,2,...)

q = number of half waves in axial direction (q = 0,1,2,...)

Figure 3.6 displays the field distribution patterns for various TM and TE modes in an empty 17.78 cm diameter cavity. These field patterns were obtained from Ansoft HFSS simulation results. The electric field patterns shown in Figure 3.6 reveal the spatial electric field distributions within the cavity applicator. The electric field patterns are plotted in two different planes (XY and YZ planes) cross sections to allow a better identification of the eigenmodes since for each mode the distribution of the electromagnetic fields are a function of angular, radial, and axial positions. For the empty cavity simulation, a perfect conductor is chosen for the boundary condition in order to simplify the numerical solution. Furthermore, for time-varying electromagnetic waves the tangential component of an electric field should be zero at the surface of the cavity walls. The red, orange, green, and blue colors indicate the intensities of the electric field in V/m with the red being the strongest and the blue is the weakest.

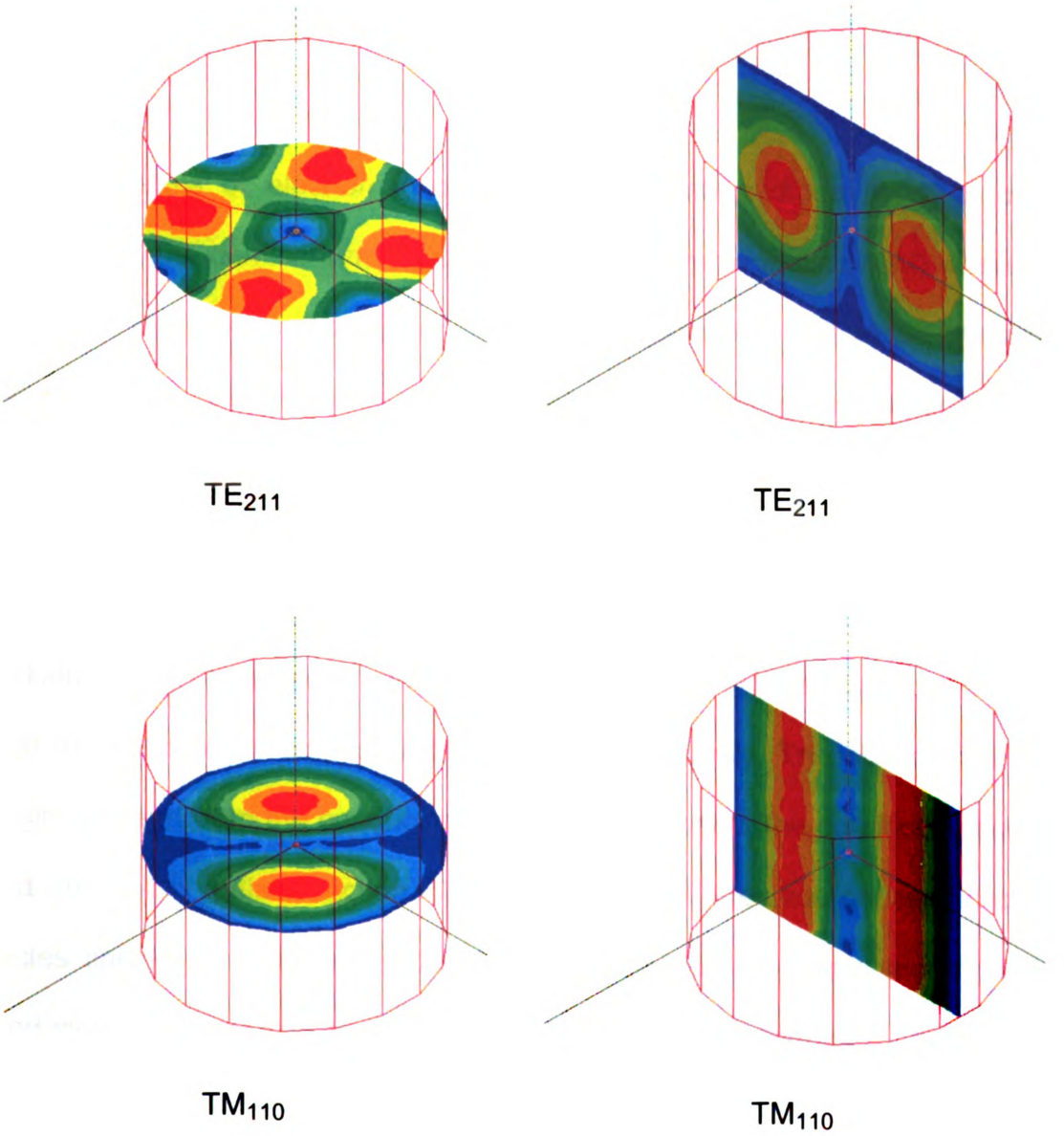

Figure 3.6 - Electric field distributions of TE_{211} and TM_{110} modes. The color indicates electric field strength in V/m with blue and red correspond to 1.2E-03 and 9.9E-01 respectively.

3.4.2 Coaxial waveguide background

In terms of electromagnetic wave propagation mode inside a coaxial waveguide, the dominant mode is transverse electromagnetic (TEM) where both the E and H are transverse to the direction of propagation. This mode propagates along air filled coaxial waveguide with the same wavelength and velocity as free space TEM plane waves. From the simple relation of $\lambda = c/f$ where c is the speed of light in air, the wavelength is 12.24 cm for 2.45 GHz excitation frequency.

Figure 3.7 shows the TEM mode field pattern inside the coaxial cavity looking at side (axial) view, and cross sectional views. The electric and magnetic field are denoted by solid and dashed line respectively. The electric field lines begin and end from the conducting boundary, normal to the conducting surface, and are in the radial direction. The magnetic field lines are concentric closed circles linking or surrounding the conduction current or displacement current produced by a time varying electric field in the center conductor. The magnetic field has no normal component to the conductor surface. In a coaxial cavity the phase varies continuously along the z-axis in the direction of the wave propagation. When the point charge is separated by a distance λ, the field is in phase. Likewise, when the point charge is separated by $\lambda/2$, it will be 180° out of phase. The sinusoidal varying radial electric field produces radial electric displacement currents between the inner and outer conductors. Both the electric and magnetic field lines are confined to a plane z = constant that resulted in E_z =

0 and $H_z = 0$ which means that the tangential electric field and the normal magnetic field components must be zero on the conductor surfaces.

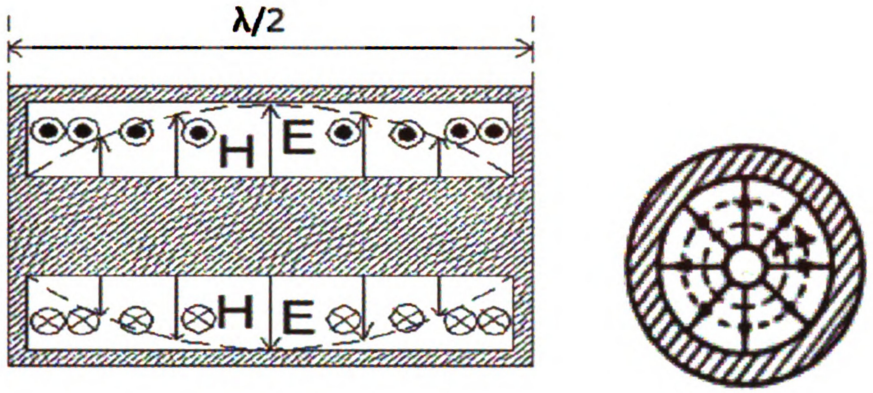

(a) (b)

Figure 3.7 - Transverse electromagnetic (TEM) mode field patterns of coaxial cavity (a) axial view (b) circular view [98].

Additional higher modes such as TE and TM modes may exist in the coaxial waveguide provided that the distance between the center and outer conductor is greater than the order of one half wavelengths. Otherwise, these higher order modes will be cut off/evanescence or non-propagating.

Consider the open coaxial cavity shown in Figure 3.8. Assume that a, b, and t are much smaller than a wavelength and Lc is a quarter wavelength. For a lossless coaxial line terminated in a short circuit at z = 0, where the z axis is directed downward, the phasor voltage for the TEM mode at any point along the line is the sum of the incident and reflected waves [97]:

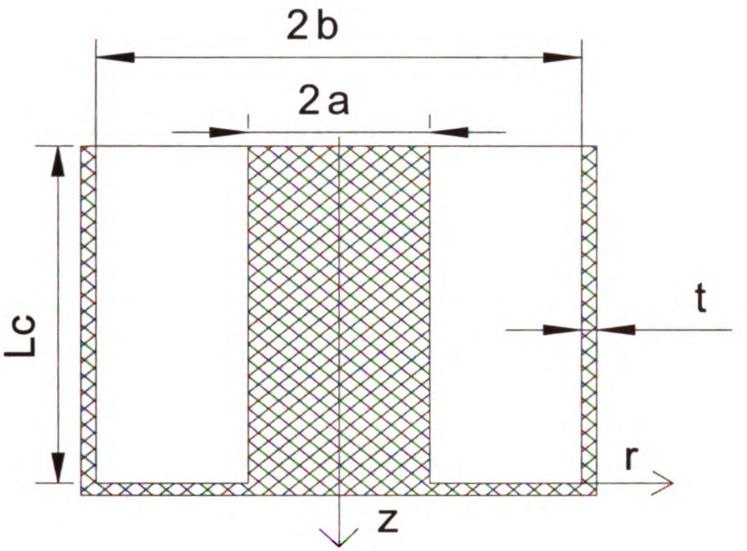

Figure 3.8 - Coaxial cavity waveguide and its variables for which b « λ. Lc is the height, t is the thickness, a is the outer radius of inner conductor and b is the inner radius of outer conductor.

$$V_s = V_0 \, e^{-j\beta z} - V_0 e^{j\beta z} \tag{3.7}$$

or

$$V_s = -j2V_0 \sin \beta z \tag{3.8}$$

and the current is given by

$$I_s = \frac{V_0}{Z_0} e^{-j\beta z} + \frac{V_0}{Z_0} e^{j\beta z} \tag{3.9}$$

or

$$I_s = \frac{2V_0}{Z_0} \cos \beta z \tag{3.10}$$

Where the phase constant β and characteristic impedance Z_0 is defined by

$$\beta = \omega \sqrt{\mu \varepsilon} \tag{3.11}$$

$$Z_0 = \frac{1}{2\pi}\sqrt{\frac{\mu}{\varepsilon}}\ln\frac{b}{a} \tag{3.12}$$

The magnetic field intensity is related to the current,

$$H_\phi = \frac{I_S}{2\pi\rho} \tag{3.13}$$

or

$$H_\phi = \frac{V_0}{\pi r Z_0}\cos\beta z \tag{3.14}$$

Thus, the electric field intensity is related to the voltage between conductors of a coaxial line,

$$E_{rs} = \frac{V_s}{r\ln\left(\frac{b}{a}\right)}\sin\beta z \tag{3.15}$$

Equation (3.14) and (3.15) give the interior fields for the lossless coaxial cavity.

Figure 3.9(a)-(b) shows examples of the electromagnetic field distributions for a few of the lowest order TM and TE modes respectively. They are TM_{01}, TM_{11}, and TM_{21}, TE_{11}, TE_{21}, and TE_{31} modes. The number on the right hand side of the drawings corresponds to: (1) cross sectional end view, (2) longitudinal side view through plane $\ell - \ell$.

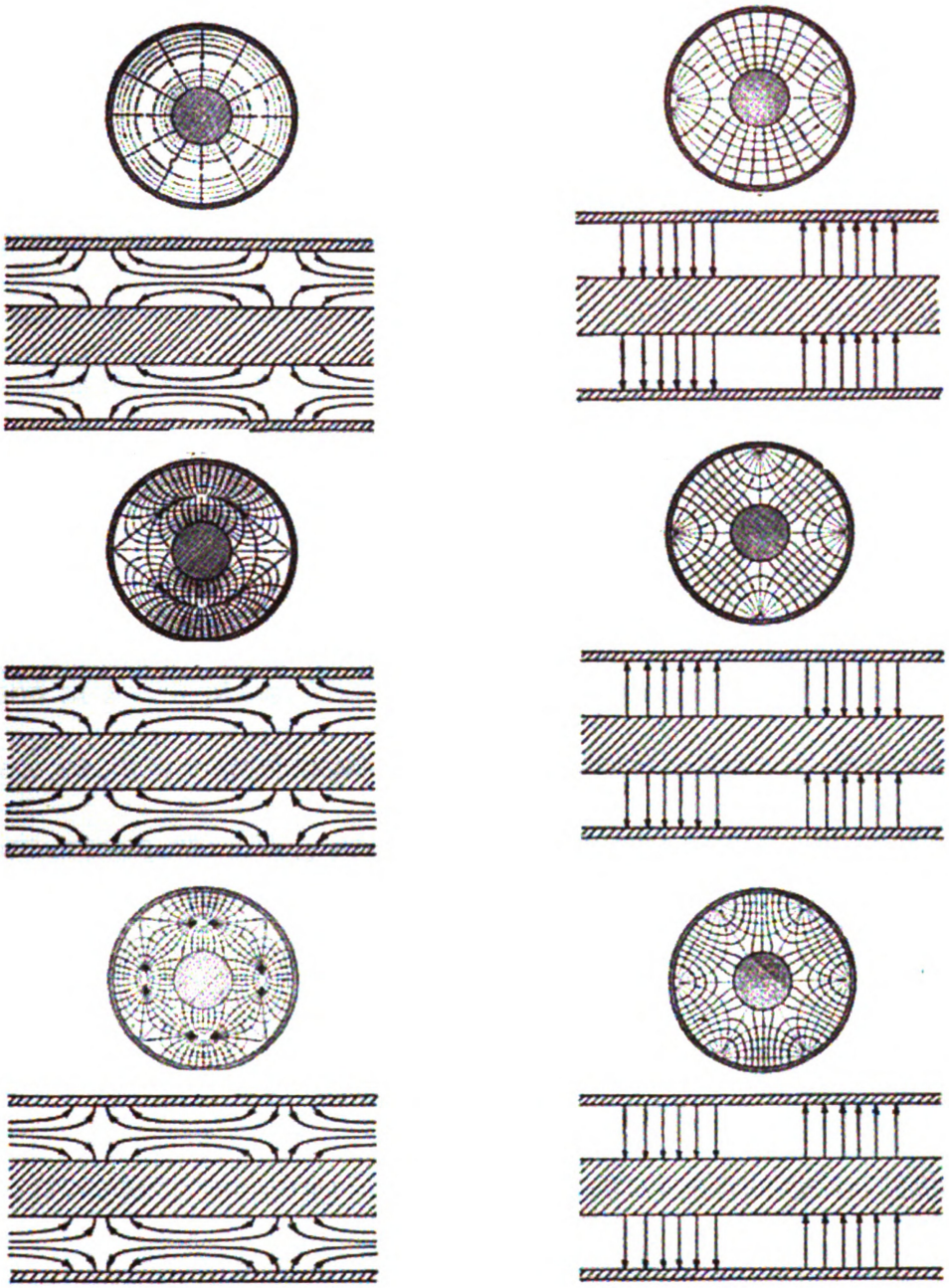

Figure 3.9 - Examples of coaxial cavity field patterns: (a) TM_{01}, TM_{11}, and TM_{21} mode (b) TE_{11}, TE_{21}, and TE_{31} mode with a=3b ratio [98].

3.4.3 Hybrid applicator design

In this investigation, the modified microwave plasma cavity reactor was redesigned to allow operation at higher discharge power densities and higher pressures. This was done as illustrated in Figure 3.3 by reducing the substrate holder radius R4 from 5.08 cm to 3.24 cm and the coaxial cavity inner conductor radius R3 from 4.13 cm to 1.91 cm. The coaxial cavity center conductor area had been reduced by about 4.5.

Figure 3.10 shows the combination of the two cavities which intersect on each end at z = 0 plane. The microwave cavity applicator is a hybrid mode applicator i.e., it is a combination of both a cylindrical and coaxial cavities. The excitation modes are TM_{013} and TEM_{001} for the cylindrical and coaxial cavity respectively plus any evanescent mode field that exist t around the z = 0 plane. The cavity height for the cylindrical section is 3/2 λ_g and the cavity height coaxial section Lc = $\lambda_0/2$.

A cross sectional view of the modified microwave plasma cavity reactor is displayed in Figure 3.11. It has a cylindrical structure that is axially aligned along the z-axis and the applicator geometry is Φ symmetric about the z-axis. Microwave energy is introduced into the applicator via the length variable coaxial coupling probe that is located in the center of the length variable, "sliding short" top plate of the applicator. The applicator consists of two coupled cavities, i.e. a cylindrical cavity section (z > 0) and a coaxial cavity section (z < 0). The two

cavities are coupled at the z = 0 plane which is also the cylindrical cavity bottom plane. The geometry of reactor shown in Figure 3.11 is a function of the following geometric variables L_s, L_p, L1, L2, R1, R2, R3, and R4.

In general, when these geometric length variables are changed the electromagnetic fields and the electromagnetic focus in the local region above and around the z = 0 plane are controlled and altered. Similarly, when a microwave discharge or plasma is present, the discharge power density, the plasma shape and position can be altered by varying one or more of the geometric variables. Thus, the diamond synthesis process can also be changed, controlled and optimized by changes in the reactor geometry.

In practice, the plasma loaded applicator is excited with the hybrid TM_{013} + TEM_{001} electromagnetic mode. In order to achieve TM_{013} excitation in the open cylindrical section L_s must be adjusted to be very close to $3\lambda_g/2$, where λ_g is the guided wavelength of the TM_{01} cylinder waveguide mode. In order to achieve TEM_{001} excitation in the coaxial section, L2 must be adjusted to approximately $\lambda_0/2$ where λ_0 is the free space wavelength. Typical discharge ignition starting lengths for process development are when L1 and L2 are equal to each other and are equal to $\lambda_0/2$. Then, ΔL is zero and the top of the substrate is even with the z = 0 plane. Typical starting lengths for the cylindrical section are $L_s \sim 3\lambda_g/2$ and the coupling probe depth $L_p \sim \lambda_g/4$.

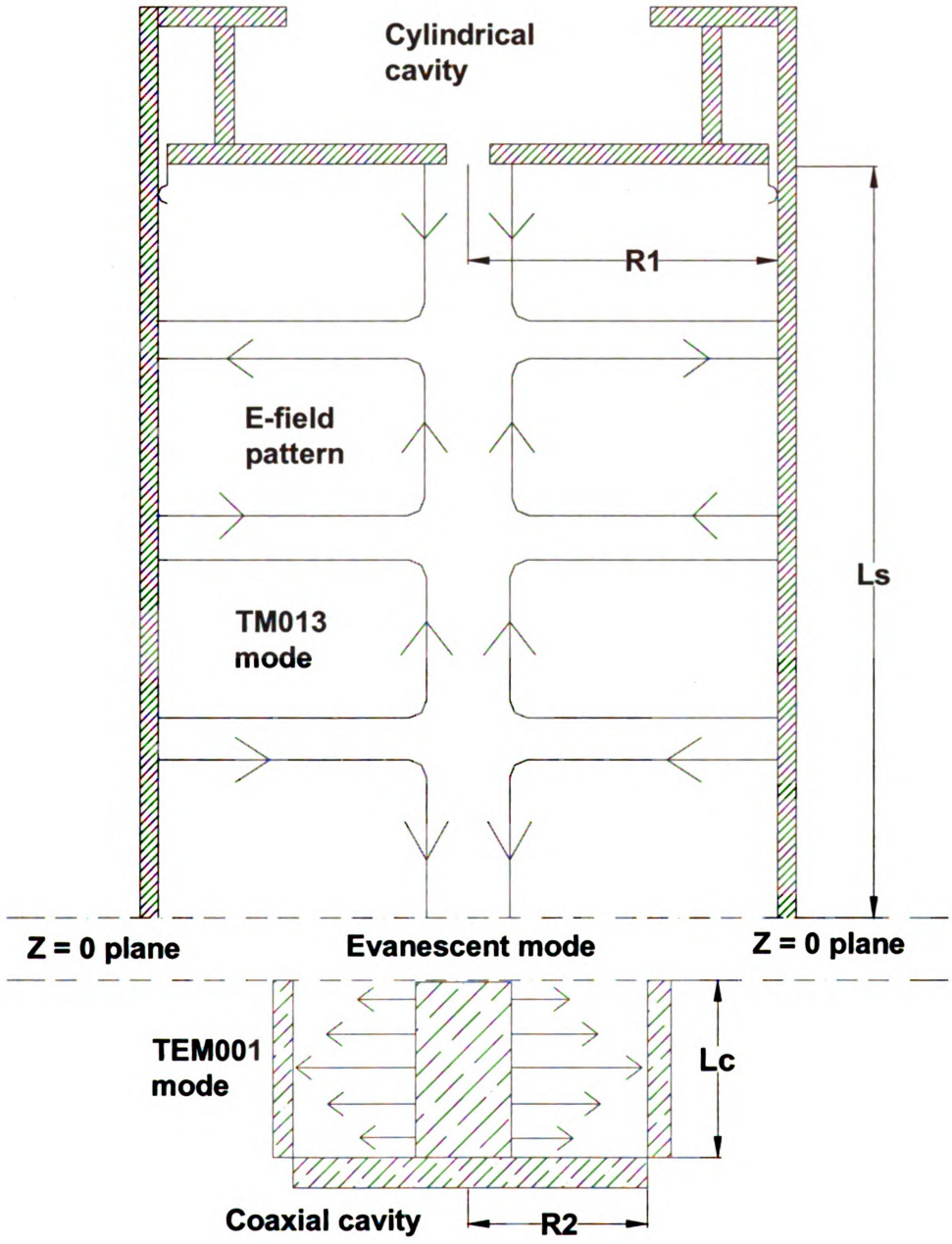

Figure 3.10 - Hybrid microwave cavity applicator consisting of cylindrical and coaxial cavities intersecting at z = 0 plane. The Ls ~ $3\lambda_g/2$ and Lc ~ $\lambda_0/2$ corresponds to the cavity height of the cylindrical and coaxial cavity section respectively.

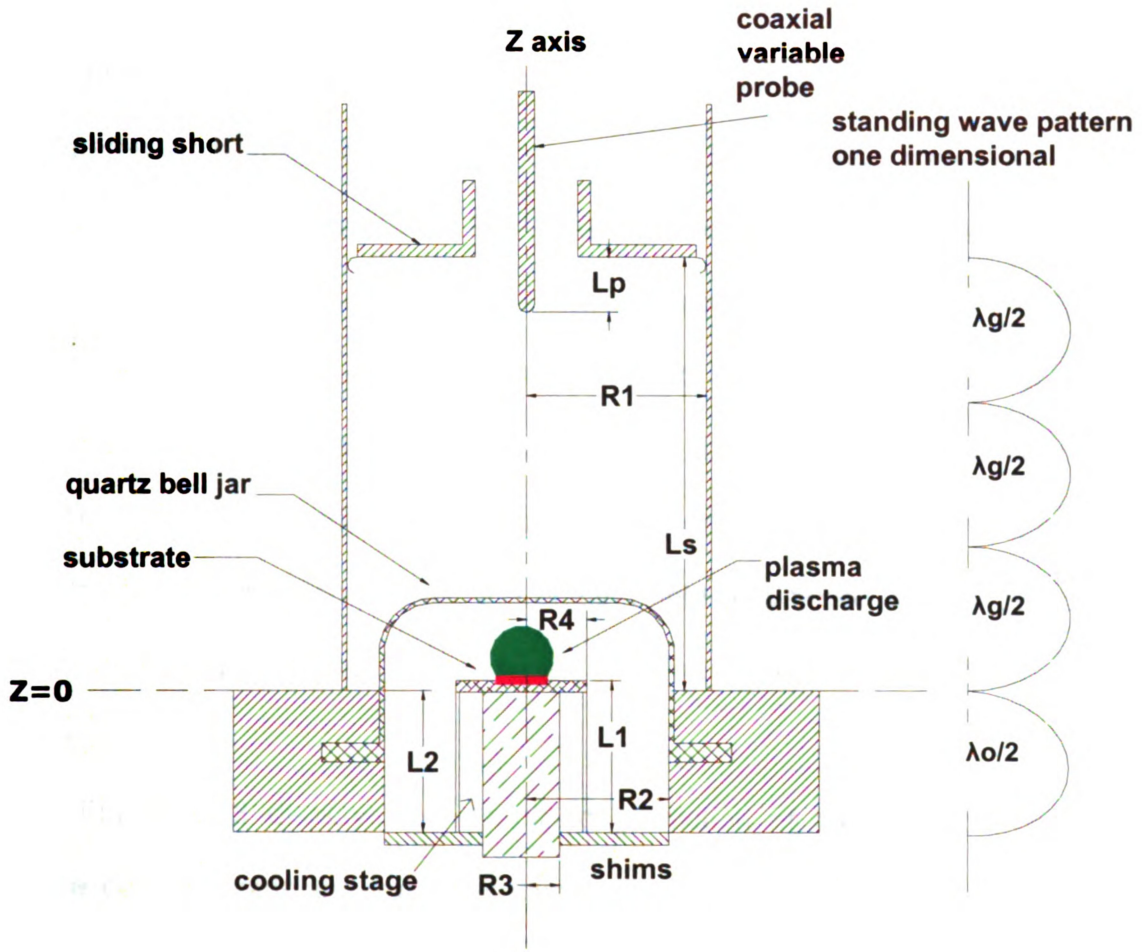

Figure 3.11 - Modified microwave plasma applicator cross section with reduced substrate holder and inner conductor radius.

Displayed in Figure 3.12 is the simulation model of the hybrid cavity applicator. The plot was obtained numerically using "RF electromagnetic solver" module of COMSOL MULTYPHYSICS. The electromagnetic waves solver allows one to visually predict the electric field distribution within the cavity applicator. Color intensities indicate the relative electric field strength in V/m. The important input parameters are: excited frequency = 2.45 GHz, cylindrical cavity radius, R1 = 8.89 cm, coaxial cavity radius, R2 = 7.04 cm, cooling stage radius, R3 = 1.91 cm, substrate holder radius, R4 = 3.24 cm, substrate holder thickness = 0.58 cm, bell jar height = 8 cm, cylindrical cavity height, Ls = 21.6 cm, coaxial cavity height, L1 = 5.65 cm, substrate holder height, L2 = 5.08 cm. The boundary condition was set to perfect electric conducting on the cavity walls. As can be seen from the simulation results, the electric field distribution for the cylindrical cavity and coaxial cavity section is showing TM_{013} and TEM_{001} mode respectively.

Figure 3.13 displays the simplified prediction of the displacement and surface current inside the coaxial section around the z = 0 plane. In order to achieve TM_{013} excitation in the cylindrical section, L_s must be adjusted to be very close to $3\lambda_g/2$, where λ_g is the guided wavelength of the TM_{01} cylinder waveguide mode. In order to achieve TEM_{001} excitation in the coaxial section, Lc must be adjusted to approximately $\lambda_0/2$ where λ_0 is the free space wavelength. As can be seen, the highest concentration of the fields is located in the vicinity of the z = 0 plane at the transition region between the cylindrical and coaxial section. The electric field is normal to the center conductor electrode. As the electrode

diameter is reduced, the normal electric field on the electrode increases. This result in high absorbed power plasma density which will be discuss in the experimental results section in Chapter 5.

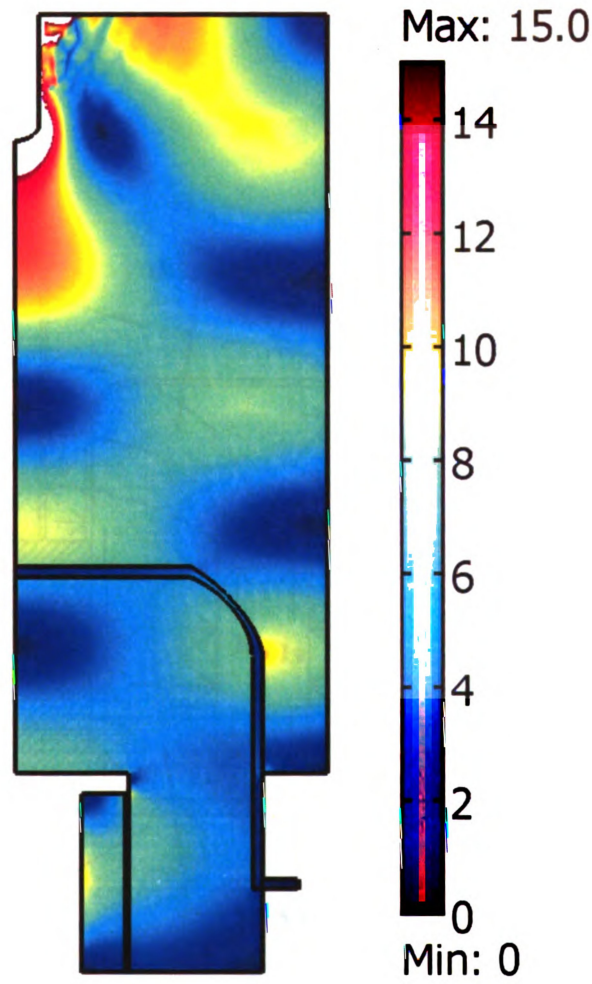

Figure 3.12 - Electric field distribution pattern inside a modified cavity applicator using COMSOL 2D axial symmetry model. The modeled cavity is assumed to be an empty cavity and without a plasma load. Color intensities indicate the relative electric field strength in V/m.

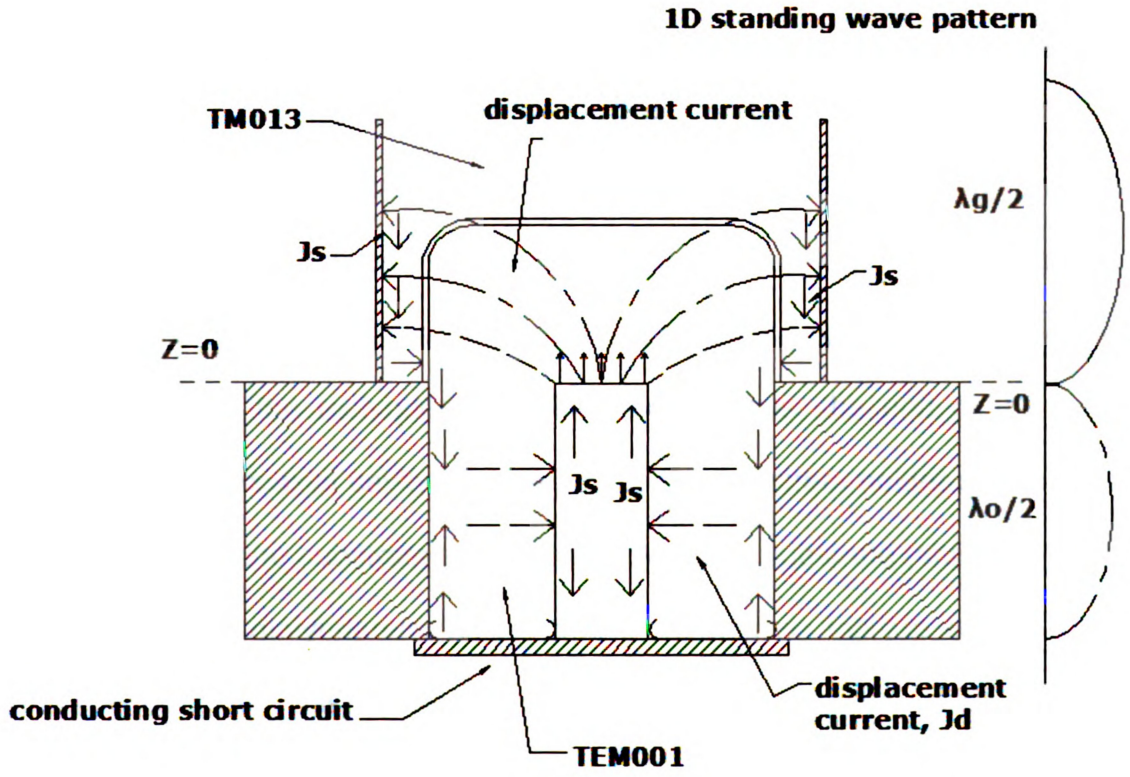

Figure 3.13 - Electromagnetic standing wave and surface current in the coaxial section of the applicator.

3.4.4 Detailed design of reactor configuration components

The design variables such as R1, R2, R3, R4, L1, and L2 dimensions and the shims variations underneath the coaxial cavity section are shown in Figure 3.14. The circular stainless shims were used to control the height of the cooling stage and the substrate holder position inside the quartz dome bell jar. Also the shims serve as an optimization tool for electromagnetic coupling and plasma discharge inside the discharge chamber. L2 can be varied from L20 = 2.03 inch ~ 5.156 cm to L21 = 2.41 inch ~ 6.12 cm. R2 has radius of 2.77" (7.04 cm). The shim has various thicknesses ranges from 1 to 10 mm thick. The substrate itself is located approximately at the z = 0 plane on top of the open end of the coaxial cavity placed on the molybdenum holder piece. Thus, the end of the center conductor of the coaxial cavity also serves as the substrate holder and is water-cooled to control the substrate temperature. A silicon substrate (shown in red) is placed upon the molybdenum holder that is located on the top of the coaxial center conductor. This center conductor substrate holder configuration is identified as the powered electrode. The difference between L1 and L2 i.e., (L1-L2), identified as ΔZ, is the distance that the top surface of the powered electrode or the substrate surface is above or below the cavity bottom plane z = 0.

In the experiments presented in this thesis L_s and L_p were adjusted to excite and match the TM_{013} mode in the cylindrical section of the applicator; i.e. L_s = ~ 20.3 cm and L_p = ~ 3.6 cm. During process optimization, L1 is held constant at 5.65 cm while L2 is varied between 5.16 cm and 6.13 cm by inserting

different shims. As the substrate axial position was varied, the electromagnetic field intensity and spatial distribution also were altered in the local region of the discharge (i.e., around the z = 0 plane).

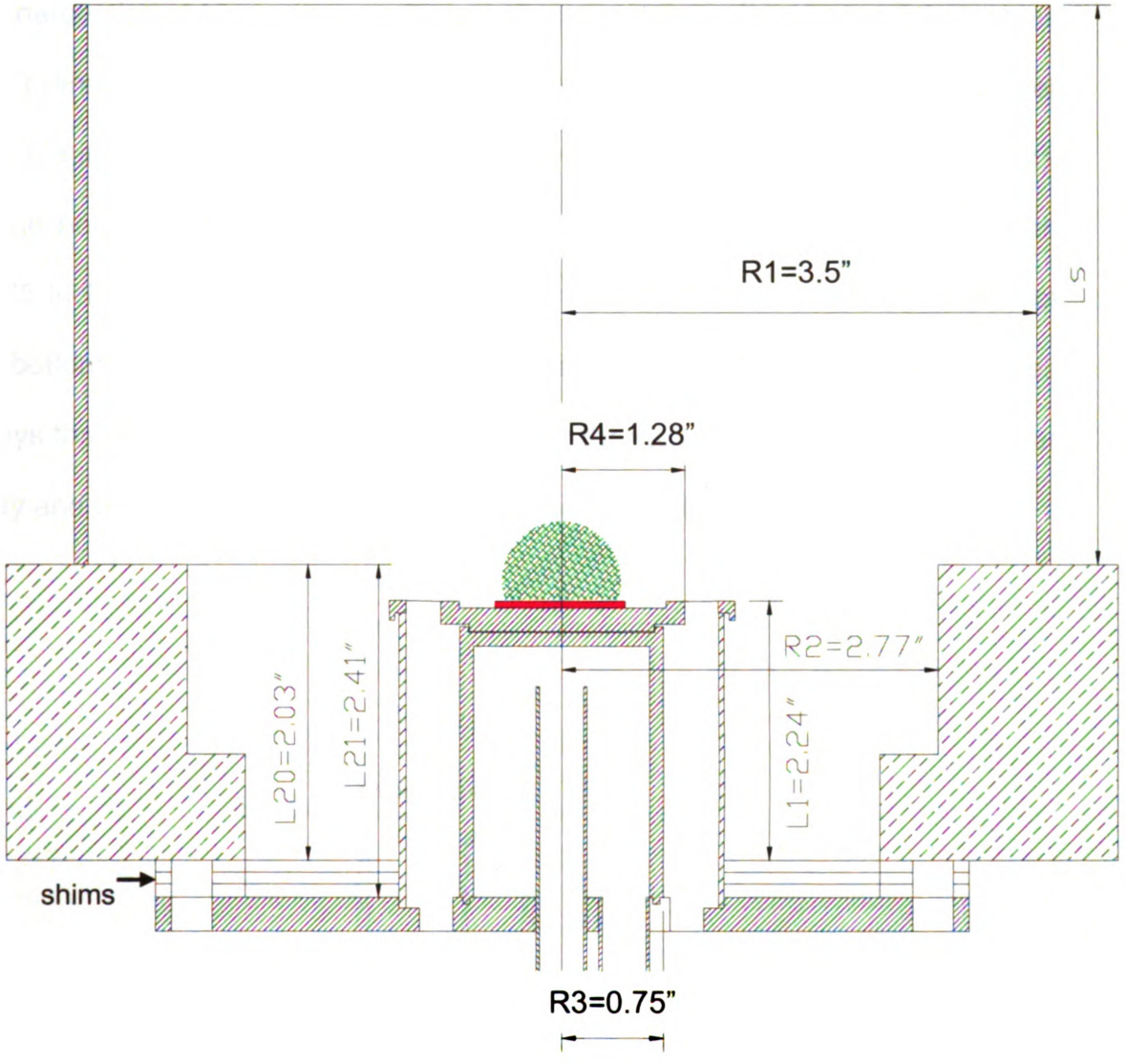

Figure 3.14 - Details cross sectional view of the inner conductor water cooling stage, substrate holder, and shims configurations. Units are in inches.

The cross section of the cooling stage that was used during the high-pressure diamond experiments is shown in Figure 3.15. Further detail on the schematic drawing can be found in Appendix A.1-A.2 This cooling stage is designed to accommodate the smaller sample substrate size and smaller plasma discharge size at high pressure. The cooling stage is made out of stainless steel. The cylinder body outer diameter is 1.5 inches (3.81 cm) and the inner diameter is 1.375 inches (3.49 cm). The height of the stainless tube is 2 inches (5.08 cm). At the bottom center of the cooling stage there are water outlet openings with 0.375 inch (0.95 cm) diameter for the water to flow in and out. The diameter of the bottom plate is 6 inches (15.24 cm). It has 0.25 inch (0.635 cm) circular holes arrays that are connected to the base plate in the vacuum chamber. The cylinder body and the bottom plate are joined by a vacuum weld.

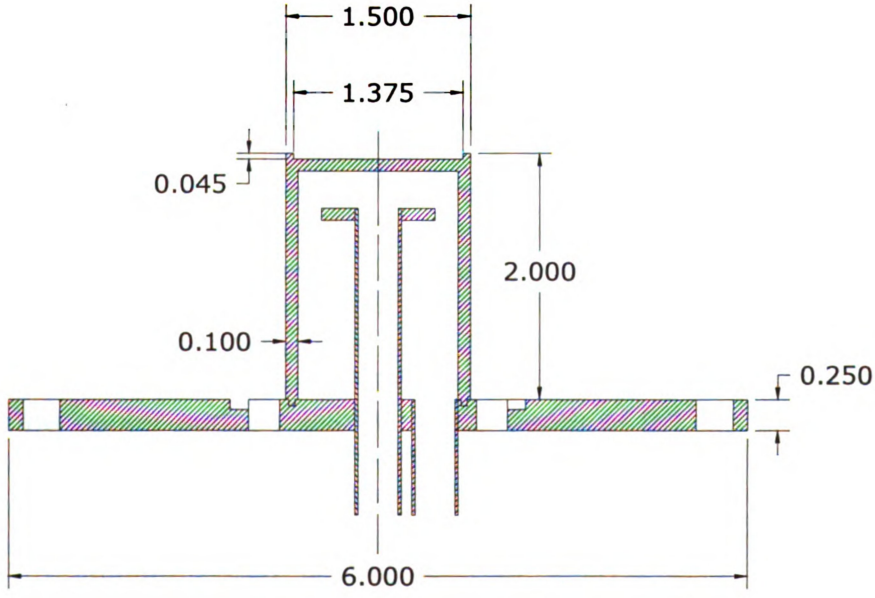

Figure 3.15 - Cooling stage inner conductor cross sections. Units are in inches.

The substrate holder drawing schematic for polycrystalline diamond is shown in Figure 3.16. Further detail on the schematic drawing can be found in Appendix A.3 The inside diameters is 1.525 inch (3.874 cm) with a thickness of 0.225 inch (0.572 cm). Since the silicon wafer sizes carried out in this research are one inch or smaller, the extra spacing on the substrate holder in this 1.5 inch holder is filled with small pieces of silicon wafers to ensure that the sample is centrally positioned on the substrate holder. The substrate holder is made of molybdenum. It has an array of 16 holes at the edge of the molybdenum piece. Each hole is equally spaced around the circumference and has an opening diameter of 0.25 inch (0.635 cm). These holes allow the gases from the quartz dome chamber to exhaust through the vacuum chamber and roughing exhaust pump.

The substrate holder for single crystal diamond cross sectional views is shown in Figure 3.17. Further detail on the schematic drawing can be found in Appendix A.4. The diamond seed is high pressure high temperature (HPHT) 3.5 x 3.5 x 3.5 x 1.5 mm^3 obtained from Sumitomo electric. This single crystal design holder is based on the experimental design of Yaran *et.al.* [99] and a U.S. Patent has been applied for by Asmussen *et.al.* [100]. A single piece of diamond seed placed at the center surface with a recess depth of 0.1 cm to ensure that the diamond substrate sits in a pocket within the diamond seed housing. The molybdenum substrate has a thickness of 0.0125 inch (0.0318 cm). The thickness is less than the polycrystalline diamond substrate holder which is 0.225 inch (0.572 cm). The thinner substrate holder was designed to provide enough

cooling and controllability of the substrate temperature during diamond deposition.

The substrate holder placed on top of the cooling stage and also supported by a quartz tube holder as shown previously in Figure 3.14. The quartz tube has an outside diameter (OD) of 6 cm and a thickness of 0.1 cm. This quartz tube is placed between the substrate holder and the cooling stage bottom plate. It provides confinement of the excess gases that descend from the substrate holder opening holes to the vacuum chamber. The height of this quartz tube is 5 cm.

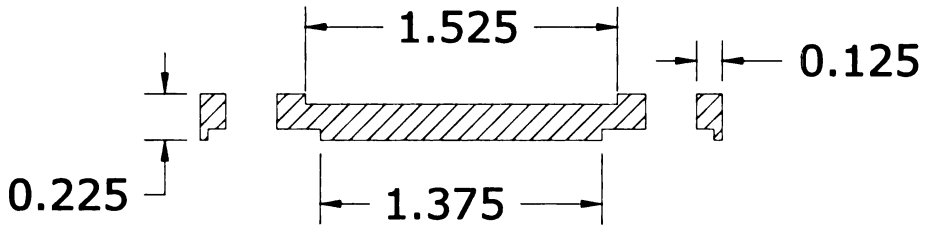

Figure 3.16 - Polycrystalline diamond (PCD) substrate holder schematic drawings. Units are in inches.

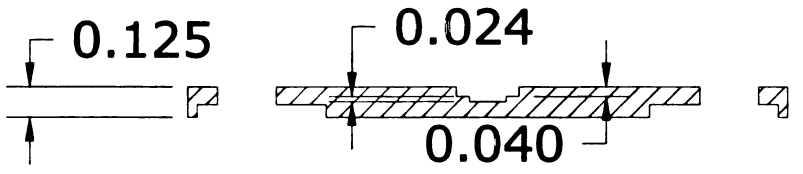

Figure 3.17 - Single crystal diamond (SCD) substrate holder schematic drawings. Units are in inches.

CHAPTER 4

MICROWAVE PLASMA ASSISTED CVD DIAMOND EXPERIMENTAL SYSTEMS AND PROCEDURES

4.1 Introduction

This chapter describes the experimental system, experimental procedures, and measurements methodologies. The overall experimental system set up consists of microwave power supply with its associated microwave transmission network, flow control and pumping systems, and additional components such as computer, water cooling chiller, air cooling fans, pyrometer, and digital cameras. The input and output experimental operating parameter space such as diamond nucleation and pretreatments procedure, start-up and shut down procedures, and diamond characterization methods are presented.

Since the MPACVD experiments were performed in a new high pressure (180-250 Torr) regime, a new safety consideration was recognized. In particular, the experiments were being performed within mostly hydrogen gas environment that if subjected to air leaks or air input, it could result in a reactor explosion. Thus, it was important that the reactor system was far from air leaks and during experimental operation, the system was continuously monitored to ensure that there were no indication of reactor failure that may lead to air leaking into the reactor during operations.

4.2 Experimental systems

The overall experimental setup is shown in Figure 4.1. The experimental microwave plasma assisted CVD system consists of five major components or subsystems. They are: (1) microwave power supply and circuit transmission network subsystem, (2) microwave plasma applicator, process chamber, and substrate holder subsystem, (3) gas flow control subsystem, (4) vacuum pumping and pressure control subsystem, and (5) computer control, camera monitor, and cooling subsystem.

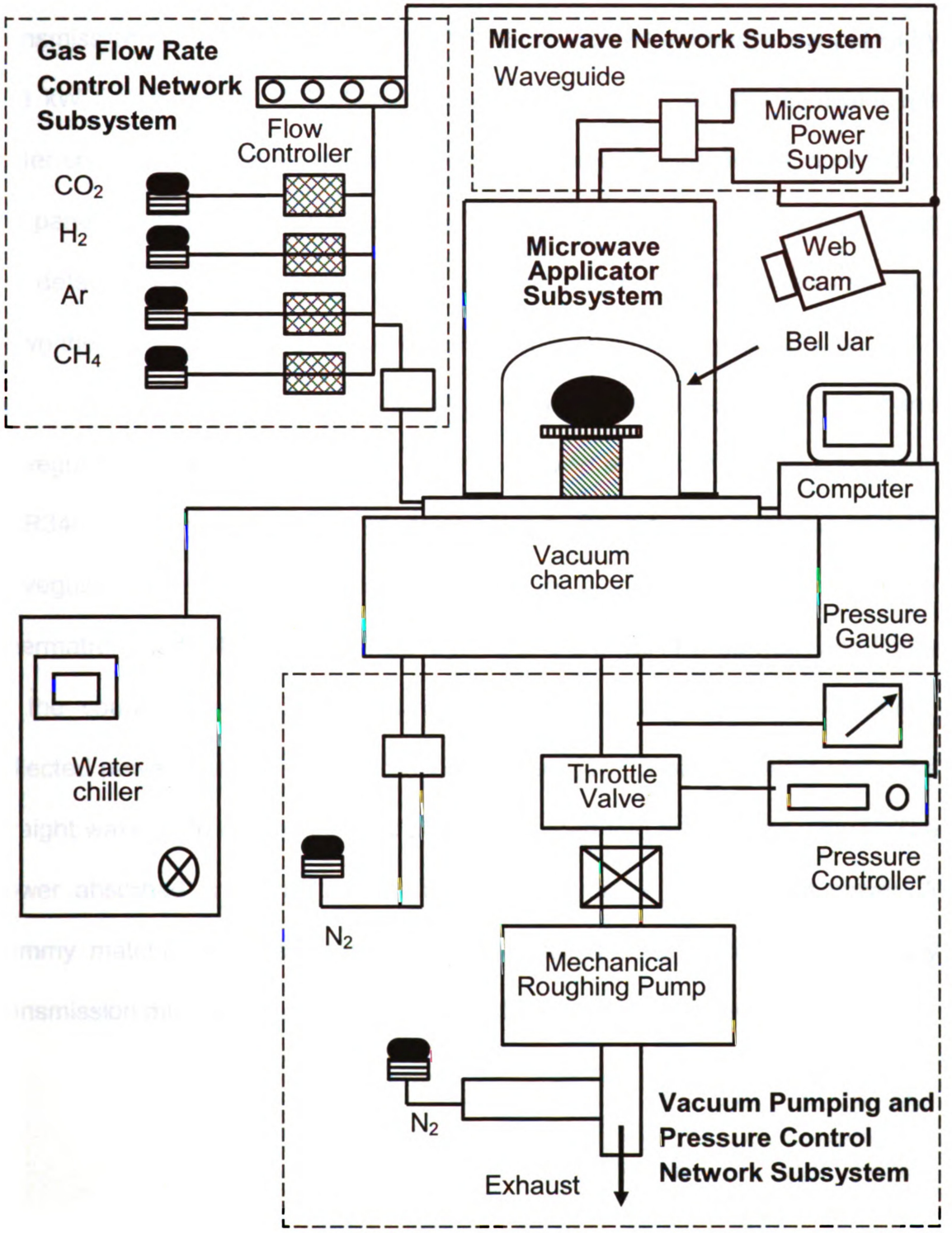

Figure 4.1 - Overall microwave plasma assisted CVD experimental system setup.

Shown in Figure 4.2 is the microwave power supply and circuit transmission network subsystem. The 2.45 GHz microwave energy is supplied by a 6 kW Cober (model S6F/4503). The magnetron tube and the circulator are water cooled inside the power box. Operating knob and controls are mounted on the panel door of the power supply box. The power supply also has a waveguide arc detector which can sense any arc or short circuit and will immediately shut down the power supply then the amber light turns on indicating standby mode.

The incident power is transmitted through multiple sets of S band waveguides in the following order: power supply to a straight copper waveguide (WR340) to a 90° E bend waveguide to a flexible non-twistable straight waveguide and then to a transition unit to a coaxial adapter (Thermex Thermatron model 4028, WR284 waveguide to 1-5/8" EIA flange type) and finally to the coupling probe of the microwave plasma cavity applicator. Incident, reflected power meters, and directional couplers (60 dB) are installed along the straight waveguide to measure the power absorbed into the plasma source. The power absorbed is defined as the input power minus the reflected power. A dummy matched load is located inside the power supply box to absorb any transmission mismatch during operation or dissipate the reflected power.

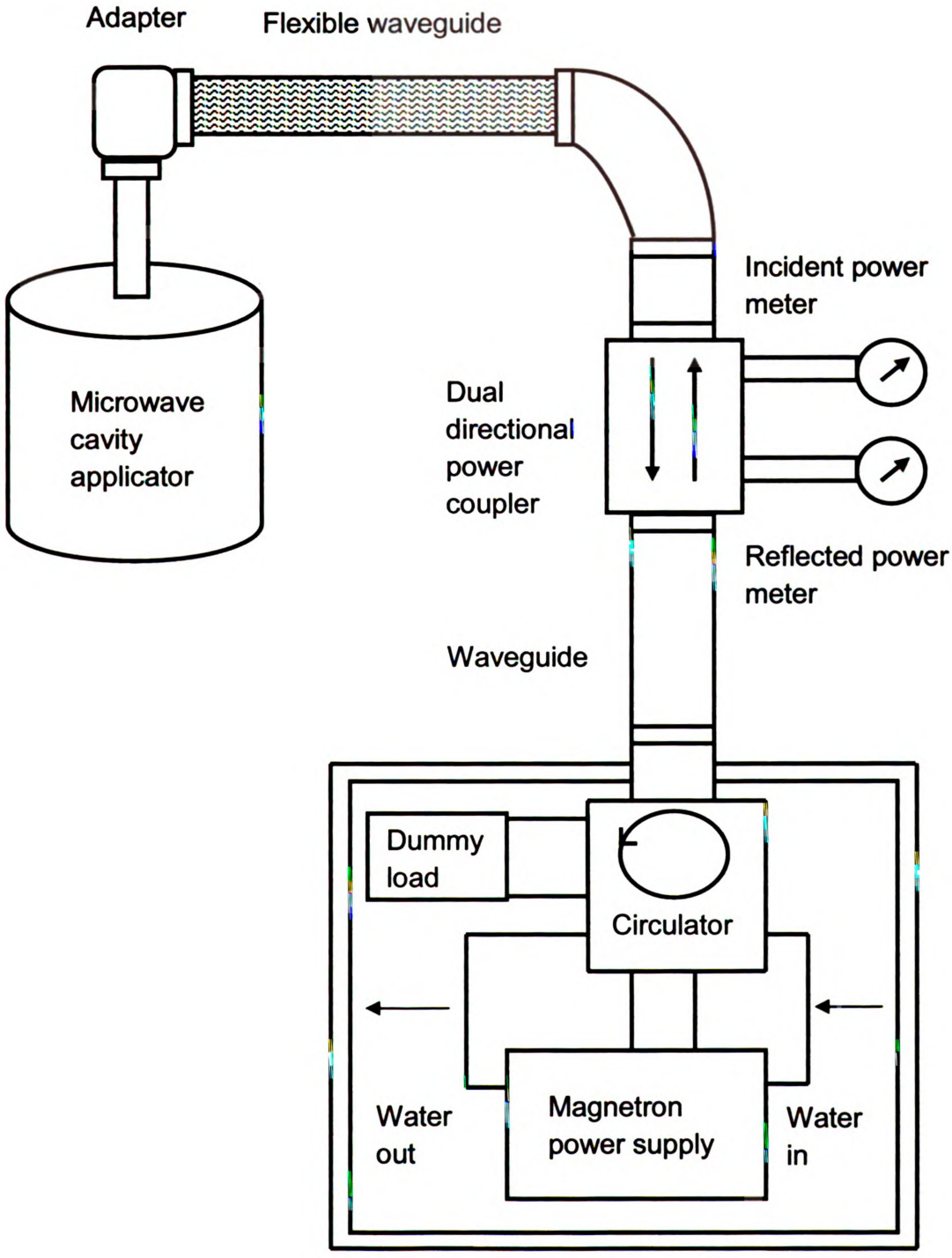

Figure 4.2 - Microwave power supply and waveguide network subsystem.

Shown in Figure 4.3 is the gas flow control subsystem. The input gas sources consist of methane (CH_4), Argon (Ar), Hydrogen (H_2), and Carbon dioxide (CO_2). The H_2 and CH_4 input gases had purity levels of 99.9995% (5.5 N) and 99.999% (5 N) respectively. The high gas purity levels minimize any impurities during diamond growth. The MKS mass flow controller (model 247C) has a four channel controls read out that measures the input gas flow. The flow rate can be set or adjusted either through the front panel controls or rear panel analog interface for remote setting. The input gases are mixed before they enter the discharge chamber and the gas flows out of an annular input gas feed plate as part of the base plate assembly. The CO_2 gas is only used during quartz bell jar cleaning procedure and is not used for diamond deposition.

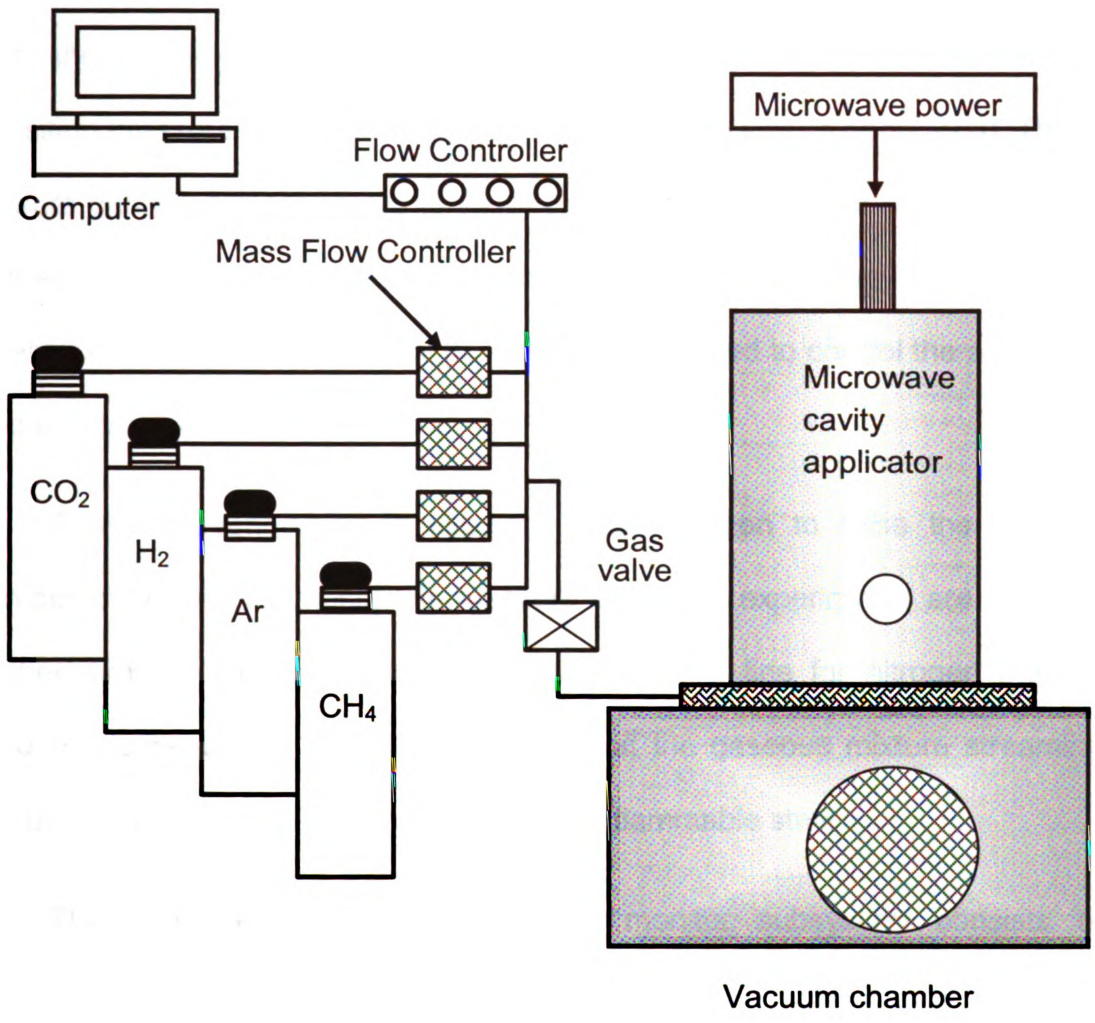

Figure 4.3 - Gas flow rate control network subsystem.

Shown in Figure 4.4 is the vacuum pumping and pressure control subsystem. A mechanical roughing pump (Alcatel 2063 CP) is used to pump down the chamber pressure to approximately 3 mTorr and the vacuum deposition pressure is measured by a pressure gauge (MKS model 627B). These pressure gauges are connected to Baratron capacitance manometers to monitor the pressure inside the vacuum chamber. The operating pressure is controlled by a pressure controller (MKS model 651) that is connected to control the automatic throttle valve and transducer.

A system vent valve is used to inject nitrogen to raise the vacuum chamber pressure to atmospheric pressure when the experiments are finished. Another exhaust valve is connected to the exhaust line for nitrogen purging purposes during the experiment to ensure that the gaseous mixture streaming from output of the roughing pump is below the flammable state.

The computer control and camera monitor subsystem consists of computer operating system, web camera, and digital camera. The gas line, operating pressure, microwave input power are all synchronized with a Lab-View computer module which is used to automatically monitor and regulate the system during the diamond deposition experiments from start up to shut down. During the experiments, the operating pressure, gas flows, and running deposition time are controlled based on the preset values. If for some reason, the reflected power is more than 25% or the operating pressure exceeds the preset value, or water-cooling is not flowing into the system, the computer will automatically shut down the microwave power supply. Under normal operating conditions, the

computer program controls and directs the system from the initial start up time until the running time expires.

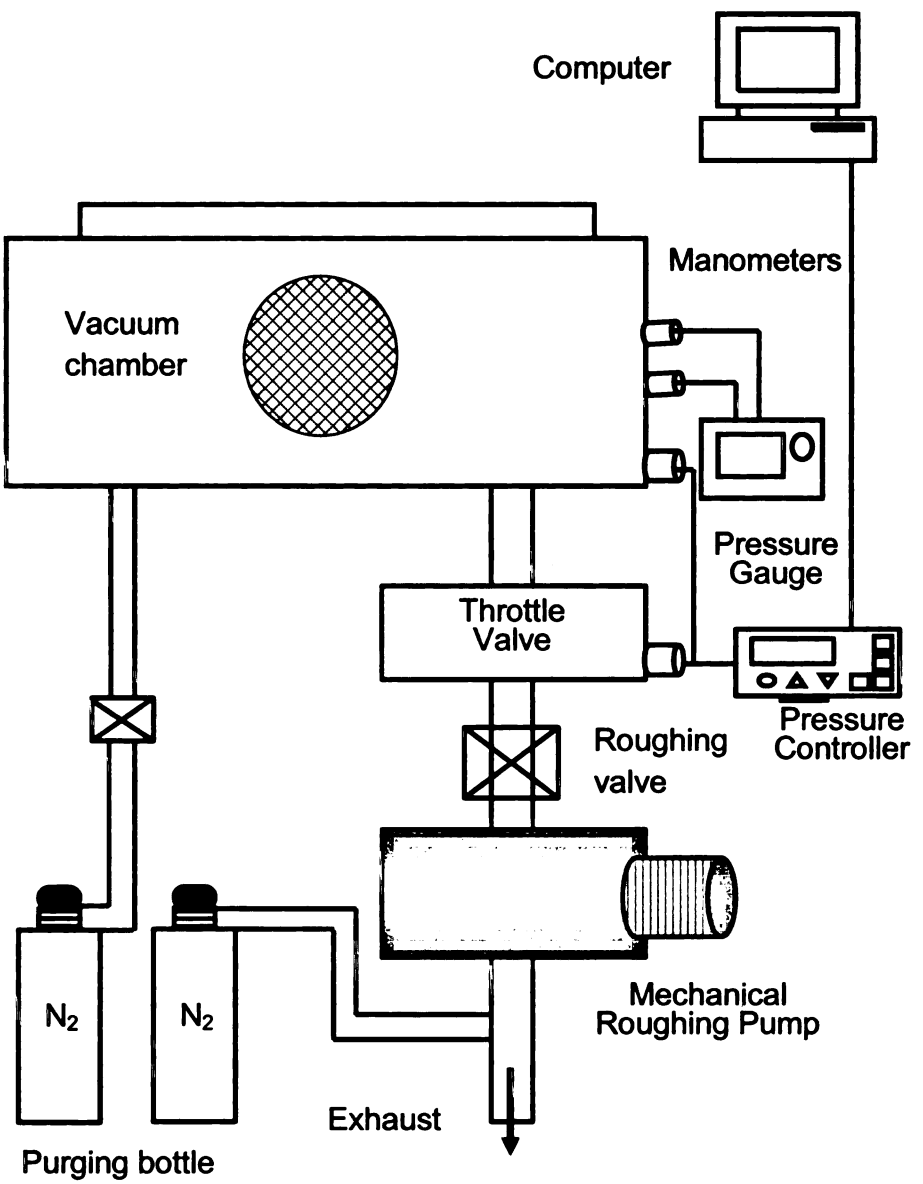

Figure 4.4 - Vacuum pumping and pressure control network subsystem.

Another monitoring device as part of the experimental system setup is the IP camera (D-Link model DCS-G900). The webcam is assigned to a static IP address that is connected to the MSU Division of Engineering computing service (DECS) domain network that allows remote monitoring of the experiments during diamond deposition. The photographic imaging during the experiments was taken using a Canon digital rebel XLR manual focus.

Additional components to the overall experimental set up are the cooling system, and temperature-reading instrument. For the air cooling, three different air fans were placed around the cavity applicator to cool the cavity walls during long hours of diamond deposition. At the back of the cavity wall there is an air blower inlet for air-cooling for the quartz bell jar dome. A water pipeline from the building is always turned on during the experiment to cool the microwave power supply. Water chiller Neslab CFT-300 cooled the substrate holder, cavity base plates, and cavity top plates. For temperature measurements, portable hand held pyrometer (Ircon UX CL1 model) with a one color with wavelength of 0.96 micrometers and temperature range reading of 600 °C to 3000 °C was used. The value of the emissivity of the pyrometer during temperature measurement is set to 0.6 and 0.1 for polycrystalline and single crystal diamond respectively.

4.3 Multi variables experimental space

The experimental multivariable experimental operating parameters can be categorized into controllable input variables, reactor design variables, internal variables, deposition process variables, and output variables. The input variables consist of microwave power, gas chemistry, gas flow rate, operating pressure, and substrate temperature. The reactor design variables include microwave cavity reactor configuration, substrate holder, and substrate cooling. The internal variables include discharge volume and absorbed power density. The deposition process variables include deposition time, substrate seeding, and substrate material type and size. The output variables consist of growth rate, diamond film uniformity, surface morphology, Raman analysis and optical transmission measurements. Listed in Table 4.1 below is an example of typical parameters value for input and output variables.

Table 4.1 – Multivariable for the diamond film high-pressure deposition

Input variables	
Input microwave power	2.1 - 3.2 kW
Gas chemistry	2-5% CH_4/H_2
Operating pressure	180 - 260 Torr
Gas flow rate	H_2 ~ 400 sccm and CH_4 ~ 6-24 sccm
Substrate temperature	950 – 1282 °C
Deposition time	2 - 10 hrs
Substrate treatment prior deposition	Scratching (PCD) Plasma etching (SCD)
Substrate material	2.54 cm silicon wafer (PCD) 3.5x3.5x1.5 mm HPHT diamond (SCD)
Output variables	
Growth rates	Weight gain over deposition time
Uniformity	Linear encoder
Morphology	Optical micrograph
Quality	Raman, FTIR and UV-VIS/NIR

4.4 Reactor start-up and shut down procedure

The general start up and shut down procedures are described as follows: After manually loading the prepared sample onto the substrate holder then placing it into the discharge chamber and setting the cavity height at the correct position at approximately 20.3 to 21.5 cm, the system was then pumped down to about 3 mTorr. Then the start up procedure was as follows:

- Turn on and warm up the power supply.
- Turn on all of the cooling fans and the cavity air-cooling motor.
- Turn on the water-cooling for the power supply, chiller and set water temperature to 18 °C.
- Turn on power meters, gas tank valves, gas regulators, and gas inlet valve
- Set the MKS pressure controller and gas flow channel to remote position
- Open the stage file (after setting the desired operating pressure, gas flow, deposition running time) from the computer Lab View module
- Enable the microwave power supply and set to 1 kW after system pressure reaches 5 Torr to ignite the plasma discharge.
- Slowly increase the input microwave power supply as the system pressure increases so that the plasma discharge covers the entire substrate and stable.
- If necessary, tune the cavity height or coupling probe to maintain zero or minimum reflected power.

- The experiment starts automatically when the desired operating pressure is reached at the preset value.
- Turn on the IP web camera to monitor the experiments remotely.

During the deposition experiments, a computer records all of the experimental input variables. When the experiment is completed, the system will undergo shut down procedure is as follows:

- For PCD, automatically turn off CH_4 gas flow.
    - The operating pressure stays at deposition pressure and going through a hydrogenation process (H_2 plasma only) for 15 minutes, then the pressure slowly drop down to a 20 Torr interval every 5 minutes.
    - Automatically turn off H_2 gas flow when the pressure reaches 20 Torr.
    - The operating pressure continue to drop to about 3 mTorr.
    - Automatically turn off the microwave power. However, the control knob must be manually set to zero position.
    - Automatically turn off the gas channels.
- For SCD, automatically turn off microwave power, CH_4 and H_2 gas flow
    - The operating pressure slowly drops down to a 20 Torr interval every 5 minutes until it reaches 3 mTorr.

- At this step, the procedure is both the same for both PCD and SCD which involves cooling down of the system and manually shut off the system.
- 20 minutes after the vacuum chamber has reached its base pressure at around 3 mTorr, turn off the chiller, turn off the air-cooling fan, gas regulator valves and gas inlet valves, turn off the microwave power supply master switch, turn off the power supply water cooling knob, turn off the nitrogen purge and air blow motor for the cavity applicator air cooling.
- Set the pressure controller back to manual mode and set to open position.
- After at least one hour or when the system has completely cooled down, open the nitrogen vent to raise the vacuum chamber pressure to an atmospheric pressure.
- Open the chamber window and unload the grown diamond sample.

4.5 Polycrystalline diamond nucleation procedures

Before the diamond substrate is placed in the process chamber, the silicon wafer must be mechanically polished and scratched using diamond powder to accelerate the nucleation growth of diamond [101-102].

A one inch diameter silicon wafer is used as the substrate. The silicon wafer has the following specifications: 2.54 cm diameter, N-type, <100> surface orientation, one side polished, 1500 micron thick. The seeding is done by mechanically scratching the silicon wafer using 0.25 micron size natural diamond powders. The scratching is done manually moving hands in a circular motion both clock wise and counter clockwise directions for about 10 to 15 minutes. Once the substrate surface is scratched and polished, a fine napkin paper cloth was applied gently to remove any diamond powder clusters or excess on the substrate surface. The substrate is then rinsed using acetone solution and blow dried using a nitrogen gun. The final step is to observe visually using an optical microscope the nucleation density on the seeded substrate to ensure that enough density and uniformity are achieved on the substrate surface. This nucleation procedure is adapted from previous thesis work at MSU [85, 103-104].

Figure 4.5 shows an example of a substrate surface after being scratched and polished. Before the sample is placed in the process chamber, the sample initial weight and thickness was measured using an electronic scale (Denver Instrument M-220D) before deposition.

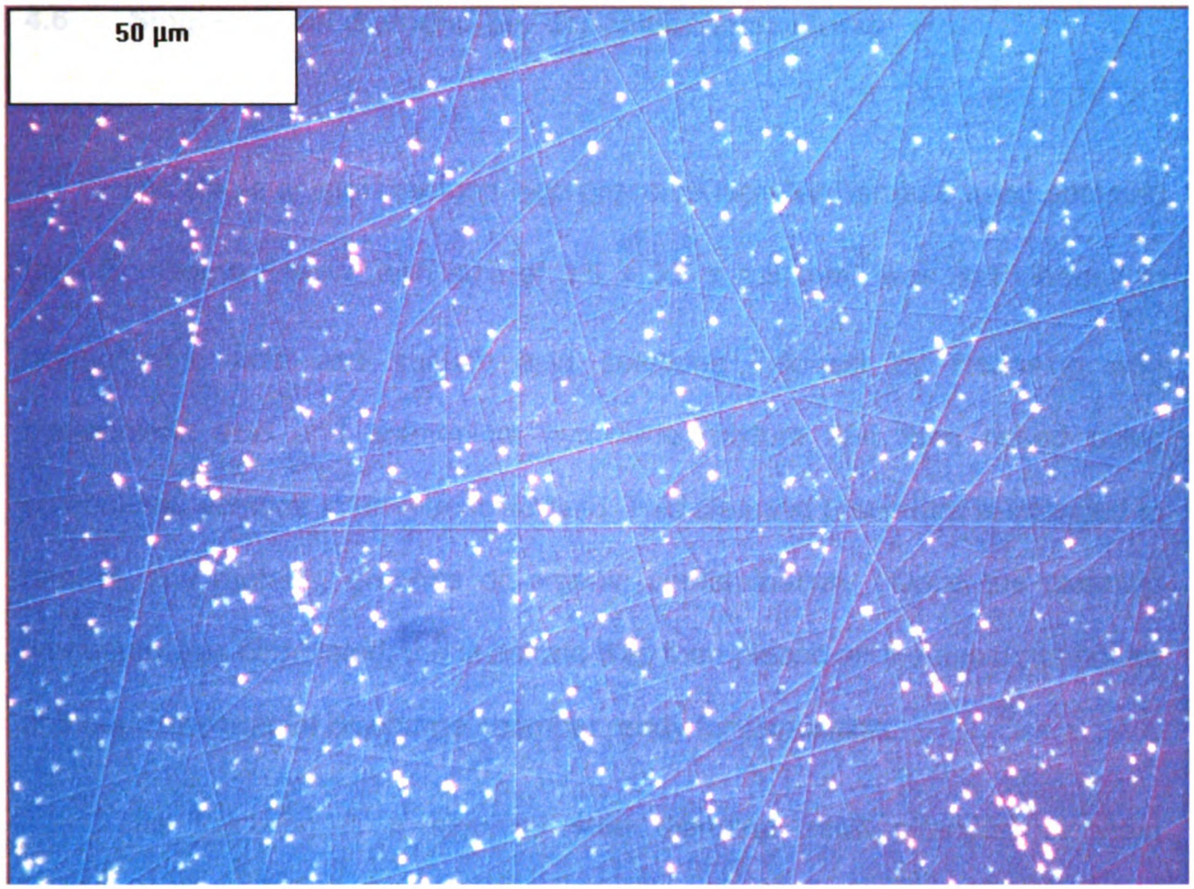

Figure 4.5 - Seeded substrate after mechanical scratching and polishing with natural diamond powder before deposition.

4.6 Single crystal diamond pre deposition procedures

The single crystal diamond high pressure high temperature seed obtained from Sumitomo Electric with size of 3.5 x 3.5 x 1.5 mm^3 was first cleaned in boiling nitric acid and sulfuric acid solutions followed by cleansing with hydrochloric acid and ammonium hydroxide mixture and then rinsed using ethanol and acetone in an ultrasonic bath. This cleaning procedure is intended to remove any metallic, graphite or organic contamination. Once the cleaning procedure was completed, the substrate was then placed on the substrate holder and put in the reactor discharge chamber ready for deposition.

The following is a step by step diamond seed chemical cleaning procedure:

1. Acidic cleaning
    a. Nitric acid (40 mL) + Sulfuric acid (40 mL) mixed in pyrex beaker, placed on the heater (setting the knob to 10) for 30 minutes. Then, rinse sample in DI water.
    b. Hydrocloric acid (40 mL) in pyrex beaker, placed on the heater (set to 10) for 15 minutes. Then, rinse sample in DI water.
    c. Ammonium hydroxide (40 mL) in pyrex beaker, placed on the heater (set to 10) for 15 minutes. Then, rinse sample in DI water.
2. Ultrasonic cleaning
    a. Ultrasonic bath with acetone (30 mL) in pyrex beaker for 15 minutes.

b. Ultrasonic bath with ethanol (30 mL) in pyrex beaker for 15 minutes.

3. Final rinsing and drying

   a. Rinse sample with DI water

   b. Blow nitrogen on the sample to remove any water

Figure 4.6 shows HPHT diamond seed 3.5 x 3.5 mm^2 prior to deposition. The diamond exhibits yellowish color due to substitutionally nitrogen incorporated during the making of the diamond seed via high-pressure high temperature method.

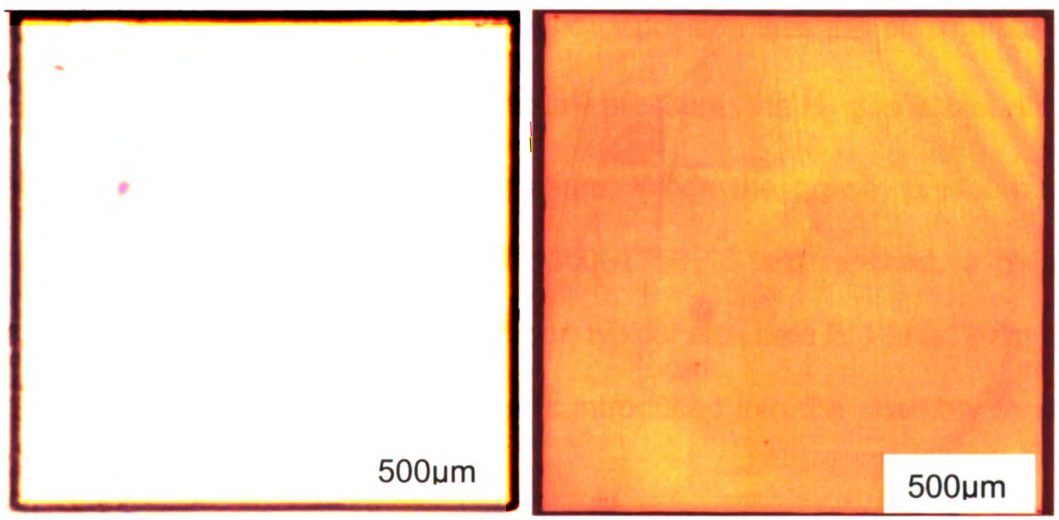

(a) (b)

Figure 4.6 - HPHT diamond seed optical micrograph 2.5x magnification view before deposition showing: (a) reflection light (b) transmission light.

The substrate holder cleaning preparation consists of the following steps:

1. Sand blasting. The molybdenum (Mo) pieces that are going to be placed inside the vacuum chamber were sand blasted first. This ensures the cleanliness of the substrate holder in order to avoid any formation of polycrystalline diamond or any impurities into the grown single crystal diamond.
2. Ultrasonic cleaning of all Mo pieces with acetone and DI water.
3. Rinsing and nitrogen blowing
4. Drying the Mo pieces in an oven dryer at about 80 °C for 20 minutes.

The next step before the actual diamond deposition was the plasma etching procedure. After igniting the discharge at low pressure, the H_2 gas is brought up to the desired deposition operating pressure. When the growth pressure and substrate temperature in the range of 1100–1150 °C are reached, a plasma etching ranging from 30 minutes to 1.5 hour, typical etch time is 1 hour. After one hour of hydrogen etching, methane gas is introduced into the chamber to start the diamond growth deposition.

4.7 Evaluation procedures of the synthesized diamond

4.7.1 Diamond growth rate

The diamond film growth rate was determined by measuring the average growth rate. This was calculated by measuring the total weight gain (mg) after deposition and dividing it by the deposited substrate area i.e., 2.54 cm diameter for a one inch wafer or and mass density of diamond (3.515 g/cm^3) then divided by deposition time (hr). This method gives the growth rate of the diamond film (μm/hr).

Growth rate = Weight gain/(deposition area x Diamond mass density)

For example, the total weight gain of a grown polycrystalline diamond measured was 21.92 mg/hr over 1 inch diameter silicon substrate. Then the growth rate is:

$$\text{Average growth rate}(\mu m/hr) = \frac{21.92\frac{mg}{hr} x \frac{10^4 \mu m}{cm}}{5.07 cm^2 x 3.51 \frac{g}{cm^3 x \frac{10^3 mg}{g}}}$$

= 12.32 μm/hr

4.7.2 Diamond uniformity

In order to be able to measure the polycrystalline diamond uniformity profile, the thickness of the grown diamond must be determined. This was done by measuring each specific point film thickness on the diamond substrate surface before and after deposition. The instrument used was a 50 nm precision Solarton linear scanning tip encoder. This technique was originally devised by Zuo *et.al.* [49] for two to three inch substrates. The point stage and number of point arrangements were modified to enable the measurement of one-inch silicon substrate. The device encoder essentially measures the linear depth of the vertical directions of the substrate as shown in Figure 4.7. The point stages are made of a spherical tip metal rod with the same dimension and shape as the vertical probe of the linear encoder. The metal rod is attached to a rectangular heavy metal base to provide strong support and to minimize any accidental movements or disturbances during point to point measurements. The substrate was placed and positioned as flat as possible between the vertical probe and point stage metal rod tip for accurate measurements. Shown in Figure 4.8 is the uniformity point arrangement both in radial and circumferential directions. Two perpendicular lines intersecting at the center of the substrate were used to guide the location of the points to be measured in the radial direction. Circumferentially, each point location to be measured is separated by 45 degrees angle along the entire circumference of the substrate. The thickness profile measurements for each sample were repeated three times and then averaged. The thirteen measured points per wafer gave good accuracy for measuring uniformity profile over an inch substrate.

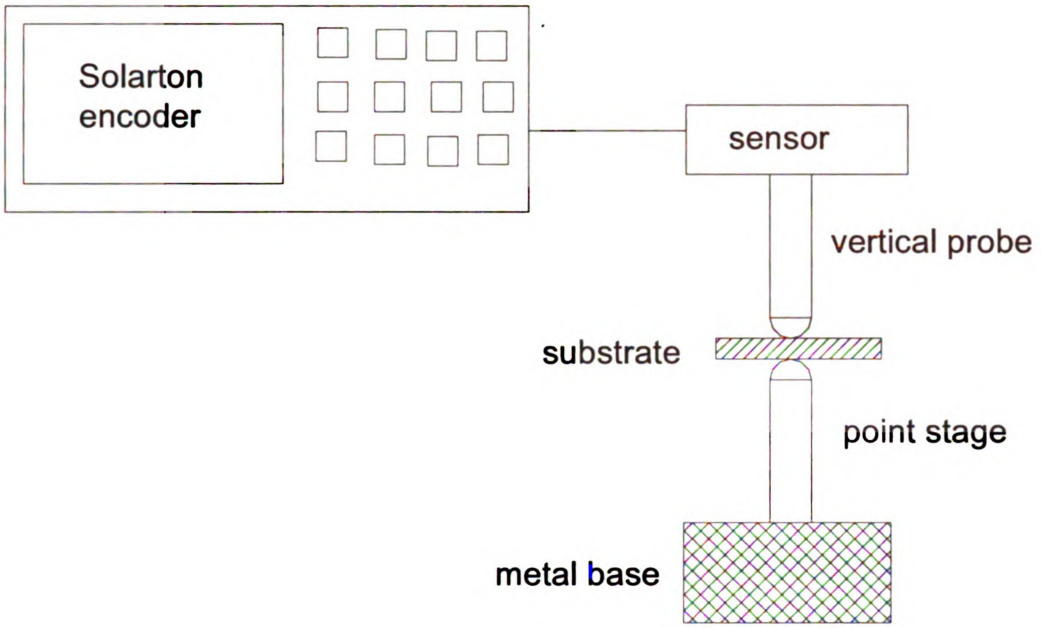

Figure 4.7 - Grown diamond thickness measurement setup using the Solarton linear encoder scanning tip and point stages.

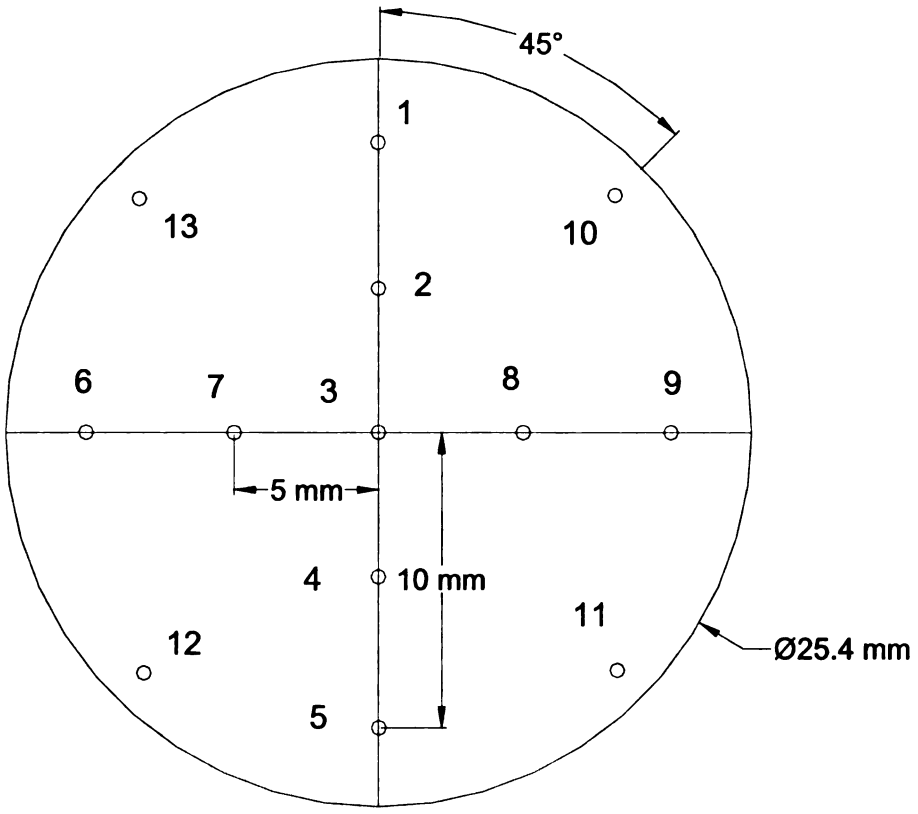

Figure 4.8 - Grown diamond thickness measurement points distribution denoted by small circles on a one inch silicon wafer substrate.

4.7.3 Diamond surface morphology

The most common shapes or facets of diamond crystal structures are octahedral {111} plane, cubic {100}, and {110} planes. These shapes vary depending on the ratio of growth velocities in the <100> and <111> directions. The shapes can be used to determine the ratio of growth rates. This growth parameter is commonly known as the "α parameter" as shown in Figure 4.9. This can be expressed by $a = \sqrt{3}\, V<100>/V<111>$. The distance from the center of the crystal to the center of each of the faces is proportional to the growth velocity in the direction perpendicular to that face. This direction always points to a corner as indicated by the arrows which shows the fastest growing direction. In terms of α relation to crystal shapes, for $\alpha = 1$, crystals grow in the form of a cube, for $1 < \alpha < 3$, crystals grow in the form of a cubo-octahedron, and for $\alpha = 3$ is in the form of an octahedron. Other crystal shapes may develop since twinning and stacking faults influence of the growth especially occurs on {111} planes.

The surface morphology of the grown diamond was evaluated using an optical microscope (Nikon Eclipse ME600) as shown in Figure 4.10. The microscope is integrated with 2-D and 3-D image processing computer program (Image Pro plus 5.1) to allow optical observation and analysis of the samples. By using this instrument, polycrystalline diamond grain size and growth surface shape can be identified. For example, common diamond surfaces such as triangular {111}, roof shape like structure {110}, and square or rectangular {100}

plane morphology. Likewise, single crystal surface smoothness or transparency can be seen through the crystal.

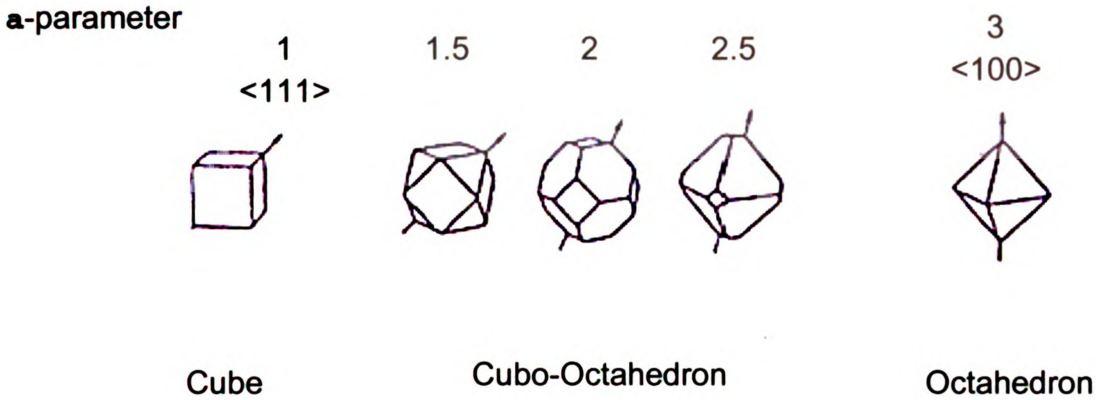

Figure 4.9 - The morphology of the diamond crystals grown at various values of α parameter. The arrows indicate the direction of fastest growth [105].

Figure 4.10 - Optical microscope photograph used to analyze diamond morphology.

Grown diamond quality was determined using various ways such as visual observation of the color and transparency of the freestanding diamond, optical microscope, Raman spectroscopy, ultra violet/visible/near infra red (UV/VIS/NIR), and Fourier transform infrared spectroscopy (FTIR). Described below are the procedures for each experimental measurements method for the experimental output.

4.7.4 Raman spectroscopy analysis

Raman spectroscopy is one of the common methods used to characterize the structural quality of grown diamond. This method provides well known spectra for graphite, amorphous diamond like carbon and other carbonaceous compounds. Also it can be used to determine diamond purity and crystalline lattice matching perfection by analyzing the peak positions and peak width. Raman spectroscopy is used to investigate quantized molecular resonances by observing transitions between vibrational energy levels caused by inelastic scattering of high energy visible photons. In Raman scattering the light photons lose or gain energy during the scattering process, and therefore increase or decrease in wavelength respectively. If the molecule is promoted from a ground to a virtual state and then drops back down to a higher energy vibrational state then the scattered photon has less energy than the incident photon, and therefore below original frequency. This is called Stokes scattering. If the molecule is in a vibrational state to begin with and after scattering is in its ground

state then the scattered photon has more energy, and therefore above original frequency. This is called anti-Stokes scattering [106-107].

Figure 4.11 displays the Raman spectra of different forms of sp^2- and sp^3-bonded carbon. The spectra exhibit a sharp peak or single phonon line at 1332 cm^{-1} indicating sp^3 diamond bonding. Assuming room temperature, the sharp peak of the diamond spectra could shift from 1331 to 1335 cm^{-1} with a bandwidth at half intensity usually less than 2 cm^{-1}. The full width half maximum (FWHM) of the line in natural perfect diamond reported is 1.5-1.8 cm^{-1} while typical FWHM in CVD diamond films is between 2 to 14 cm^{-1} [105]. The spectra above the diamond one phonon band is related to sp^2 carbon such as graphite with a peak at 1580 cm^{-1}, microcrystalline graphite with two broad band at 1580 and 1350 cm^{-1} which also commonly known as the band D (disorder) and band G (graphite) respectively, amorphous carbon with asymmetric band peaking at 1500 ± 40 cm^{-1}. The peak frequency could downshift with temperature and upshift when internal stresses are present. The broadening of the band may be due to several factors such as thermoelastic stresses, thermal effects, internal stresses (intrinsic tensile and thermal compressive), crystallite grain size, and the density of defects in the crystal.

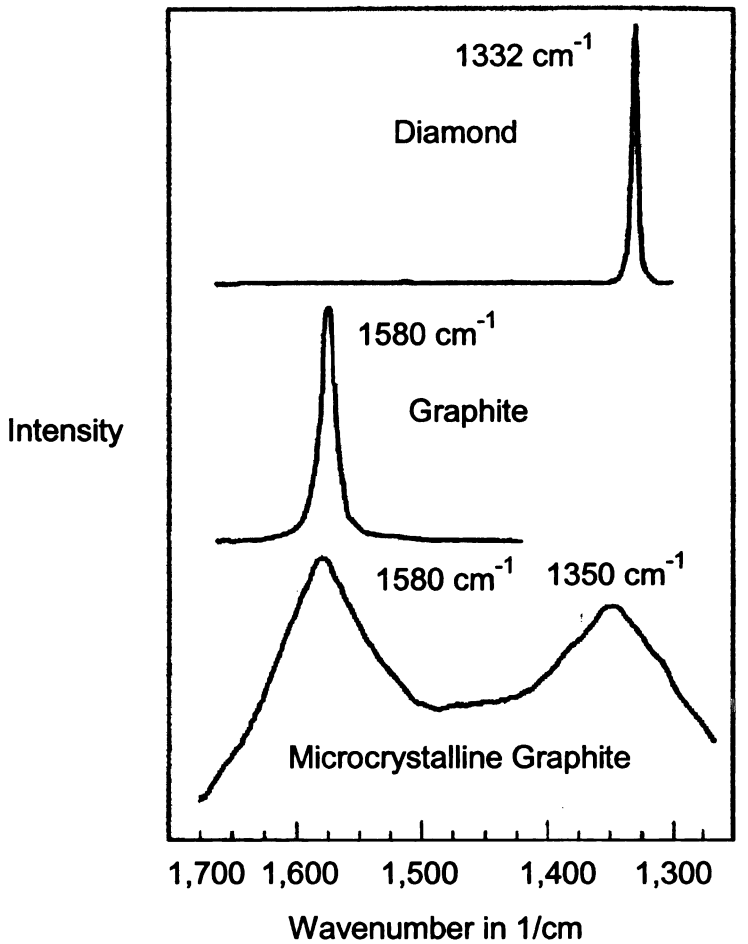

Figure 4.11 - Raman spectra of different forms of sp^2- and sp^3-bonded carbon [107].

Figure 4.12 shows the instrument set up layout schematic. The general operation of the Raman components can be summarized as follows: initially, the light source from the laser is focused on the sample, then the sample scatters the light which is mostly Rayleigh scattering i.e., same wavelength. However a small amount is Raman scattered which produces different wavelength. The gratings inside the monochromator diffract the incident light on selected wavelength then the charge-coupled device (CCD) produces an electrical signal according the intensity of the light and finally passes on to the computer for analysis. The instrument specification used during the Raman measurement was a SPEX 1250M spectrometer connected to a HORIBA Jobyn Yvon symphony charged-coupled device (CCD) detector and an Olympus BH-2 optical microscope. The laser source was an argon ion green laser with 514.532 nm with spot size at about 25 micron and power density of 0.28 W/cm^3. The penetration depth of the laser beam into the sample surface is approximately a few micrometers. The spectrometer slit width of 50 micron with high resolution grating of 1800 grooves/mm provides data resolution of 0.3 cm^{-1} with spectral width of 2.92 cm^{-1}. Integration time of less than 60 seconds and CCD image binning of 1 was utilized in order to increase signal/noise ratio and produce high intensity counts. A Gaussian/Lorentzian curve fit baseline correction is used to position the spectra peak and evaluate the full width half maximum. The frequency was scan from 1150 to 1800 cm^{-1} to sweep both the diamond and graphite bands. The computer program used to collect the Raman spectra was Lab Spec 4.01.

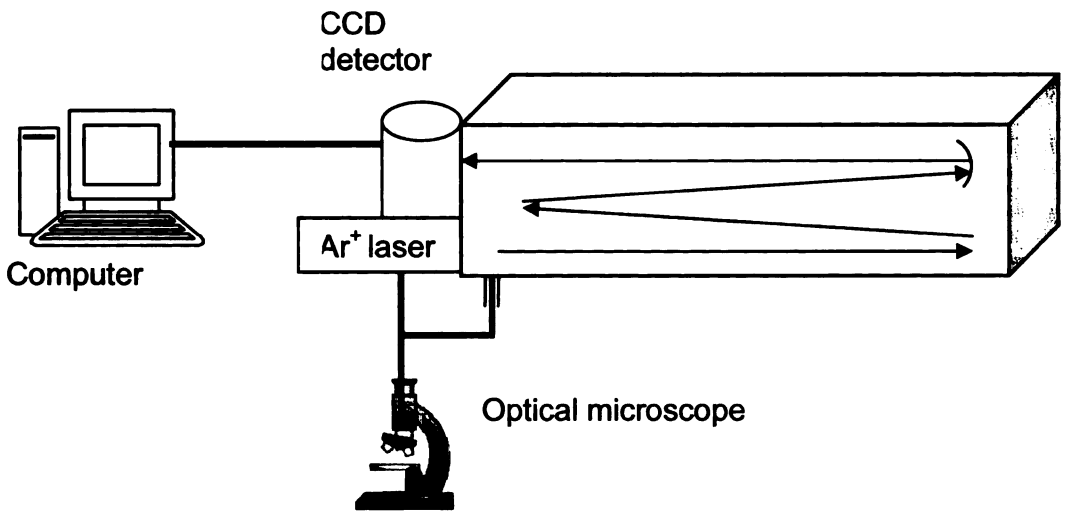

Figure 4.12 - Raman spectroscopy instruments general layout set up schematic.

4.7.5 Optical transmission measurements

Both polycrystalline and single crystal diamonds have a great potential for optical applications as mentioned in chapter two; however, the grown diamond must have a very smooth surface and an excellent optical transparency. The optical transparency of the grown diamond in the infra red can be affected by a number of reasons such as absorption by chemical impurities and defects due to incorporation of nitrogen into the diamond. This nitrogen incorporation into sp^3 and sp^2 bonded carbon could result in loss of lattice symmetry hence the loss of transmission. Another possible cause of optical transparency degradation is the scattering loss due to surface roughness of the grown diamond and reflectance loss due to high refractive index of diamond at about 2.41.

Figure 4.13 shows the calculated optical transmission results for an ideal 1 μm thick diamond film on a 1 mm thick glass substrate reported by Ulczynski *et.al.* [108]. Ideal in this case refers to lossless and optically smooth diamond on glass hence zero scattering and zero absorption. The refractive index of diamond calculation for this plot is described in. As can be seen from the figure, near ultraviolet to near infrared spectrum is plotted versus transmission. The transmission average varies from 67% to approximately 89% depending on the refractive index. The interference effects are due to multiple reflections at the diamond-air and diamond-glass interfaces.

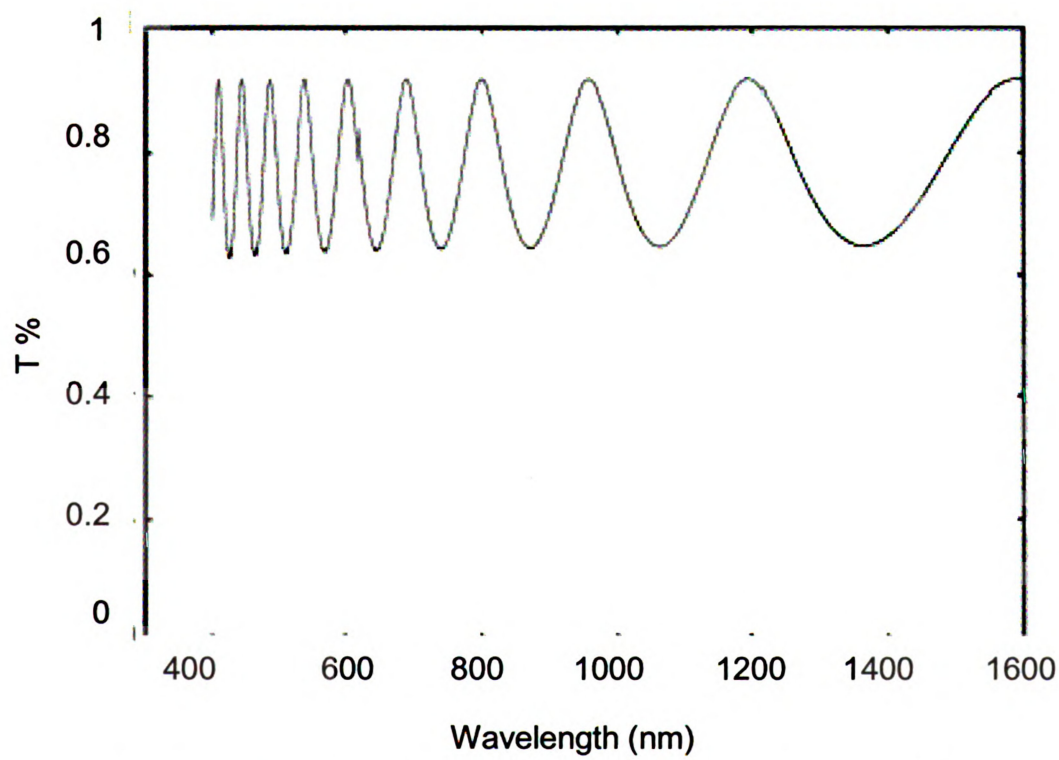

Figure 4.13 - Calculated optical transmission results for 1 μm thick diamond film on 1 mm thick glass with zero scattering and zero absorption [108].

Prior to UV/VIS/NIR and FTIR measurements, the deposited polycrystalline diamond film must be back etched to obtain freestanding diamond**. This can be achieved by silicon substrate removal via wet etching with the following recipe [109]:

1. Initially the silicon side is abraded using an Emory cloth (600 grit size).
2. Then the abraded sample is placed on a Teflon holder pedestal with the silicon side facing up.
3. Then the Teflon holder which contained the sample is immersed in the Teflon beaker on mixed solution (50 ml of HNO_3, 40 ml of H_2O, and 30 ml of HF) for a few hours. Typically this solution mixture can remove 1 mm of silicon in approximately 2 hours at 50 °C.

Then, the freestanding polycrystalline diamond must be polished and lapped in order to remove the rough surface and produce a smooth surface. This rough surface could cause scattering during the transmission measurements. Generally, the surface roughness of the grown polycrystalline diamond increases as the thickness increases. This could result in an average surface roughness (Ra) value in the order of micrometers [110]. Hence, the optical transmission losses due to scattering are fairly high (except in far infrared) and thus it is important to polish and lap the diamond surface in order to obtain excellent transmission in the visible and UV.

***Dr. Reinhard is thanked for the help in post processing step for the optical transmission measurements used for general guideline in this thesis.*

The lapping and polishing of the sample was done using a Logitech LP 50 system and surface roughness was measured using surface profilometer Dektak D6M. Prior to lapping and polishing, plasma etching of the nucleation side sometimes is needed in order to remove any silicon carbide layer that might be formed during the deposition. Plasma etching is typically done using O_2, Ar, and SF_6 gas chemistries as reported by Chakraborty *et.al.* [111] and Tran *et.al.* [112].

Perkin Elmer Lambda 900 UV/Vis/NIR spectrophotometer was used for the optical transmission measurements of the grown polycrystalline diamond in the ultra violet and visible spectrum. The instrument can measure reflection, absorption or transmission in the range of 180 nm < λ < 3300 nm (0.4 eV < E < 6.9 eV), equipped with monochromator holographic grating 1440 lines/mm (UV/VIS) and 360 lines/mm (NIR), with photo multiplier detector.

Perkin Elmer Spectrum one Fourier Transform Infra Red spectroscopy (FTIR) spectrometer was used to measure the optical transmission in the infra red spectrum. The computer program used to analyze the spectra was Spectrum 5.01 with the following typical input parameters: scan range from 4000 cm^{-1} to 450 cm^{-1}, resolution 4 cm^{-1}, and transmittance as the output axis. The diamond was inserted into a metal housing where only the diamond can absorb the laser beam and the metal housing was then mounted on a multipurpose metal holder compartment.

The procedure to do the transmission measurements using UV/VIS/NIR is as follows [113]:

1. Turn on back right top corner green switch to forward down
2. Open center front panel
3. Insert the sample and the metal holder into the magnetic holder housing
4. Shut the top lid
5. Open Lambda 900 program
6. Double click on the spectra rainbow icon in the tool bar and enter the input parameters with abscissa: nm, start: 3,000, end: 210
7. Select the "inst" tab from the tab window and enter the following input parameters: ordinate mode: %T, data interval: 1 nm (very fine) and 10 nm (more coarse), integration time: NIR = 0.04, UV/VIS = 0.2, slit: NIR = fixed, UV/VIS = servo.
8. Click auto zero with BL for 100% and BO for 0%.
9. When background scan is done. Select "sample" tab and enter file name and click "start" to initiate the transmission measurements. Hope for 100%.
10. Take sample out, save file name with ASCII file format.

CHAPTER 5

MICROWAVE PLASMA ASSISTED CVD DIAMOND EXPERIMENTAL RESULTS

5.1 Introduction

This chapter presents the experimental results of the newly modified reactor. The chapter begins with the description of the overall experimental multivariable operating parameter space, followed by experimentally measured absorbed plasma discharge power density, and then presents the experimental results of polycrystalline and single crystal diamond synthesis. Discussion of experimental results of the synthesized materials is also presented. In particular, the growth rate, uniformity, surface morphology, and optical quality of the synthesized diamond are discussed. During the testing of the modified reactor's performance, the total experimental runs i.e., growth time for both PCD and SCD synthesis was approximately 500 hours total runs. Most of the diamond synthesis experiments were conducted at duration of 8 hours.

These experimental results show that the redesign of the existing reactor works. For example, it is able to synthesize PCD and SCD at high pressure, it can produce high absorbed power density plasma, and it operates robustly within the define parameters. The general evaluation of the synthesized PCD and SCD such as growth rates, uniformity, morphology, and optical quality describes in this thesis could provide guidance for further optimization of the MSU microwave plasma cavity reactor for diamond deposition.

5.2 High pressure CVD plasma behavior and reactor performance

5.2.1 Plasma discharge characteristics

During ignition at about 5 Torr, the plasma discharge initially filled the whole discharge chamber, which was observed similarly on the reference reactor. However as the pressure was gradually increased the plasma size began to shrink and pull away from the quartz walls at about 60 Torr to 120 Torr and gradually became smaller as the pressure reached 240 Torr.

An important difference between high pressure and low pressure microwave discharges is that at low pressures the microwave discharge fills the discharge chamber and produces a diffusion loss dominated, cold (gas temperatures are less than 1000 K), non-equilibrium plasma, while in the high pressure regime the microwave discharge is hot (gas temperatures are greater than 2000 K), is volume recombination dominated and becomes a more thermal-like discharge. Plasma densities for 2.45 GHz hydrogen discharges operating at 100-200 Torr are estimated to be 10^{11} cm^{-3} to 10^{13} cm^{-3} [114-115]. At these high pressures the discharge separates from the walls and can become freely floating taking on shapes that are related to the shape of the impressed electromagnetic fields. The discharge can even move about the discharge chamber as it reacts to the buoyant forces on the discharge and to the convective forces caused by the gas flows in the discharge chamber.

Shown in Figure 5.1 are the visual images of the plasma discharge at different operating pressures varying from 20, 60, 100, 140, 180, and 220 Torr. Microwave absorbed power was 2.5 kW, 3% CH_4/H_2. As can be seen, the plasma discharge color turned from purple to violet and then to greenish around the plasma ball as pressure increases.

At high pressures (~100 Torr and above) the microwave discharge tends to separate from the walls and becomes "constricted" and thermally inhomogeneous. Thus the discharge becomes a recombination dominated discharge. Discharges constrict and become arc like when (1) a large temperature gradient exists between the center of the discharge and the discharge boundary, (2) a significant degree of gas heating is present (gas phase recombination heats the neutral gas), and (3) a large recombination rate is present in the discharge because of three body collisions. Thus, when the gas temperature gradients are sufficiently high, the recombination rate, which is greater than the diffusion rate, increases rapidly away from the discharge center. The rapid increase in recombination rate versus distance from the center restricts the discharge to the central region of the discharge enclosure.

Figure 5.2 displays the photographs of the discharge hovering over the silicon substrate as the operating pressure is increased from 180 to 240 Torr. At high pressure the discharge has a green color and has an intense almost white center core. As shown in Figure 5.2 the discharge becomes more visually intense, and shrinks in size as the pressure increases and the absorbed power density increases. As a result, this leads to an increase in the density of

hydrocarbon growth species (CH_3, C_2H_2) and atomic hydrogen. Hence, higher atomic hydrogen concentration means higher diamond growth rate.

20 Torr 60 Torr 100 Torr

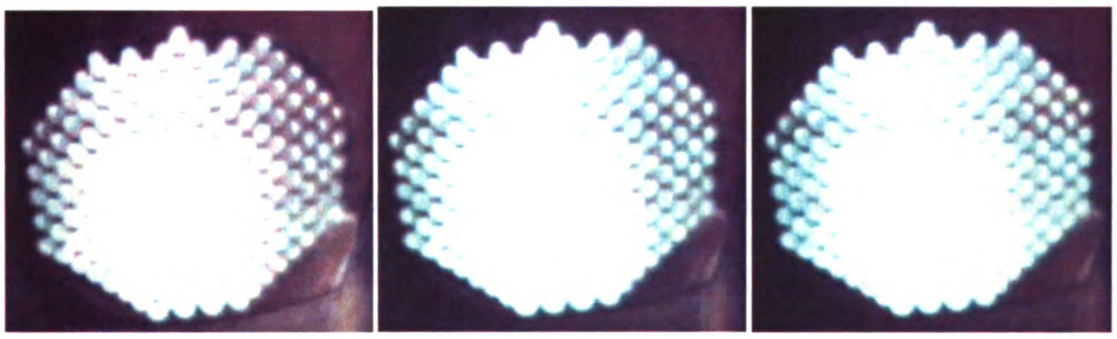

140 Torr 180 Torr 220 Torr

Figure 5.1 - The plasma discharge shape and intensity as the operating pressure increased from 20 Torr to 220 Torr. The discharge color turned from purple to violet and then to greenish around the plasma ball. Microwave absorbed power was 2.5 kW, 3% CH_4/H_2.

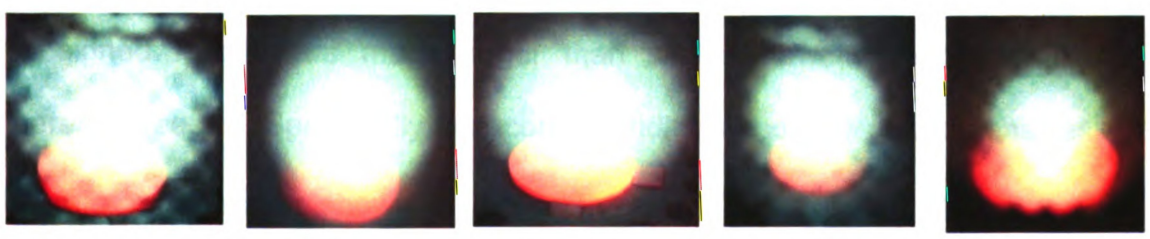

180 Torr 200 Torr 220 Torr 240 Torr 260 Torr

Figure 5.2 - Photographs of the discharge over the silicon substrate as the operating pressure is increased from 180 to 260 Torr. The microwave absorbed power ranged from 2.0 to 2.5 kW as pressure increases.

An example of the experimentally measured discharge power density versus pressure for the modified high pressure reactor is displayed in Figure 5.3. The experimental data were taken with fixed reactor geometry where L2 was held constant at 6.13 cm as the pressure was increased from 60 Torr to 240 Torr. The input microwave power was varied from 1.4 kW to 2.8 kW. The discharge power density is defined as the input absorbed microwave power divided by the plasma volume. The input absorbed microwave power is determined from the difference between the incident and the reflected power meters. The plasma volume is approximated by taking length calibrated photographs of the discharge, defining the discharge volume as the volume of the brightest luminescence of the discharge, and then determining the discharge volume from the visual photographs.

As shown in Figure 5.3, the discharge power density increases from about 80 W/cm^3 to about 500 W/cm^3 as the pressure increases from 60 Torr to 240 Torr. In Figure 5.3 the high pressure reactor is also compared with the power densities of the reference reactor. As expected the power densities of the redesigned reactor are much larger than similar power densities from the reference reactor. Specifically, the corresponding absorbed power densities for the reference reactor shown in Figure 5.3 vary from 20 to 45 W/cm^3 as the pressure increases from 80-140 Torr [84] while the corresponding discharge power densities of the redesigned reactor vary from 80 to 225 W/cm^3. The reduction of the center conductor area by about 4.5 increases the power density by a factor 4-5. Thus, for a constant pressure the reduction of the powered

electrode diameter significantly increases the power density of the discharge. The increase in power density is inversely proportional to the substrate area.

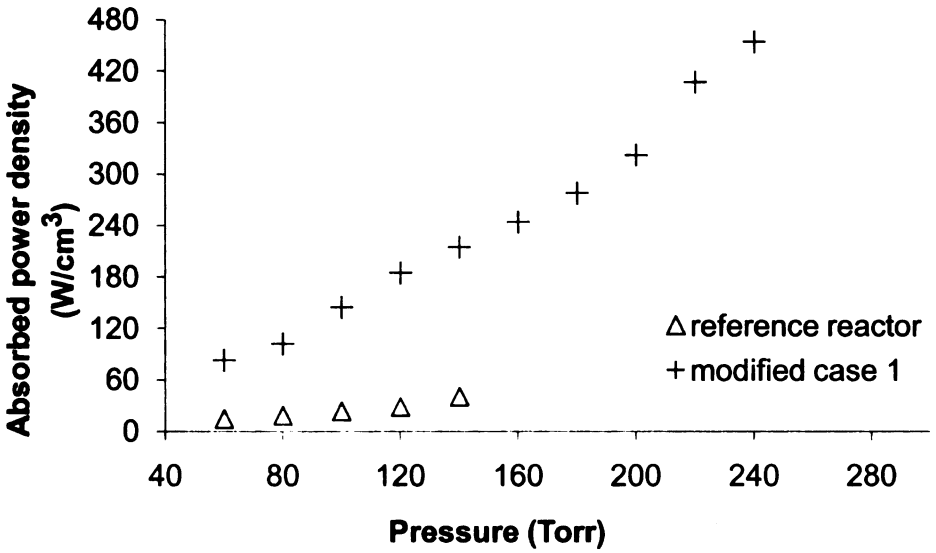

Figure 5.3 - The absorbed plasma power density for both the reference and modified reactor with increasing operating pressure. Modified case 1 denotes ΔZ position of -4.8 mm.

5.3.2 Reactor operation and optimization

When the reactor geometry, substrate size and total gas flow rate are held fixed, the deposition process is a function of input power, pressure, substrate temperature, and methane concentration. The major variables are the input power, pressure and substrate temperature. The relationship between these variables is nonlinear and the relationship between them can best be understood

by experimentally measuring and plotting a reactor roadmap curve [47, 85]. Figure 5.4 displays such a set of curves for the modified reactor where the reactor geometry is held fixed at L_s = 20.5 cm, L_p = 3.5 cm, and L2 = 6.13 cm and the total gas flow rate is 412 sccm, and methane percentage is 3%.

Each of the experimental curves in Figure 5.4 is plotted for a constant pressure and the set of curves displays the variation of the substrate temperature versus input microwave power over the entire 60-240 Torr pressure regime. The safe and process useful operating region is enclosed by the dashed line parallelogram; i.e., the enclosed region displays the acceptable experimental operating region for process operation and optimization. The left hand side of the parallelogram is determined by the minimum power required to generate a discharge of sufficient size to cover the substrate while the right side of the parallelogram is determined by the power required to completely cover the substrate without touching the discharge chamber walls. Thus, at each operating pressure the right hand side of the data points represents the approximate limit of the maximum input power at that pressure before reactor wall heating becomes a problem.

Figure 5.5 shows a closer view of the reactor roadmap for operating pressure of 180 to 240 Torr. As can be seen, the substrate temperature increases as the microwave power increases. For microwave absorbed power of 2.0 to 2.5 kW, the substrate temperature ranges from 1020 °C to 1175 °C. Also, higher operating pressures result in higher substrate temperature. For example, for 180 Torr operating pressure, the substrate temperate varies from 1025 °C to

1080 °C while at 240 Torr operating pressure, the substrate temperature ranges from 1055 °C to 1175 °C for the same range of selected microwave power.

Several observations can be made from the curves of Figure 5.4 and 5.5. First, as the pressure and input power increase the substrate temperature increases. At low pressures, the change in substrate temperature is less sensitive to input power changes than at high pressure. That is when compared to the reference reactor roadmap [49], the slope of the temperature at high pressure in the modified reactor is steeper i.e., the increase in the substrate temperature is much faster versus increase in input power. The substrate temperature is also more sensitive to pressure changes at low pressures than at high pressures. Thus, for fixed reactor geometry the experimental performance is more sensitive to input power changes at high pressures than at lower pressures.

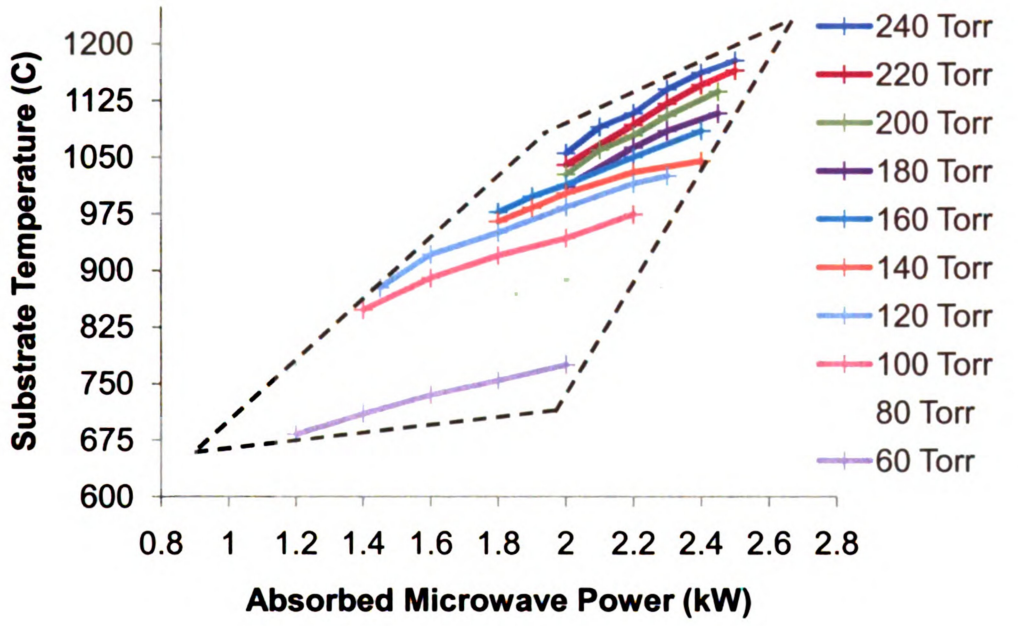

Figure 5.4 - The operating roadmap of the improved plasma reactor showing the substrate temperature versus absorbed microwave power at various operating pressures. The dashed-line region defines the allowable reactor operating region.

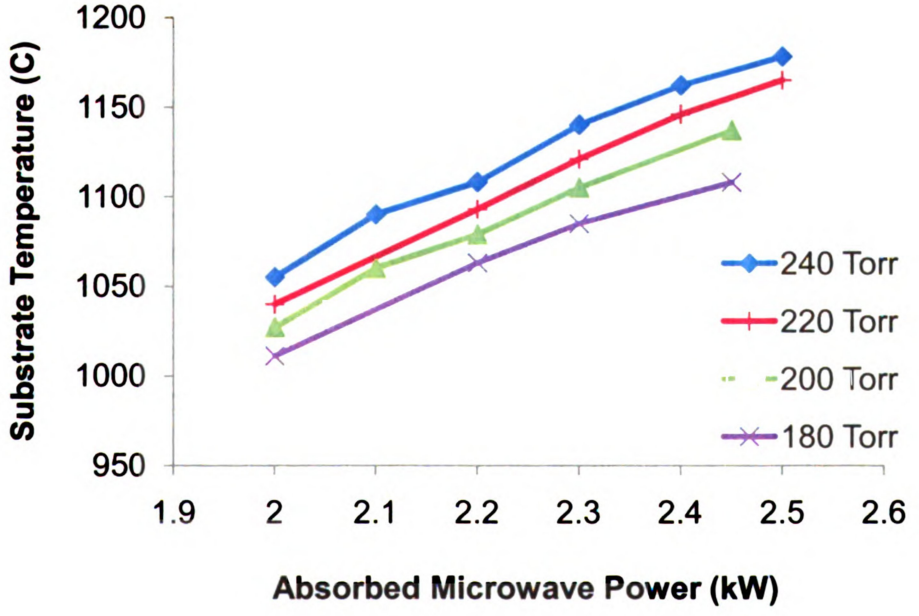

Figure 5.5 - The operating roadmap of the improved plasma reactor at pressures between 180-240 Torr. Operating conditions: Ls = 20.5 cm, Lp = 3.5 cm, L2 = 6.13 cm, H_2 = 400 sccm, CH_4 = 3 %, and ΔZ = -3.1 mm.

When operating at a constant pressure within the allowable deposition region shown in Figure 5.4, the reactor performance can be further optimized by length tuning the coaxial cavity. Thus, within the allowable deposition region shown in Figure 5.4, each curve can be modified by adjusting the coaxial cavity section of the applicator. When this is done, the electromagnetic focus is altered around the z = 0 region and the substrate also is moved changing its axial position from above to the below the z = 0 plane. As the substrate position changes the position, size, shape and power density of the microwave discharge is also varied in a complex nonlinear fashion.

Figures 5.6 and Figure 5.7 display the variations of substrate temperature and discharge power density versus pressure as the substrate position is varied from above to below the z = 0 plane, i.e. ΔZ varies from +4.9 mm to -4.9 mm. These curves demonstrate that at a constant pressure, the substrate temperature can vary more than 300 °C and the associated plasma power density also changes dramatically. For example, as shown in Figure 5.6, at 240 Torr as the substrate position is varied from +4.9 mm to -4.9 mm, the substrate temperature changes from 875 °C to 1175 °C. The substrate temperature increases as the substrate is lowered below the z = 0 plane. As the substrate is lowered, the discharge shape and size are changed, its volume is reduced and the discharge becomes more intense. The associated discharge power densities are displayed in Figure 5.7 vary from about 225 W/cm^3 at z = +4.9 mm to 475 W/cm^3 at z = -4.8 mm with variable absorbed microwave power from 1.8-2.1 kW over the pressure 140-240 Torr. These experiments clearly demonstrate the ability to alter

the substrate temperature and the discharge position and power density as the coaxial cavity size is changed.

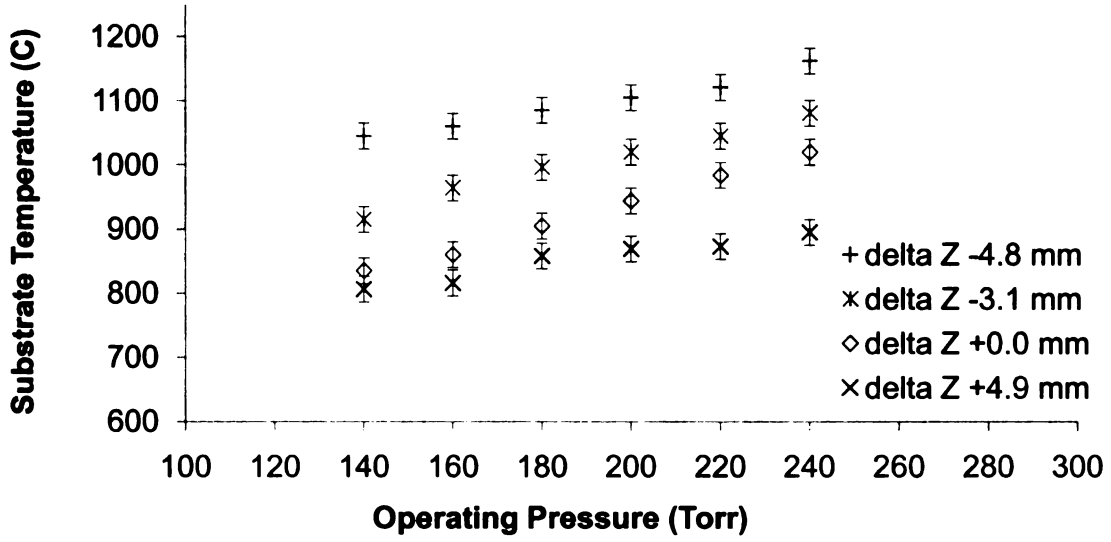

Figure 5.6 - Substrate temperature with different substrate positions, ΔZ versus operating pressures. The vertical bars represent the maximum/minimum variation of substrate temperature over the 2.54 mm diameter substrate.

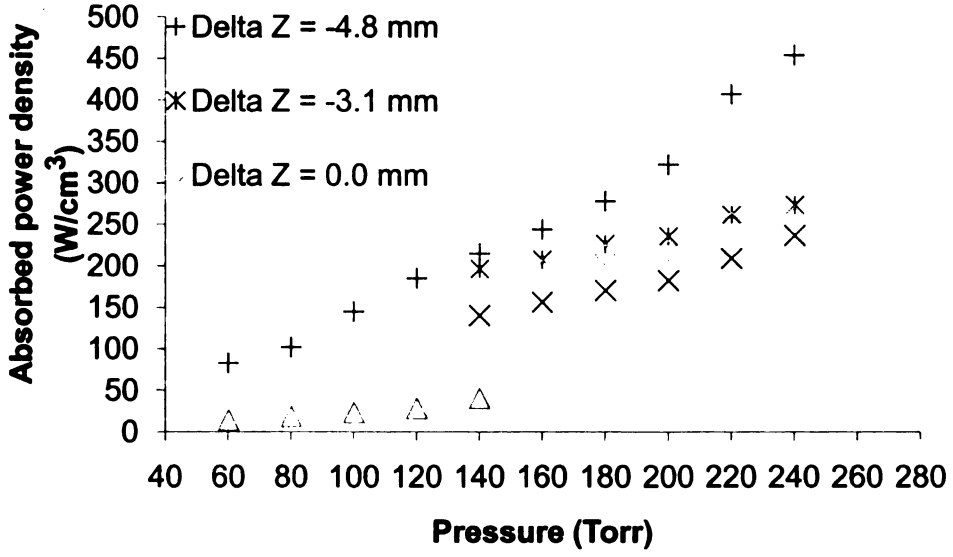

Figure 5.7 - The absorbed plasma power density with increasing pressure of the modified reactor at various ΔZ positions. Operating conditions: Ls = 20.5 cm, Lp = 3.5 cm, L2 = 6.13 cm, H_2 = 400 sccm, CH_4 = 12 sccm.

A set of separate eight hour deposition experiments were performed that investigated the deposition rate variation versus substrate position, i.e. versus L2. They were performed at a constant pressure of 220 Torr and a constant 3% methane concentration. L1 was held constant while L2 was varied in five steps and the substrate position varied from +4.9 mm to -4.9 mm. Input microwave power varied slightly from 2.6-2.8 kW. The experimental results are displayed in Figure 5.8 (a-b). For each of the experimental data points presented in the figure, the discharge size was slightly adjusted by varying the input power to achieve uniform deposition. Generally, it is desired to have the size of the plasma discharge cover the entire substrate in order to achieve deposition uniformity. However, at higher-pressure operation, the plasma discharge size can be slightly smaller than the substrate surface area and still achieve uniform deposition. As long as the plasma hovers around and remains in good contact with the substrate it will produce a uniform temperature distribution on the substrate.

As can be observed from the measurements presented in Figure 5.8, very small adjustments of L2 have a big influence on the deposition rates. As L2 is varied, the electromagnetic fields in the region around the z = 0 plane are greatly changed resulting in a variation in the shape and the position of the discharge. By varying the substrate position a few millimeters the deposition rates vary from 5.4 to 9.5 μm/h. At ΔZ = -4.9 mm the deposition rate decreases. In this case, the substrate temperature has begun to decrease since the discharge is starting to separate from the substrate. Thus, these experimental measurements indicate

that reactor tuning adjustments are very useful and necessary in order to control and optimize the deposition process.

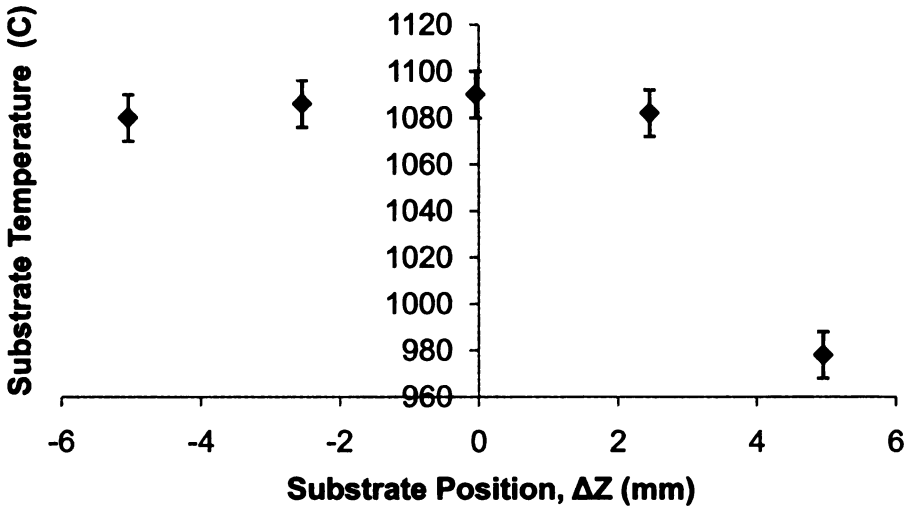

(a)

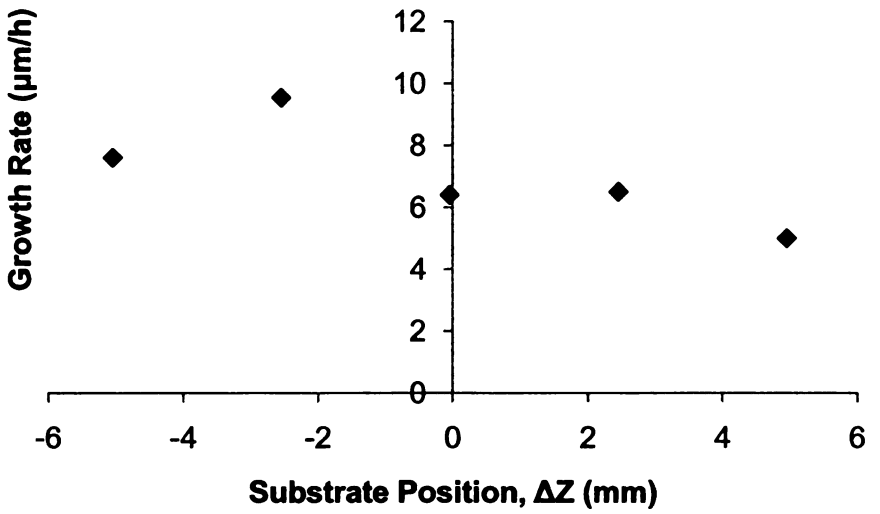

(b)

Figure 5.8 - Substrate temperature (a) and diamond growth rate (b) versus substrate position, ΔZ. Operating pressure = 220 Torr, CH_4/H_2 = 3%, microwave input power = 2.6-2.8 kW.

This new reactor design which decreases the substrate holder R4 from 5.08 cm to 3.24 cm, the inner conductor R3 from 4.13 cm to 1.91 cm, and allows the coaxial cavity section to be adjusted; it then focuses the electromagnetic energy on the reduced diameter substrate holder and increases the axial electric field intensity and the associated displacement current density at the location of the substrate surface. This redesign not only increases the plasma absorbed power density above the substrate but also facilitates operation at higher pressure. The electromagnetic field focus at and above the substrate is additionally controlled and varied during process development by length tuning L1, L2, L_s and L_p. When a discharge is present, this length tuning changes the electromagnetic field focus and in turn, changes the location and the shape of the plasma.

5.3 Polycrystalline diamond synthesis

5.3.1 Diamond growth rate

Diamond film synthesis was investigated over a range of process conditions and the experimental results are displayed in Figure 5.9. The polycrystalline films were deposited on 2.54 cm silicon wafers as pressure was varied from 180-240 Torr and methane concentrations were varied from 2-5%. Input microwave power levels were varied from 2.1-2.8 kW. For each of these measurements the reactor lengths were adjusted to yield good deposition rates. For all the data points in Figure 5.9 the cavity lengths, Ls, Lp, were kept fixed while ΔZ were varied. In all experiments above 200 Torr, ΔZ = -0.48 cm and at 200 Torr and below, ΔZ = -0.31 cm. In both cases the substrate was located below the z = 0 plane in order to produce good deposition rates. As is shown in Figure 5.9, the linear deposition rates increase as pressure and methane concentration increased. The substrate temperature during the deposition varied from 1030 °C to 1150 °C as the pressures were increased from 180 to 240 Torr.

A comparison of these deposition rates with the lower pressure and lower power density performance of the reference reactor indicated a significant improvement in linear deposition rates. When operating the reference at 130-140 Torr the maximum deposition rates were about 6 μm/h using 3% methane concentrations [8, 84-85]. In this improved reactor, maximum deposition rates exceed 10 μm/h and at the higher pressures and methane concentrations are

above 20 μm/h. These deposition rates also compare favorably with the rates reported at 200 Torr with a millimeter wave plasma assisted CVD reactor [115].

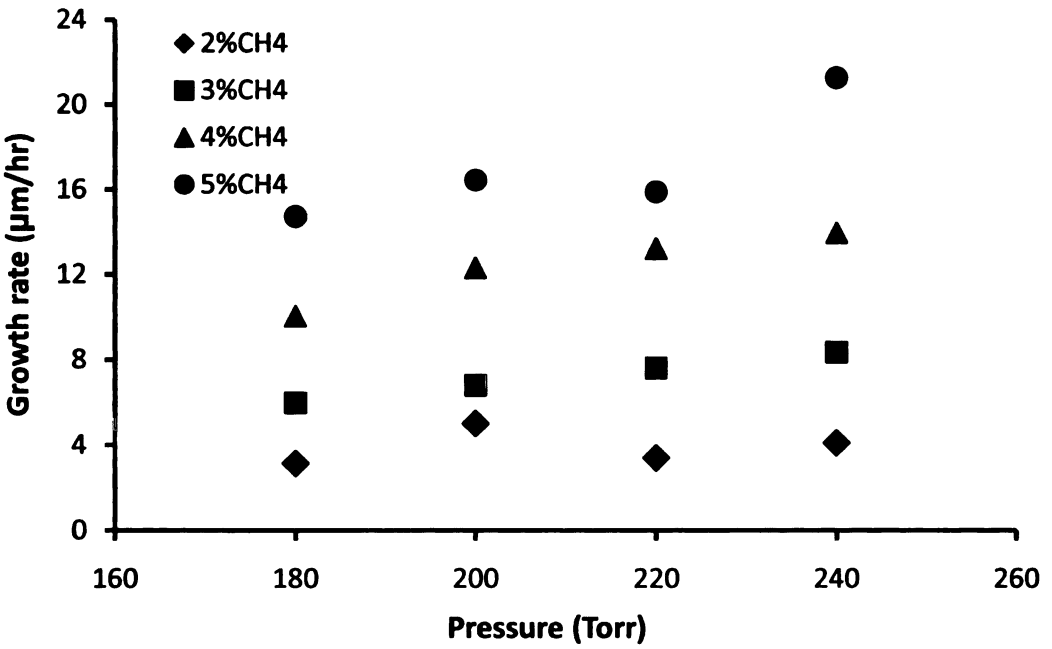

Figure 5.9 - Diamond growth rate with increasing operating pressure with CH_4 gas chemistries ranging from 2-5% with no addition of nitrogen gas into the system.

Shown in Figure 5.10 is diamond growth rate versus substrate temperature under various operating pressures range from 180-240 Torr at a fixed 3% methane concentration. The growth rates range from 5 to 9.7 micron/hour and substrate temperature varies from 1019 °C to 1173 °C for pressure of 180 to 240 Torr. As can be seen from the figure, the highest growth rates approximately at 10 μm/hr occurred at substrate temperature range between 1050 °C to 1090 °C.

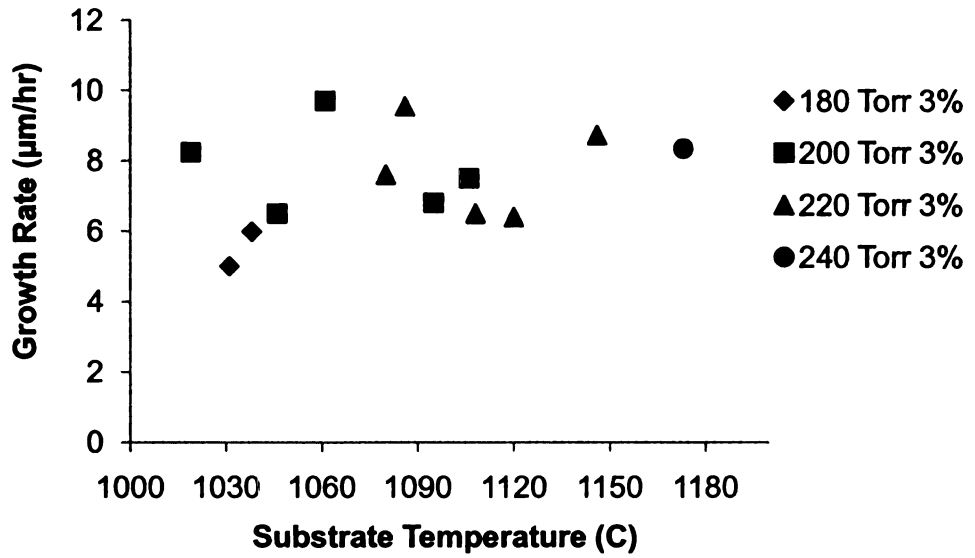

Figure 5.10 – Polycrystalline diamond growth rate versus substrate temperature at a fixed 3% methane concentration under operating pressure between 180 to 240 Torr. ΔZ varies between -1.4 mm to 4.95 mm.

5.3.2 Diamond uniformity

Six different samples were evaluated to investigate the uniformity of the grown polycrystalline diamond using the modified reactor. Described here is three of the best grown diamond uniformity achieved during the testing of the modified reactor. The uniformity may still be able optimized further when operating at pressure regime of 180-240 Torr. Since the plasma discharge will becomes smaller and the substrate temperature will increase, a new substrate holder insert design, shims adjustments, and retuning the cavity height and probe depth may be necessary.

Figure 5.11, Figure 5.12, and Figure 5.13 show typical results of the achievable uniformity of the synthesized polycrystalline diamond over one inch substrate. A good uniformity of grown diamond can be achieved at this operating high pressure similar to the deposition at lower pressures.

In order to achieve this uniformity, a series of experimental runs and adjustment were performed. The variable parameters such as L1 = 5.65 cm, L2 = 6.05 cm, L_s = 20.3 cm, L_p = 3.6 cm were kept fixed while microwave absorbed power, pressure and methane concentration varied from 2.3-2.5 kW, 200-220 Torr, and 3-4% respectively.

The uniformity of the grown polycrystalline diamond film thickness was evaluated by its thickness percent deviation. Lower percentage of deviation indicates higher film uniformity. The thickness percent deviation is given by the following equation:

$$\pm\left[\frac{\frac{1}{2}t_{max}-t_{min}}{\frac{1}{N}\sum_{i=1}^{N}t_i}\right]x100\% \qquad (5.1)$$

Where t_i is the thickness of the films at a point i and N is the total number of points measured along one of the two perpendicular lines shown in Figure 4.8. For radial percentage deviation, the points were obtained from the two perpendicular lines along the substrate while for the radial percentage deviation; additional points along the circumference of the substrates were used for the uniformity evaluation. The films thickness measured by linear encoder and film non-uniformity percentage deviation calculated from equation 5.1 is displayed in Table 5.1, Table 5.2, and Table 5.3 for each sample. Also, the radial and circumferential diamond film uniformity is shown in Figure 5.11, Figure 5.12, and Figure 5.13 with its corresponding operating conditions. The nominal average thickness of the film measured using the linear encoder shown in Figure 5.11 is 77.3 μm with variation in the thickness non-uniformity is 12-15.8% radially and 14.6% circumferentially. The nominal average thickness of the film shown in Figure 5.12 is 71.7 μm with variation thickness non-uniformity of 10.2-12.2% radially and 13.3% circumferentially. Likewise, the nominal average thickness of the film shown in Figure 5.13 is 167.8 μm with variation thickness non-uniformity of 12.1-12.2% radially and 14.8% circumferentially. These variations were determined based on average of maximum and minimum thickness values across the substrate surface points. This non uniformity is probably due to variation in temperature and species across the substrate during deposition.

Table 5.1 – Diamond film KWH34 thickness measured by linear encoder and the film non-uniformity calculated using the percentage deviation formula Eq. 5-1.

Point	1	2	3	4	5	6	
Thickness (μm)	83.4	94.3	92.0	82.8	73.9	65.4	
Point	7	8	9	10	11	12	13
Thickness (μm)	87.2	87.6	87.9	79.8	76.5	70.1	78.4
Deviation of circumferential points (%) ±		14.6	Ave. thickness (μm)	77.3			

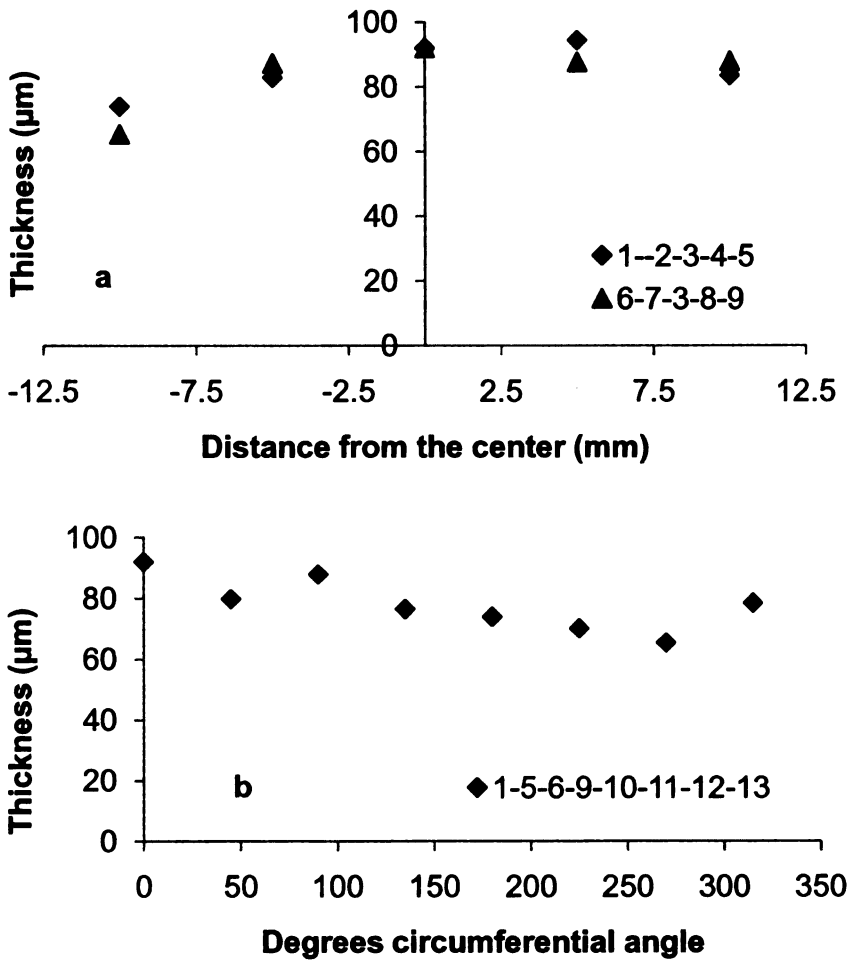

Figure 5.11 - Diamond film uniformity for KWH34 showing film thickness: (a) radial distribution and (b) circumferential distribution at a radial distance of 10 mm from the center. Operating conditions: pressure = 220 Torr, CH_4/H_2 = 3%, microwave absorbed power = 2.3 kW, substrate temperature = 1120 °C, L_s = 20.3 cm, L_p = 3.6 cm, L1 = 5.65 cm, L2 = 6.05 cm.

Table 5.2 – Diamond film KWH32 thickness measured by linear encoder and the film non-uniformity calculated using the percentage deviation formula Eq. 5-1.

Point	1	2	3	4	5	6	
Thickness (μm)	61.8	64.3	73.5	74.2	76.0	59.6	
Point	7	8	9	10	11	12	13
Thickness (μm)	77.1	76.5	72.7	61.2	77.7	70.5	64.4
Deviation of point 1-5 (%) ±		10.2	Deviation of point 6-9 (%) ±		12.2		
Deviation of circumferential points (%) ±		13.3	Ave. thickness (μm)	71.7			

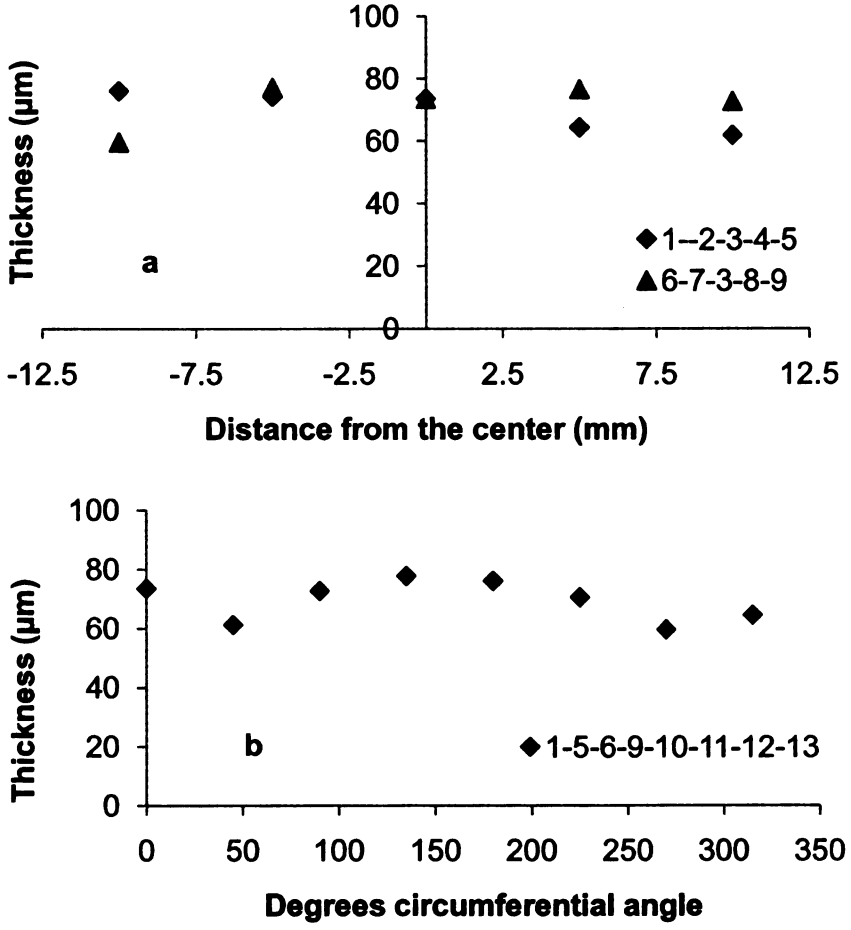

Figure 5.12 - Diamond film uniformity for KWH32 showing film thickness: (a) radial distribution and (b) circumferential distribution at a radial distance of 10 mm from the center. Operating conditions: pressure = 200 Torr, CH_4/H_2 = 3%, microwave absorbed power = 2.4 kW, and substrate temperature = 1048 °C, L_s = 20.3 cm, L_p = 3.6 cm, L1 = 5.65 cm, L2 = 6.05 cm.

Table 5.3 – Diamond film KWH36 thickness measured by linear encoder and the film non-uniformity calculated using the percentage deviation formula Eq. 5-1.

Point	1	2	3	4	5	6	
Thickness (μm)	156.7	182.2	194.8	175.8	152.9	173.6	
Point	7	8	9	10	11	12	13
Thickness (μm)	168.8	191.4	169.6	139.1	187.5	169.5	156.5
Deviation of point 1-5 (%) ±		12.1	Deviation of point 6-9 (%) ±		12.2		
Deviation of circumferential points (%) ±		14.8	Ave. thickness (μm)	167.8			

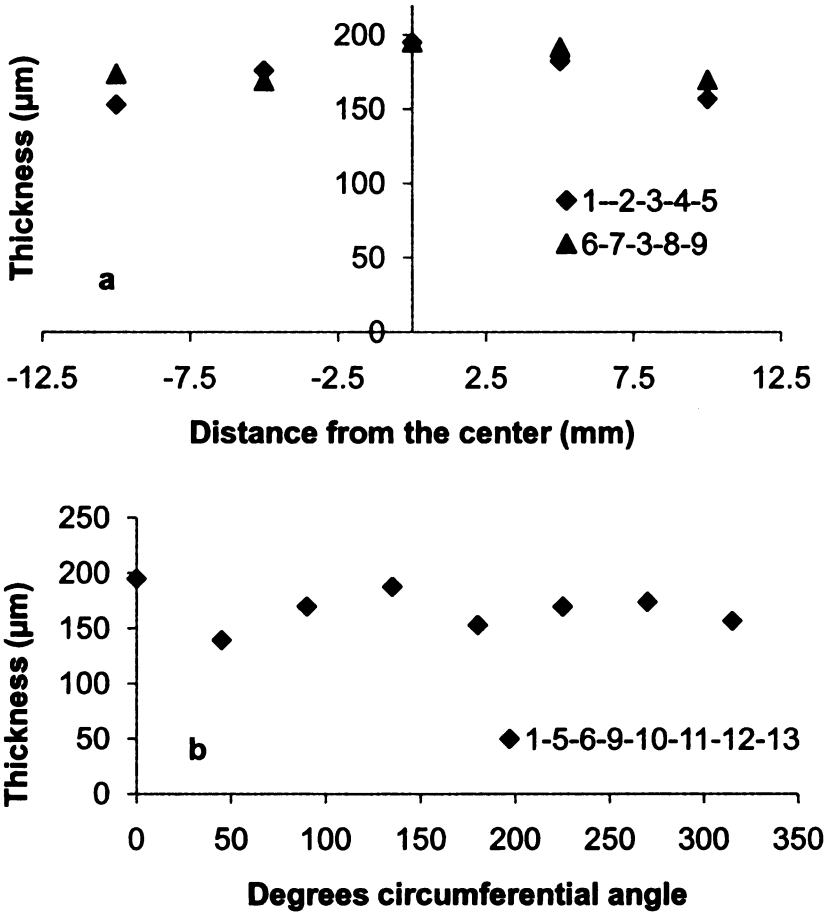

Figure 5.13 - Diamond film uniformity for KWH36 showing film thickness: (a) radial distribution and (b) circumferential distribution at a radial distance of 10 mm from the center. Operating conditions: pressure = 220 Torr, CH_4/H_2 = 4%, microwave absorbed power = 2.44 kW, and substrate temperature = 1093 °C, L_s = 20.3 cm, L_p = 3.6 cm, L1 = 5.65 cm, L2 = 6.05 cm.

5.3.3 Diamond surface morphology

Figures 5.14 to 5.17 display typical diamond surface morphologies grown at various methane concentrations and operating pressures. The methane concentration was varied from 2 to 5% and operating pressure varied from 180 to 240 Torr. The grown polycrystalline diamond exhibits a pyramidal shape, square, and roof like structure as can be seen from the figures. These shapes are dependent on the operating pressure, gas chemistry, microwave input power, substrate temperature, and deposition time. The grain size varies along the surface of the substrate and it is also dependent upon the operating pressure, gas chemistry and deposition time. As the deposition time increases, the grain size tends to increase up to several tenths of micrometers. Typical grain sizes observed using the micrograph range from 10-40 μm for 180 to 240 Torr and 2-5% CH_4 gas chemistry.

These morphology results demonstrate that the newly modified reactor is capable of producing polycrystalline diamond over a range of conditions and comparable to the reference reactor.

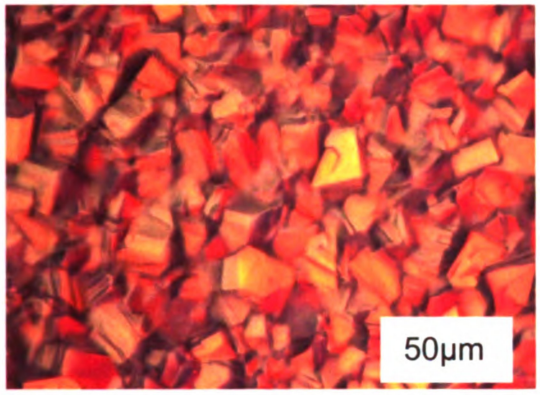

(a) CH_4/H_2 = 2%

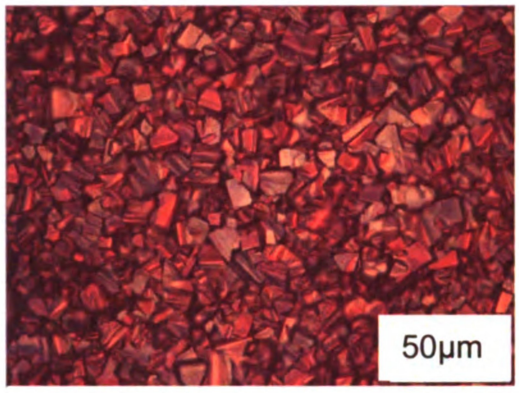

(b) CH_4/H_2 = 3%

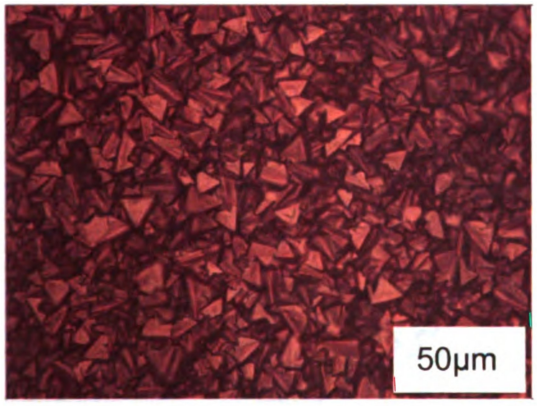

(c) CH_4/H_2 = 4%

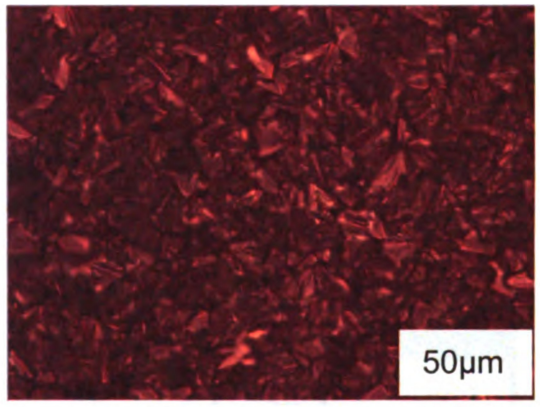

(d) CH_4/H_2 = 5%

Figure 5.14(a)-(d) - Surface morphology of polycrystalline diamond at operating pressure of 180 Torr versus methane concentration from 2-5%. Growth conditions: (a) KWH7, absorbed power = 2.62 kW, substrate temperature = 1054 °C, growth time = 8 hours, growth rate = 3.14 µm thickness = 25 µm (b) KWH2, absorbed power = 2.73 kW, substrate temperature = 1031 °C, growth time = 8 hours, growth rate = 5 µm, thickness = 40 µm (c) KWH14, absorbed power = 2.70 kW, substrate temperature = 938 °C, growth time = 3 hours, growth rate = 10 µm, thickness = 30 µm and (d) KWH17, absorbed power = 2.39 kW, substrate temperature = 1058 °C, growth time = 4 hours, growth rate = 14.72 µm, thickness = 59 µm.

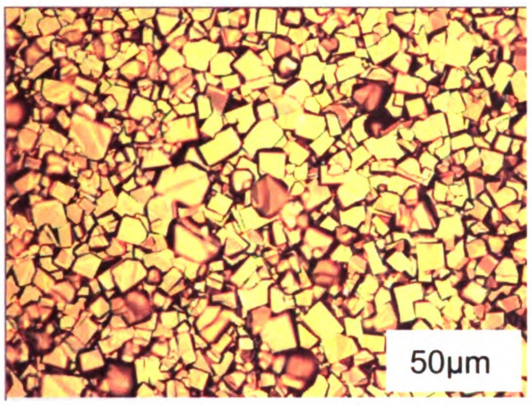

(a) CH_4/H_2 = 2%

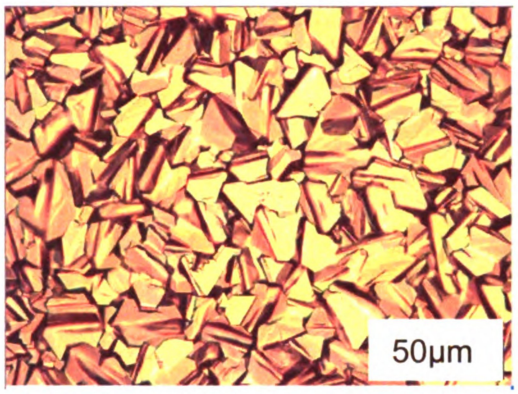

(b) CH_4/H_2 = 3%

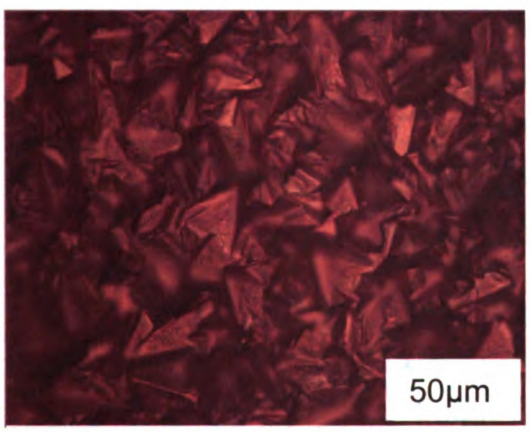

(c) CH_4/H_2 = 4%

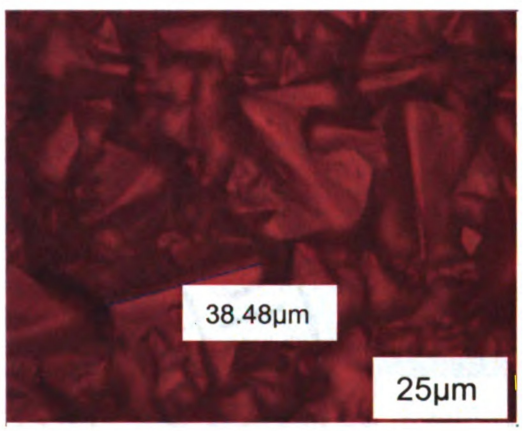

(d) CH_4/H_2 = 5%

Figure 5.15(a)-(d) - Surface morphology of polycrystalline diamond at operating pressure of 200 Torr versus methane concentration from 2-5%. Growth conditions: (a) KWH28A, absorbed power = 2.15 kW, substrate temperature = 1037 °C, growth time = 10 hours, growth rate = 3.1 µm, thickness = 31 µm (b) KWH12, absorbed power = 2.48 kW, substrate temperature = 1019 °C, growth time = 8 hours, growth rate = 8.24 µm, thickness = 66 µm (c) KWH10, absorbed power = 2.69 kW, substrate temperature = 1158 °C, growth time = 8 hours, growth rate = 12.3 µm, thickness = 98 µm and (d) KWH11, absorbed power = 2.55 kW, substrate temperature = 1223 °C, growth time = 3.5 hours, growth rate = 14.83 µm, thickness = 52 µm.

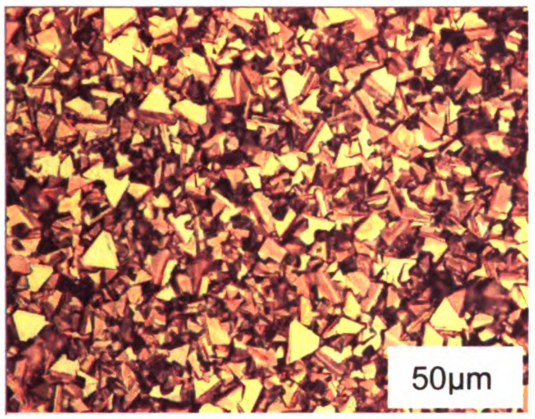

(a) CH_4/H_2 = 2%

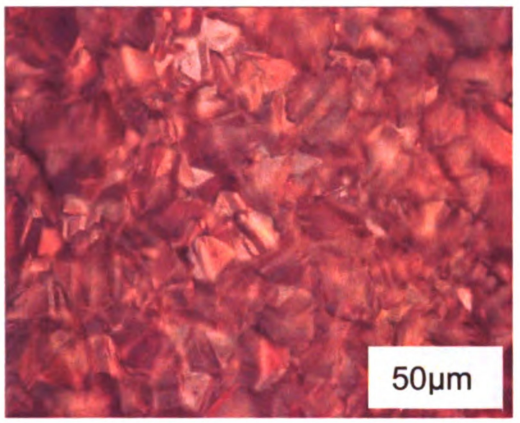

(b) CH_4/H_2 = 3%

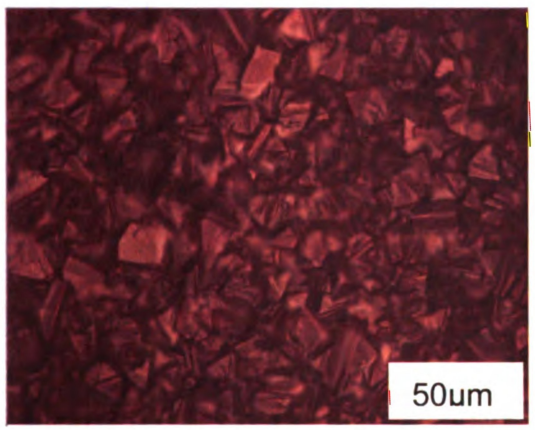

(c) CH_4/H_2 = 4%

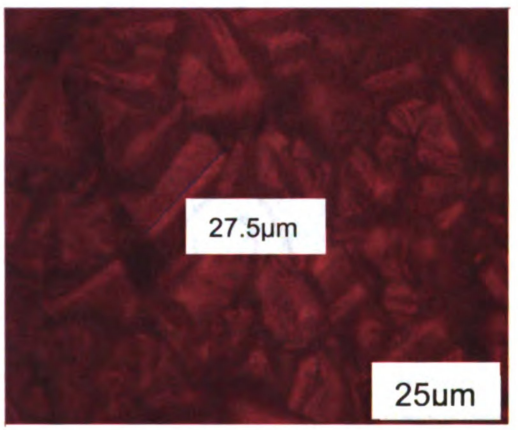

(d) CH_4/H_2 = 5%

Figure 5.16(a)-(d) - Surface morphology of polycrystalline diamond at operating pressure of 220 Torr versus methane concentration from 2-5%. Growth conditions: (a) KWH13, absorbed power = 2.76 kW, substrate temperature = 1140 °C, growth time = 5 hours, growth rate = 3.39 µm, thickness = 17 µm (b) KWH4, absorbed power = 2.64 kW, substrate temperature = 1080 °C, growth time = 8 hours, growth rate = 7.6 µm, thickness = 61 µm (c) KWH15, absorbed power = 2.44 kW, substrate temperature = 1102 °C, growth time = 3 hours, growth rate = 13.2 µm, thickness = 39.6 µm and (d) KWH9, absorbed power = 2.57 kW, substrate temperature = 1066 °C, growth time = 3 hours, growth rate = 15.88 µm, thickness = 47.6 µm.

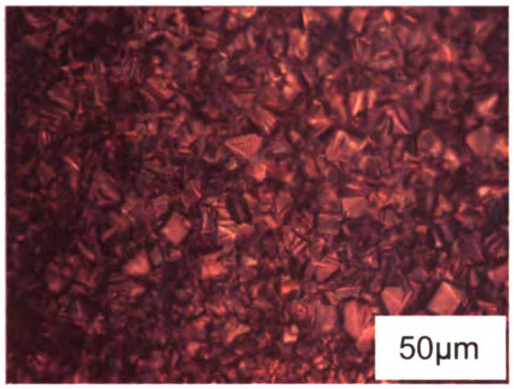

(a) CH_4/H_2 = 2%

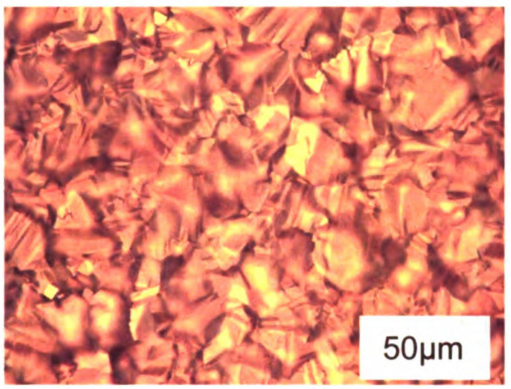

(b) CH_4/H_2 = 3%

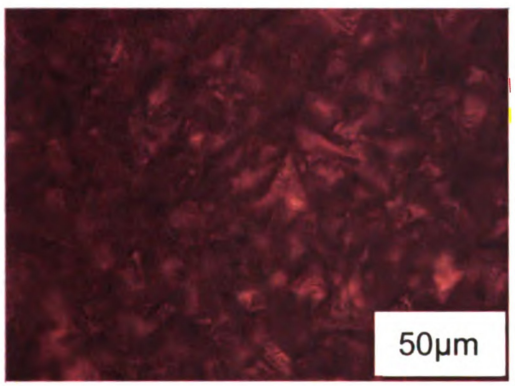

(c) CH_4/H_2 = 4%

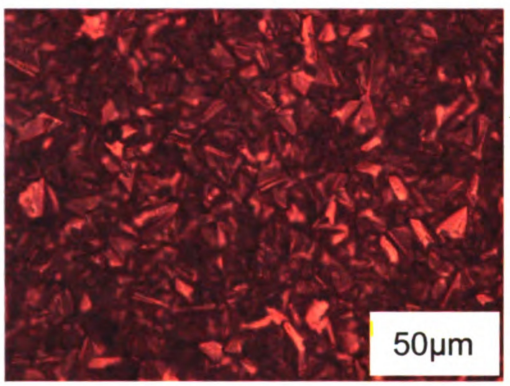

(d) CH_4/H_2 = 5%

Figure 5.17(a)-(d) - Surface morphology of polycrystalline diamond at operating pressure of 240 Torr versus methane concentration from 2-5%. Growth conditions: (a) KWH8, absorbed power = 2.54 kW, substrate temperature = 1166 ºC, growth time = 8 hours, growth rate = 4.10 µm, thickness = 33 µm (b) KWH6, absorbed power = 2.51 kW, substrate temperature = 1173 ºC, growth time = 8 hours, growth rate = 8.34 µm, thickness = 67 µm (c) KWH16, absorbed power = 2.61 kW, substrate temperature = 1180 ºC, growth time = 2 hours, growth rate = 13.9 µm, thickness = 28 µm and (d) KWH19, absorbed power = 2.58 kW, substrate temperature = 1146 ºC, growth time = 2 hours, growth rate = 21.26 µm, thickness = 42 µm.

Figure 5.18(a)-(b) displays the surface morphology at the center and edge of the grown substrate. The temperature measured during deposition at the edge and center was 974 °C and 1059 °C respectively. As can be seen, substrate temperature variation could result in different diamond shape such as square or roof like. When the diamond was grown at three different durations, the surface morphology shows some changes as shown in Figure 5.19(a)-(c). For example, after two hours of growth, the size of the crystal is very small with square shapes. After four hours, the diamond crystal size starts to increase to several microns and with pyramidal shapes. Finally after eight hours, the diamond crystal size reaches over 10 microns and the crystal mostly showing pyramidal or (111) triangular facets. These micrograph images were taken at the center of the substrate.

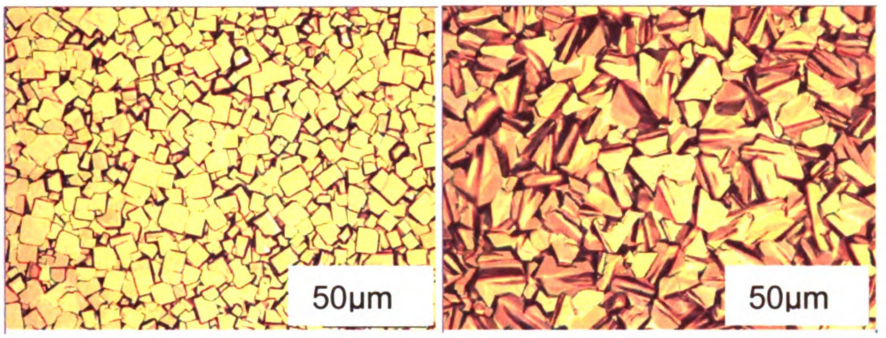

(a) T_s = 974 °C (b) T_s = 1059 °C

Figure 5.18(a)-(b) - Surface morphology of polycrystalline diamond (KWH12) at the edge and center of the substrate versus substrate temperature.

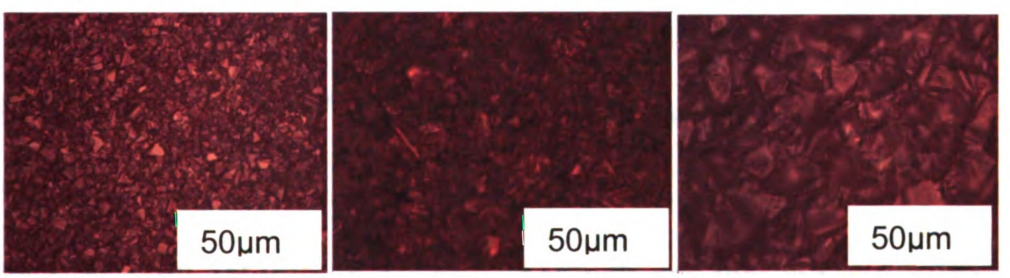

(a) Dep. time = 2 hrs (b) Dep. time = 4 hrs (c) Dep. time = 8 hrs

Figure 5.19(a)-(c) - Surface morphology of polycrystalline diamond versus deposition time varied between 2, 4, and 8 hours.

5.3.4 Diamond quality

Shown in Figure 5.20 is a typical Raman spectrum from a CVD diamond film containing multiple carbon bonding components such as sp^2 and sp^3 carbon bond. The appearance of sp^2 peaks indicates the presence of silicon carbon (520 cm^{-1}) and graphite carbon (1597 cm^{-1}) in the diamond film while sp^3 peak at around 1333 cm^{-1} indicates a diamond carbon material in the film.

Figure 5.21 shows wide Raman spectra from 1200 to 1800 cm^{-1} of the grown diamond at various operating conditions. The spectra scan is plotted separately shifted vertically for clarity purposes. As can be seen, the Raman spectra exhibited a strong sp^3 bonding diamond peak at 1332.5 cm^{-1} without any sp^2 peaks between 1500 to 1600 cm^{-1}. This indicates that the grown diamond contains little graphitic content in the film and it is a good polycrystalline diamond quality.

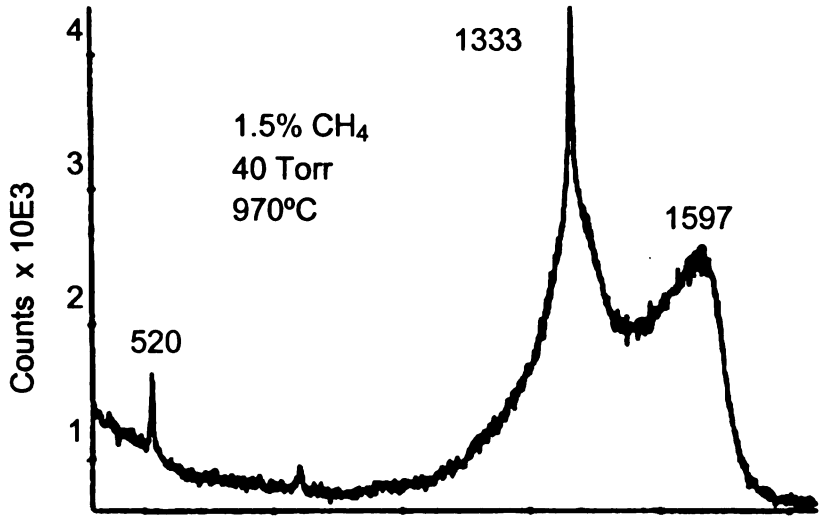

Figure 5.20 – Raman spectrum for a CVD diamond film containing multiple carbon bonding sp^2 peaks silicon carbon at 520 cm^{-1} and graphite carbon at 1597 cm^{-1} and sp^3 peak diamond at 1333 cm^{-1} [105].

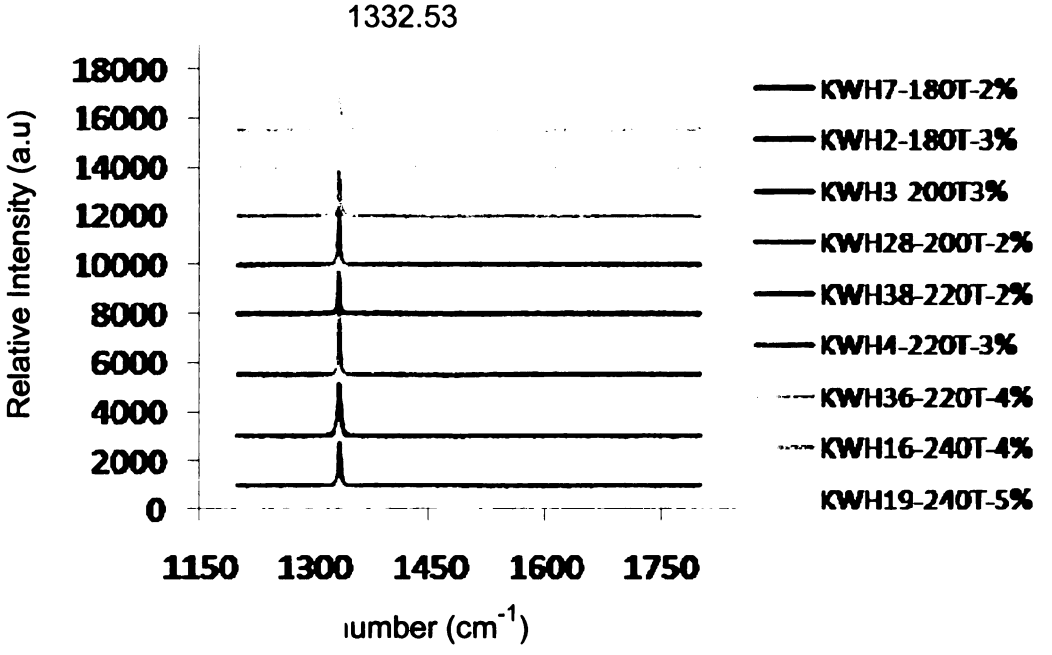

Figure 5.21 - Wide scan of Raman spectra for grown diamond at various growth conditions. The spectra show strong sp^3 peak at 1332.5 cm^{-1} without any sp^2 graphite peaks at around 1560 cm^{-1}. Each Raman plot is shifted vertically for clarity purposes.

5.3.4.1 Visual transparency

Visual observations of the color and transparency of the freestanding films were performed. Additionally, diamond quality was determined from Raman scattering, UV-Vis and infra red transmission measurements of freestanding films. In order to obtain the freestanding diamond, the deposited diamond film was back etched. The silicon substrate removal was performed via wet etching as described in chapter 4.

In terms of diamond transparency quality, when the gas chemistry is varied from 2% to 4% at an operating pressure of 180 to 240 Torr, several freestanding polycrystalline diamond films are shown in Figure 5.22. These grown films are smooth on the nucleation side and rough on the growth side since they are unpolished. As can be visually seen, the transparency of the grown diamond decreases as the gas chemistry is increased from 2% to 4%. The quality of the 2% and 3% films appears to be good since one can see through them and they are also white suggesting the synthesis of good quality polycrystalline diamond films. The visual clarity variation from the center outward to the edge i.e., radial direction shows that along the edges of the substrate shows darker transparency. This can be seen in Figure 5.22(c). Note that the film in Figure 5.22(c) is thicker and was grown with a higher methane concentration, so it is not surprising that it is more difficult to see through the logo underneath.

Shown in Figure 5.23 is a polished and lapped freestanding diamond film grown at 200 Torr, with 2% methane concentration, 30 hours deposition time,

and growth rate of 3.5 μm/h. As can be seen, the grown diamond exhibits a good visual transparency showing Michigan State University Sparty logo underneath the sample.

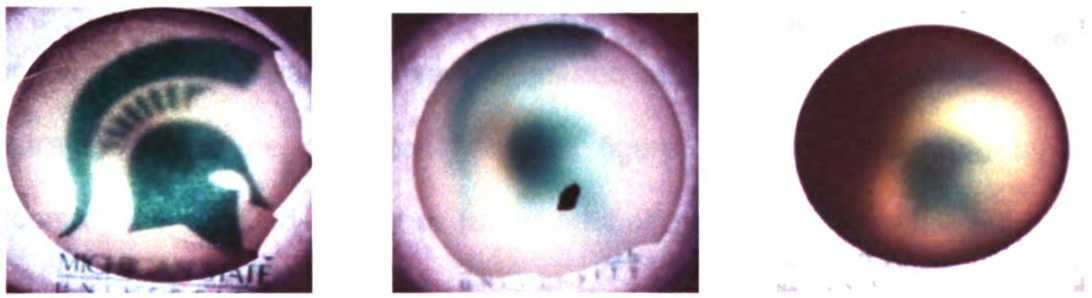

(a) (b) (c)

Figure 5.22 - Freestanding unpolished polycrystalline diamond grown at different methane concentrations. The thickness of the grown diamond is: (a) KWH8, 2%, 32μm thick, (b) KWH25, 3%, 68 μm, and (c) KWH23, 4%, 133 μm.

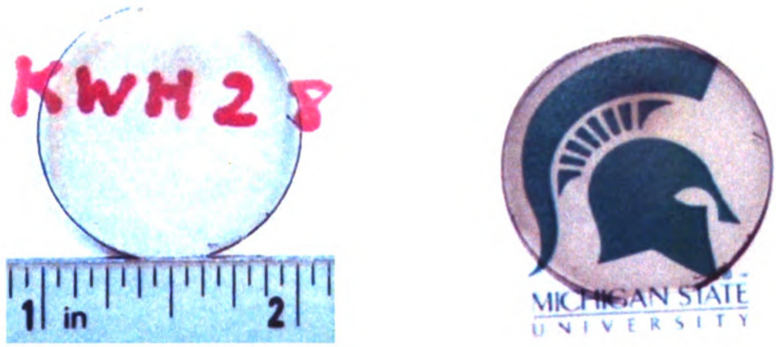

(a) (b)

Figure 5.23 - Freestanding diamond grown after being polished, lapped and silicon substrate removal via wet etching. (a) Diamond film placed above a ruler, (b) diamond film placed on top of Michigan State University logo for clarity reference. KWH28 growth conditions: pressure = 200 Torr, methane concentration = 2%, substrate temperature = 1077 ºC, growth rate = 3.5 μm/hr, film thickness = 105 μm.

5.4.4.2 Raman FWHM Measurements

Figure 5.24 shows the Raman full width half maximum (FWHM) measurements of the diamond films grown at various pressures and methane concentrations. The samples were measured at around the center area of the substrate. As can be observed from the figure, in general higher methane concentrations resulted in higher full width half maximum. The full width half maximum of the grown diamond varies from 2.56 to 9 cm^{-1}. These values depend on growth conditions such as operating pressure, methane concentration, deposition time, grain size, microwave input power, substrate temperature, and shims adjustments, ΔZ. In general, the grown films exhibited Raman spectra similar to those reported for thick films grown elsewhere [115-116], and in the reference reactor [96-97] while operating at lower pressure.

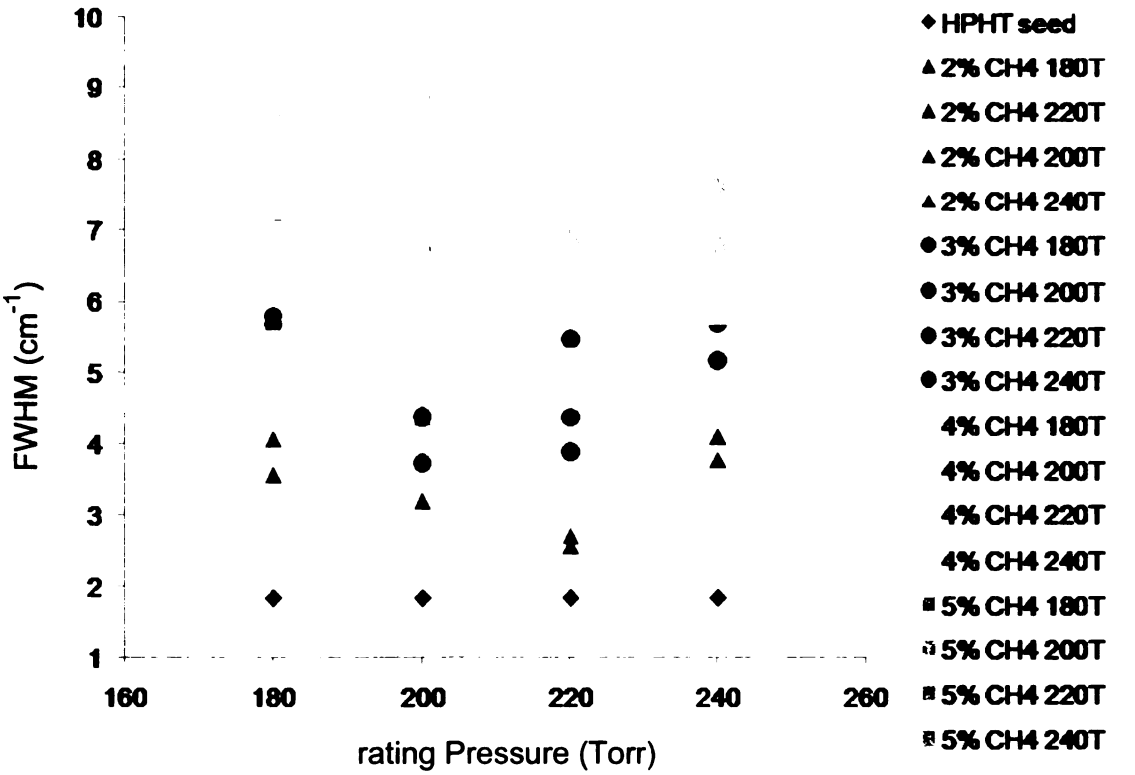

Figure 5.24 – Full width half maximum (FWHM) values of grown polycrystalline diamond under various operating pressure 180-240 Torr and methane concentrations 2-3%.

Several grown diamond samples were analyzed at various locations or points along the one inch substrate. One of major purpose of Raman measurements was to determine the variation of the full width half maximum value within a sample. Shown in Figure 5.25 is the selected point configuration where the laser was pointed onto the substrate. Each point is located approximately one cm away from the center in radial direction namely left, right, top, and bottom edge. Figure 5.26 displays examples of the Raman full width half maximum obtained from grown diamond films under various operating pressures and methane concentrations. As can be seen from the figure, higher methane concentration resulted in higher FWHM. For example, the FWHM for 220 Torr 2% CH_4/H_2 ranges from 2.56 to 3.89 cm^{-1} while 200 Torr 5% CH_4/H_2 ranges from 6.79 to 8.86 cm-1. There are some variations in the range of measured FWHM values along different points within the same substrate but they are not significantly large. These variations are probably due to the grain size, thickness and substrate temperature during deposition.

Table 5.4 summarizes the Raman measurements of the diamond films grown at various pressures and methane concentrations with its corresponding full width half maximum value and sp^3 diamond peak position. The diamond sp^3 peak for the reference HPHT diamond seed is 1332.53 cm^{-1} while the grown polycrystalline diamond sp^3 peak ranges from 1332.15 to 1333.47 cm^{-1}.

Shown in Figure 5.27(a)-(b), 5.28(a)-(b), and 5.29(a)-(b) are the Raman plot of the polycrystalline diamond at various pressure and methane concentration taken from some samples listed on Table 5.4. Figure 5.27(a)-5.29(a) shows the overall view or wide scan from 1150 to 1500 cm-1 and Figure 5.27(b)-5.29(b) zoom in view or narrower scan at around 1332 cm^{-1} of the diamond peak position versus the wavenumber for clarity. The single crystal diamond HPHT seed Raman spectra is included in the plot for comparison purposes. The surface morphology of the grown diamond is shown for each location where the FWHM was measured on the substrate. These points are denoted as P1, P2, P3, P4 and P5 which corresponds to the left, center, right, bottom and top edge point respectively.

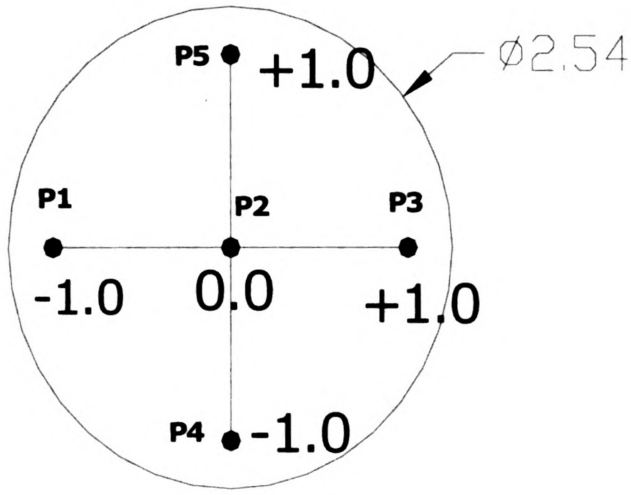

Figure 5.25 - Point distribution along the substrate for Raman measurements

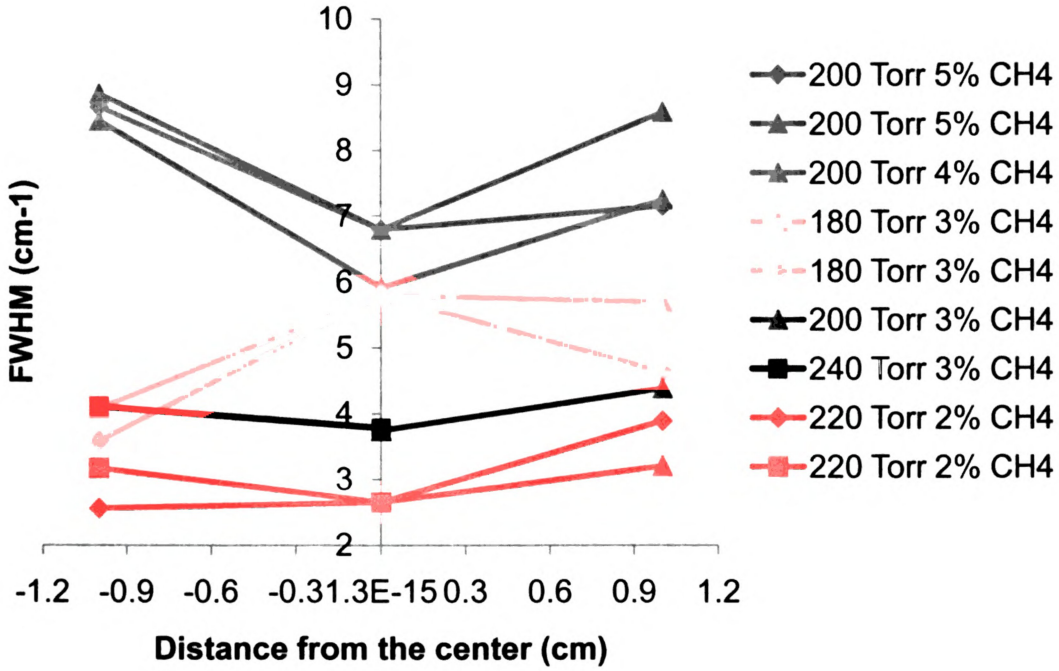

Figure 5.26 – Full width half maximum (FWHM) along radial direction of several diamond films grown under various operating pressures and methane concentrations.

Table 5.4 – Examples of diamond quality evaluated by Raman FWHM versus their growth conditions

Sample	Pressure (Torr)	CH_4/H_2 (%)	Pabs (kW)	Ts (°C)	Growth Time (hr)	Growth Rate (μm/hr)	Avg Thickness (μm)	Avg Grain Size (μm)	Peak Position (cm^{-1})	FWHM (cm^{-1})
HPHT diamond seed									1332.63	1.84
KWH2-P1	180	3	2.73	NA	8	5.0	40	22	1333.16	3.58
P2				1031					1333.26	5.8
P3				NA					1332.97	4.08
P4				NA					1333.77	5.69
P5				NA					1332.65	4.63
KWH12-P1	200	3	2.48	NA	8	8.24	66	26	1332.66	3.74
P2				1019					1332.93	4.38
KWH10-P1	200	4	2.69	1245	8	12.3	98	38	1333.77	8.45
P2				1158					1333.34	5.91
P3				1143					1332.44	7.25
KWH11-P1	200	5	2.55	NA	3.5	14.83	52	19	1333.33	6.79
P2				1223					1332.89	8.86
P3				NA					1332.71	8.66
P4				NA					1332.65	7.15
P5				NA					1332.71	8.58
KWH38B-P1	220	2	2.17	NA	20	4.38	87	14	1332.99	3.17
P2				926					1333.31	3.2
P3				NA					1332.56	2.65
P4				NA					1332.57	2.56
P5				NA					1332.28	3.89
KWH6-P1	240	3	2.51	1276	8	8.34	67	20	1332.39	3.78
P2				1173					1332.98	4.11

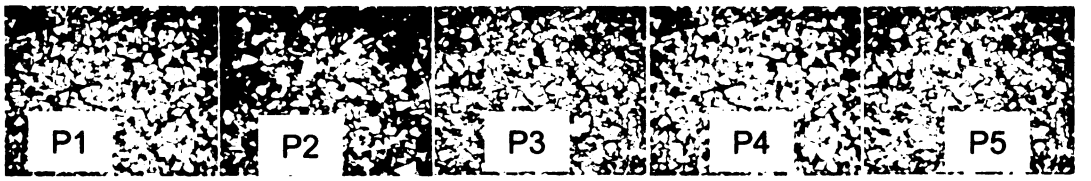

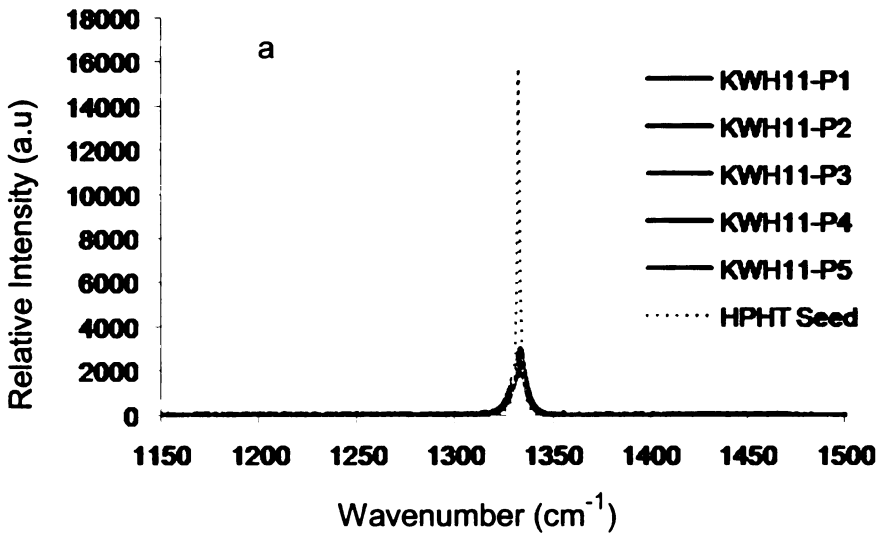

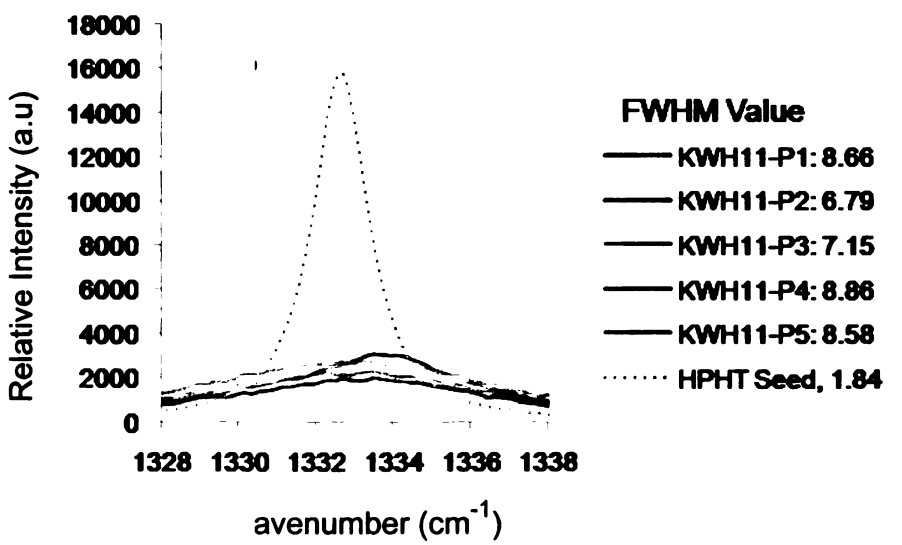

Figure 5.27 – Figure 5.28 – Raman spectra of KWH11 (200 Torr, 5% CH_4/H_2) at points P1 through P5 on the substrate surface in comparison with a HPHT diamond seed (a) overall view (b) zoom-in view.

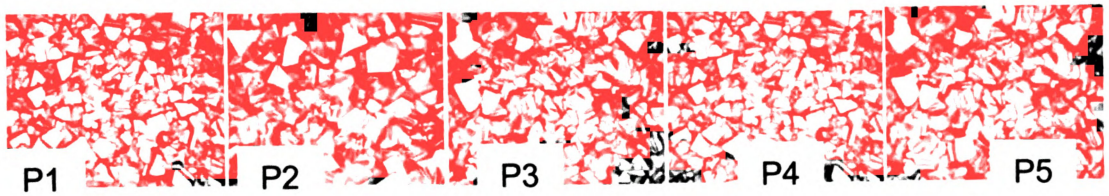

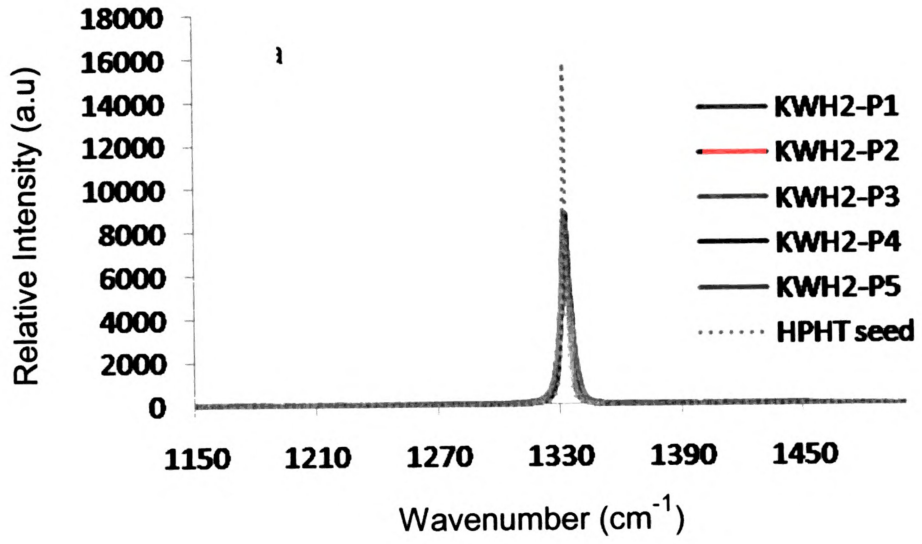

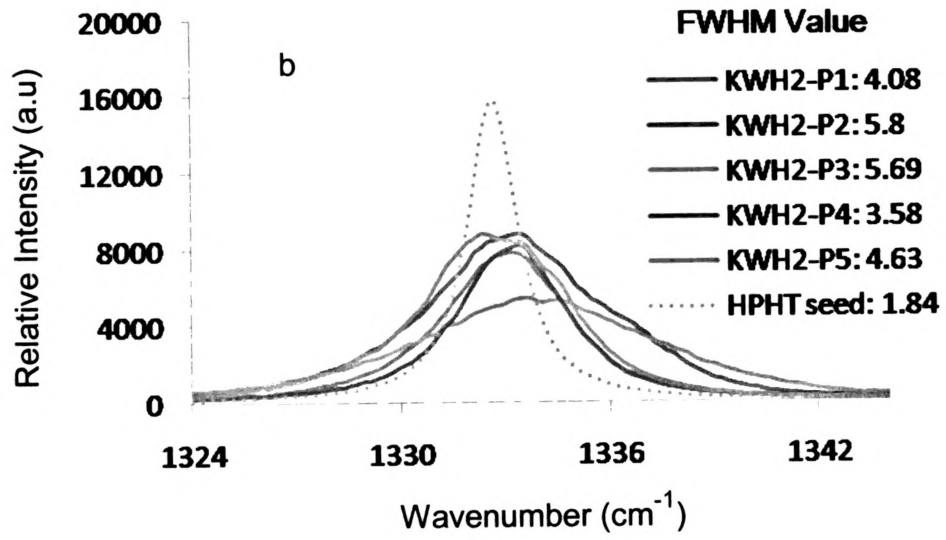

Figure 5.28 – Raman spectra of KWH2 (180 Torr, 3% CH_4/H_2) at points P1 through P5 on the substrate surface in comparison with a HPHT diamond seed (a) overall view (b) zoom-in view.

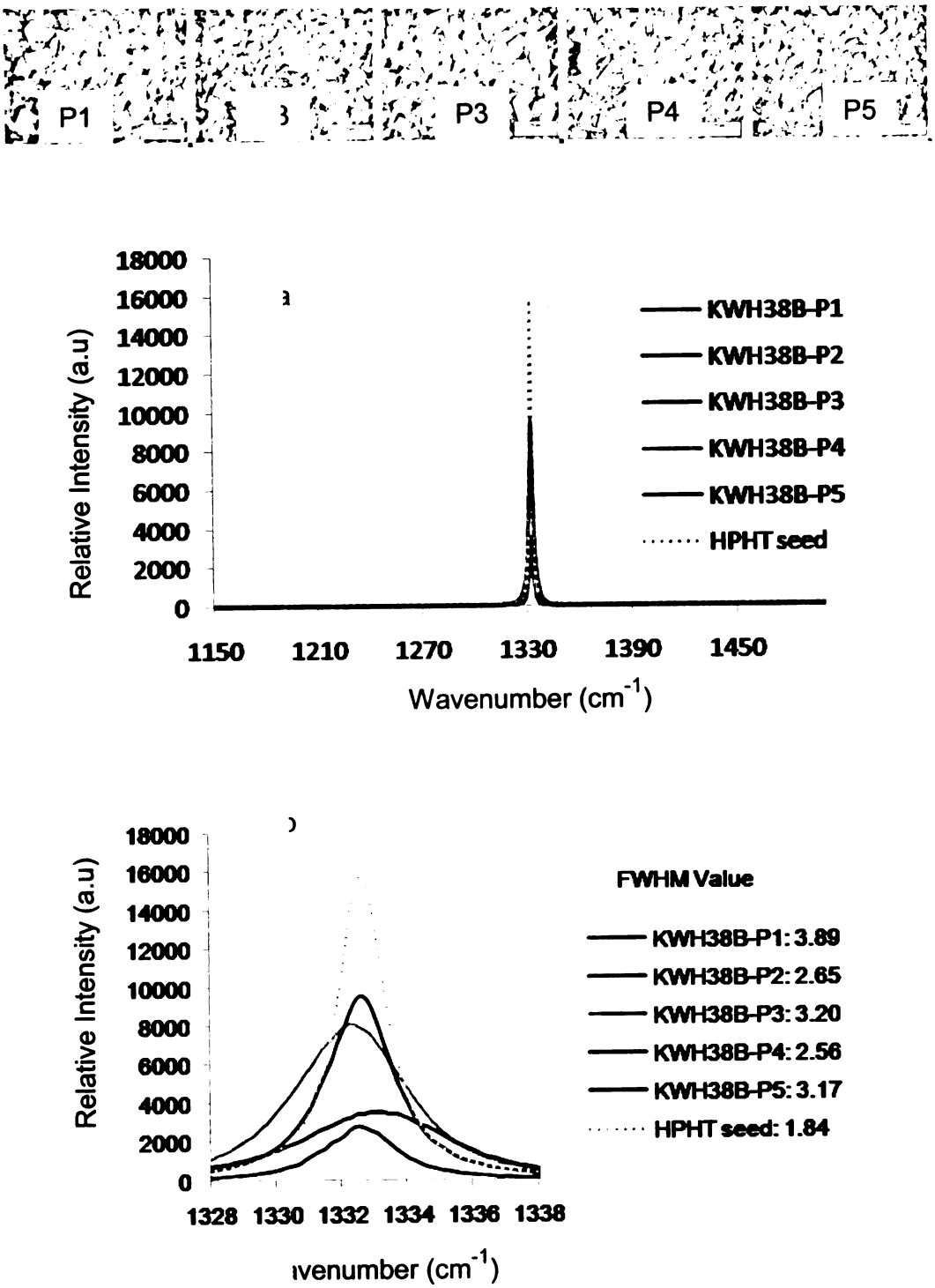

Figure 5.29 – Figure 5.28 – Raman spectra of KWH38B (220 Torr, 2% CH_4/H_2) at points P1 through P5 on the substrate surface in comparison with a HPHT diamond seed (a) overall view (b) zoom-in view.

5.4.4.3 Optical transmission quality

The optical transmission measurements were helped by Dr. Donnie K. Reinhard and it is described in this section. The films were back etched, polished and lapped prior to the transmission measurements.

Figure 5.30 shows the transmission measurements for freestanding diamond films KWH28 and KWH36 grown respectively at operating pressures of (1) 200 Torr with 2% and (2) 220 Torr with 4% methane concentrations. FTIR transmission measurements from 2.5-22 micrometer wavelengths are combined with additional transmission measurements from 3.0-0.2 micrometer wavelength to generate the transmission curve in Figure 5.30. The highly monochromatic FTIR region of the data shows interference maxima and minima about an average of approximately 71% in the mid-IR, as expected for a diamond refractive index of 2.38. The UV transmission drops to zero upon the onset of band-gap absorption at 222 nm. The absorption observable between approximately 3 and 5 micrometers is principally due to two-phonon absorption that occurs in intrinsic diamond. For the 2% methane window, surface-roughness limited transmission continues throughout the visible and ultraviolet portion of the spectrum until dropping to zero upon the onset of band-gap absorption at 5.5 eV. However the 4% methane window shows optical absorption beginning in the near-infrared and becoming substantial in the visible. The higher methane percentage, higher growth-rate, window may be appropriate for long wavelength applications but the lower methane percentage is required for good performance in the visible and ultraviolet.

Results are also plotted as transmission versus photon energy in order to observe the difference between the two plots behavior especially at the shorter wavelength. Shown in Figure 5.31 are the measured transmissions for the 2% methane window and also for a 170 μm thick window deposited at 220 Torr and 4% methane for 15 hours. At the low energy (long wavelength) portion of Figure 5.31, both windows shows transmission of approximately 71% as expected for a diamond infrared refractive index of 2.38. The absorption observable for both windows between approximately 25 and 40 meV (3 to 5 μm wavelength) is principally due to two-phonon absorption that occurs in intrinsic diamond.

Another set of freestanding diamond films (KWH14 = 180 Torr, 4% CH4 and KWH15 = 220 Torr, 4% CH4) were analyzed using the FTIR and UV-Vis transmission. By further increasing deposition pressure, improved quality is achieved with higher methane concentrations. Figure 5.32 and Figure 5.33 show optical transmission of a polycrystalline diamond layer grown at 180 Torr and 220 Torr at 4% methane concentration with thickness of 23 μm and 26 μm respectively after being polished and lapped. Figure 5.32 shows infrared (IR) transmission through the sample. At longer IR wavelengths, the transmission approaches the ideal value of approximately 71% for lossless diamond with refractive index equal to 2.38. In the visible portion, as shown in Figure 5.33, transmission drops to approximately 35% in the violet portion of the spectrum. Analysis indicates that the drop-off may be largely explained by surface roughness considerations. The effect of surface roughness on transmission is calculated using a model reported previously [49]. Surface profile meter

measurements with a 4.8 mm scan length and a high-pass filter of 20 μm yielded polished surface roughness results of approximately 30 nm for this sample. Surface roughness values of the unpolished nucleation of the sample are approximately 12 nm. This was also the case for the earlier work reported diamond layers grown at 120 Torr with 1.0-1.5 % methane by Zuo *et.al.* [49]. Thus the optical transmission of the diamond films grown with 4% methane at 220 Torr is comparable to transmission grown of diamond film grown with significantly lower methane concentration at lower pressure.

Comparing the two samples (KWH14 and KWH15), to the human eye, both appear comparably transparent. As measured in the visible, KWH15 shows slightly higher transmission (50% versus 48% at 550 nm wavelength) than KWH14 in spite of being slightly thicker (26 μm versus 23 μm). KWH15 also shows slightly higher transmission in the infrared. Hence, for the same methane concentration at 4%, KWH15 grown at 220 Torr has better transmission than KWH14 grown at 180 Torr. These imply that at fixed methane concentration (4%) a 220 Torr film is of higher optical quality than a 180 Torr film. However, the differences are not large and could also be explainable by other means, such as a difference in surface smoothness or other growth conditions during diamond deposition.

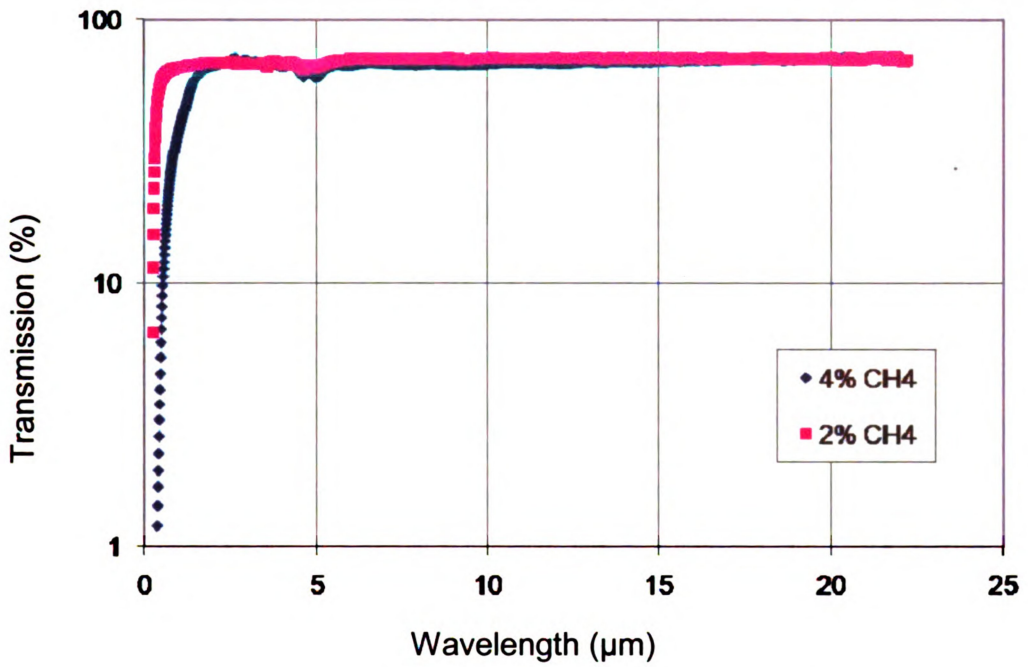

Figure 5.30 - Transmission spectra for the polycrystalline diamond window grown at 200 2% (KWH28) and 4% (KWH36) methane in terms of wavelength.

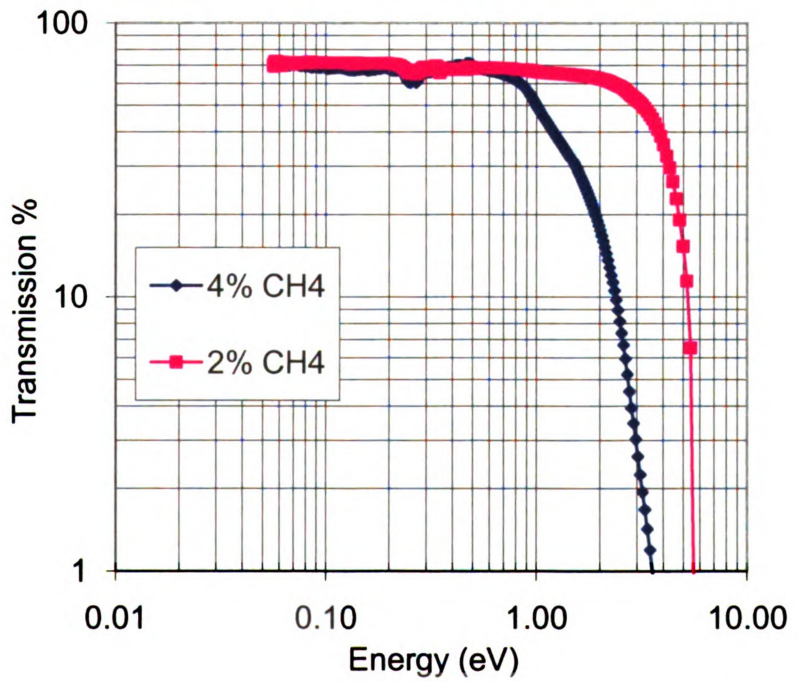

Figure 5.31 - Transmission spectra for polycrystalline diamond windows grown at 200 Torr at 2% (KWH28) and 4% (KWH36) in terms of photon energy.

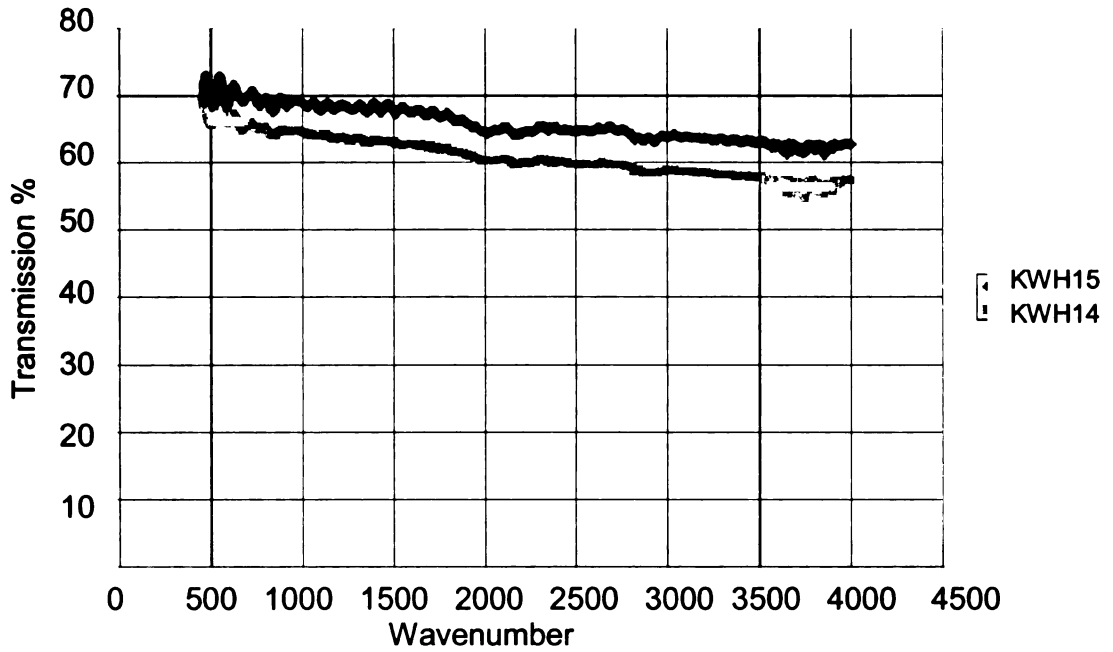

Figure 5.32 - Optical transmission of KWH14 (180 Torr, 4% CH_4, grown thickness = 30 μm, polished thickness = 23 μm, Ts = 938 °C) and KWH15 (220 Torr, 4% CH_4, grown thickness = 39 μm, polished thickness = 26 μm, Ts = 1102 °C) in infrared spectrum.

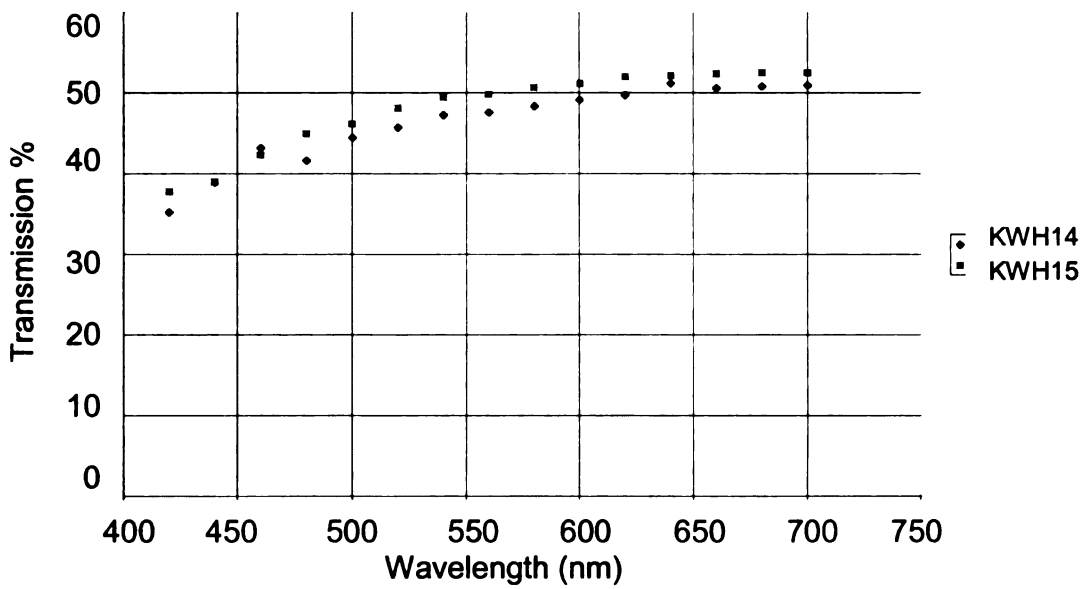

Figure 5.33 - Optical transmission of KWH14 (180 Torr, 4% CH_4, grown thickness = 30 μm, polished thickness = 23 μm, Ts = 938 °C) and KWH15 (220 Torr, 4% CH_4, grown thickness = 39 μm, polished thickness = 26 μm, Ts = 1102 °C) in visible spectrum.

5.4 Single crystal diamond synthesis

The multi variable experimental parameter space for the single crystal diamond synthesis can be categorized in the following: controllable input variables, reactor design variables, internal variables, deposition process variables, and output variables. The input variables consist of microwave input power, operating pressure, gas chemistry, and flow rate. The microwave input power varies from 1.8 to 2.5 kW, deposition pressure varies from 180-250 Torr, and gas chemistry employs hydrogen and methane mixture with flow rate fixed at 400 sccm for H_2 and 8-20 sccm of CH_4. The reactor geometry design variables consist of shims heights adjustment, ΔZ and substrate holder designs. The ΔZ varies from -3.1 mm to +2.5 mm and substrate holder designs consist of an open and pocket holder type as shown in Figure 5.34-35. The internal variables consist of substrate temperature and discharge volume. The deposition process variables consist of deposition time and hydrogen plasma etching time. The deposition time ranges from 4 to 23 hours and plasma etching prior to deposition varies from 30 to 60 minutes. The output variables consist of diamond growth rate, surface appearance and quality.

Initially, the single crystal diamond seed were deposited using the open type holder. It was observed that by employing the open type holder, it resulted in higher growth rates and higher substrate temperatures. However, when using the open type holder, the grown single crystal diamond was accompanied by the formation of a polycrystalline border or frame on the sides of the seed substrates.

i.e., a polycrystalline rim around the substrate was produced. In order to avoid this polycrystalline formation and to achieve a better control of the plasma substrate environment, most single crystal diamond depositions were performed using the pocket type holder which produced a lower growth rate.

The substrate position, ΔZ was initially varied at -3.1 mm, 0 mm, and 2.5 mm for the 3% methane concentration but later on was mostly kept fixed at -3.1 mm especially for the 5% methane concentration. This substrate position at -3.1 mm was the optimum position obtained from the reactor roadmap experiments and polycrystalline diamond deposition.

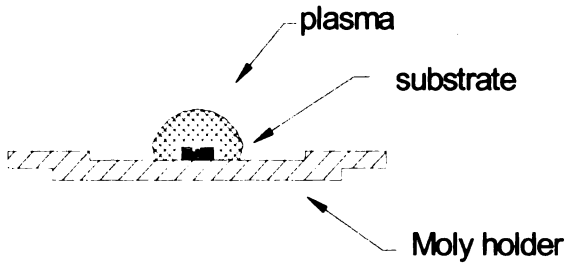

Figure 5.34 – Open type single crystal diamond holder

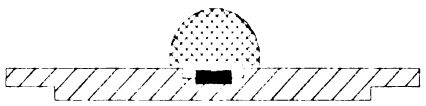

Figure 5.35 – Pocket type single crystal diamond holder

5.4.1 Diamond growth rate

Shown in Figure 5.36 is the single crystal diamond growth rate for open holder and pocket holder types. The operating pressure was kept fixed at 240 Torr, methane concentration was kept fixed at 5% CH_4/H_2 (flow rate of 20 sccm), and substrate position ΔZ was kept fixed at -3.1 mm. As can be seen, the open holder design resulted in higher growth rates up to 36 μm/hr compared to the pocket holder type at 21.4 μm/hr. The lowest growth rate at 16.8 μm/hr using the open holder is possibly due to the very high substrate temperature at 1361 °C.

Figure 5.37 displays the growth rate of the single crystal diamond using the pocket holder. The methane concentrations were varied from 3% to 5% and operating pressure varied from 180 Torr to 250 Torr. As the pressure and methane concentration increase, the diamond growth rates tend to increase. The single crystal diamond growth rate ranges from 8 μm/hr to 21.4 μm/hr. No nitrogen was added into the system gas chemistry. Some variations in the growth rate are probably due to the substrate holder type, ΔZ position, and substrate temperature. For example, the two data points at operating pressure of 240 Torr with 5% CH_4/H_2 are significantly higher to one another. This could be due to the difference in substrate temperature during deposition. The 16.87 μm/hr and 21.4 μm/hr correspond to 1076 °C and 1149 °C respectively. The data point at 180 Torr with 3% CH_4/H_2 shows higher growth rate compared to other 3% CH_4/H_2 is probably due to the shims height. The sample with growth rate of 6 μm/hr was

grown using -3.1 mm shims compared to +2.5 mm shims for the sample with growth rate of 8 μm/hr.

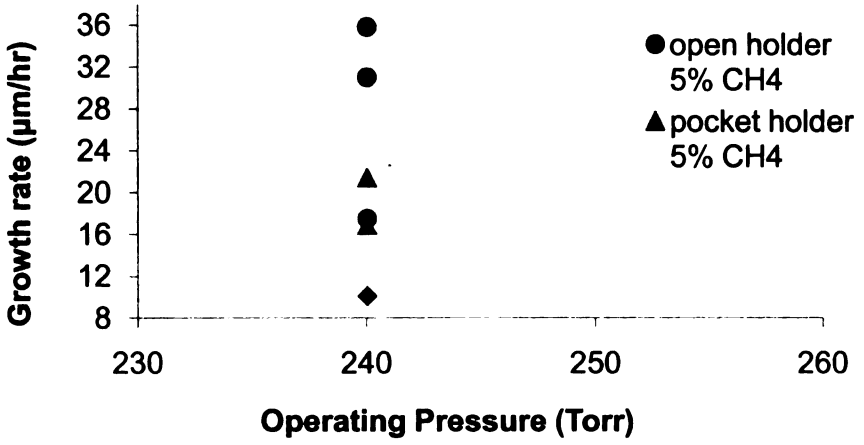

Figure 5.36 - Single crystal diamond growth rate for the open versus pocket holders. Deposition pressure fixed at 240 Torr, methane concentration fixed at 5% CH_4/H_2, and substrate position ΔZ fixed at -3.1 mm.

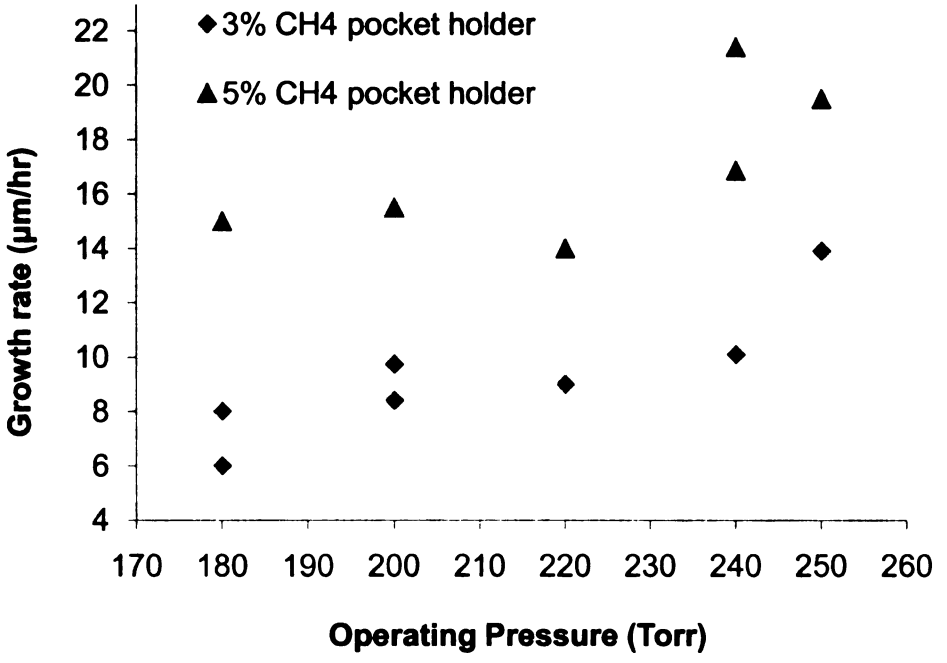

Figure 5.37 - Single crystal diamond growth rate at 3% and 5% methane concentrations (H_2 flow rate of 400 sccm) and deposition pressure of 180-250 Torr.

Figure 5.38 and Figure 5.39 shows the growth rates as a function of substrate temperature under various operating pressures, holder types, and methane concentrations at 3% and 5% CH_4/H_2. The temperature of the substrate during deposition ranges from 867 °C to 1361 °C. The diamond growth rate increases as substrate temperature increases. This trend was observed for the 5% CH_4/H_2 using the pocket type holder. Moreover, higher methane concentration results in higher substrate temperature deposition window. For the open type holder with 5% methane concentration and 3% pocket type holder, the growth rate initially increases and later decreases when a certain deposition substrate temperature limit has been reached. For example, Figure 5.39 displays such behavior. The growth rates drops from 36 μm/hr to 17.5 μm/hr when the diamond was grown at substrate temperature of 1282 °C and 1361 °C respectively .

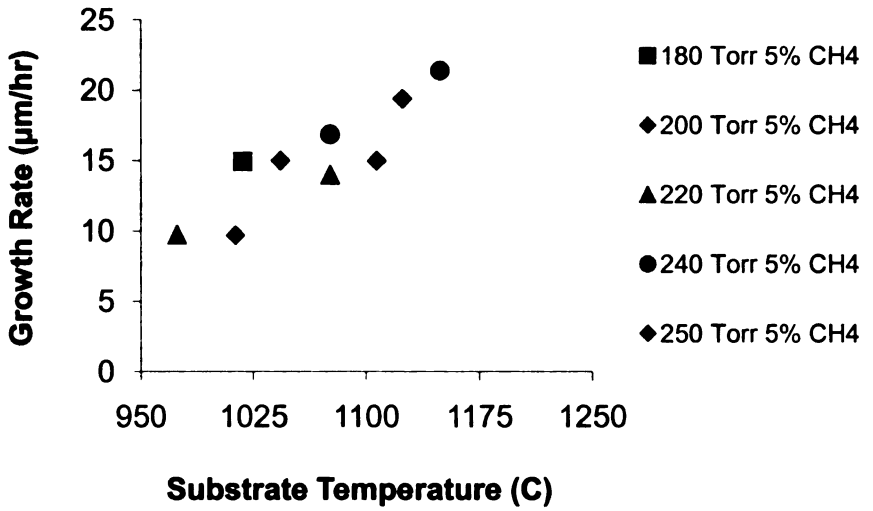

Figure 5.38 - Substrate temperature versus growth rates at a fixed 5% methane concentration under various operating pressures.

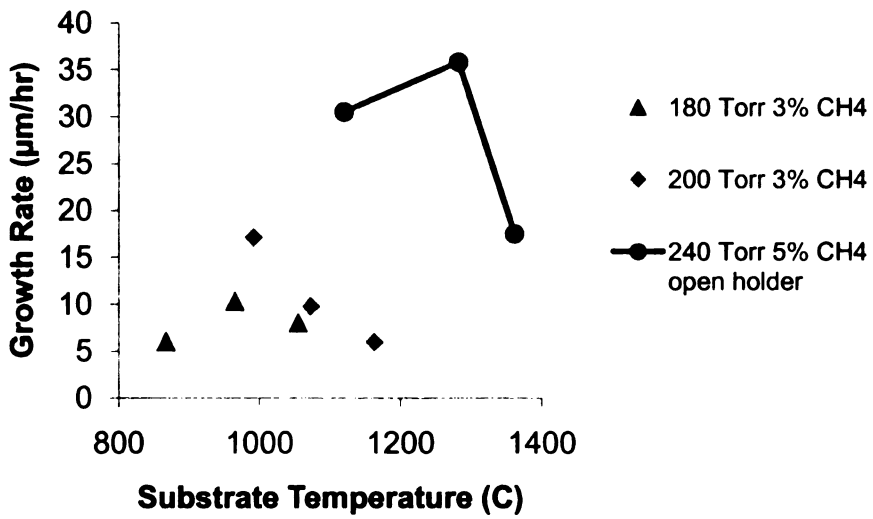

Figure 5.39 - Substrate temperature versus growth rates at a fixed 3% methane concentration under various operating pressures.

5.4.2 Diamond surface appearance

The grown single crystal diamond surface appearance is shown in Figure 5.40 through Figure 5.45. The reflection and transmission light were used to capture the images on the microscope with magnification of 2.5X, 10X, and 50X for closer view i.e., zoom in on the grown diamond surface.

Figure 5.40(a)-(d) to 5.41(a)-(d) display some examples of surface defects observed on some of the grown single crystal diamond surface depending on the growth conditions. These defects include non epitaxial crystallites or dark particles, pyramidal hillocks, round conical hillocks, and step bunching. Etch pits or shallow craters also observed on the surface of the films with various shapes such as circular, square/rectangular, or pyramidal shapes. These hillocks may be due to diffusion and temperature gradient during the growth. Another possible reason of these defects could be due to the fact that the high pressure high temperature (HPHT) diamond seed itself may contain some imperfections or defects prior to deposition. The seed imperfection such as inclusions, growth sectors related to the crystal planes directions, and surface damage could influence the outcome of the grown diamond.

Bauer *et.al.* [117] suggested that the growth of non-epitaxial particles and continuous increased in lateral size during the deposition process does not necessarily start directly at the Ib substrate surface. Instead, the nucleation occurs at local instabilities or impurities on the grown film rather than from structural defects in the substrate.

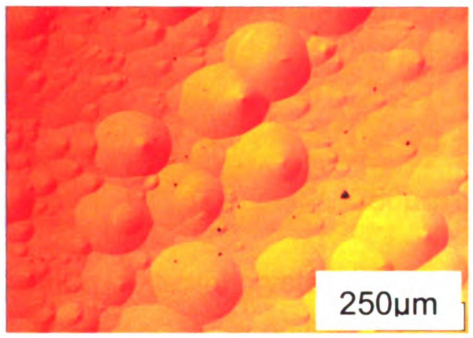

(a) Conical round hillocks

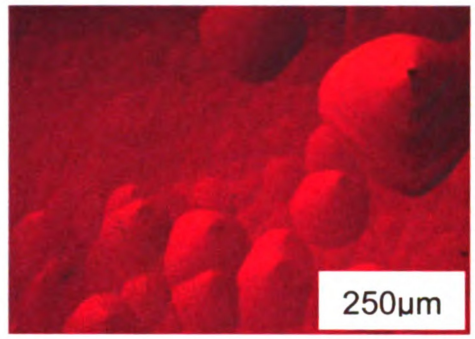

(b) Conical round hillocks

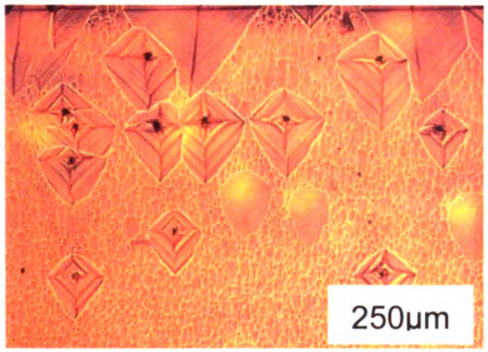

(c) Pyramidal square hillocks

(d) Pyramidal square hillocks

Figure 5.40(a)-(d) - Examples of surface defect on the grown single crystal diamond. The micrograph images are top view of the grown surface using transmission and reflection light. (a)-(b) conical round hillocks, 10X (c)-(d) pyramidal square hillocks, 10X and 50X.

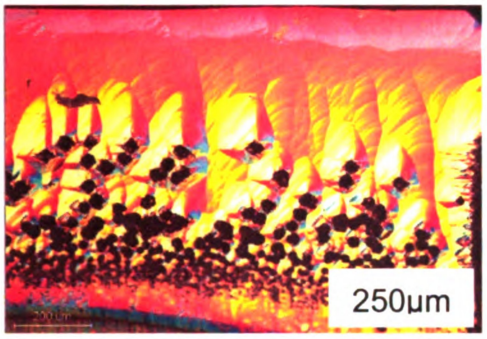

(a) non-epitaxial crystallites

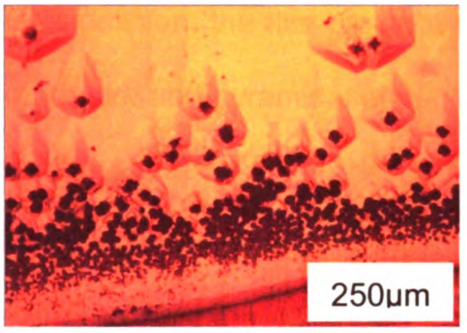

(b) non-epitaxial crystallites

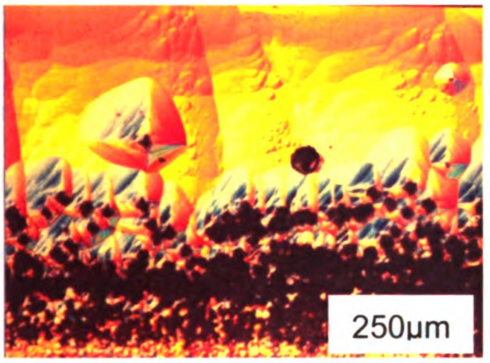

(c) non-epitaxial crystallite

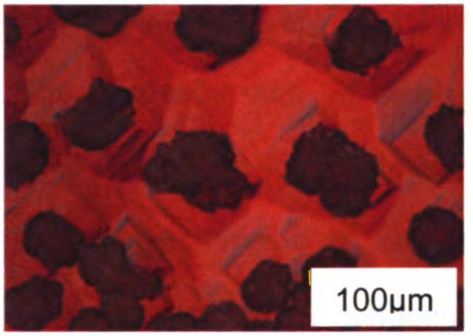

(d) non-epitaxial crystallite

Figure 5.41(a)-(d) - Examples of surface defect on the grown single crystal diamond. The micrograph images are side view of the grown surface using transmission and reflection light. (a)-(b) non-epitaxial crystallites or dark particles, 10X (c)-(d) dark particles or non-epitaxial crystallites, 50X.

In terms of hydrogen etching time prior to deposition, the film grown with etch time of 30 minutes shows a large number of square and pyramidal etch-pits structure on the surface exhibits dark pyramidal pit like feature along the edges as can be seen in Figure 5.42(a)-(b). The side faces of the pyramids show a sequence of macro steps. With longer etch time, the grown diamond shows less defects or pyramidal hillocks on the surface. Also, the grown diamond starts to show along the edges "frame like" appearance as shown in Figure 5.42(c)-(d). Some pyramidal hillocks are still observed with increasing etch time but less dense compared to 30 minutes etching time. The increasing time of etching before deposition on the substrate from 30 minutes to 60 minutes seemed to help in preventing the formation of square or pyramidal shaped hillocks as can be seen in Figure 5.42(c)-(d). With over an hour of hydrogen etching, the surface is free of pyramidal hillocks but some "crater" or "orange peel" like feature can be observed on the grown diamond film.

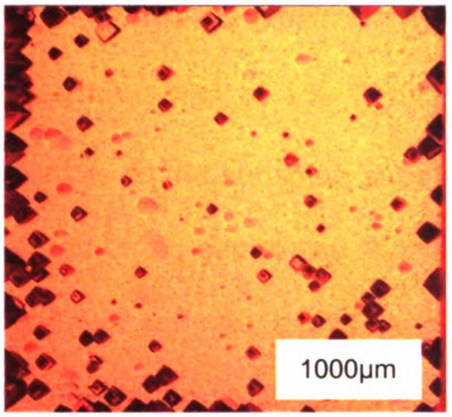

(a) 30 minutes H_2 plasma etch

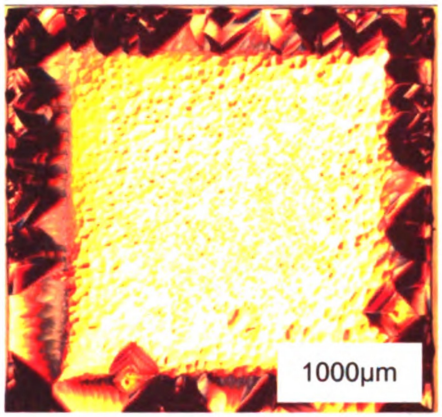

(b) 30 minutes H_2 plasma etch

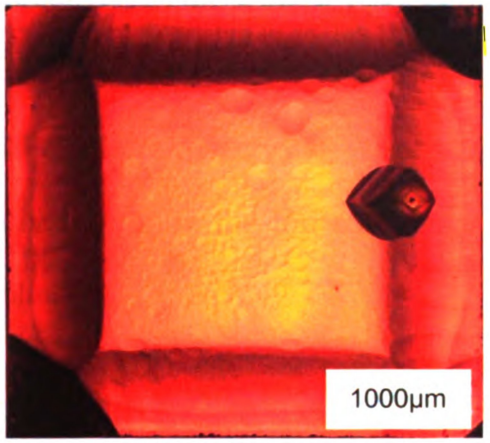

(c) 60 minutes H_2 plasma etch

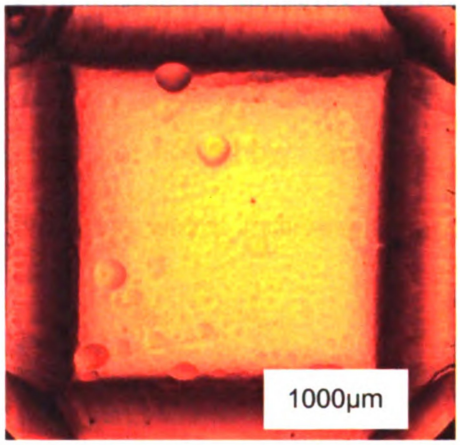

(d) 60 minutes H_2 plasma etch

Figure 5.42(a)-(d) – Surface appearance of grown single crystal diamond versus etching time. Growth conditions: (a) pressure = 220 Torr, CH_4/H_2 = 3%, microwave absorbed power = 2.04 kW, substrate temperature = 1224 °C (b) pressure = 240 Torr, CH_4/H_2 = 3%, microwave absorbed power = 1.73 kW, substrate temperature = 1110 °C (c) pressure = 200 Torr, CH_4/H_2 = 5%, microwave absorbed power = 2.009 kW, substrate temperature = 1050 °C (d) pressure = 220 Torr, CH_4/H_2 = 5%, microwave absorbed power = 2.05 kW, substrate temperature = 979 °C. All samples deposition time = 8 hours.

When the grown diamond is compared versus the methane concentration, the grown film at 3% CH_4/H_2 exhibits some etch pits, round and pyramidal hillocks on the substrate surface as shown in Figure 5.43. Towards the substrate edges of the sample as shown Figure 5.43(a)-(b), the film shows a terraced like structure with steps or ridges. The rims formation on the samples might be the source of the steps and the thickness at the rims of the samples were greater compared with the centers of the substrate. At around the center of the sample as shown in Figure 5.43(c)-(d), some square hillocks growth formation is also observed. The square hillocks formed a multilayer or stacked on top of one another and more likely at some point after longer period of growth, it will formed a single layer crystal. The square hillocks do not show any non epitaxial crystallites on the top surface of the grown films which indicate a good quality film.

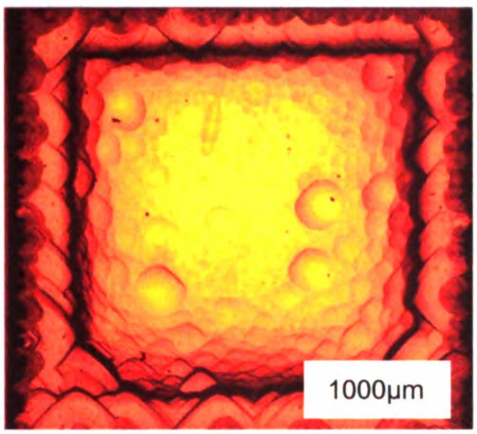

(a) 3% CH_4/H_2, 180 Torr, refl. 2.5X

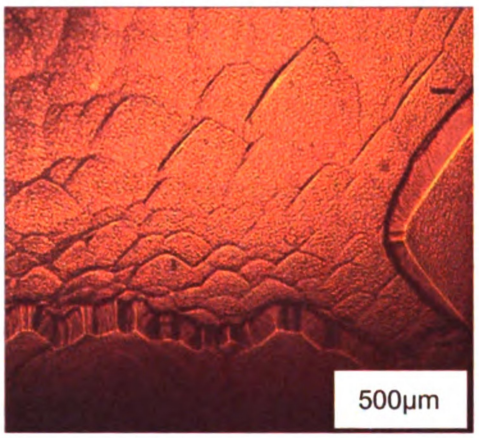

(b) 3% CH_4/H_2, 180 Torr, trans. 10X

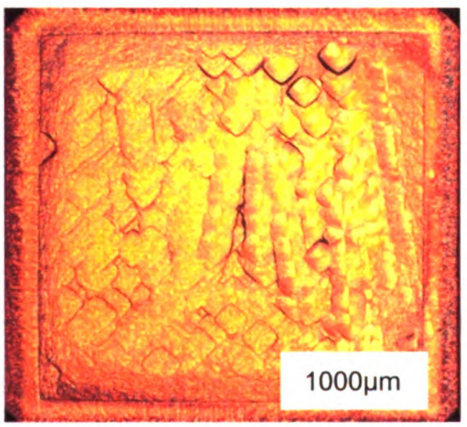

(b) 3% CH_4/H_2, 200 Torr, refl. 2.5X

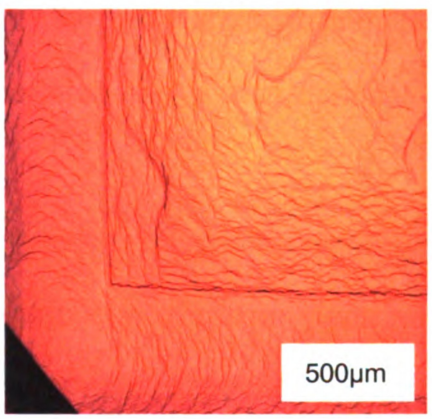

(d) 3% CH_4/H_2, 200 Torr, trans. 10X

Figure 5.43 - Surface appearance of single crystal diamond grown at 3% methane concentrations. Growth conditions: (a)-(b) pressure = 180 Torr, CH_4/H_2 = 3%, microwave absorbed power = 2.25 kW, substrate temperature = 965 °C, deposition time = 8 hours, growth rate = 10.3 µm/hr (c)-(d) pressure = 200 Torr, CH_4/H_2 = 3%, microwave absorbed power = 2.30 kW, substrate temperature = 991 °C, deposition time = 8 hours, growth rate = 17.1 µm/hr.

When the methane concentration was increased to 5%, the surface appearance improved compared to 3% CH_4/H_2. The films showed no non epitaxial crystallites and free of dark particles but microscopically rough "frame" like appearance along the edges was observed as shown in Figure 5.44(a)-(d) through Figure 5.45(a)-(d). The size of the frame structure increases at 180 Torr compared to 220 or 240 Torr. As can be seen, the edge of the area grows faster than the center part of the diamond surface. At the beginning, the growth process starts all over the surface and then the growth can proceed by lateral spread of preexisting lattice planes. Only the upper edge of the sample growth immediately requires the nucleation of new planes. The lateral spread is then dominated by frame like feature.

At the center of the substrate, no hillocks were observed on the growth surface. The surface shows a homogenous distribution of macro steps without large features or non-epitaxial particles. This area is macroscopically smooth with "orange peel" appearance. Within this region there are already several round conical hillocks and one can expect that with increasing growth time their size will become larger and increase the thickness of the whole surface.

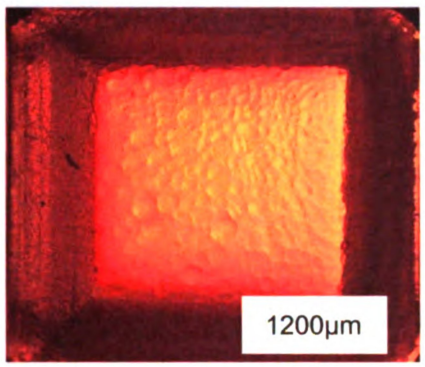

(a) 5% CH_4/H_2, 180 Torr, refl. 2.5X

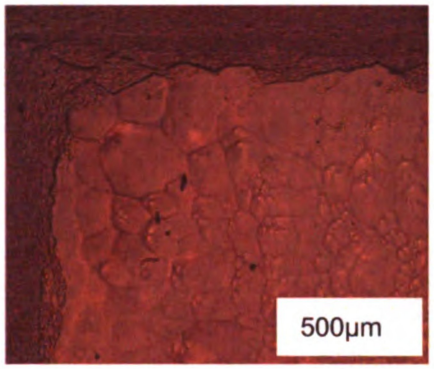

(b) 5% CH_4/H_2, 180 Torr, trans. 10X

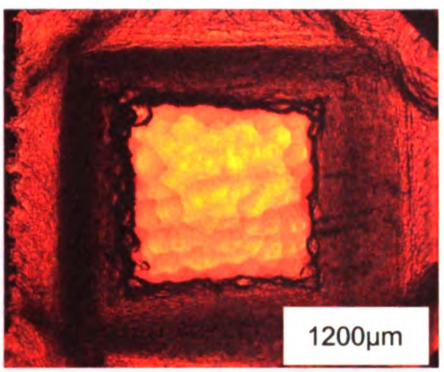

(c) 5% CH_4/H_2, 220 Torr, refl. 2.5X

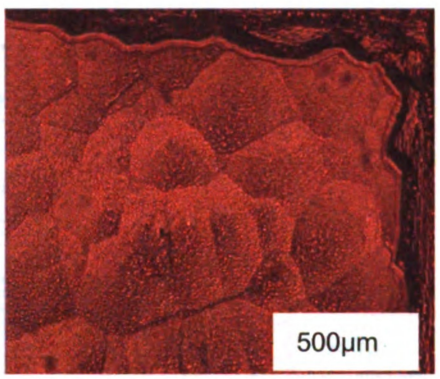

(d) 5% CH_4/H_2, 220 Torr, trans. 10X

Figure 5.44 - Surface appearance of single crystal diamond grown at 5% methane concentrations. Growth conditions: (a)-(b) pressure = 180 Torr, CH_4/H_2 = 5%, microwave absorbed power = 2.16 kW, substrate temperature = 1018 °C, deposition time = 8 hours, growth rate = 14.95 µm/hr (c)-(d) pressure = 220 Torr, CH_4/H_2 = 5%, microwave absorbed power = 2.29 kW, substrate temperature = 974 °C, deposition time = 8 hours, growth rate = 9.75 µm/hr

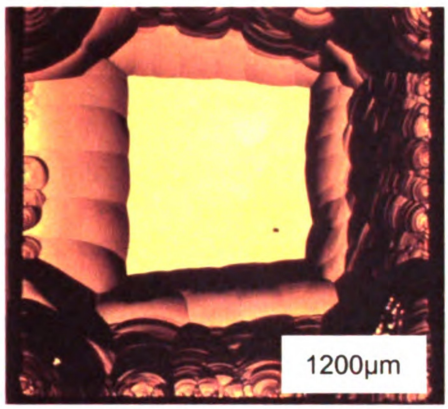

(a) 5% CH_4/H_2, 240 Torr, refl. 2.5X

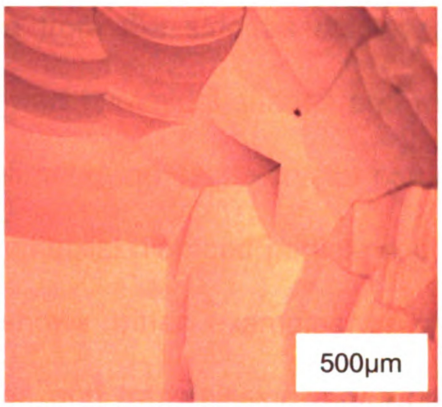

(b) 5% CH_4/H_2, 240 Torr, refl. 10X

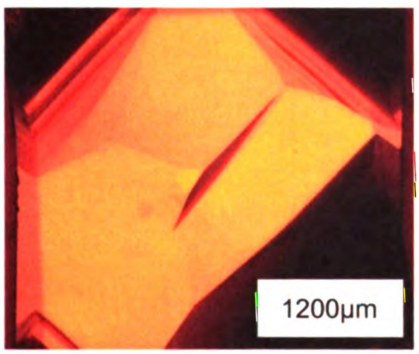

(c) 5% CH_4/H_2, 240 Torr, refl. 2.5X

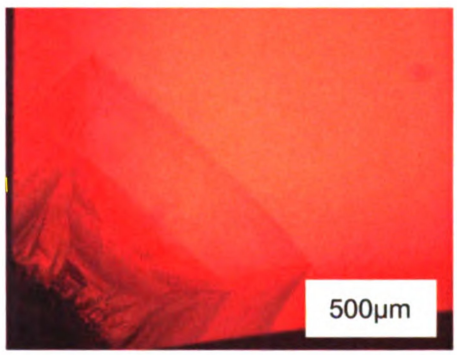

(d) 5% CH_4/H_2, 240 Torr, refl. 10X

Figure 5.45 - Surface appearance of single crystal diamond grown at 5% methane concentrations. Growth conditions: (a)-(b) pressure = 240 Torr, CH_4/H_2 = 5%, microwave absorbed power = 2.135 kW, substrate temperature = 1120 °C, deposition time = 8 hours, growth rate = 30 µm/hr (c)-(d) pressure = 240 Torr, CH_4/H_2 = 5%, microwave absorbed power = 2.01 kW, substrate temperature = 1282 °C, deposition time = 10 hours, growth rate = 35.8 µm/hr.

Viewing the grown diamond substrate from the side as displayed on Figure 5.46(a)-(b), one can see the films showed pyramidal shapes and macro steps running along the (110) directions, confirming the single-crystal nature of the film. Some pyramidal hillocks free of non epitaxial diamond particle could be observed on the films. Figure 5.46(c)-(f) shows other examples of grown diamond viewed from the side using reflection and transmission mode on the micrograph.

(a) Grown diamond side view, refl. 2.5x

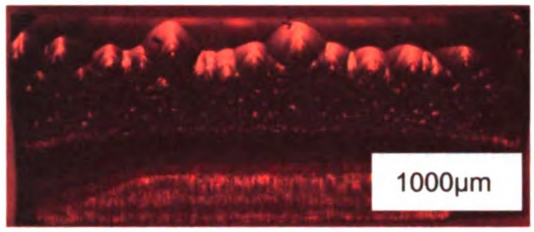

(b) Grown diamond, transmission 2.5x

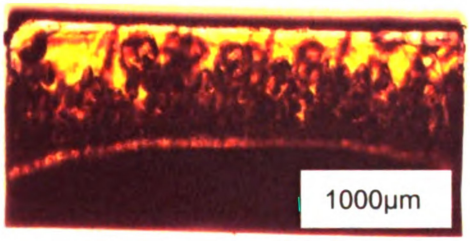

(c) Side view, transmission 2.5X

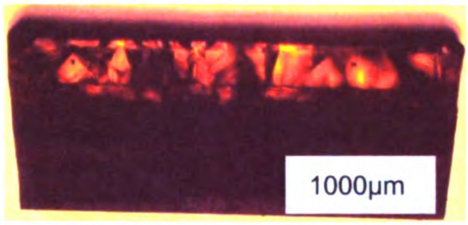

(d) Side view, reflection, 2.5X

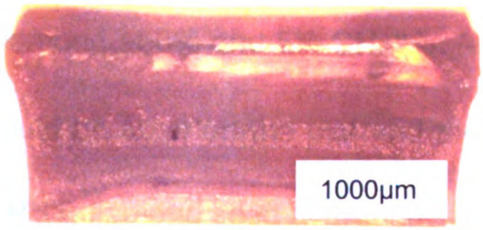

(e) Side view, refl. 2.5x

(f) Side view, reflection 2.5x

Figure 5.46(a)-(f) - Side view of overall growth of single crystal diamond. Growth conditions: (a)-(b) pressure = 240 Torr, CH_4/H_2 = 5%, microwave absorbed power = 2.2 kW, substrate temperature = 1149 ºC, growth rate = 21 µm/hr (c) pressure = 240 Torr, CH_4/H_2 = 3%, microwave absorbed power = 1.836 kW, substrate temperature = 1110 C, growth rate = 10.1 µm/hr (d) pressure = 200 Torr, CH_4/H_2 = 3%, microwave absorbed power = 1.854 kW, substrate temperature = 1013 ºC, growth rate = 9.73 µm/hr (e) pressure = 220 Torr, CH_4/H_2 = 5%, microwave absorbed power = 2.096 kW, substrate temperature = 1076 ºC, growth rate = 14 µm/hr (f) Pressure = 240 Torr, CH_4/H_2 = 5%, microwave absorbed power = 2.135 kW, substrate temperature = 1120 ºC, growth rate = 30 µm/hr.

5.4.3 Raman measurements

The single crystal diamond grown at 3% and 5% of methane concentration at operating pressures 180-250 Torr were characterized using the Raman analysis. As shown in Figure 5.47, the wide scan of the Raman spectra from 1175 cm^{-1} to 1800 cm^{-1} shows no sp^2 or graphitic peak which indicates high purity grown single crystal diamond. The CVD single crystal diamond was still attached to the substrate allowing for measurements of the thin film in the as-grown state. As expected, the grown single crystal diamond full width half maximum is very close to the reference HPHT diamond at 1.78. Figure 5.48 and Figure 5.49 display the Raman peaks and FWHM of the grown single crystal diamond at 3% and 5% CH_4/H_2. As expected, strong sp^3 peaks at 1332.53 cm^{-1} could be seen on the plot and the FWHM values is very close to the reference HPHT diamond seed at around 1.78 cm^{-1}.

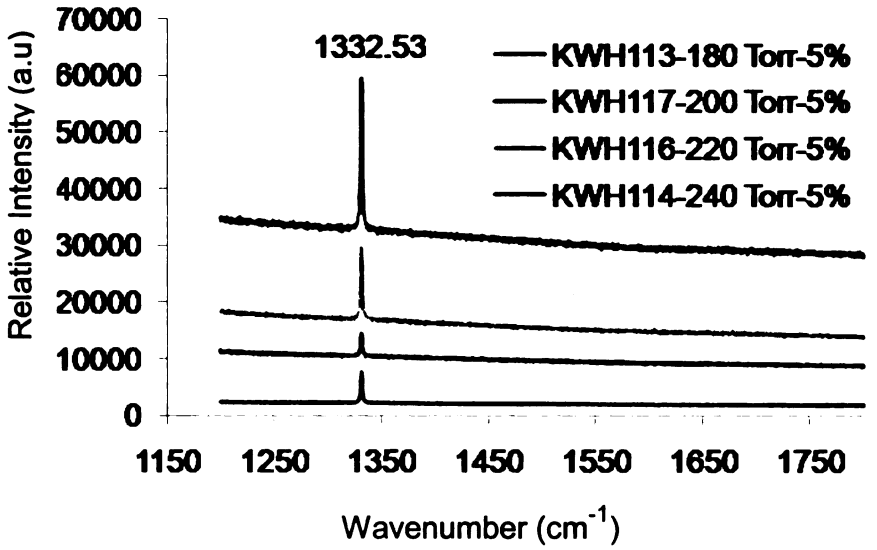

Figure 5.47 - Wide scan of Raman spectra for diamond sp^3 peak and graphite sp^2 peak wavelengths at operating pressure of 180-240 Torr at 5% methane concentrations.

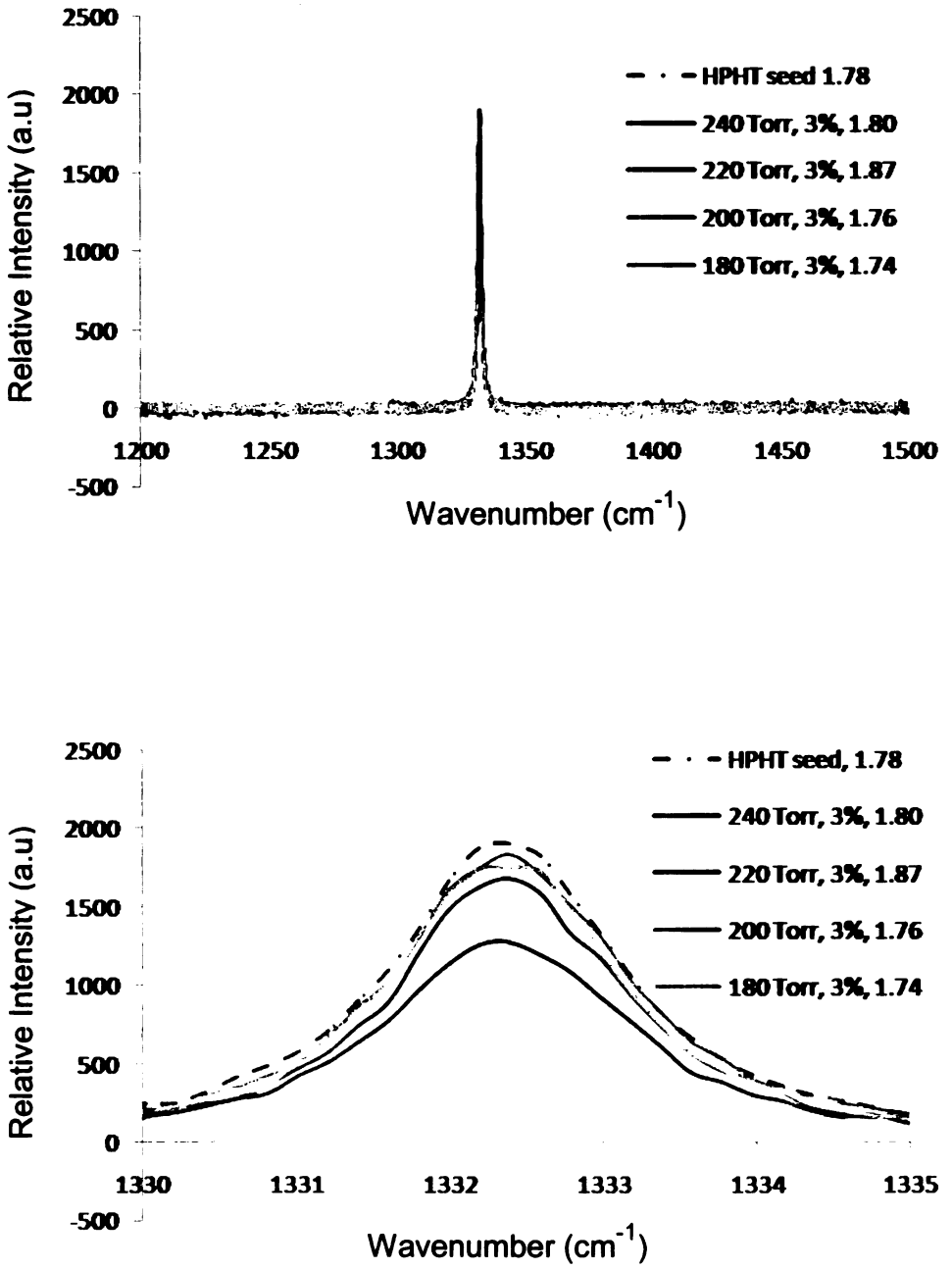

Figure 5.48 - Raman spectra and its FWHM value of the single crystal diamond grown at 3% methane concentration at operating pressure of 180-240 Torr. (a) Spectra scan from 1200 to 1500 cm^{-1} (b) closer view of the sp^3 diamond peak at 1332.5 cm^{-1}.

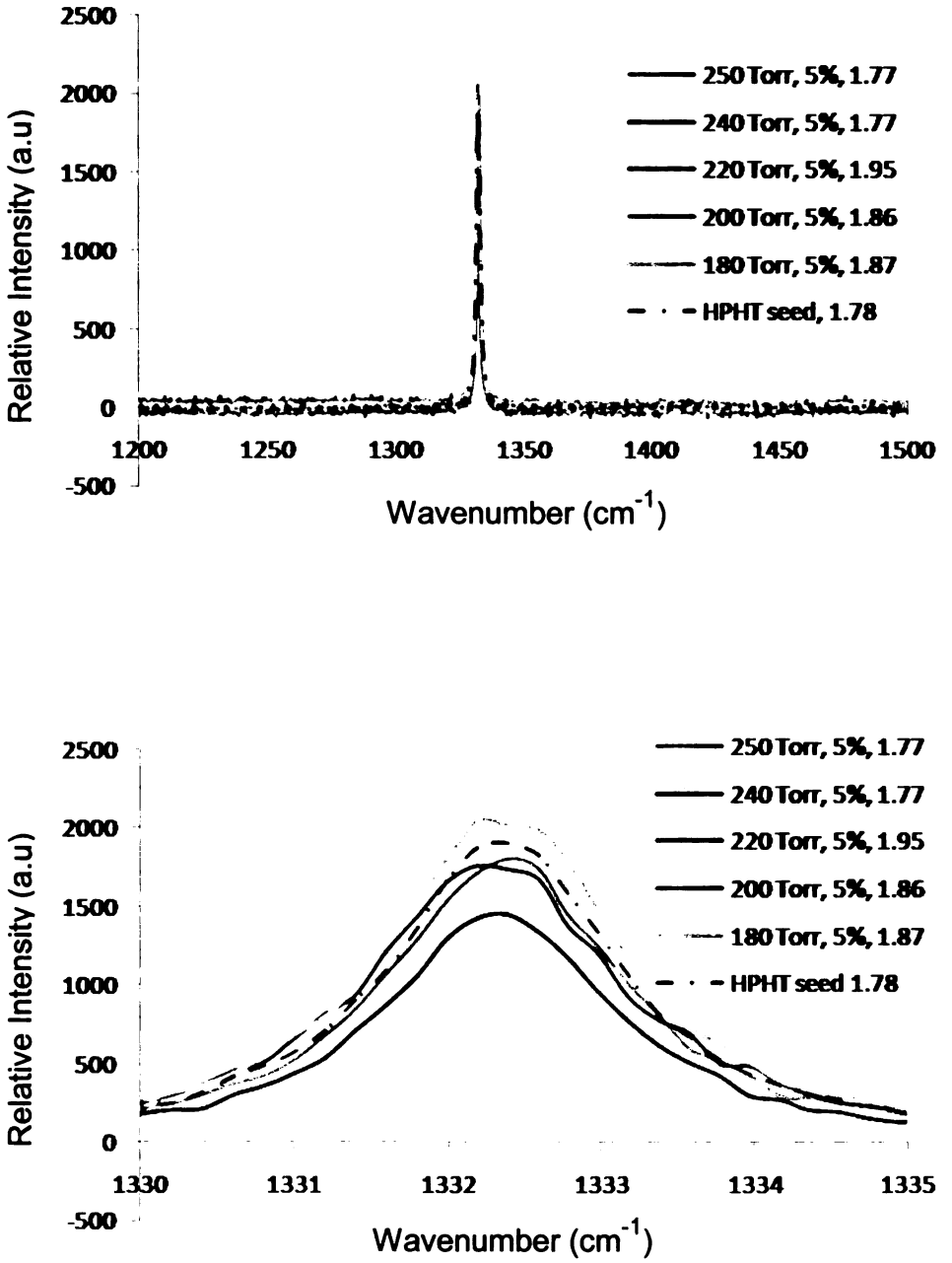

Figure 5.49 - Raman spectra and its FWHM value of the single crystal diamond grown at 5% methane concentration at operating pressure of 180-250 Torr. (a) Spectra scan from 1200 to 1500 cm^{-1} (b) closer view of the sp^3 diamond peak at 1332.5 cm^{-1}.

5.5 Summary

The microwave plasma cavity reference reactor were redesigned and experimentally evaluated by synthesizing polycrystalline and single crystal diamond films over the 180-250 Torr pressure regime. This redesign not only increased the plasma absorbed power density above the deposited substrate but also enabled operation at higher pressure. The major design changes were the reduction of the inner conductor cooling stage radius by more than a factor of two to 1.91 cm and introducing the position/length tuning of the substrate holder. The reduction of the inner conductor area increased the discharge power density and produced very intense discharges with adjustable power densities of 150-475 W/cm^3 in the 180-240 Torr pressure regime. The length tuning of the substrate holder allowed the electromagnetic focus to be varied above the substrate and allowed the control of the discharge shape, size and position.

Without any nitrogen gas addition into the gas chemistry, polycrystalline diamond film synthesis rates varied from 3-21 μm/h as the operating pressure varied from 180-240 Torr and the methane concentration was varied from 2-5%. Likewise, the growth rates for the single crystal diamond range from 8-36 μm/hr. The substrate temperature during diamond synthesis ranged from 950-1150 °C and 951° to 1282 °C for polycrystalline and single crystal diamond respectively. Good uniformity and excellent optical quality polycrystalline diamond films were produced using the modified reactor. In addition to the smooth surface appearance of the grown single crystal diamond, other surface morphology such

as pyramidal square hillocks, round conical hillocks, orange peel/crater like, and dark particles/non epitaxial crystallites were also observed. Raman measurements indicate that the grown single crystal diamond exhibits a good quality.

CHAPTER 6

MICROWAVE PLASMA ASSISTED COMBUSTION BACKGROUND

6.1 Introduction

This chapter gives a brief overview of the plasma assisted combustion and microwave plasma assisted combustion literature.

In the past, many researchers [13-14, 16, 118-122] have investigated techniques that combine electrical energy with a flame. They demonstrated the potential to modify the combustion process with the addition of electric energy. In particular, it was found that by impressing an electric field or high voltage into the flame, the flame stability limits were extended, the flame propagation speed was increased and the flame chemistry was altered. As observed by various research groups, the creation of reactive radicals or hydrogen generation resulted in combustion enhancement. Studies of hydrocarbon-air and carbon monoxide-air premixed flames in RF discharge plasmas demonstrated that large fractions of the fuels are burned in RF plasma generated flames [120]. A DC plasmatron was used for the pretreatment of the fuel to improve the combustion process and the conversion of methane to hydrogen [121]. In the dielectric barrier discharge (DBD), the plasma power increased the flame propagation rate resulting in a faster burn rate. The DBD has been usually used to investigate the efficiency of the combustion process. Leaner burning conditions can result when the flame is subjected to the non-thermal plasma discharge [122-124]. In ignition, the

combustion processes are typically initiated by high temperature air or spark discharges that cause the thermal decomposition of the fuels into various highly reactive radical species. The utilization of transient plasma during the formation phase of pulse-ignited atmospheric discharges in a pulse detonation engine confirmed that the transient plasma produces shorter ignition delay times and pressure rise times compared to spark ignition [125]. This leads to cleaner combustion.

The application of electrical power can promote combustion through the formation of active species such as free radicals or excited state molecules or the dissociation of fuel molecules into smaller, more easily combusted fragments. The electric energy applied to the combustion flame can generate non thermal plasma i.e., the electrons are in non equilibrium such that the electron temperature can exceed the temperature of the heavy particles (atoms, molecules, ions) by orders of magnitude. Usually the main mechanism initiating chain reactions in non thermal plasma is via electron driven dissociation and excitation.

Shown in Figure 6.1 is a one-dimensional model of what may occur in a plasma combustion flame for a premixed flame. The gases flow from the left or upstream region, pass through the reaction zone and continue to flow downstream. A flame usually has a thickness, δ, in which all of the chemical reactions take place and where the temperature rises from essentially ambient to the final equilibrium adiabatic flame temperature, T_{af}. Each of the flame layers has its own distinct role and structure. The first sublayer is the preheat layer, $\delta_{l,}$,

followed by an inner fuel consumption layer, δ_{II},, followed in turn by a *CO* and H_2 oxidation layer, δ_{III}. The vertical lines denote the approximate boundaries of these sub-layers. The preheat layer is a region of active radical formation and upstream radical diffusion. It is believed that when more radicals or reaction accelerants such as *OH*, *H*, *O*, CH_3, etc are formed, this layer's enhancement by adding microwave power can potentially accelerate the exothermic combustion process in the fuel consumption sublayer. Radicals are formed in δ_I where they oxidize reactants and form intermediates like *CO* and H_2 radicals in the δ_{II} layer and final products like CO_2 and H_2O are formed in δ_{III}. In terms of temperature profile, as shown in Figure 6.1, the gas temperature increases rapidly at the reaction zone and saturates downstream.

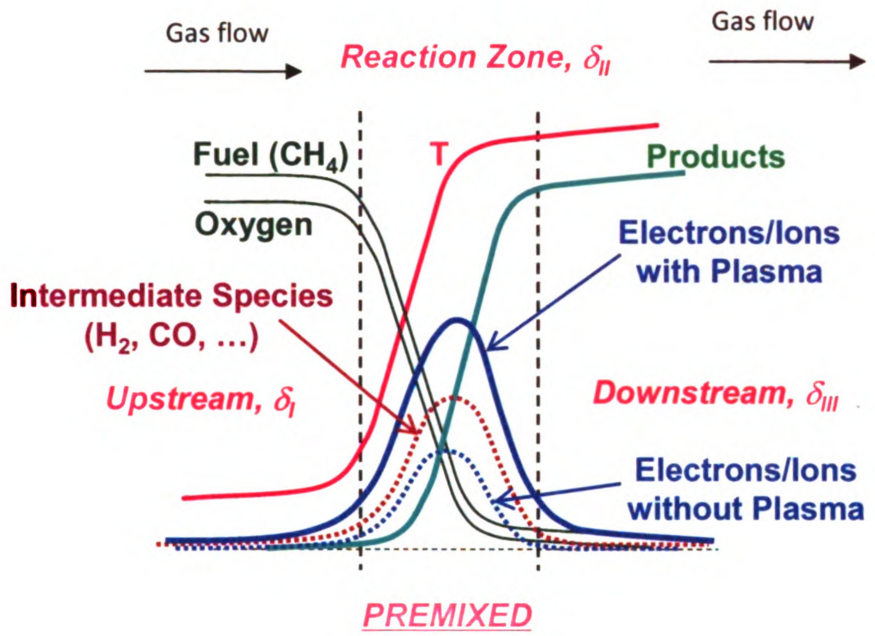

Figure 6.1 - Combined flame and plasma in premixed and diffusion flames. Structure of a typical hydrocarbon/oxygen premixed flame 1D model [126].

When the microwave energy is coupled into the applicator/flame load, electron gas heating takes place which results in the increase of electron gas temperature, Te above the gas temperature, T_g ($T_e > T_g$) and non-equilibrium cold plasma is created. Thus as the microwave electric field and microwave power are increased the electron temperature will increase to the level where some electron – neutral collisions are inelastic and thus the microwave excited electron gas will produce new radical and excited species. If electric field strengths and power levels are further increased, ionization collisions may also occur.

At atmospheric pressure, the flame mean free path for the electron molecule/radical collisions are of the order of one micron and the collision frequency for momentum transfer is of the order of 10^{11}/sec. The mean free path is calculated using the ideal gas law and molecular cross sections constants [127], and assuming the gas temperature is 3000 K and the pressure is one atmosphere. Since the mean free paths for collisional processes are very small the radical and ionized species will also be produced in or directly adjacent downstream from the electron gas. As the excited neutral gas flows downstream the radical and excited species will de-excite and recombine through three body collisions there-by increasing the local gas temperature.

The microwave electron gas heating is expected to occur in or very near the inner cone region of the flame. In this reaction zone, there is a region where the gas temperature is very high, low collision frequency, and high electron density. The microwave electric field will heat the electron gas in this region via

elastic electron – neutral collisions, i.e. electron gas heating occurs by a collisional or ohmic heating process that is governed by the following equation [127]:

$$< P_{abs} > (\vec{r}) = \frac{1}{2} \frac{n_{oe}(\vec{r}) e^2}{2 m_e \upsilon_m} \left(\frac{\upsilon_m{}^2}{\omega^2 + \upsilon_m{}^2} \right) | \vec{E}(\vec{r}) |^2$$

where $< P_{abs} > (\vec{r})$ = the absorbed microwave power density,

$n_{oe}(\vec{r})$ = the electron density versus position $\vec{r}$ in the electron gas,

υ_m = the electron neutral collision frequency for momentum transfer,

$\vec{E}(\vec{r})$ = the impressed electric field strength.

Therefore, by adding microwave plasma energy into the combustion process, it can greatly enhance rates in the reaction zone. This takes place through the combined influence of increased bulk gas temperature and increased plasma temperature of the free electrons, producing higher concentrations of *H* and *O* atoms through reactions like $O_2 + e^- \rightarrow O + O + e^-$, $H_2 + e^- \rightarrow H + H + e^-$. These mechanisms will increase the concentration of *OH* and other radicals that potentially can accelerate the chemical reactions.

6.2 Microwave plasma assisted combustion literature review

Microwave plasma-assisted hydrocarbon treatment was initially investigated for IC engine improvement [13-17] and for the conversion of hydrocarbons into methane and acetylene gases [18]. More recently the conversion of hydrocarbons into hydrogen fuels has been investigated [19]. The application of microwave energy has been shown to assist ignition and flame holding, flame speed enhancement, and flame extinction limits [128-130].

Ward [14] investigated the potential uses of microwave energy to increase internal combustion engine efficiency as well as to reduce the exhaust pollutants. It was speculated that the electrons give up a large portion of their excess energy to excitation of internal energy levels of molecules that accelerate chemical reaction rates. Engine cylinders loaded by the ignited air fuel mixture can absorb microwave energy through coupling at the flame front that in turn resulted in rapid burning of lean, cool, and low polluting flame. Another study Ward conducted was the interaction of propane air laminar flame plasmas with the microwave TM_{010} mode excited in a cylindrical combustion bomb cavity [15]. He used a 3-inch diameter cavity as a combustion chamber, a spark plug for ignition, a 50 MHz sweep oscillator with a sweep time of 20 ms. The Q was measured and it was found that the loading of the cavity by plasma both reduces the peak amplitude and broadens the Q curve. It was concluded that the propane air laminar flame plasma electrically loading the internal combustion (IC) engine cylinder excited in the TM_{010} mode lowered the Q. The flame density

approximated was in the order of 10^{12} electrons/cm^3 and confined to a sheet of thickness of order 0.03 mm.

Maclatchy *et.al.* [16] also investigated the effect of microwave radiation on a propane air flame and measured the electron temperature, ionization density, and flame speed. The experiments were conducted in a conventional microwave oven. The microwave oven operation frequency was 2.5 GHz, input power was 500 W with 50% duty cycle and the line frequency was 60 Hz. By using a Langmuir probe, they measured the electron temperature, ionization density and flame speed. It was observed that electron temperature in the flame front increased by 55 % (at about 0.34 eV) but no increase in ionization density and flame speed.

Groff *et.al.* [131] conducted experiments to study the microwave effects on fuel lean laminar premixed flames. By using a cavity resonator at excitation frequency of 2.4 GHz and electric field intensity strength of 10^5 V/m, the burning velocity increased with electric field intensity up to 6%. The flame deflection increased with increase in electric field intensity and equivalent ratio.

Whitehair *et.al.* [132] conducted microwave combustion flame experiments in the mid 80s. Using a similar cylindrical cavity describes in this thesis, a candle was placed in the center of the cavity and once it was lit then applied microwave input power in the range of 100 Watts into the flame. The experimental set up is shown in Figure 6.2. As the cavity was adjusted to resonance, the flame changed its length but only for about 15 seconds and the flame went out. The combustion products were found to be contaminating the cavity walls possibly because of the microwave energy coupling to the candle wax and heating it. A different flame source was tried by using propane on Bunsen burner and placed it inside the cavity. The electromagnetic mode that he tuned for optimum coupling was the TM_{012} mode. In order to increase the electric field strength in the flame, he placed a piece of screen across the bottom opening of the cavity. In terms of reflected power versus frequency, it was observed that the frequency shift in the order of 0.2 MHz and a slight drop in the Q. It was concluded that the presence of the flame inside the cavity definitely affecting the microwave field patterns. However, only a small interaction between the flame and the microwave energy was detected.

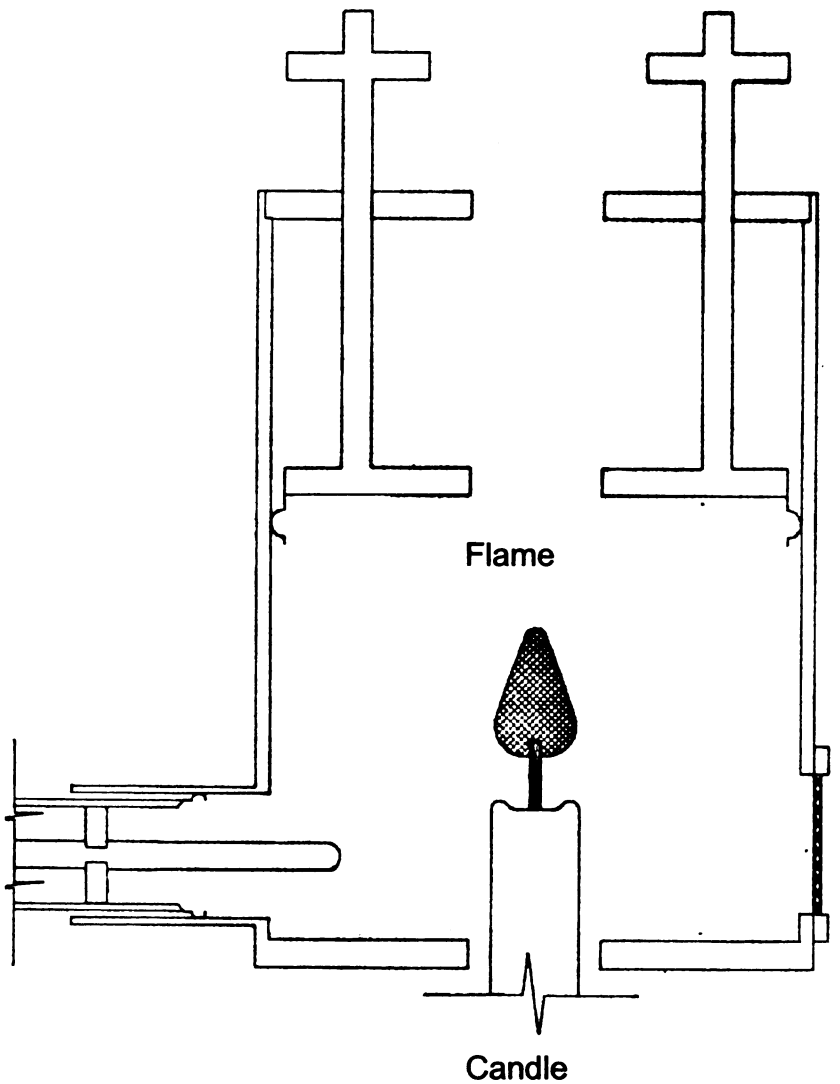

Figure 6.2 – Candle flame in a microwave cavity experiment set up [132].

Zaidi *et.al.* [129] measured the hydrocarbon flame speed in high Q microwave cavity. He demonstrated that by adding a microwave power to the flame combustion zone, the speed of both laminar and turbulent flames can be greatly enhanced. However, due to the unsteady nature of the microwave and flame interaction, the flame speed was difficult to make. The experimental set up consisted of a flat flame burner with a sonic nozzle and using a WR-430 rectangular waveguide, 2.45 GHz excitation, three stub tuner, input power in the range of 1300 up to 4500 Watts, and TE_{10} mode as microwave cavities components. The schematic cross section is shown in Figure 6.3.

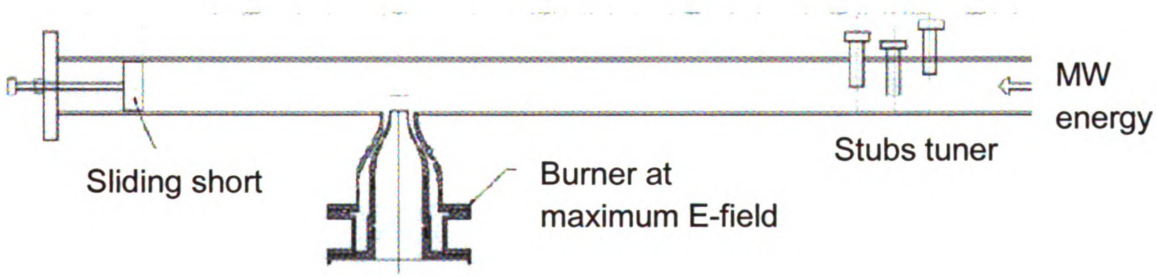

Figure 6.3 - The high Q microwave flame experimental set up schematic [129].

Figure 6.4 shows a series of photographs showing the flame (methane-air) position as a function of input microwave power. As the microwave power level was increased from 0 to 2600 W, the flame clearly moved down towards the burner exit and against the flow of the fuel/air jet towards the burner exit. The flame came back to its original position after the microwave power was turned off. They also observed that the microwave field strength in the resonator cavity was below that required to initiate or even sustain plasma without the flame. Since microwave absorption in the neutral gas molecules was negligible, the effect of the field on the burning speed indicated that the microwave field was coupled to the very thin flame front region where the reaction rate peaks, maintaining that coupling as the flame front moves. Some additional coupling may occur in the region behind the flame front due to the presence of residual ions but that appears to be much less than in the flame front. This coupling to the flame front also means that the total microwave power absorbed is quite low.

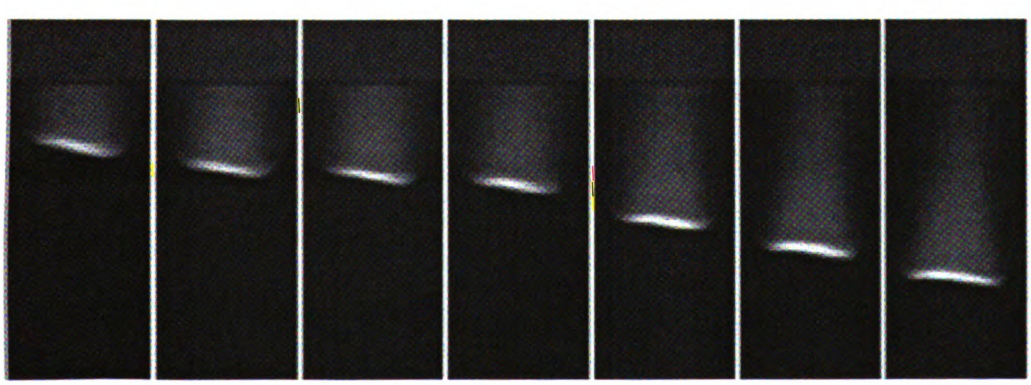

Figure 6.4 - Images inside the cavity as the microwave is applied, the flame move downward into the burner exit [129].

Esakov *et.al.* [133] investigated microwave discharge in air-propane mixture at moderate and high pressure. Figure 6.5 shows the experimental setup. A linear antenna vibrator was placed along the axis of the supersonic stream. The center cross section of the vibrator was placed at a distance of 6 cm from the outlet of the nozzle. The vibrator was held by a streamlined pylon at a certain height over a metallic screen, which was located outside the supersonic stream. A linearly polarized beam of EM radiation with a wavelength of λ = 12.5 cm, input power of 1.5 kW, and a transverse size 9 cm was introduced perpendicular to the screen surface. A propane–air mixture then injected through internal tubes in the pylon and vibrator. Their output operating parameters were geometric characteristics of the discharge, color distribution of the emission and combustion flame velocity. Figure 6.6 shows the direction of the flame stream moving from left to right when microwave energy was applied to the propane fuel in an open air. The length of the propane combustion region decreases with increasing velocity. They concluded that the use of under critical microwave discharge can initiate and sustain the combustion air/propane mixture in a cold supersonic flow.

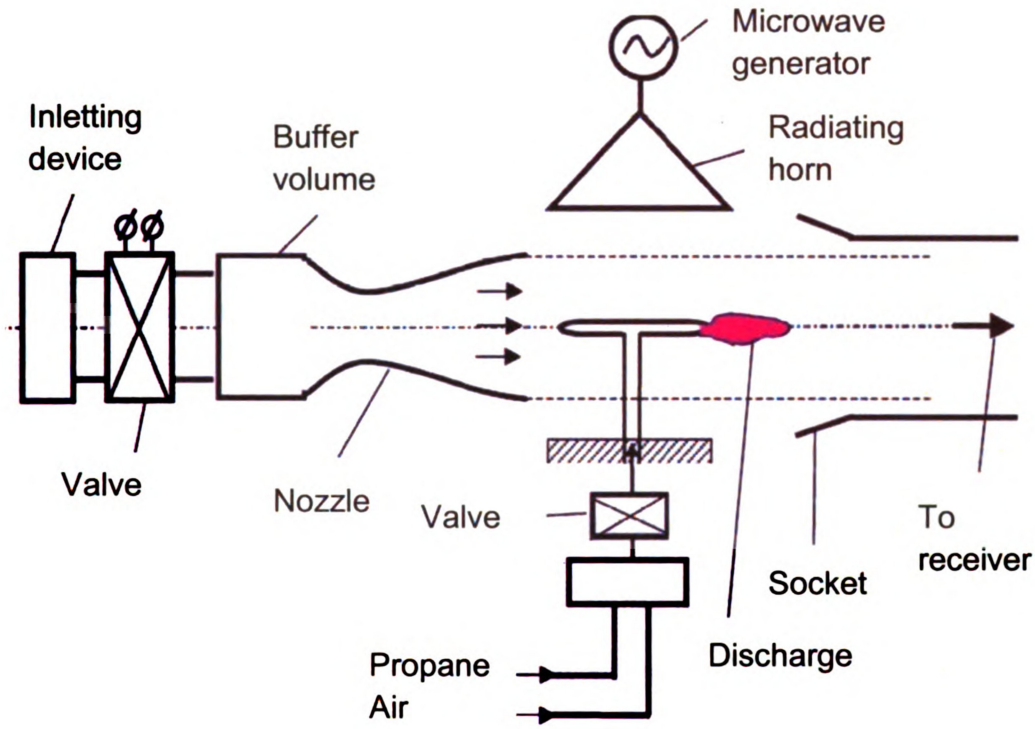

Figure 6.5 - Experimental set up for the propane air mixture combustion [133].

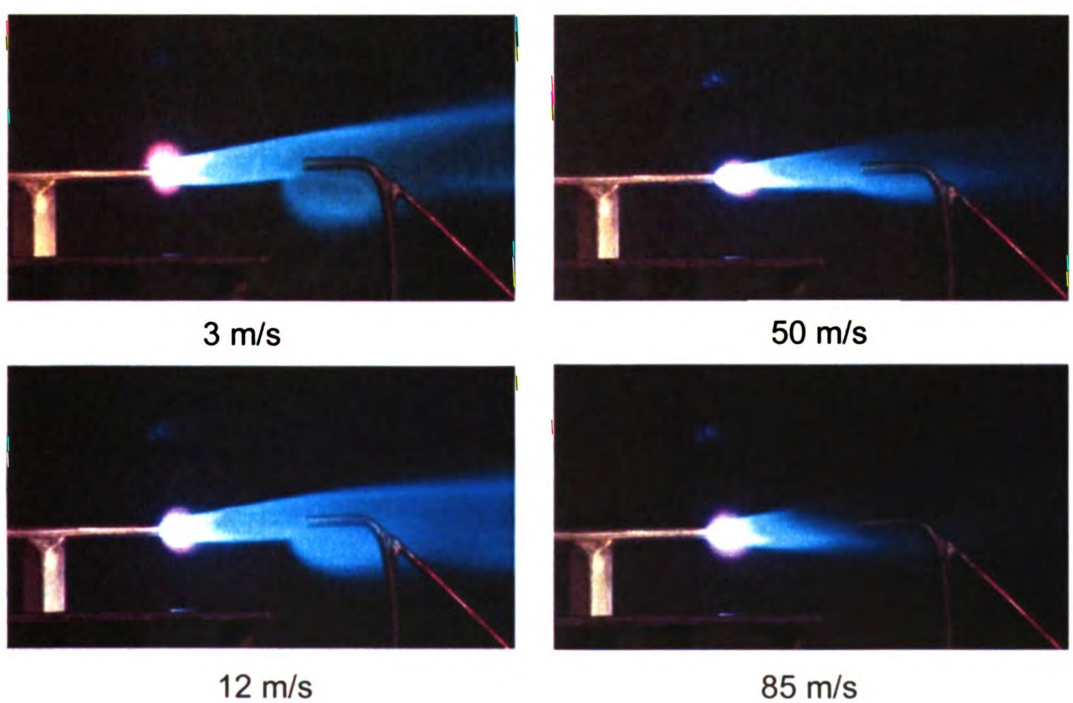

Figure 6.6 - Microwave discharge in airflow at varying velocity with pure-propane injection [133].

CHAPTER 7

MICROWAVE PLASMA ASSISTED COMBUSTION EXPERIMENTAL SYSTEMS AND PROCEDURES

7.1 Introduction

In this chapter, microwave plasma assisted combustion systems are presented. Two different microwave cavity applicators were employed in order to couple the microwave energy into the combustion flame.

The first applicator is a seven inch cylindrical cavity combined with a miniature plasma torch burner. The premixed combustion flame is ignited inside a cavity and then microwave energy of up to 100 Watts is introduced and coupled into the flame and experimental measurements are then performed. The microwave energy was coupled into a flame that was located inside a high Q, tunable, 17.8 cm diameter cylindrical microwave cavity applicator. The idea of employing a tunable cavity applicator to impress, focus and match microwave energy into a load has been applied earlier to material heating [134] and to a variety of microwave plasma source [85, 88, 135-139] applications. This method of microwave coupling and matching has been shown to be an efficient and controllable method for coupling microwave energy into dynamically varying loads such as microwave plasmas and microwave heated material loads. However this microwave applicator system was physically large and therefore additional improvements were desirable. In particular a reduction in the applicator

size and a further improvement in the microwave coupling efficiency were desirable.

The second applicator system is an improved experimental microwave plasma-assisted combustion apparatus, which employs a more efficient and more compact microwave applicator that positions the flame in a region of high microwave electric field strength. The applicator consists of a tunable, re-entrant coaxial cavity [123] that has been modified to allow the combustion flame to be excited in a small (≤ 2 mm) variable gap located in a high electric field region of the applicator. The inner conductor of the re-entrant cavity has an inner conductor that has a nozzle orifice similar to that used in the miniature torch burner and the premixed combustion flame is ignited outside the cavity with low microwave energy level in the range of 1-25 Watts. The impressed electric field modifies the combustion process by coupling energy into the electrons gas. Also, the impressed microwave electric field produced microplasma microwave discharges in the gap region, which further modified the combustion process. These microwave microplasmas have the interesting potential of producing non-local thermal equilibrium plasmas at atmospheric pressure [140-141].

7.2 Experimental system setup

7.2.1 Microwave circuit network, gas handling, and cavity applicator

Figure 7.1 displays the external microwave circuit. All experiments were performed in open air at atmospheric pressure. The microwave oscillator is a 2.45 GHz, continuously variable, 0-100 Watt power supply. It is connected to one port of a three-port circulator via a 50-dB directional coupler, which measures the incident power, P_{inc}. Another port of the circulator is connected to a 30 dB directional coupler, which measures the reflected power, P_{ref}. This 30 dB directional coupler is connected to a matched load, which absorbs any reflected signal from the transmission mismatch. Thus input power absorbed by the applicator and the flame is $P_{abs} = P_{inc} - P_{ref}$. All of the microwave circuit components are connected by 50 Ω low power flexible coaxial cables. The general cross-sectional view of the microwave applicator and the input gases handling system is also shown in Figure 7.1. More detail cross sectional view and description for each cavity applicator i.e., hybrid and re-entrant cavity applicators is described in chapter 8 and 9 respectively. The gas handling system consists of flow meters and gas bottles for methane, oxygen, nitrogen, and argon. The premixed gas, which is regulated by the mass flow controllers, flows through the inner conductor of the applicator from gas feed tanks. A digital camera and/or spectrometer capture the flame image and its emission intensity respectively, outside the cavity applicator end plate.

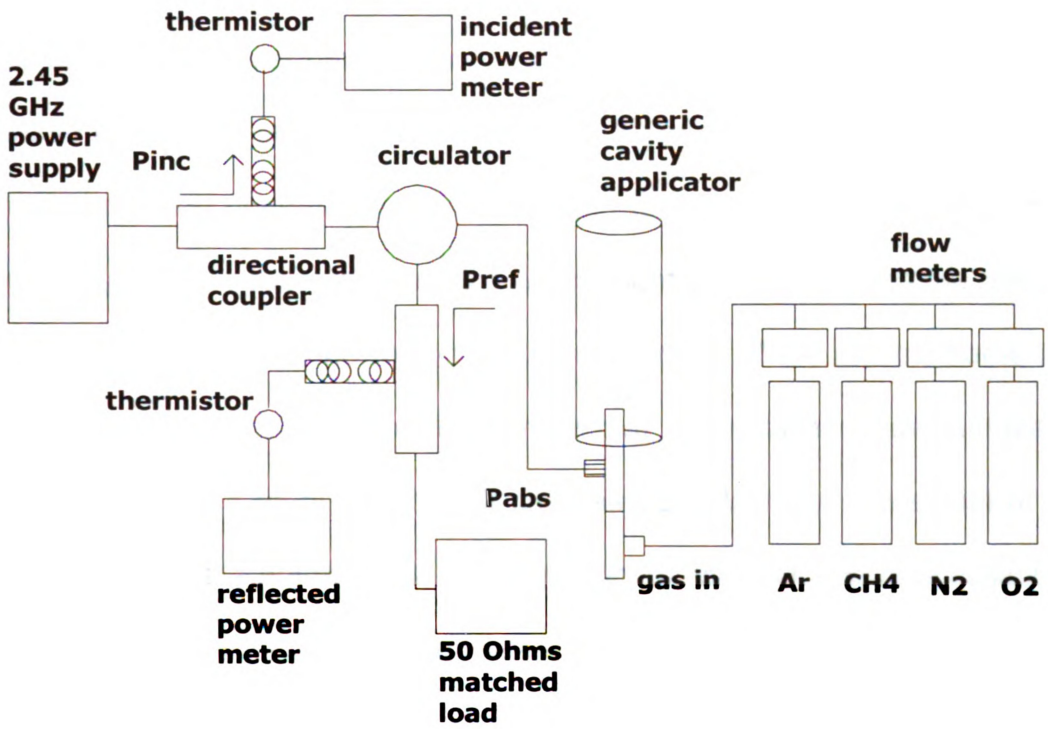

Figure 7.1 - Microwave network, microwave cavity applicator, and gas handling system experimental setup at atmospheric pressure in open air.

7.2.2 Optical emission spectroscopy measurement

Figure 7.2 shows the optical emission spectroscopy measurement setup that was used to characterize the plasma flame discharge gas temperature. This setup was adapted from experiments reported in [142-143]. The spectrometer model utilized was McPherson model 216.5, 0.5 meter, f/8.7, plane grating monochromator. The entrance slit was set to 20 micron. The grating has 2400 grooves/mm which operates in the wavelength range of 1050-10000 Angstrom. The optic signal was collected across a line of sight passing through the reaction zone meaning near the cone region on the center line of the plasma flame in a core part of the flame a few millimeters above the nozzle orifice surface. A biconvex lens with a focal length of 5 cm was used to focus the signal of the plasma flame into the entrance slit of the monochromator. During data collection, the scanning motor of the spectrometer is initiated at scanning speed of 5 Angstrom/minute to sweep the desired wavelength spectrum. This scanning speed produced optimum resolution spectrum without noticeable offset from the instrument. The spectrometer contained a photo multiplier tube EGI-GENCOM RPI QL/20 model which convert the light signals into electrical signals. The ORIEL 70705 supplied a bias voltage of -900 V into the photo multiplier tube. The Keithley 6485 picoammeter detected the current signal sent by the photo multiplier tube. A GPIB interface bus connected the picoammeter into the CPU. A Quick BASIC program on the computer is used for data recording during signal collection.

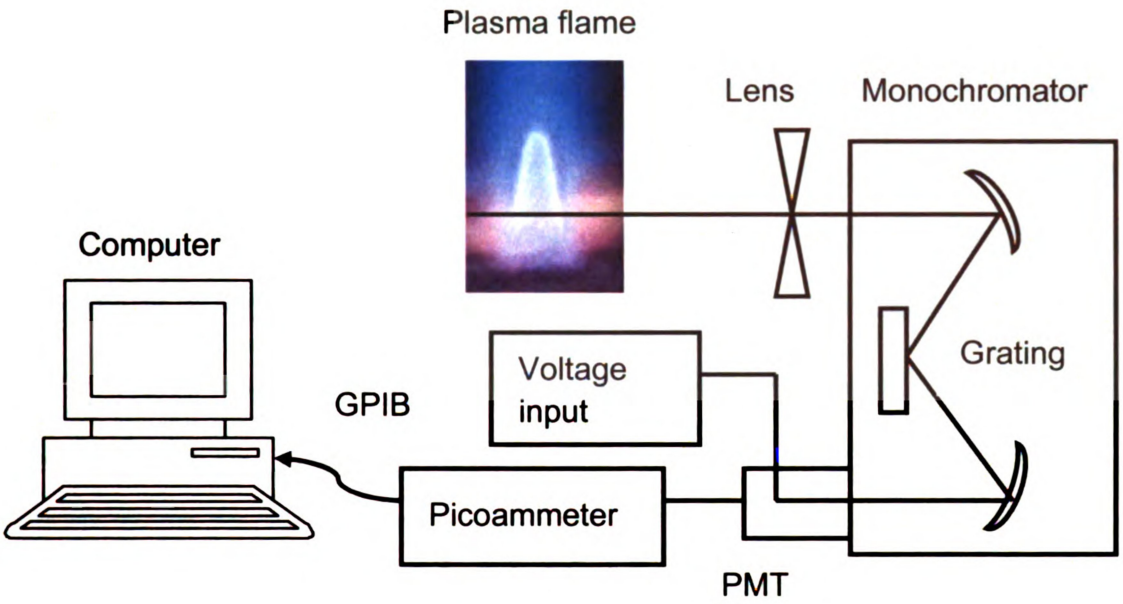

Figure 7.2 - Optical Emission Spectroscopy measurement setup for plasma flame diagnostics.

7.3 N_2 gas temperature calculation procedure

Rotational temperature is a measure of the energetic level of molecule where all rotational modes are fully excited. The rotational population distribution of the gas kinetic temperature follows the Boltzmann distribution [144-146]. The total energy of a given state of diatomic molecule is the summation of electronic energy (T_e), translational energy (T_t), vibrational energy (G), and rotational energy (F) with unit in wave number.

$$T = T_e + T_t + G + F \tag{7.1}$$

In a given vibrational and electronic state, the changes in rotational energy are small compared to the thermal translational energy hence, the rotational energy (F) can be assumed to be a small number. On the other hand, the gas molecule collisions produce changes in the vibrational or electrical quantum numbers less frequently than in rotational quantum numbers because the rotational energies are lower and the changes are easier to excite. The rotational energy (F) can be defined in terms of J, rotational quantum number 1, 2, 3,..., B_v which is the rotator rotational spacing or rotation radius, and D_v the first anharmonic correction to the rotational spacing.

$$F = B_V J (J+1) - D_v J^2 (J+1)^2 + \ldots \tag{7.2}$$

where

$$B_v = B_e - \alpha_e\left(v+\frac{1}{2}\right)+... \qquad (7.3)$$

$$D_v = D_e - \beta_e\left(v+\frac{1}{2}\right)+... \qquad (7.4)$$

where v is the vibrational state, B_e and D_e are constants of equilibrium separation, α_e and β_e are the first anharmonic corrections. The constant values for nitrogen are B_e = 1.8259, α_e = 0.0197. Each atomic molecule has its own system designation based on the quantum state and selection rule. For example, N_2 second positive band system ($C^3\Pi_u$ to $B^3\Pi_g$) has upper (u) or lower (g) states with electronic angular momenta, Λ. Hence, two or three lines or branches may appear which are the P, Q, and R branches. If Λ=0 in both upper and lower electronic states, the transition with ΔJ=0 is forbidden, thus only ΔJ= ±1are allowed. The ΔJ=+1 transition gives rise to the R branch and ΔJ= -1 transition gives rise to the P branch. An example of vibrational and rotation energy levels transitions including the P, Q, and R branches are displayed in Figure 7.3.

The relative rotational line intensities I of Boltzmann distribution can be defined as:

$$I = K_v^4 SJ'J''\exp(-\frac{B_{v'}J'(J'+1)hc}{kT_r} \qquad (7.5)$$

where K is a constant for all lines originating from the same electronic and vibrational level, v is the frequency of the radiation, SJ'J" is the Honl-London

factor, $B_{v'}$ is the molecular rotational constant for the upper vibrational level, J is the rotational quantum number, h is the Planck's constant, c is the speed of light, K is the Boltzmann's constant and T_r is the rotational temperature. The prime and subprime notations represent the quantum number of the upper and lower energy level respectively. It can be deduced from equation (7.5) that the intensity is proportional to the frequency where frequency is inversely proportional to the wavelength ($v = \frac{c}{\lambda}$).

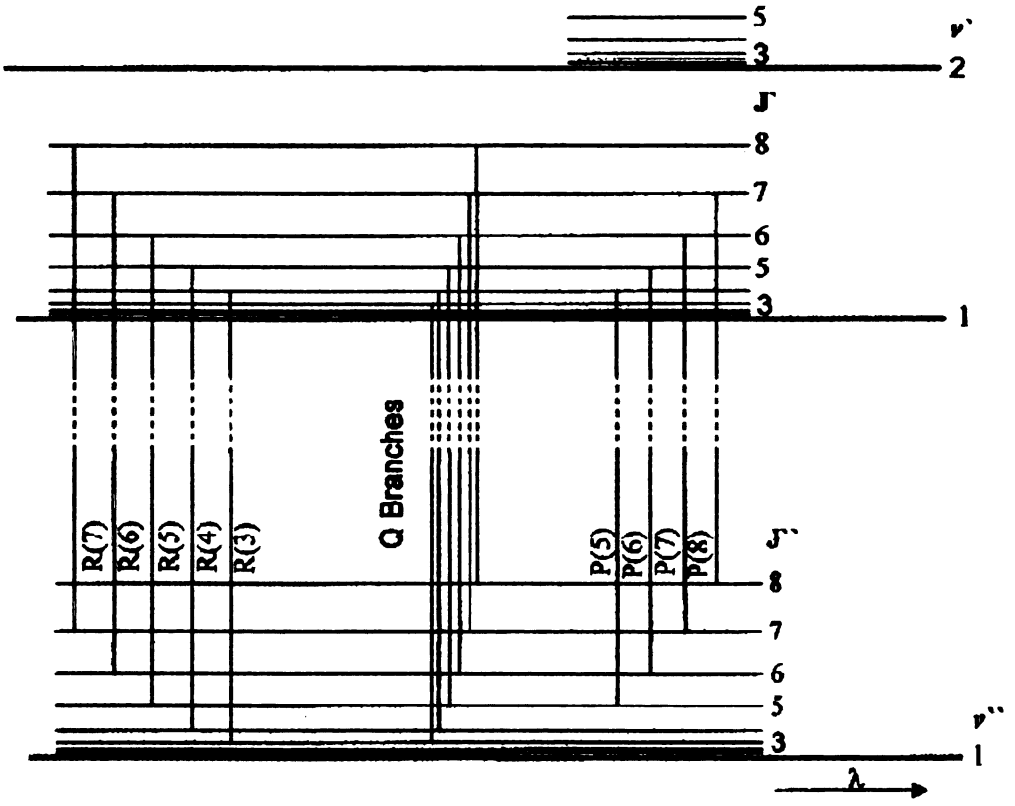

Figure 7.3 - The vibrational (J) and rotational (v) energy level transitions including the relative to wavelength (λ), P, Q, and R branches [145].

The Honl-London factor indicates the line strength of rotational spectra which is dependent on J. For R branch, the Honl-London factor can be defined as:

$$S = \frac{(J'+\Lambda'+1)(J'-\Lambda'+1)}{J'+1} \qquad (7.6)$$

Since $\Lambda\Lambda = 0$, the equation 7.6 can be simplified to S=J+1.

The experimental data is fitted to the equation 7.5 using several R branch emission lines to determine the rotational temperature, T_r. The plot of natural log of (I/S) is a linear function of the upper rotational energy for the diatomic molecules employed in this research. Table 7.1 shows some values of the rotational lines from spectrum wavelength of 3758-3780 Angstrom with its corresponding relative upper level energy and Honl-London factor.

Table 7.1 - Nitrogen rotational lines, wavelength, relative upper energy, and Honl-London factor for the linear temperature fit calculation of R branch (2, 0) second positive band.

Rotational line	Wavelength (Angstrom)	Rel. upper level energy (cm-1)	Honl-London factor
R20	3780.44	837.76	19.80
R21	3778.58	917.42	20.81
R22	3776.66	1000.67	21.82
R23	3774.68	1087.51	22.83
R24	3772.64	1177.95	23.83
R25	3770.53	1271.97	24.84
R26	3768.37	1369.57	25.85
R27	3763.14	1470.76	26.85
R28	3763.86	1575.51	27.86
R29	3761.51	1683.84	28.86
R30	3759.11	1795.74	29.87

Figure 7.4 shows an example of Boltzmann plot for the nitrogen rotational temperature calculations. This plot is obtained from experimental set of data using combustion plasma flame with flow rates of 70/110 CH_4/O_2 with microwave input power of 50 Watts without injecting nitrogen into the gas mixture. The nitrogen molecule was excited from the ambient air around the flame. The margin of error of the rotational temperature using this linear fit is within 100 K based on the reproducibility of the data collected.

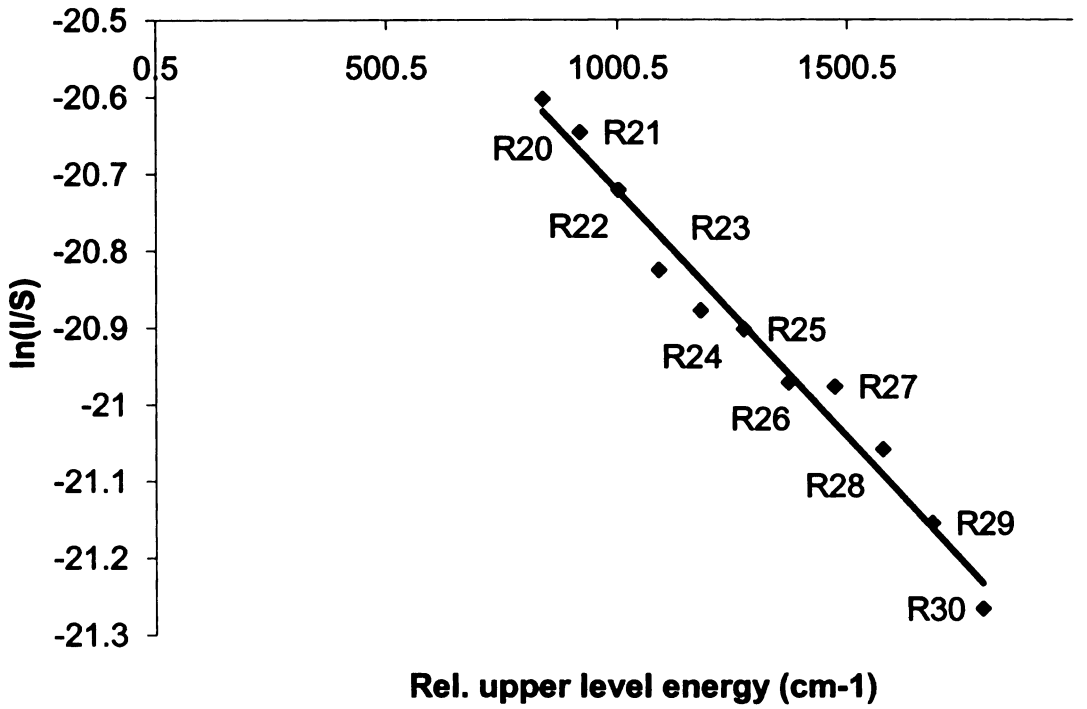

Figure 7.4 - Boltzmann plot for the lines of R20-R30 for nitrogen spectrum.

The Second Positive System (SPS) nitrogen emission band spectrum was used to determine the rotational temperature. The nitrogen rotational temperature reflects the plasma flame gas temperature. The SPS describes the energy level transition from $C^3\pi_u$ to $B^3\pi_g$. The strongest signal intensity detected by the spectrometer was the (2, 0) band-head vibrational transition as shown in Figure 7.5.

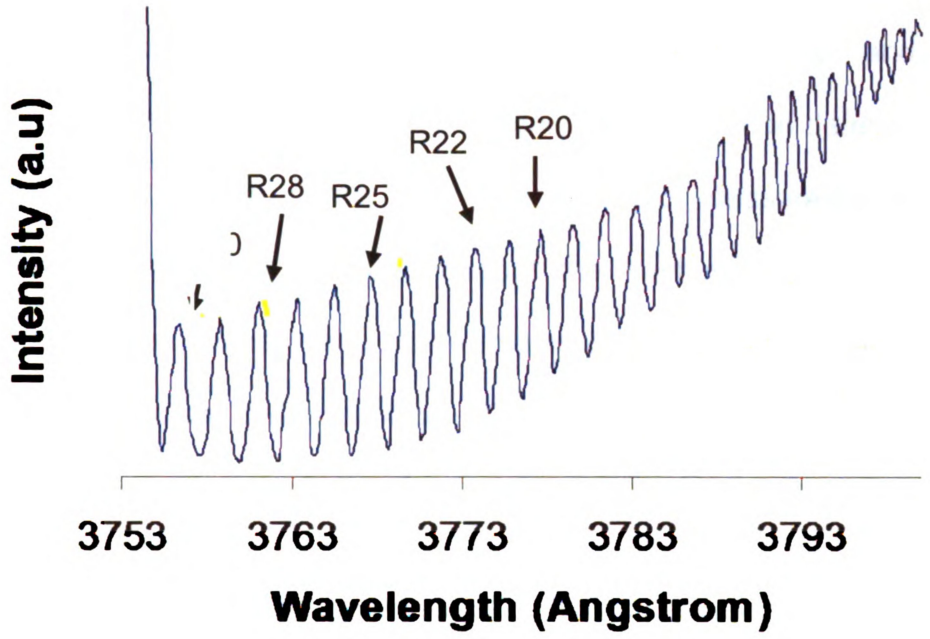

Figure 7.5 - The R-branches of the nitrogen 2nd positive system (2, 0) used for plasma gas temperature measurement.

7.4 CH gas temperature calculation procedure

Spectroscopic optical diagnostics on spectra intensity and gas temperature were performed. The CH radical species was used to determine the temperature of the plasma flame. The spectroscopic measurements were conducted across a line of sight passing through the reaction zone i.e., near the cone region on the centerline of the plasma flame in a core part of the flame a few mm above the nozzle orifice surface. The rotational temperature of CH in the plasma flame was measured at various microwave power levels and different equivalence ratios.

Similar to the N_2 calculation procedure, using the relative intensity of the rotational lines associated with the system I, $A^2\Delta \longrightarrow X^2\Pi$ (0, 0) pure rotational electronic transitions, the chemiluminescene, located near 4300 Angstrom, from the excited CH molecules as a major source of visible light from hydrocarbon flames. The rotational energy distribution of CH molecules in this electronic state can be represented by Boltzmann distribution since the rotational temperature is in equilibrium with the translational temperature [40]. The scan of the three rotational branches of CH for CH_4/O_2 combustion flame at atmospheric pressure is shown in Figure 7.6. The Boltzmann plot for CH line intensity data of ln (I/S) versus E_j/kT respectively. The gradient of the best fit line yields the rotational temperature of the plasma flame is displayed in Figure 7.7.

The intensity (I) of the spectral emission line is given by:

$$I = C\, S_{j'j''}\, \lambda^{-4} \exp(-E_{j'}/kT) \qquad (7.8)$$

where C is a proportionality constant, $S_{j'j''}$ is the Honl-London factor, λ is the transition wavelength, $E_{j'}$ is the energy of the upper rotational state of the transition, k is the Boltzmann's constant, T is the rotational temperature. The j' and j" relate to the upper (j'=n'± ½) and lower state (j"=n" ± ½) with total angular momentum quantum number n', electron spin quantum number ± ½. Applying Boltzmann plot and natural logarithm of weighted intensities:

$$\ln(I\, \lambda^4 / S_{j'j''}) = -(E_{j'}/kT) + \ln C \text{ versus } E_{j'}/kT \qquad (7.9)$$

give a straight line and the slope of the line is the inverse of the temperature.

Displayed in Table 7.2 is the values of some of the rotational line (n"), spectrum wavelength (λ), Honl-London factor ($S_{j'j''}$), and the associated energy rotational energy (E'_{rot}).

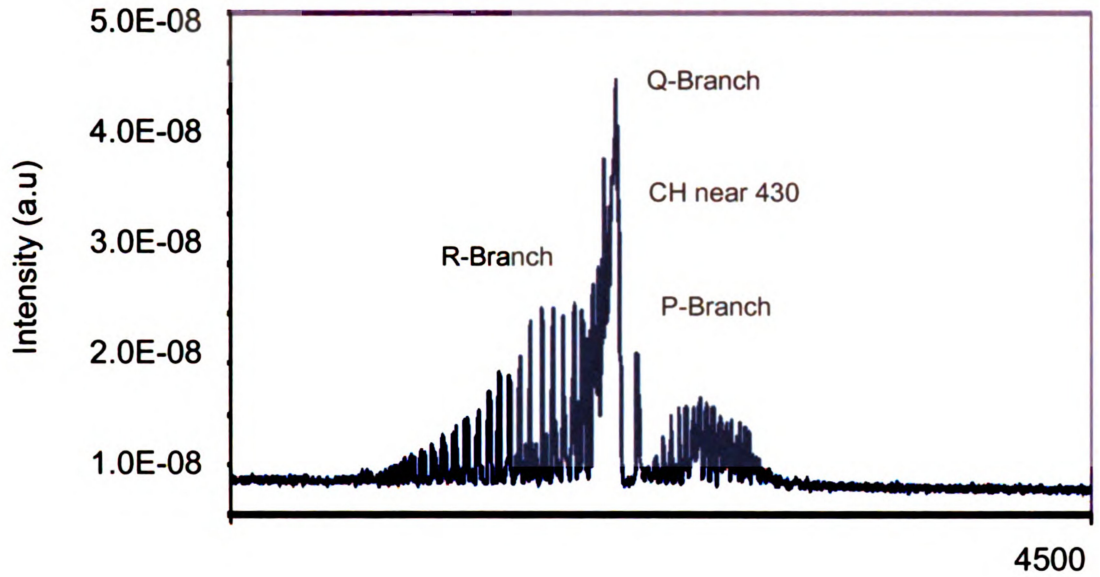

Figure 7.6 - A resolved scan of the three rotational branches of CH for CH_4/O_2 combustion flame at atmospheric pressure.

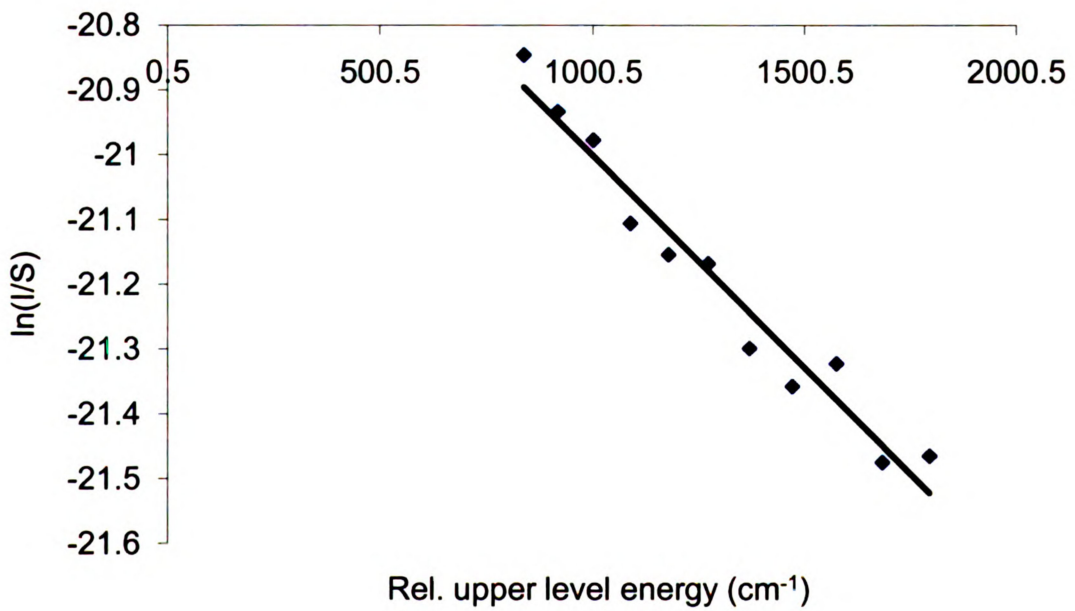

Figure 7.7 - Boltzmann plot for CH line intensity data of ln (I/S) versus E_j/kT respectively. The gradient of the best fit line yields the rotational temperature of the plasma flame.

Table 7.2 - Wavelength, Honl-London factors, and rotational term energies for the R branch transitions of $A^2\Delta \longrightarrow X^2\Pi$ (0, 0) system I of CH band.

Values for R_2 (N") Transitions			
Rotational line n"	**Wavelength λ (Å)**	**Honl-London factor $S_{J'J"}$**	**Upper rotational energy E'_{rot} (cm^{-1})**
11	4242.46	7.234	1831.00
12	4236.12	7.736	2161.34
13	4229.77	8.238	2517.39
14	4223.49	8.739	2898.75
15	4217.21	9.240	3304.91
16	4210.97	9.741	3735.43
17	4204.75	10.240	4189.66
18	4198.64	10.740	4667.28
19	4192.56	11.240	5167.50
20	4186.62	11.740	5690.00

CHAPTER 8

MICROWAVE PLASMA ASSISTED COMBUSTION

APPLICATOR #1: HYBRID CAVITY PLASMA FLAME BURNER

8.1 Introduction

This chapter describes the first applicator i.e., hybrid cavity plasma flame burner which was utilized for the microwave plasma assisted combustion study. It is the first attempt to couple microwave energy into a combustion flame at open air atmospheric pressure. The investigation results have been published in Applied Physics Letters, 89, 141501 (2006).

8.2 Description of applicator #1

The microwave plasma flame cavity burner system consists of two separate applicators i.e., cylindrical cavity applicator and coaxial plasma torch applicator. It is a hybrid system where the miniature coaxial plasma torch is inserted into the end of a length tunable, single mode, 17.8 cm diameter cylindrical microwave cavity applicator [147-154]. The photographs of the two different applicators are shown in Figure 8.1 (a) and (b). The miniature coaxial microwave cavity plasma torch has been patented under United States Patent # 7,442,271 [155].

The cross section of the microwave plasma torch is shown in figure 8.2. It consists of a coaxial structure applicator with center and outer conductor diameters of 4.75 mm and 11.1 mm, respectively. The overall applicator diameter is 12.5 mm. Two pieces of center conductor were built with different sizes of nozzle orifices. The working gas can flow through a nozzle hole of 0.23 mm or 0.40 mm in diameter located at the end of the center conductor. The axial position of the center conductor is adjustable. The microwave input power enters the torch from the side via an N-type coaxial connector. The tapered section from the input connector to the center conductor shown in figure 8.1 (a) is designed to have an impedance of 50-ohms. Between the inner conductor and the outer conductor away from the nozzle, a moveable tuning short is placed in order to provide matched load impedance within the structure. A circular microwave coupling structure, which consists of finger stock and a brass tube, allows the inner conductor to slide and provide electromagnetic contact into the system. The

center conductor is water-cooled in order to prevent over heating of the nozzle tip during the experiments. The water flows in through a 1.6 mm brass tube inside the 4.75 mm center conductor and flows out at the right end of the center conductor.

The cross section of the hybrid system is shown in Figure 8.3. As shown in the figure, input feed gases flow through a small tube that is located coaxially inside the center conductor and exit into the cavity applicator by passing through a 0.4 mm diameter orifice located at the end of the center conductor. The axial position of the center conductor is adjustable and can be inserted into the cylindrical microwave cavity applicator. When the center conductor is inserted the appropriate depth into the cavity applicator, the cylindrical cavity electromagnetic modes can be efficiently excited. Therefore as the microwave cavity applicator sliding short is tuned to the appropriate length, i.e. approximately 14.2 cm, the cavity applicator electric fields assume the TM_{012} mode field patterns as shown in Figure 8.3. The electric fields at the output end of the miniature torch applicator change from a radial coaxial transverse electromagnetic (TEM) waveguide electric field inside the coaxial section into a high intensity, nearly axial electric field at the end of the center conductor. Thus with the application of microwave power and the appropriate tuning the miniature torch applicator electric field couples directly to the TM_{012} cavity mode fields and creates an atmospheric microwave discharge at the end of the center conductor. A window that is located in the seven inch cylindrical microwave cavity applicator side wall allows

visual and photographic observation as well as spectrographic diagnostic measurements.

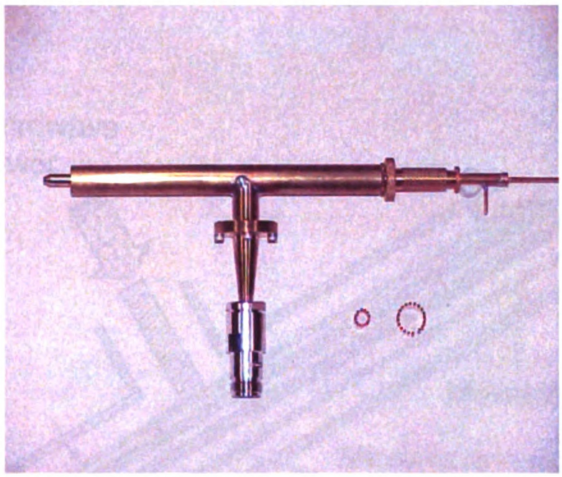

(a)

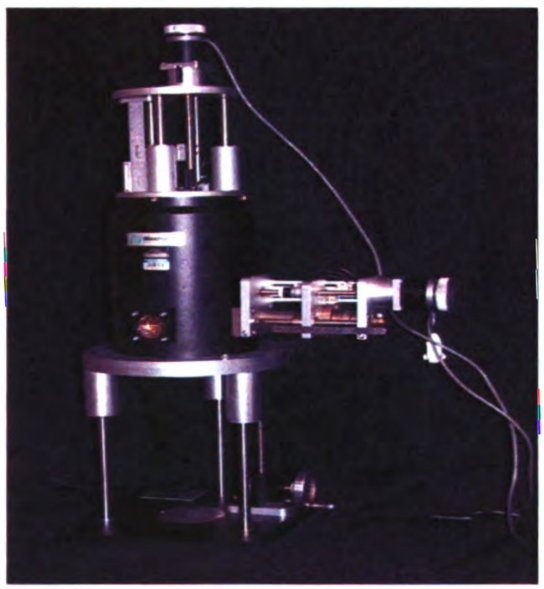

(b)

Figure 8.1 - photographs of (a) coaxial plasma torch and (b) cylindrical cavity applicators.

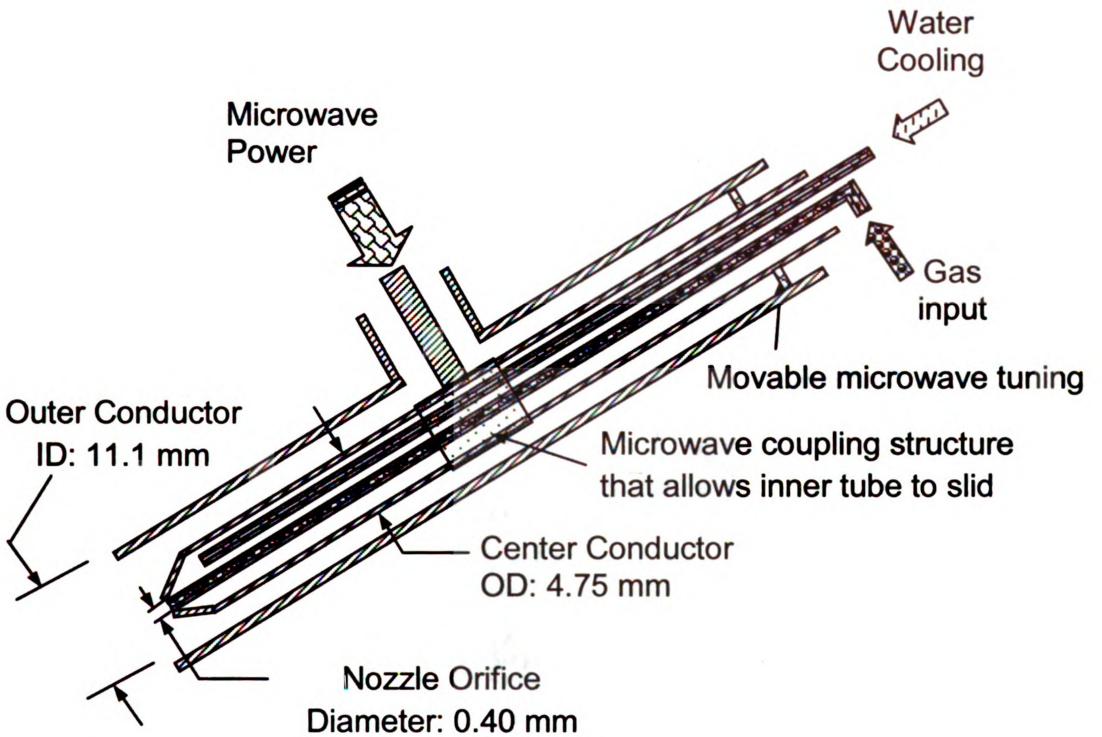

Figure 8.2 - Cross section of the microwave coaxial plasma torch applicator.

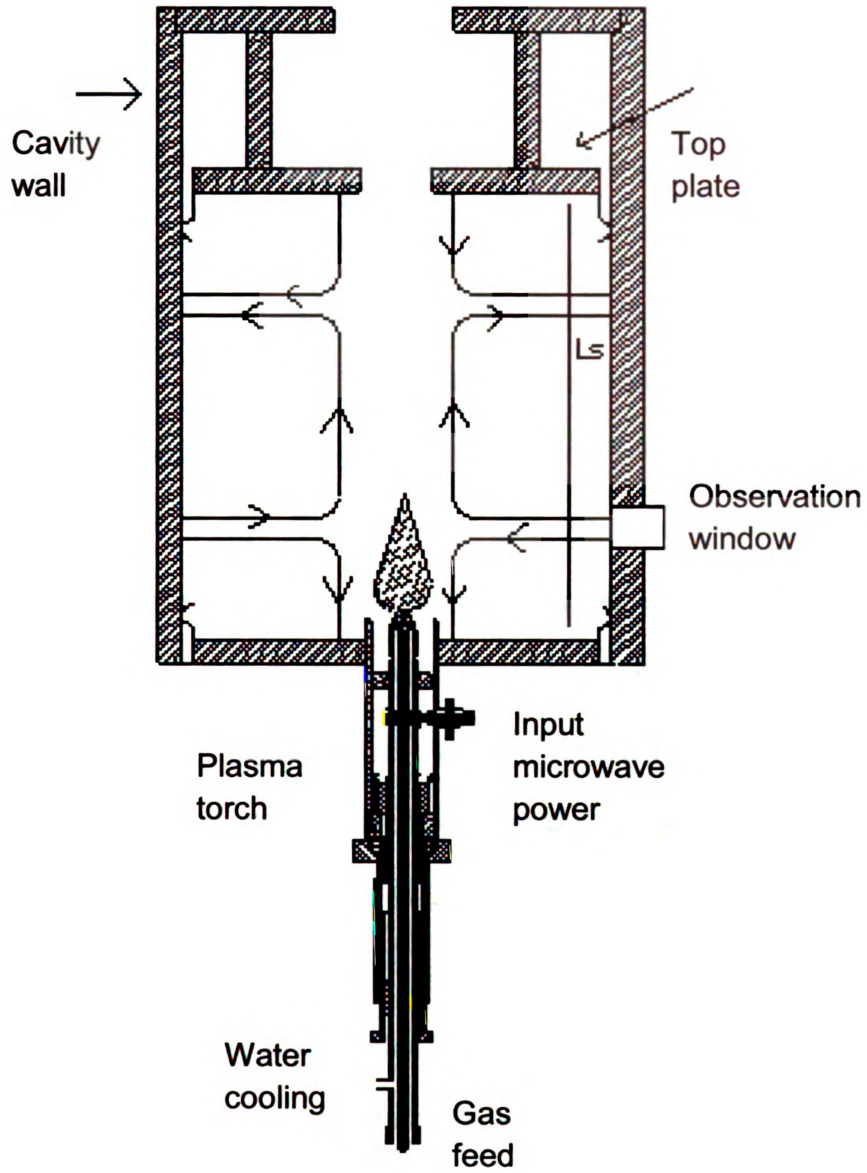

Figure 8.3 - Cross section of the hybrid microwave cavity plasma flame burner.

8.3 Experimental results

8.3.1 Influence of microwave coupling on the flame

The miniature plasma torch and microwave cavity applicator system can operate with a wide variety of input gases at atmospheric pressure: (1) as a miniature plasma torch, (2) as a combustion flame, and (3) as hybrid microwave excited combustion flame. The photographs of the applicator excited with combustion flame, plasma discharge and combination of both combustion flame and plasma discharge are displayed on Figure 8.4 (a)-(d). The combustion flame as shown in Figure 8.4 (a) was ignited using a butane lighter on the premixed gas. When the miniature plasma torch was placed inside the cylindrical cavity as shown in Figure 8.4 (c), the cavity height was set to 14.2 cm which excite the TM_{012} mode, and then microwave power was applied to the combustion flame. This resulted in a hybrid plasma flame discharge which is displayed in Figure 8.4 (d). While the miniature plasma torch was capable of operating at atmospheric pressure without being connected to the microwave cavity applicator, the addition of the microwave cavity applicator to the system efficiently focuses/matches the microwave energy. Furthermore, by utilizing the microwave cavity applicator with its length tuning capability, it improved the coupling efficiency of microwave energy into the flame. When the miniature plasma torch and microwave cavity applicator was operated in this hybrid mode, a triangular cone-shaped discharge can be formed with several watts of absorbed power. The discharge size was less than 1 mm base diameter and typically 2-4 mm in length.

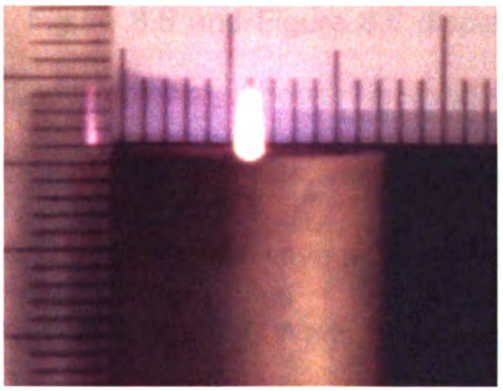

(a) plasma only mode

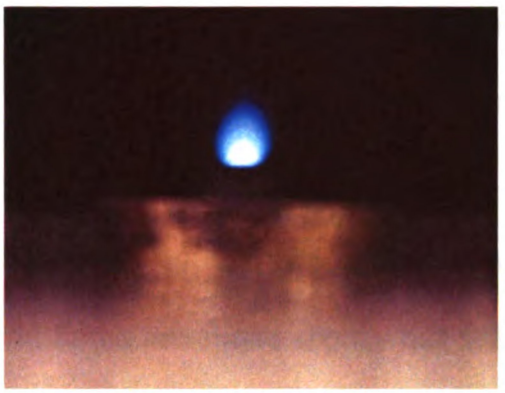

(b) combustion only mode

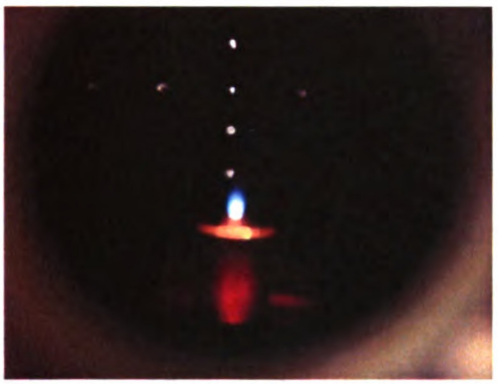

(c) combustion only mode

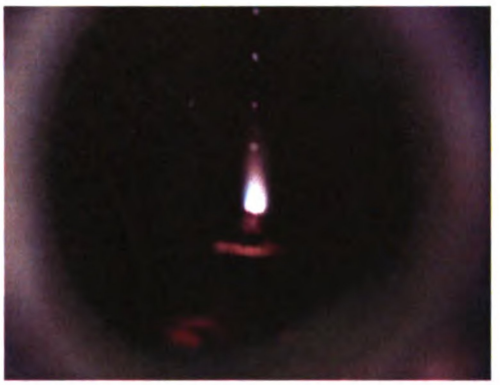

(d) plasma flame hybrid mode

Figure 8.4 - Photographs of microwave plasma torch at various modes. (a) plasma only mode outside cylindrical cavity, microwave power: 20 W, argon flow rate: 200 sccm (b) combustion only mode outside cylindrical cavity, flow rate CH_4/O_2: 45/90 sccm (c) combustion only mode, plasma torch placed inside cylindrical cavity, flow rate: CH_4/O_2 25/50 sccm (d) plasma flame discharge hybrid mode, microwave power 20 W, flow rate: CH_4/O_2 25/50 sccm.

Figure 8.5 and Figure 8.6 display the visual images of the flame as the absorbed microwave power is gradually increased from 1-100 Watts. The CH_4/O_2 input gas flow rate was held constant at 24/70 sccm and at 70/153 sccm. As the absorbed microwave power increases the flame appearance changes. In the P_p < 10 Watts - 30 Watts ranges the hybrid flame increases slightly but still resembles a premixed combustion flame. An abrupt change in visual size occurs as the absorbed power increases from 30 to 40 Watts. As power is further increased over the P_p > 40 Watts range, the visual image size grows and brightens. At the very highest absorbed powers the visual image appears to be microwave energy dominated.

Shown in Figure 8.7 are the visual images of the plasma flame when the absorbed microwave power was increased from 30 to 40 Watts and decreased from 40 to 30 Watts. The jump or transition in intensity of the plasma flame was observed between 35 to 38 Watts. As the microwave power increases, the sudden jump in flame volume occurs at 38 Watts, however when the microwave decreases, the transformation does not occur until 35 Watts. The discharge exhibits hysteresis in this power range (35-38 Watts). Above this power range, the microwave power starts to dominate the combustion flame that resulted in the increase of plasma flame discharge intensity and volume.

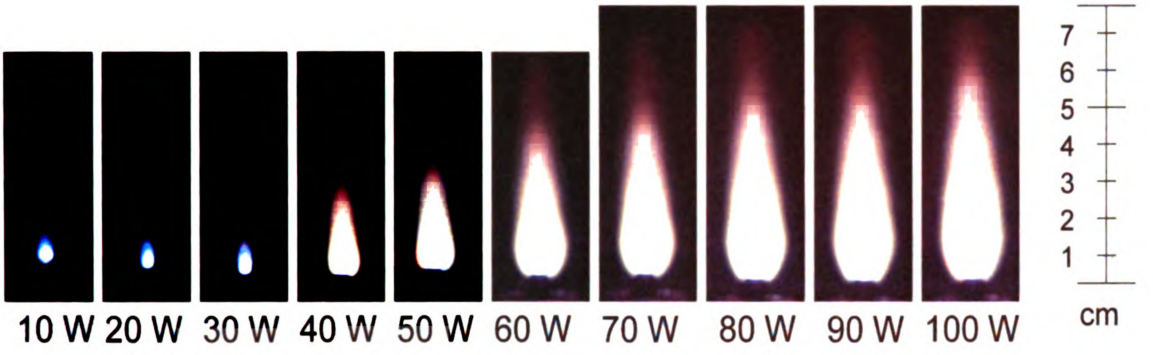

Figure 8.5 - Visual images versus increasing absorbed microwave power with flow rate of 24 sccm of CH_4 and 70 sccm of O_2.

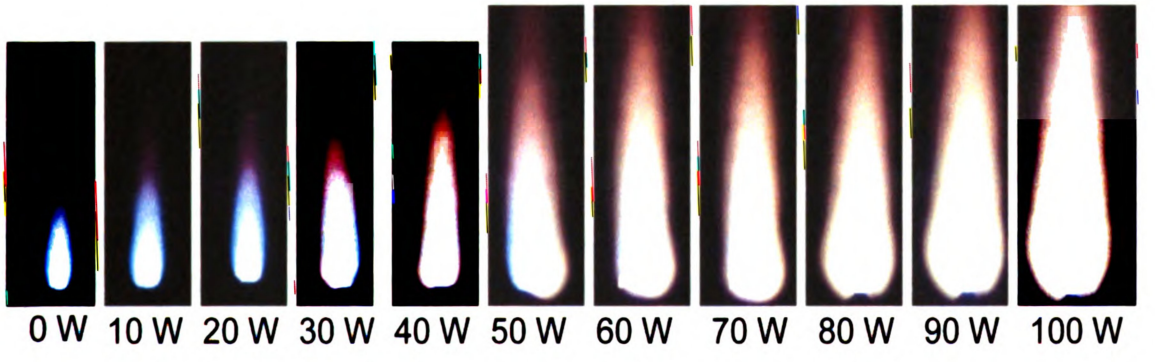

Figure 8.6 - Visual images versus increasing absorbed microwave power with flow rate of 70 sccm of CH_4 and 153 sccm of O_2.

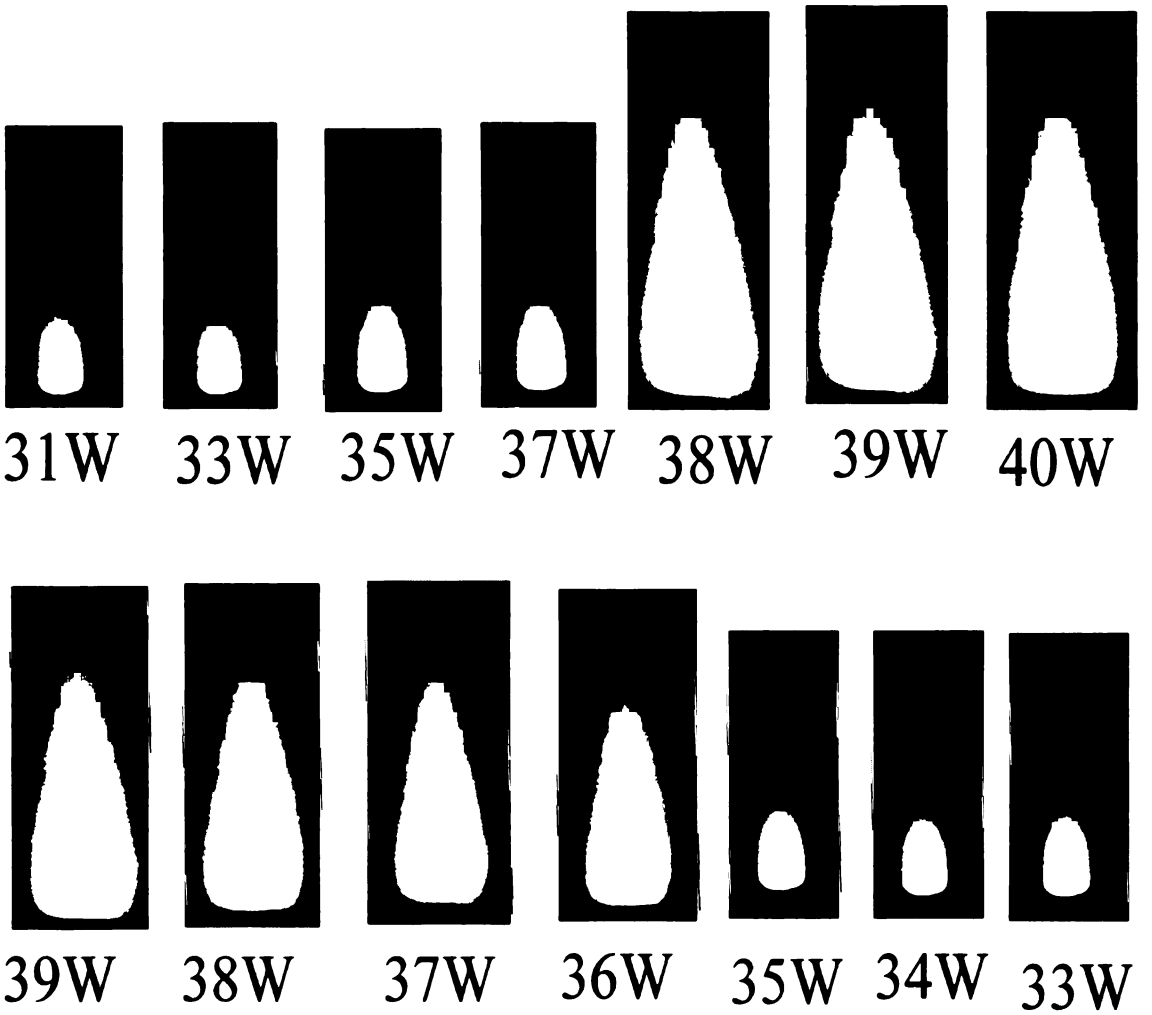

Figure 8.7 - Visual images with increasing and decreasing absorbed microwave power with flow rate of 24 sccm of CH_4 and 70 sccm of O_2.

Figure 8.8 examines the hybrid flame/discharge power density for two input gas flow rates and stoichiometries versus $\overline{P}$ where $\overline{P} = P_p/(P_p + P_c)$, P_c is the combustion power, and $(P_p + P_c)$ is the total input power. The combustion power is approximated using the higher heating value (HHV) tabulated in text [156] for gaseous methane based on stoichiometric combustion with air, a value of 55, 528 kJ/kg, and a CH_4 density of .68 kg/m^3. Power density is calculated by dividing the total power by the photographically measured hybrid flame volume. The hybrid flame photographs were taken using a Nikon XLR digital camera adjusted to a 4.5 aperture and a 1/30s shutter speed. The white central core regions shown in Figure 8.5-8.6 are the volumes used for the power density calculations. The two curves in Figure 8.8-8.9 indicate that in the low power regime (0 - 30 Watts) the power density increases 2-3 times as the input microwave power increases. As the input power is increased beyond 40 Watts ($\overline{P}$ = 0.7 for the 70/24 sccm case, $\overline{P}$ = 0.42 for the 153/65 sccm O_2/CH_4 case) the power density abruptly decreases and the discharge/flame volume simultaneously increases. The power density behavior in the high input power regime is similar and even less than the power density of the flame with zero input microwave power. The large increase in flame/discharge power density in the low power regime suggests that the electric field impressed on the flame is substantial and is increasing as input microwave power increases until the dramatic jump in flame/discharge size occurs. In the high input power regime a twofold increase in total power decreases the power density by five. In both regimes the coupled microwave energy clearly has an impact on the hybrid

flame/discharge. The flame heights versus total input power for two different fuel mixture ratio. As expected, the height or length of the flame increases as more input power was applied into the combustion flame.

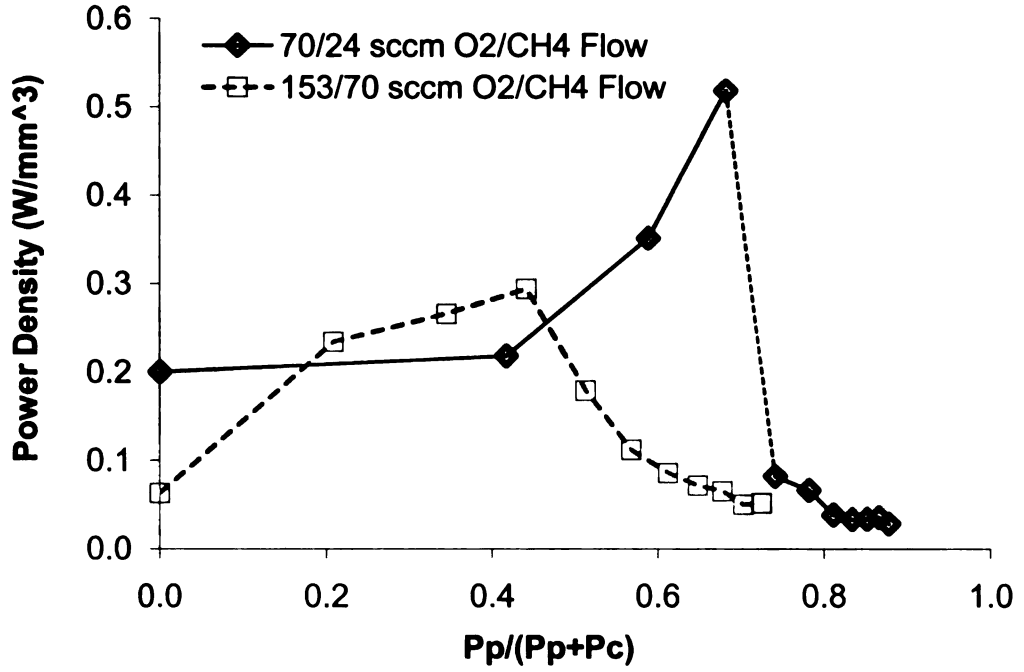

Figure 8.8 - Flame/discharge power densities versus the input microwave power to total power.

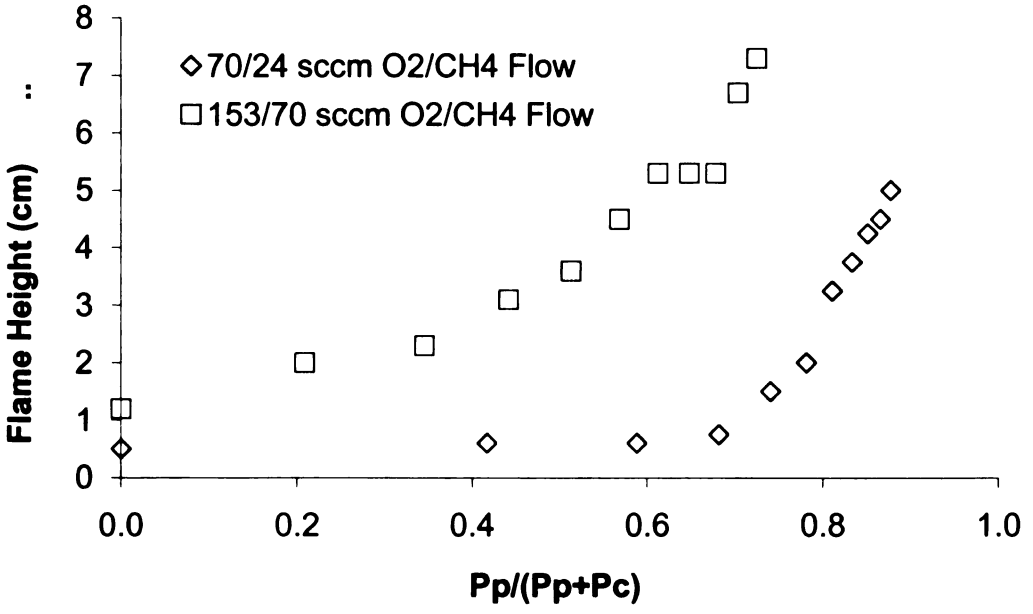

Figure 8.9 - Flame/discharge heights versus the input microwave power to total power.

8.3.2 Flammability limits

Preliminary measurements have investigated the extension of the hybrid flame/discharge to leaner operating conditions. Figure 8.10 shows the extinction plot. The equivalence ratio (ER) is defined as the ratio of fuel/oxidizer of the experiment divided by the fuel/oxidizer for stoichiometric burning of CH_4/O_2. The addition of just 10 W of microwave power to the combustion is seen to extend the equivalency ratio by 5-12%. The numbers next to the data points in Figure 8.10 for the combustion-only and 10 W curves are the power values from the CH_4/O_2 combustion power (excluding any added microwave power). The addition of 20 W or more of microwave power allows the operation at all lean burning conditions up to the point of no fuel, i.e. ER=0.

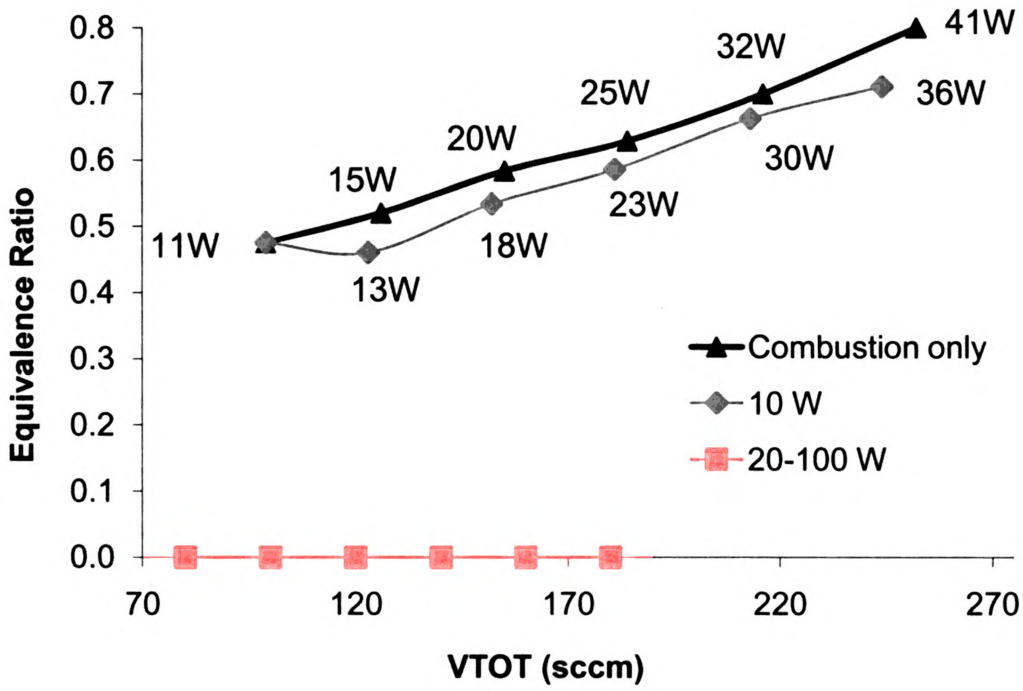

Figure 8.10 - Flame extinction curves for combustion flames with 0, 3, 5, 6 Watts additional of microwave power. The corresponding combustion power is displayed for each data point.

8.3.3 Radical species and gas temperature

Shown in Figure 8.11 is the optical emission spectroscopy spectra scan of combustion flame only and hybrid plasma flame at visible wavelength from 2750 to 6250 Angstrom. As can be seen from the figure, the intensity of the hybrid plasma flame with 40 Watts addition of microwave power increases dramatically particularly for the CH molecule. Other major species that were produced in the plasma flame discharge are OH, O_2, N_2, C_2, and H_2. The corresponding wavelengths are shown in the figure. This observation suggests that the coupling of microwave energy into the combustion flame greatly enhanced and altered the combustion process.

Figure 8.12 shows an emission spectroscopy spectra scan for N_2 of the combustion plasma hybrid flame at various microwave power from 10 Watts to 80 Watts. As the microwave input power was increased at 10 Watts interval, the intensity of nitrogen line increases. Figure 8.13 shows emission spectroscopy spectra scan for C_2 of the combustion plasma hybrid flame at various microwave power from 0 Watts to 100 Watts. As can be seen, the addition of microwave power increases the radical species intensity which indicated the increase of flame gas temperature.

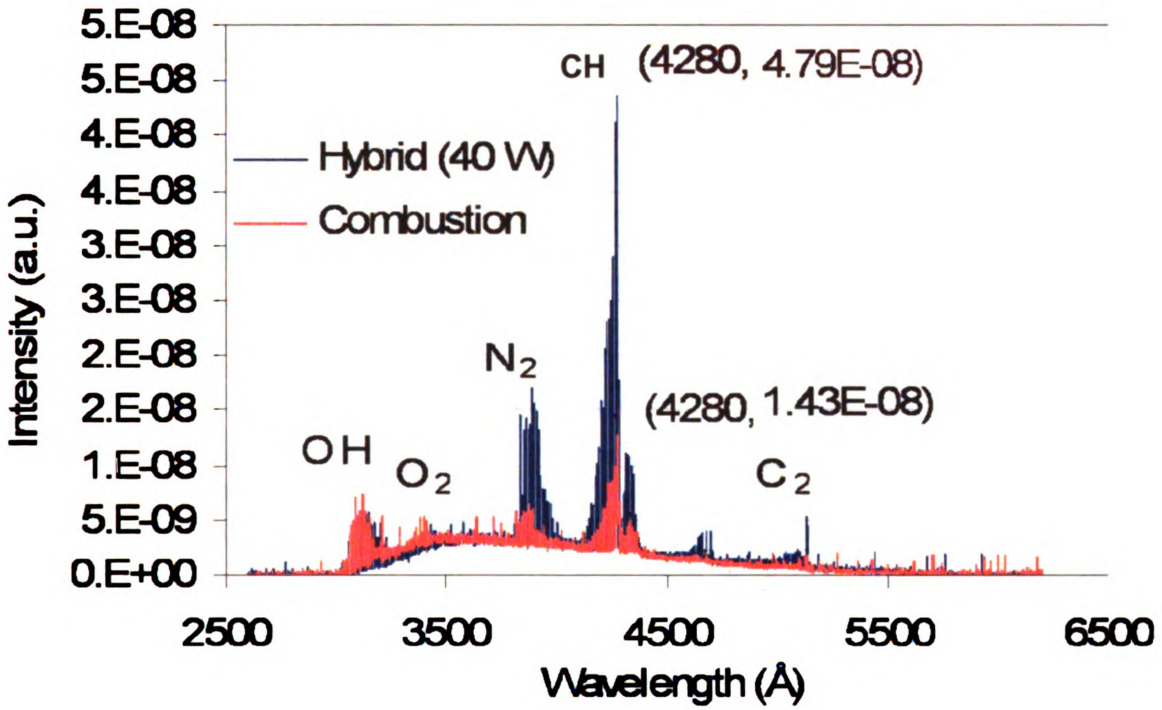

Figure 8.11 - Optical emission spectroscopy spectra scan of combustion flame only and hybrid plasma flame with 40 Watts of absorbed microwave power.

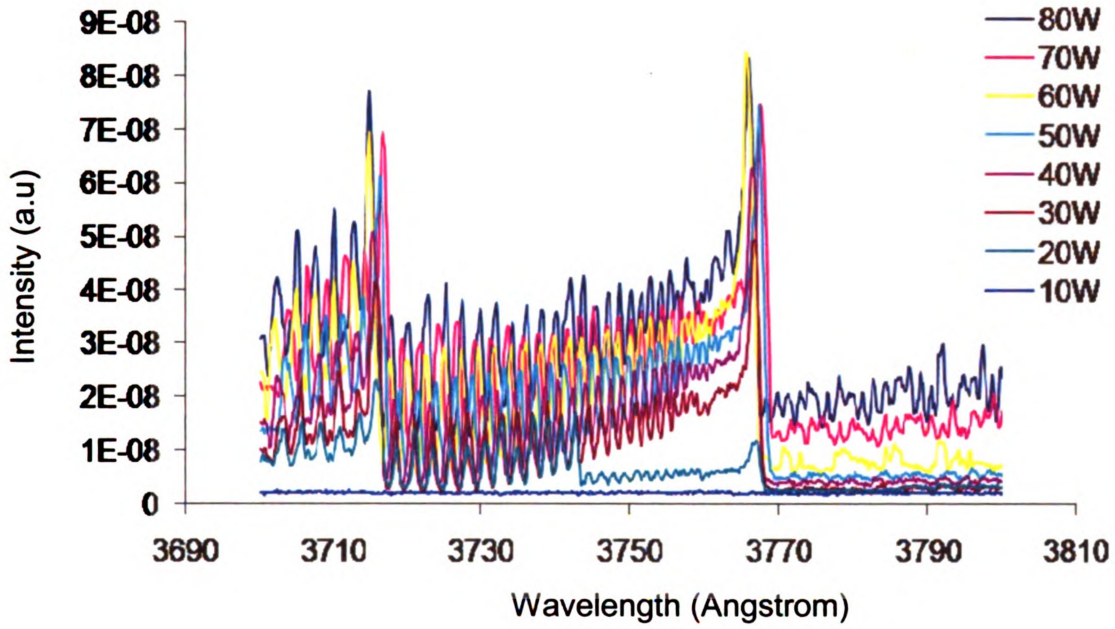

Figure 8.12 - Emission spectroscopy spectra scan for N_2 of the combustion plasma hybrid flame at various microwave power from 10 Watts to 80 Watts.

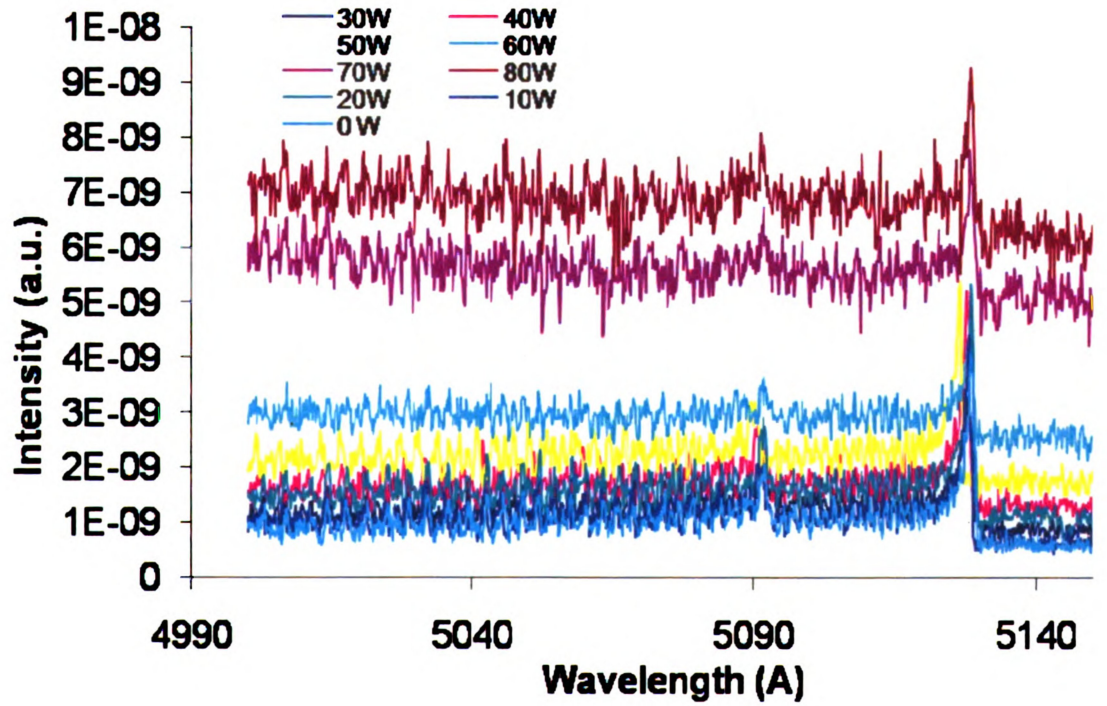

Figure 8.13 - Emission spectroscopy spectra scan for C_2 of the combustion plasma hybrid flame at various microwave power from 0 Watts to 100 Watts.

Figure 8.14 shows rotational temperature of the plasma flame discharge under stoichiometric fuel mixture ratio at various flow rates. The temperature ranges from 2200 K to 3600 K. The flame rotational temperature using nitrogen agrees well within the range of the theoretical flame temperature. Typical oxygen/methane flame adiabatic temperature reported is around 3000 K [157] while the measured flame temperature using a thermocouple is at around 2253 K [158]. Figure 8.15 displays rotational temperature under fuel rich, fuel lean and stoichiometric fuel mixture ratios at a fixed flow rate. The gas temperature increases as the microwave power is added into the combustion flame. The rotational temperature ranges from 1950 K to 3700 K depending on the gas flow rate and input microwave power. Given the same amount of input power applied into the flame, there is a little variation in temperature range. This range could probably due to some variation of the experimental set up or tuning position of the plasma torch within the "sweet spot" inside the cylindrical cavity. Moreover, as the plasma flame volume increases, more heat loss could result in temperature drops. However, regardless of the fuel mixture ratio or total flow rates, the flame gas temperature increases with addition of microwave power.

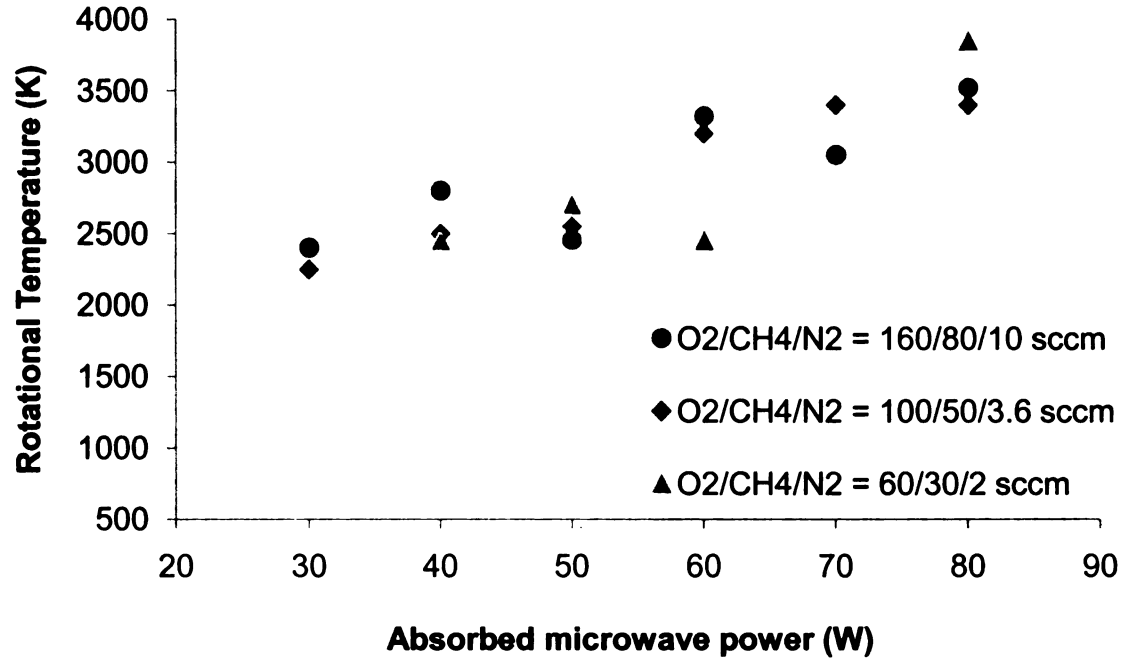

Figure 8.14 - Rotational temperature at constant fuel mixture with varying total flow rate.

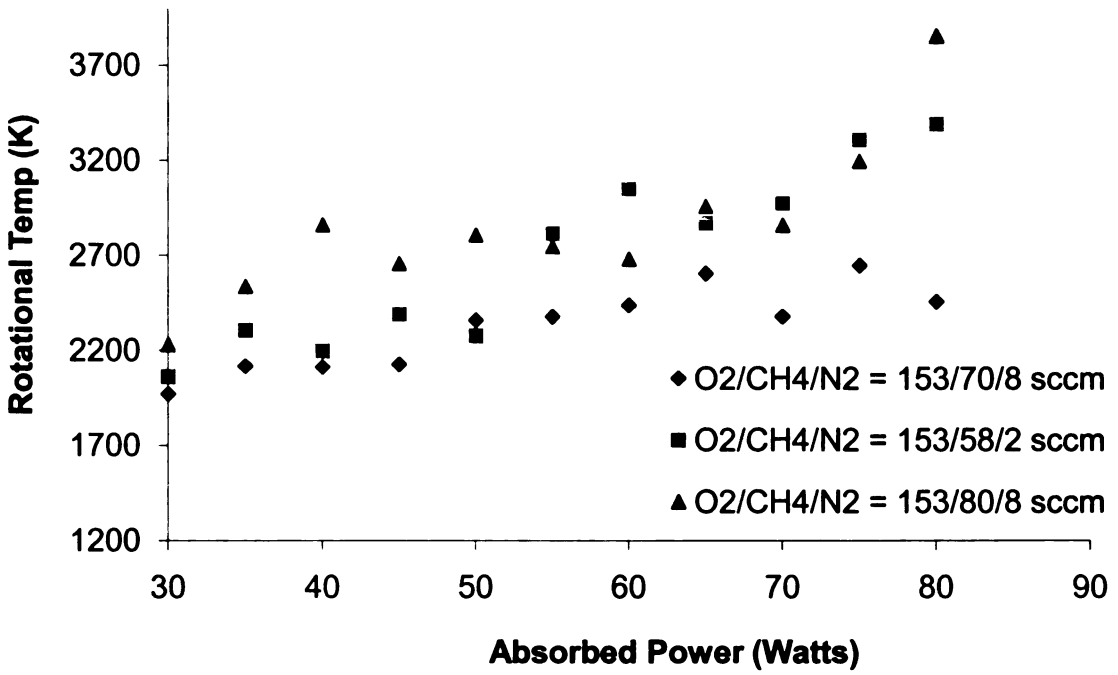

Figure 8.15 - Rotational temperature at varying fuel mixture (fuel rich, fuel lean and stoichiometric) flow rates.

8.4 Summary

An experimental test bed which consists of cylindrical microwave cavity applicator and miniature plasma torch was developed. This system enables the controllable coupling of microwave energy into a flame and the steady-state low and high power coupling of microwave energy into a combustion flame. As the input microwave power was increased from a few watts to approximately 30 Watts the impressed electric field and the flame/discharge power density increased dramatically. Between impressed powers of 30 to 40 Watts the hybrid flame/discharge abruptly jumped in size and the power density decreased. At the highest microwave input power levels of 50-100 Watts the flame/discharge appeared to be discharge dominated. The generation of a hybrid plasma flame with 10 to 30 Watts of input microwave power resulted in the increase of plasma flame discharge stability.

CHAPTER 9

MICROWAVE PLASMA ASSISTED COMBUSTION

APPLICATOR #2: RE-ENTRANT CAVITY PLASMA FLAME BURNER

9.1 Introduction

This chapter presents the second applicator i.e., re-entrant cavity plasma flame burner which was utilized for the microwave plasma assisted combustion. The first applicator described in chapter 8 demonstrated that microwave energy could be efficiently coupled into a combustion flame that was placed inside a tunable microwave cavity. However this microwave applicator system was physically large and therefore additional improvements were desirable such as a reduction in the applicator size and a higher microwave coupling efficiency. In this chapter, an improved experimental microwave plasma-assisted combustion apparatus, which employs a more efficient and more compact microwave applicator that positions the flame in a region of high microwave electric field strength, is presented. The investigation results have been published in the Review of Scientific Instruments, 80, 053507 (2009).

9.2 Description of applicator #2

The re-entrant cavity applicator employed in this investigation is a compact coaxial re-entrant one inch cavity with an inner conductor that has a nozzle orifice similar used in the miniature torch burner [159-160].

Figure 9.1 (a) displays the microwave re-entrant cavity applicator placed adjacent to a one-inch diameter silicon wafer and Figure 9.1 (b) shows the microwave applicator exciting a combustion flame. The cylindrical applicator has a 3.5 cm diameter and length of 12 cm. As shown in Figure 9.1 (b) the microwave excited flame extends through a circular hole at the end of the applicator. Thus, the flame reaction zone can be observed outside of the applicator. Microwave coupling occurs in a variable gap, L_g, located at the open end of the applicator.

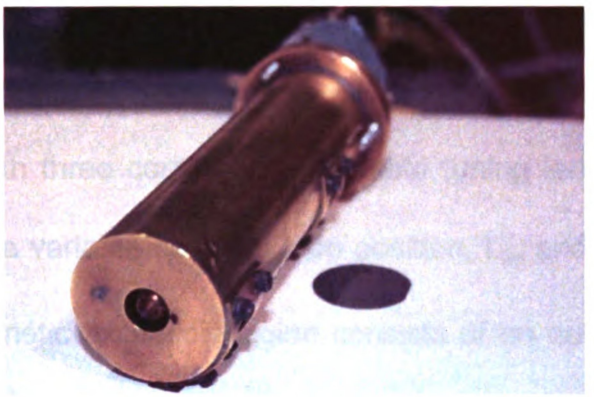

(a)

(b)

Figure 9.1 - Photographs of the microwave re-entrant cavity applicator. Figure 9.1 (a) displays the overall microwave re-entrant cavity applicator adjacent to a one-inch silicon wafer. Figure 9.1 (b) shows the microwave applicator exciting a premixed flame.

Figure 9.2 displays a cross-sectional view of the cylindrical cavity applicator. The applicator is a short-gap, re-entrant, brass cavity excited in the TEM mode [135] with three continuously variable tuning lengths: (1) a variable short length, L_s; (2) a variable coupling loop position, L_p; and (3) a variable gap, L_g. The electromagnetic excitation region consists of an outer cylinder (4) with an 3.2 cm inside diameter, a 1.2 cm outside diameter, inner coaxial, cylindrical center tube (5), a length adjustable sliding short (6), and an endplate (7) that is soldered to the outer cylinder (4). These cylindrical brass conducting pieces (4-7) form a continuous, adjustable conducting path within the excitation region. Thus, the cavity applicator is a variable length coaxial transmission line that is short circuited at one end. In the absence of a flame it has a capacitive gap at the other end.

Microwave energy is coupled into the cavity via a micro coaxial cable (8), which is terminated with a coupling loop (9). The input coupling cable (8) and loop (9) can be adjusted for optimal coupling by varying the position, L_p (2) and its orientation (phi, ϕ). A brass nozzle plug (10) is inserted into the end of the center conductor (5). The brass nozzle has top circular surface of 4.8 mm in diameter with a tapered section 0.7 cm in length extending from the top surface to the opening of the center conductor (5). The brass nozzle is press fitted into the inner conductor (5). The gap length, L_g (3), can be varied by $\pm$ 5 mm above and below the x = 0 reference plane shown in Figure 9.2 by varying the independently adjustable center conductor (5). Input feed gases flow through a brass tube (11) located inside the inner conductor (12), which is coaxially placed

inside the center conductor (5). Combustion gases, oxygen and methane, exit through a 0.4 mm diameter orifice (13) into the cavity capacitive gap region. A Teflon spacer (14) is placed between the center conductor (5) and inner brass tube (12) to provide support for the gas feed and water cooling systems. The brass tube (12) is water cooled in order to prevent the plug (10) from overheating during microwave energy interaction with the flame. The premixed flame (15) and its inner cone (16) are located at the end of the nozzle. A one cm diameter circular hole (17) at the end plate enables the gases and the flame to exhaust and extend out of the cavity applicator.

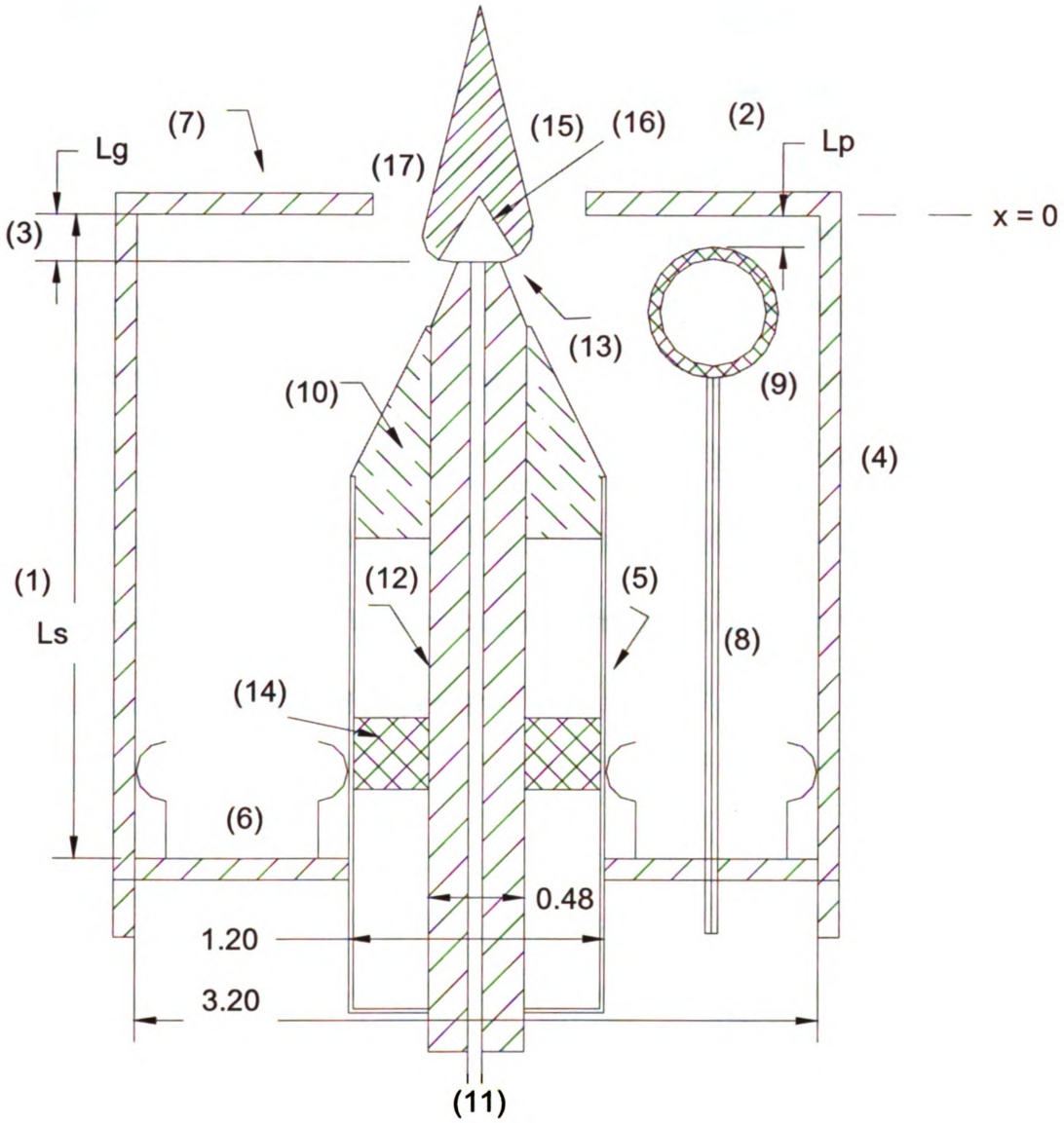

Figure 9.2 - The cross-section of the microwave re-entrant coaxial cavity applicator.

The tuning adjustments and the microwave matching of this cavity has already been demonstrated with both low and high power microwave excitation levels in microwave discharge applications [86, 135]. As the flame loading changes due to changes in input gas flow rates, gas mixtures and variations in the input power the applicator must be slightly retuned to achieve an efficient matched operating condition. The tuning adjustments that are necessary for matching the microwave energy into the cavity are: (1) gap length, L_g; (2) sliding short length, L_s; and (3) coupling loop length, L_p and (4) phi, ϕ, positions. All tuning variables, i.e. L_g, L_s, L_p and loop orientation, ϕ, are continuously variable. Typical experimental operating positions are L_g = 0.1 cm, L_s = 2.8 cm, L_p = 0.2 cm, and $\phi = 180°$.

9.3 Re-entrant cavity equivalent circuit

In this investigation, the cavity applicator is excited with 2.45 GHz energy and the applicator is excited in the transverse electromagnetic (TEM) coaxial wave mode. The cutoff frequency of the next lowest mode for the coaxial waveguide, i.e. the TE_{11} mode, is 5.4 GHz, hence only the TEM mode can be excited in the coaxial section of the cavity. The wavelength, λ, for the TEM mode is the free space wavelength and is ~12.24 cm at 2.45 GHz. The cavity quality factor, Q, is a measure of the electromagnetic energy loss per cycle of the resonant applicator. Lower loss implies a higher Q. The empty non-flame cavity Q depends on the condition of the cavity walls, sliding short, etc., and varies between approximately 500-1000. When the applicator is adjusted with a small gap, the length of L_s for resonance is approximately less than a quarter wavelength. When the applicator is adjusted for resonance the electric field intensity is the highest in the gap region. When the cavity is empty, i.e. when the flame is not ignited, the cavity can be adjusted by tuning the gap length, L_g, and the sliding short position, L_s, to a critically coupled resonance. Then the applicator is matched to the external 2.45 GHz power supply. This impedance matching increases the microwave electric field intensity in the gap region. When the applicator is matched the gap electric field can also be varied by changing the input power. The applicator has a very small excitation volume and given a specific input power it operates with a large impressed electromagnetic power density.

Figure 9.3 displays the equivalent circuit model of the coaxial re-entrant cavity applicator. For simplicity the microwave losses due to the surface currents on the coupling loop and the application are neglected. The circuit consists of a variable length (L_s-L_g), 50 Ω transmission line, which extends from the sliding short to the gap region, the coupling loop circuit, and the gap circuit. The impedance of the shorted transmission line is given by $Z_{sc} = j\ 50 \tan \beta_0 (L_s-L_g) = j\ X_{line}$, where Z_{sc} is the input impedance of the shorted line, $Z_0 = 50$ is the characteristic impedance of the coaxial applicator, (L_s-L_g) is the length of the transmission line, β_0 is the propagation constant of the line and is equal to $2\pi/\lambda$, where λ is the free space wavelength.

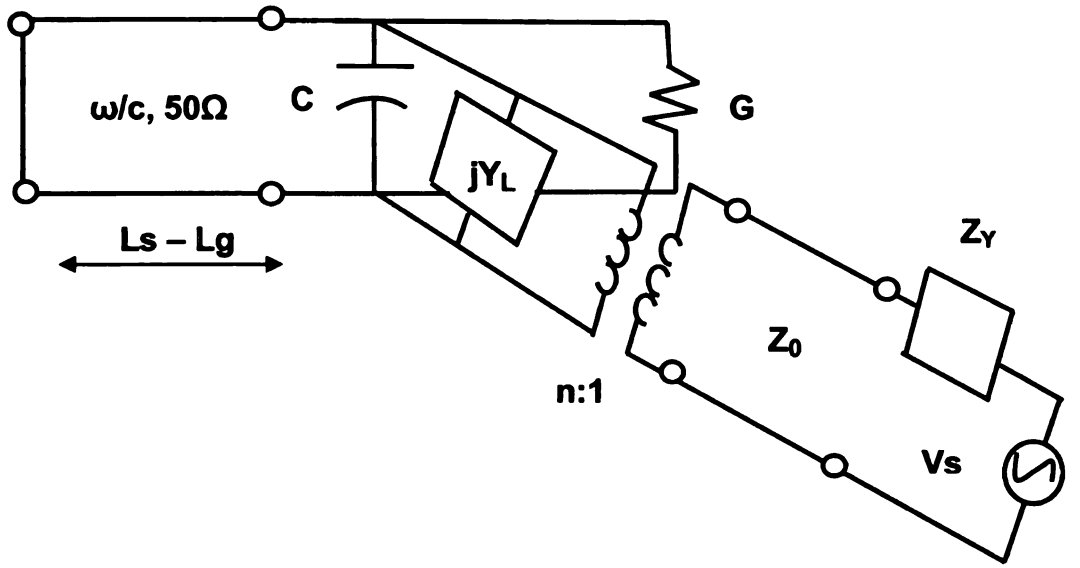

Figure 9.3 - Equivalent circuit of the microwave re-entrant cavity applicator with a flame as a load.

The coupling loop is modeled as an ideal transformer with an n:1 turns ratio and the lumped circuit reactance jY_L. This reactance represents the stored energy of evanescent fields associated with the near electric field of the loop. The coupling loop circuit is connected to the microwave power generator and the external microwave power measurement system. These external circuits are shown in Figure 9.3 as an equivalent transmission line with a characteristic impedance of Z_0. This transmission line is connected to the microwave power supply and is modeled as an internal impedance of Z_Y (Z_0 is approximately equal to Z_Y) and an equivalent ideal voltage source V_s. The gap region is modeled as an equivalent circuit consisting of a lumped capacitor C and resistor G, which are connected in parallel with each other and with the sliding short transmission line and the input coupling circuit. The capacitance is the equivalent lumped circuit capacitance C that is produced by the strong electric fields that exist at the end of the applicator between the center conductor nozzle plug (10) and the endplate (7). When there is no flame present, we assume for simplicity that the gap conductance is infinite, i.e., $G = \infty$, neglecting the microwave losses due to the surface currents on (7) and (10). Then, for simplicity the gap is modeled as an equivalent parallel plate capacitance that is given by

$$C = \frac{\varepsilon_0 A_{eff}}{L_g} \tag{9.1}$$

where A_{eff} is defined as the equivalent effective parallel plate area of the gap region and L_g is the gap spacing referred to the x = 0 plane. When the gap length is varied, A_{eff} also changes.

When the flame is ignited, the gap capacitance is further modified by the presence of the hot neutral gases and the low-density electron and ion gases produced by combustion. Microwave energy is introduced into the applicator by adjusting the applicator to an electromagnetic resonance at the 2.45 GHz excitation frequency, and then the microwave energy is coupled into the flame via Ohmic heating of the flame electron gas. The flame loaded gap impedance then becomes complex and has a real part represented by the conductance G and an equivalent effective gap capacitance C shown in Figure 9.3. The conductance G represents the equivalent resistance produced by the Ohmic heating losses due to the coupling between the microwave energy and the flame electron gas, and the gap capacitance can be modeled as equivalent plasma filled capacitor. As the impressed microwave power increases the densities of the electron and ion gases in the flame increase due to increased inelastic collision processes. The effective gap impedance is expected to be further changed by the presence of these higher charge densities and the Ohmic heating losses and at the higher input microwave power levels also due to the formation of microdischarges between the edge surfaces.

At resonance, jY_L is usually much larger than the admittance of the gap and usually can be neglected. When the applicator is adjusted for resonance the

capacitive reactance of the flame and plasma loaded gap must be canceled by the inductive reactance of the short-circuited transmission line. This can be expressed mathematically as

$$jX_{gap} + jX_{line} = 0, \tag{9.2}$$

where jX_{gap} is the effective capacitive reactance of the gap and $j X_{line}$ is the reactance of the short-circuited transmission line. The capacitive reactance of the gap region is given by

$$jX_{gap} = \frac{1}{j\omega C} = \frac{-j}{\omega C}. \tag{9.3}$$

Thus Eq. (9.2) becomes

$$jX_{gap} = - jX_{line} = - j\ 50 \tan \beta_0(L_s - L_g), \tag{9.4}$$

where $\beta_0 = \omega/c$ and c is the speed of light. Noting that $L_s >> L_g$ and solving for L_s yields

$$\beta 0 Ls \leq \tan^{-1}\left(\frac{1}{50\omega C}\right) \tag{9.5}$$

if C is small we have $\beta 0 Ls = \frac{\pi}{2}$ and $Ls = \frac{\lambda}{4}$, and then for all C, as C increases, the line resonant length becomes shorter. Thus,

$$Ls \leq \frac{2\pi / \beta 0}{4} < (\frac{\lambda}{4} \approx 3.1cm) \tag{9.6}$$

This result indicates that the resonant length L_s is less than a quarter wavelength and varies with the gap reactance. The experimentally observed lengths L_s vary from 1.9 to 2.8 cm depending on the gap size and the flame and microplasma loading. As the loading varies due to the changes in the chemistry, flow rate or microwave input power, the applicator length L_s and/or the gap length L_g must be slightly varied to achieve optimal coupling and a microwave matched applicator.

9.4 Experimental results

9.4.1 Influence of microwave coupling on the flame

Figure 9.4 displays the visual images of the plasma flame as the input microwave power levels were varied from 0 to 20 Watts. The plasma torch burner was oriented vertically. The O_2/CH_4 gas flow rate was held constant at 50/25 sccm (a), 98/49 sccm (b) and 150/75 sccm (c) respectively. As can be seen from the photographs, the flame intensity and luminosity were greatly enhanced by the addition of microwave power as opposed to combustion only flame at 0 Watt. As the input power increases the flame length, width, and intensity also increases. Moreover, the flame color also changed from red to yellowish suggesting a change in the combustion process due to the presence of new radicals. When subjected to microwave power up to 20 Watts, the length of the flame increases gradually from about 2 mm up to 10 mm. Even at low input power levels of 3 to 8 Watts, the flame size and intensity increases suggesting that at these low input power levels microwave energy is coupled into the electron gas which in turn transfers its energy into excited radicals. At the higher input power levels of 10 to 20 Watts the flame continues to increase in size and intensity, and the flame appears to have a strong interaction with the microwave input energy resulting in additional ionization and in an increase in electron and ion densities, and under certain conditions micro plasma appear in the gap region between the edge conducting surfaces.

Figure 9.5 displays the visual images of the flame as the absorbed microwave power was increased from 1 to 18 Watts with the torch oriented horizontally. The O_2/CH_4 gas flow rate was held constant at 50/25 sccm (a), 98/49 sccm (b) and 150/75 sccm (c) respectively. As the absorbed microwave power increases the flame intensity, length and volume change.

At microwave power levels greater than 15 Watts the power coupled into the applicator is approaching or is of the same order of magnitude as the combustion flame power which is 29 Watts. Thus, at the higher power levels shown in Figure 9.4-9.5 a microwave discharge flame is produced. This behavior is similar to the seven inch cylindrical cavity applicator except here the changes in the flame occur with much lower input microwave power levels. Also, the changes in the appearance of the flame are more gradual and continuous versus increases in input power. Clearly, the coupling of microwave power into the premixed flame changes the physical appearance of the flame and the microwave energy coupling is more efficient, i.e. with only a few Watts to 10 Watts, instead of 30 to 50 Watts as observed with the seven inch cylindrical cavity which is larger and less efficient applicator system.

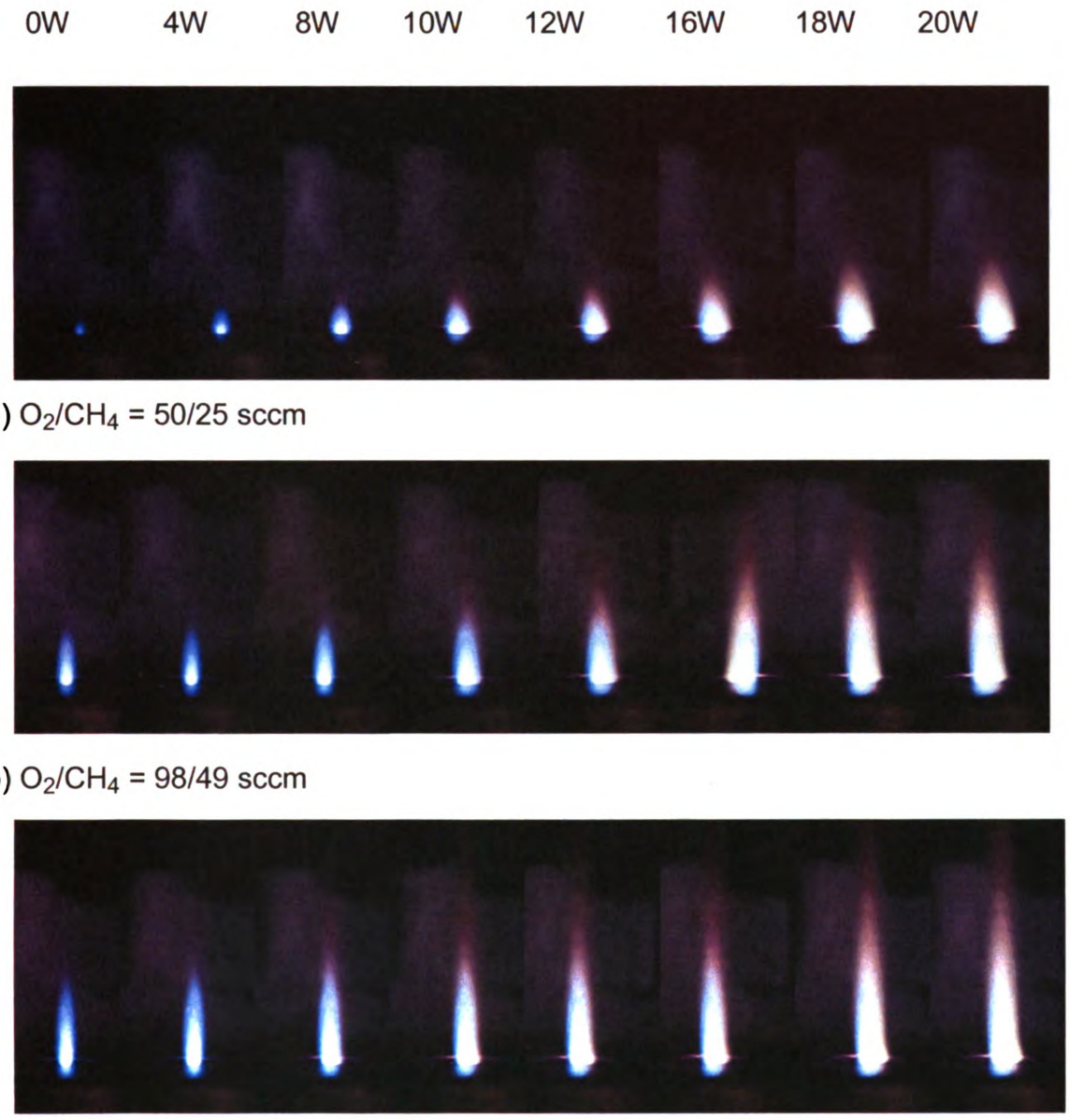

Figure 9.4 - Visual images of the flame at various absorbed microwave power from 0 to 20 Watts. The plasma torch burner was oriented vertically. The O_2/CH_4 gas flow rate was held constant at 50/25 sccm (a), 98/49 sccm (b) and 150/75 sccm (c) respectively.

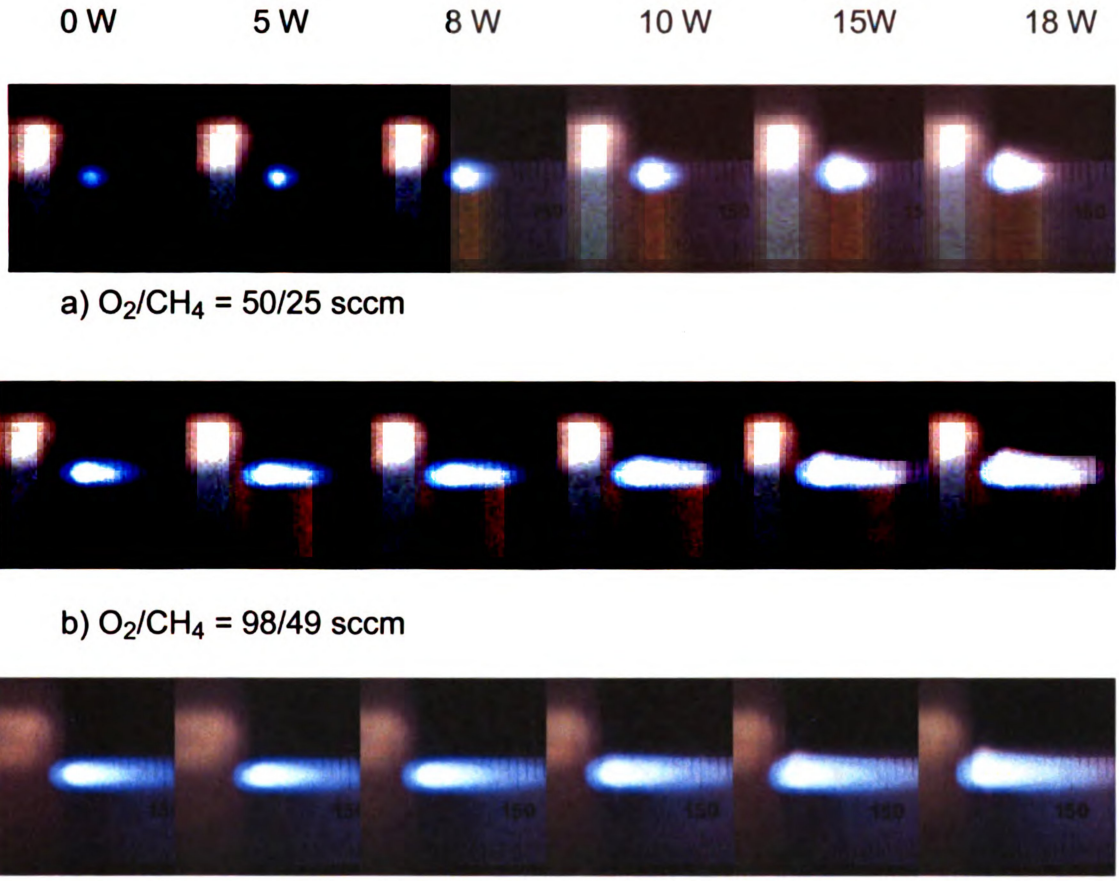

Figure 9.5 - Visual images of combustion flames as microwave power levels are varied from 0-20 Watts. The O_2/CH_4 gas flow rate was held constant at 50/25 sccm (a), 98/49 sccm (b) and 150/75 sccm (c) respectively.

A closer view of the flame is displayed in the photos of Figure 9.6. It was observed that as microwave input power is applied to the combustion flame, the intensity of the flame inner cone in the ignition zone increases and the cone shifts slightly up stream as the input power increases. Furthermore, as observed in Figure 9.6, as the input power increases, the size and intensity of the flame downstream "afterglow" increases. This suggests that as the microwave power is coupled into the flame the downstream chemical activity and energy of the combustion flame increases. Also, microplasma formation is observed, which can be seen in the 10 Watts picture of Figure 9.6 as an increased intensity, outer pink ring of excited species. Since the operation of the premixed flame is at atmospheric pressure, the plasma region in the flame is relatively thin and the microwave heating of the electron gas takes place in or near to the intense cone region of the flame. When the electrons are excited and heated their inelastic collision rates with the neutral gas molecules are increased, and electron and ion impact reactions can significantly impact the hydrogen chemistry of the fuel. In particular, it can lead to changes in the fuel gas chemistry and heat release channels involving CO and CO_2 conversion by introducing new and intermediate species and radical byproducts that result in a larger visual downstream flame volume. The appearance of yellowish color at the flame edge downstream at higher microwave power above 10 Watts could be due to emission from alternative species, nitrogen entrainment, and changes in species concentration. This compact applicator design with the tapered coaxial inner conductor focuses

a strong electric field into the flame region located at the nozzle tip, enabling the efficient coupling of microwave energy into the flame.

As shown in Figure 9.2 the inner cone or ignition zone and some part of the downstream afterglow of the flame is located in the high electric field gap region of the applicator. Thus, any electron gas that exists within the flame due to combustion is also located in the high electric field region of the flame. It is expected that the combustion produced electron gas is localized and will have densities much lower than the critical density ($< 10^{11}/cm^{-3}$ for 2.45 GHz excitation). Thus, the flame plasma is low density plasma and the impressed microwave electric fields freely penetrate the electron gas to accelerate the electrons between collisions. In this atmospheric flame (T_g = 2500-3600 K) the mean free path (m.f.p.) for the electron molecule/radical collisions are of the order of one micron. The collision frequency for momentum transfer is of the order of 10^{11}/sec. Thus the microwave electric field will heat the electron gas via elastic electron – neutral collisions, i.e. electron gas heating occurs by a collisional or ohmic heating process [127].

When the microwave energy is coupled into the flame, electron gas heating takes place and the electron gas temperature, T_e, increases above the gas temperature T_g ($T_e > T_g$) creating a non-equilibrium plasma. As the microwave electric field and microwave power are increased the electron temperature will increase to the level where some electron – neutral collisions are inelastic. Through this inelastic collision process the microwave excited electron gas

produces new radical and excited species. If electric field strengths and power levels are further increased ionization collisions may also occur. When the impressed electric field strength is sufficient to cause breakdown, microplasmas can be produced in the region between the conducting surfaces. Microwave electron gas heating is expected to occur in or very near the inner cone region of the flame. Since the mean free paths for collision processes are very small (of the order of a micron) the radical and ionized species will also be produced in or directly adjacent downstream from the electron gas. As the excited neutral gas flows downstream the radical and excited species de-excite and recombine through three body collisions thereby increasing the local gas temperature. The gas temperature of the downstream microwave excited flame is consequently expected to increase as the input microwave power is increased.

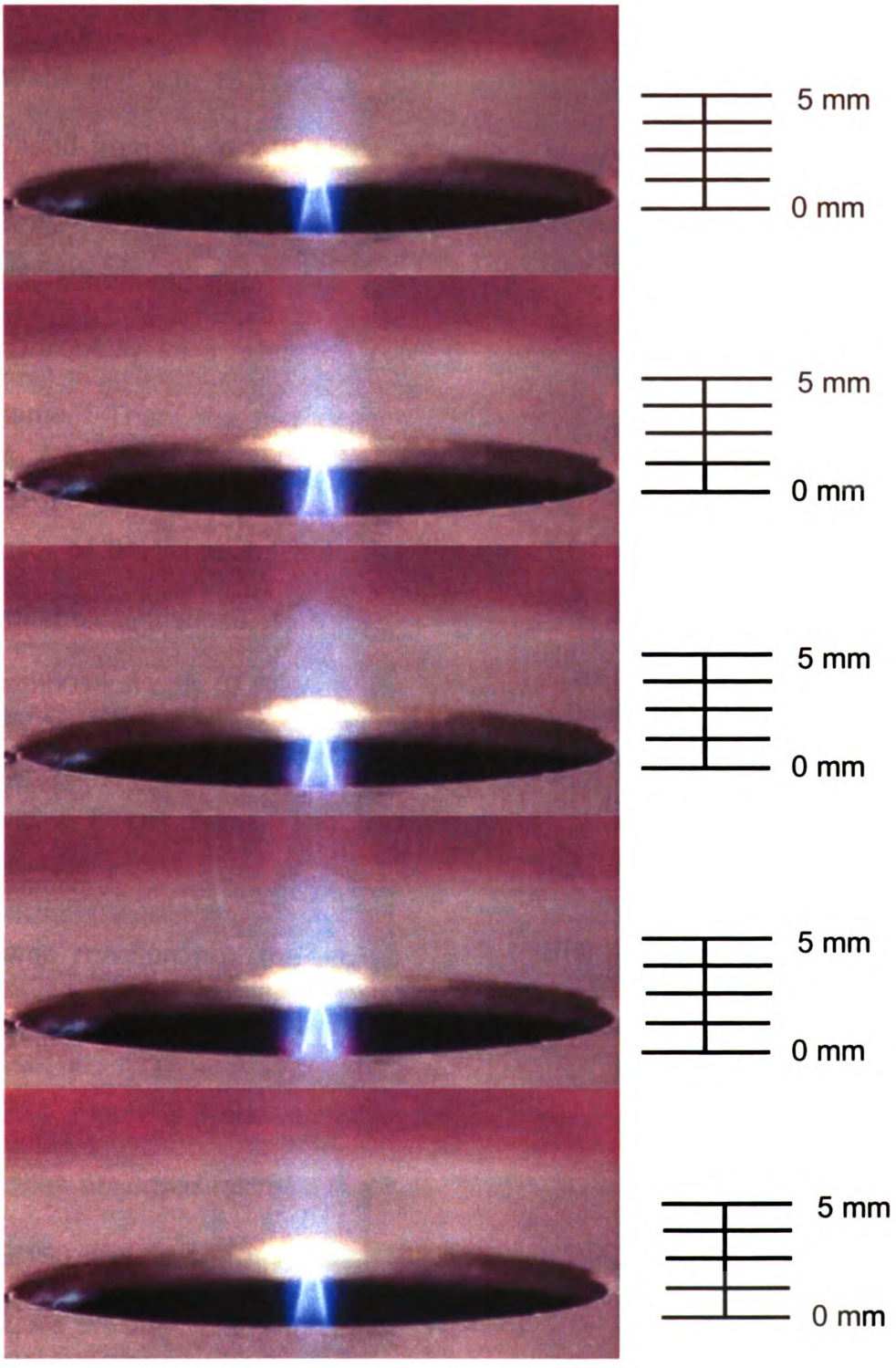

Figure 9.6 - Visual images of the inner cone premixed flame reaction zone with increasing microwave power (top to bottom) from 0 W, 5 W, 8 W, 10 W, and back to 0 W at flow rates of 70/140 sccm CH_4/O_2.

Figure 9.7 displays the variation of flame volume versus flow rate with 0 Watts and with 15 Watts of input microwave power. The total flow rates were varied from 45 to 240 sccm. The flame volume was calculated based on the brightest luminescence of the visual images that are obtained from photographic measurements. Two rulers were placed by the combustion flame vertically and horizontally as a reference point to measuring the length and diameter of the flame. Then, the two dimensional images conical shape obtained from the camera photographs was quantified. The appearance of the afterglow and outer layer of the flame on the visual images was not taken into account for these volume calculations. As shown in Figure 9.7 the flame volume increases for both combustion only (0 W) and also with the addition of 15 W of microwave power. These results are expected since higher total gas flow results in a larger diameter and a longer flame. The increase in flame volume with the application of microwave power suggests that the plasma is impacting the flow velocity prior to flame reaction and the increase in flame size past the reaction zone is an indication that the reaction itself is being energized.

Figure 9.8 shows the variation of the flame volume for three flow rates versus absorbed microwave power. The three different flow rates of CH_4/O_2 are 75/150 and 50/100 and 25/50 sccm. As is displayed visually in Figure 9.4 and Figure 9.5 the volume of the flame increases as the microwave power varies from 0 to 20 Watts. Clearly, higher total flow rates resulted in larger flame lengths and volume.

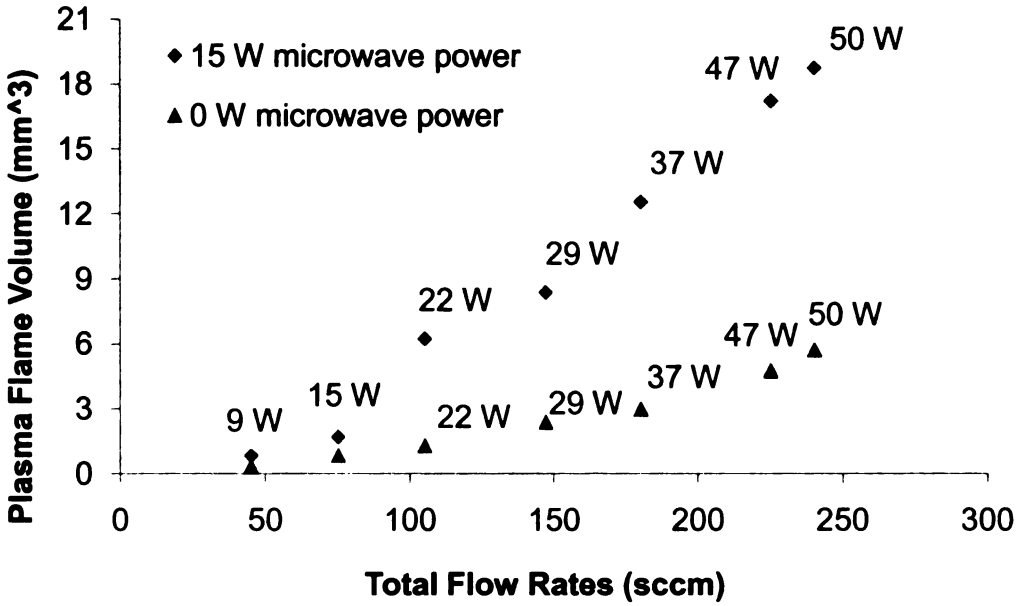

Figure 9.7 - Plasma flame volume versus total flow rates at 0 and 15 W microwave power with its corresponding combustion flame power.

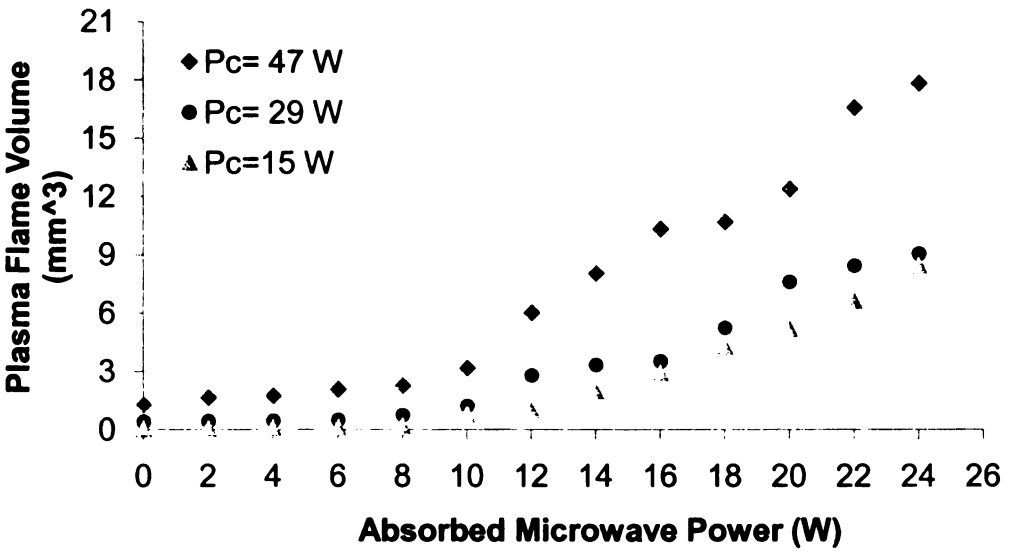

Figure 9.8 - Plasma flame volume with increasing microwave energy at various total flow rates with its corresponding combustion power. Pc corresponds to the combustion power at each flow rate.

9.4.2 Flammability limits

In terms of flammability limits, i.e. the limit of the flame to sustain itself in a fuel rich or fuel lean mixture ratio, the extension of the flame discharge to leaner burning operating conditions is shown in Figure 9.9. The flammability limit or blowout tests were performed by holding the oxygen flow constant and lowering the methane flow rate until the flame blew out. The x-axis of the graph represents the total flow rates of the fuel and oxidizer. The y-axis represents the equivalence ratio (ER), which is defined as the volume flow rate ratio of the experimental fuel/oxidizer divided by the fuel/oxidizer for stoichiometric burning of CH_4/O_2, which is (1/2).

$$ER = (V_{CH4}/V_{O2})/(1/2) \qquad (9.7)$$

where V_{CH4} and V_{O2} are the total flow rates of the fuel and oxidizer gas. The experiments were run several times to ensure the accuracy of the results. The flow rates accuracy was ± 1 sccm. The addition of 3 Watts of microwave power to the combustion flame can lower the equivalence ratio compared to combustion only. The addition of 6 Watts or higher of microwave power allows operation at lean burning conditions to the point of zero fuel, i.e., ER = 0. When the combustion flame is operated under fuel rich condition i.e., more methane than oxygen concentration, the addition of 2 and 4 Watts extends the flammability limit of the flame as shown in Figure 9.10. Above 4 Watts of microwave power, the flame can be maintained only using methane without any oxygen gas flow.

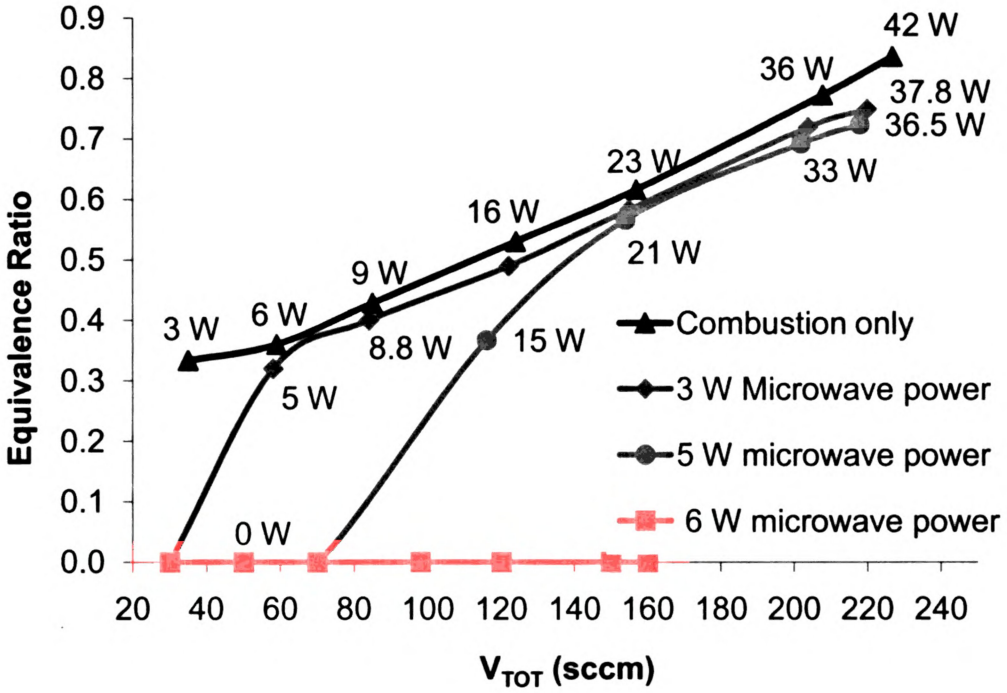

Figure 9.9 - Flame extinction curves for combustion flames with 0, 3, 5, 6 Watts additional of microwave power. The corresponding combustion power is displayed for each data point.

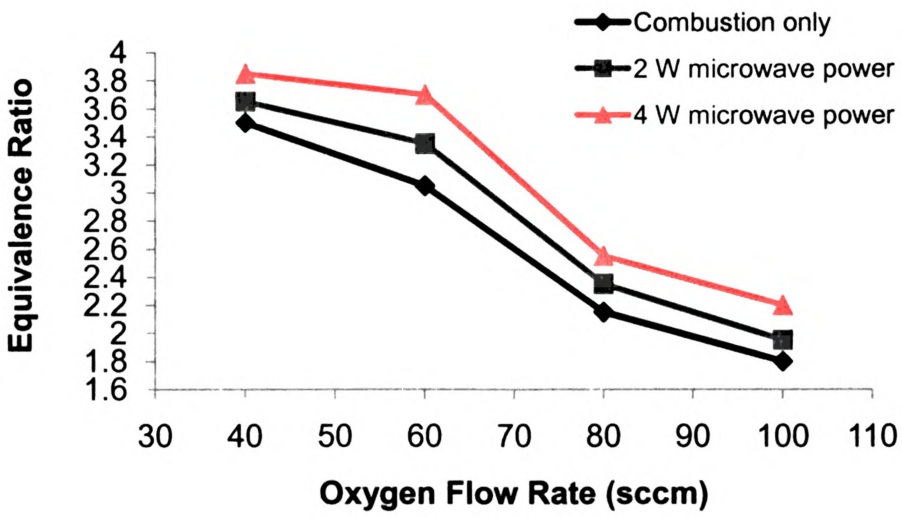

Figure 9.10 - Flame extinction curves under fuel rich combustion flames with 0, 2, and 4 Watts additional of microwave power.

9.4.3 Radical species and gas temperature

Optical emission wide scans of combustion only and combustion with the addition of 10 Watts of microwave power into the combustion flame is displayed in Figure 9.11. The emission spectra were scanned from 3000 to 6000 Angstrom visible wavelength. Clearly, with 10 Watts addition of microwave absorbed power to a flame with a combustion power of 29 Watts, the intensity of the spectra increases dramatically compared to combustion only. This clearly indicates that the microwave energy input alters the combustion flame. The nitrogen electronic excitation and other molecules were also detected when microwave power was added into the combustion flame. Major species that were detected in the hybrid plasma flame discharge are OH, N_2, O_2, CH, C_2 and H_2 with its corresponding wavelength at visible spectrum.

Shown in Figure 9.12 are the optical emission spectra for a nitrogen emission without and with the addition of microwave power from 3 Watts to 10 Watts. The spectral intensities were increased with only 5 Watts of input microwave power. With the application of microwave energy, the excited flame front was altered and the number of excited states of species was increased.

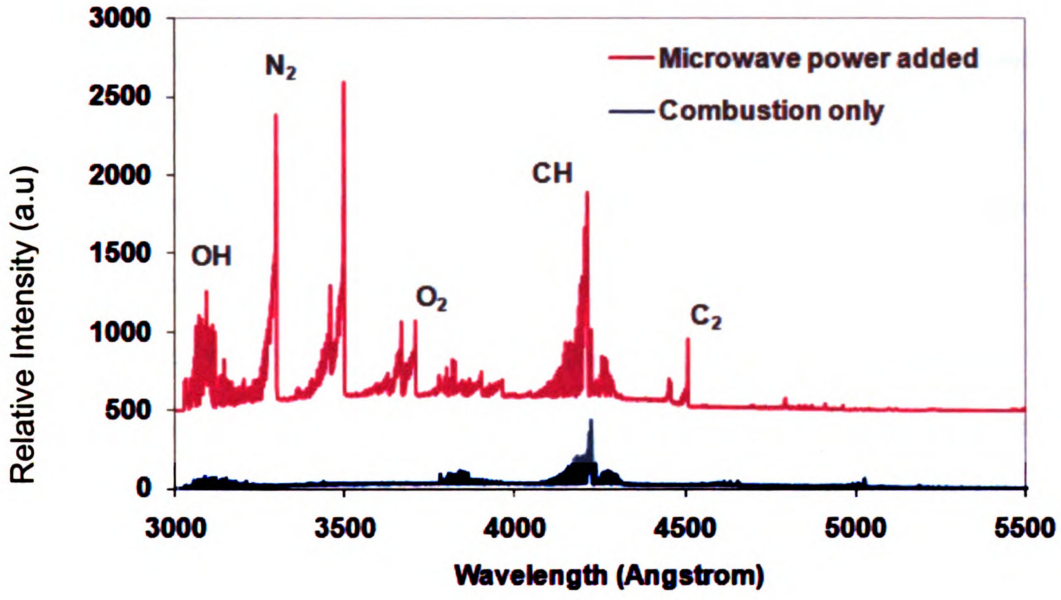

Figure 9.11 - Optical emission spectroscopy spectra scan of combustion flames with and without addition of microwave power energy into the flame. Flow rates: 50/100 sccm CH_4/O_2, microwave input power: 10 Watts.

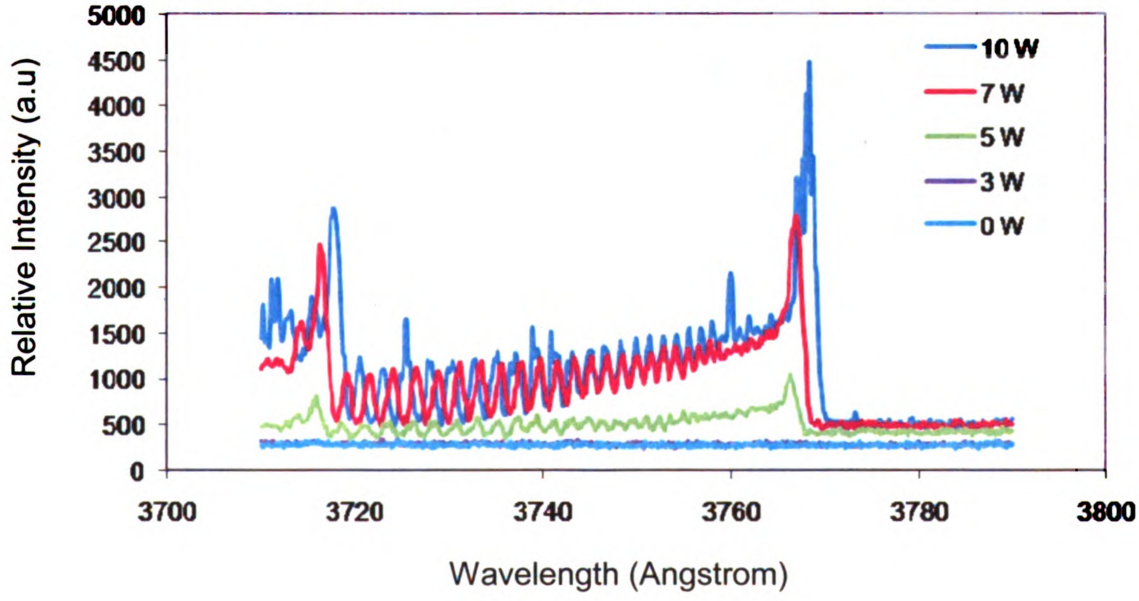

Figure 9.12 - Optical emission spectroscopy nitrogen line spectra of the plasma flame with 0, 3, 5, 7, 10 Watts addition of microwave power into the combustion flame. Note that 0 and 3 Watts spectra are over lapping.

Figure 9.13 shows the CH rotational temperature of the hybrid plasma flame at various microwave power levels for three different flow rates; fuel lean (ER=0.6), ideal (ER=1.0) and fuel rich (ER=1.4). The measured rotational temperature ranges from 2500 to 3600 Kelvin. The temperature increases as microwave power is added into the combustion flame. The influence of microwave power on the plasma flame temperature was more pronounced when operating at much leaner flames. Under fuel lean equivalent ratio, the rotational temperature was consistently higher compared to fuel rich or stoichiometric conditions.

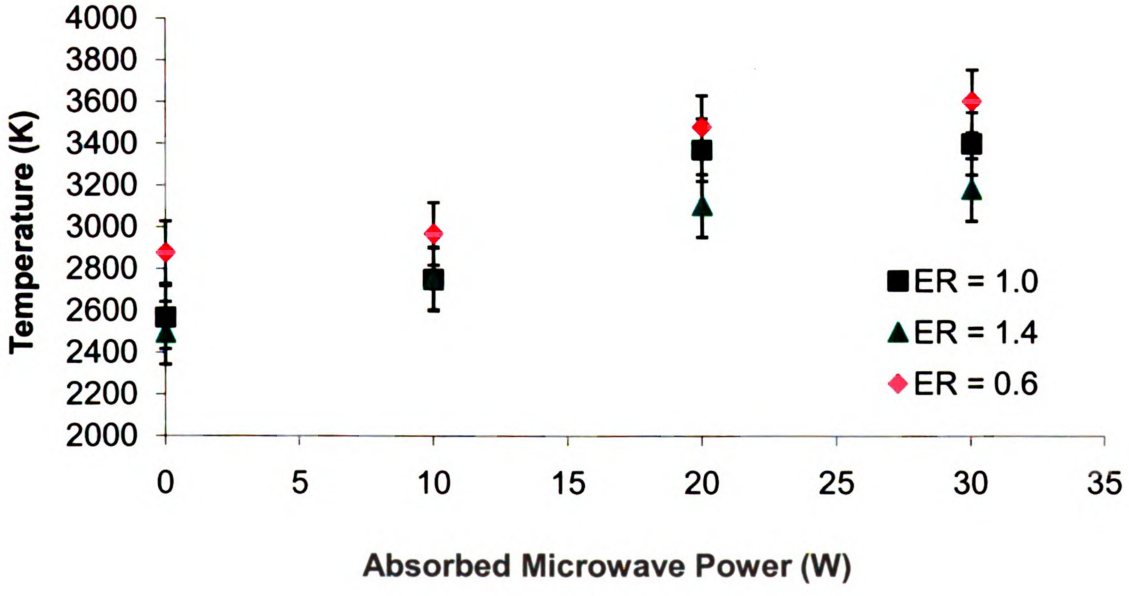

Figure 9.13 - Plasma flame temperature profile as microwave power is added into the flame at three different equivalent ratios CH_4/O_2: 70/100, 50/100, and 25/100 sccm. ER is the equivalent ratio which corresponds to flame fuel composition with ER =1.0 as an ideal flame.

9.5 Summary

A coaxial re-entrant cavity applicator has experimentally demonstrated the microwave energy excitation of a premixed flame. The applicator coupled and focused the microwave energy into a small gap region where the flame was positioned. The mechanical tuning of the applicator allows for the efficient matching of microwave power into the flame and also allows the optimal positioning of the flame with respect to the impressed electric field. By coupling microwave power of less than 10 Watts into the combustion-premixed flame, the flame intensity, length, volume, and temperature were altered, and as the power was increased from 10 to 20 Watts, microplasmas were produced in and adjacent to the flame. Microwave energy can be continuously coupled into the flame from a few watts to over 30 watts resulting in a range of hybrid flame behaviors. That is, at the very low input power level microwave energy may directly interact with the flame electron gas and as the input power level was increased further inelastic processes become important resulting in the formation of microplasmas. Clearly, the applicator tuning and the improved microwave focus greatly enhance the microwave flame coupling efficiency. The applicator itself, and the entire input waveguide system consists of coaxial waveguides and coaxial cables yielding a compact overall microwave system. The applicator's inherent efficiency may allow it to be excited with compact low-power solid-state microwave power supplies, thereby yielding a compact, portable overall hybrid microwave plasma combustion system. This applicator-coupling concept can be scaled up to larger burner sizes. Because of the coaxial structure it can also be excited with lower frequencies.

CHAPTER 10

SUMMARY AND RECOMMENDATION

10.1 Summary

10.1.1 Microwave plasma assisted CVD diamond synthesis

An improved high pressure and high absorbed power density microwave plasma cavity reactor has been designed and experimentally evaluated by synthesizing polycrystalline and single crystal diamond films over the 180-250 Torr pressures regime. Major design changes were: (1) the reduction of the substrate holder electrode by more than a factor of two to a radius of 1.91 cm and introducing (2) the position/length tuning of the powered substrate holder electrode. The reduction of the powered electrode area by 4.5 increased the discharge power density by a factor of 5-8 over the reference design when operating at pressures of 100-160 Torr and produced very intense hydrogen gas discharges with adjustable power densities of 200-550 W/cm^3 in the 180-240 Torr pressure regime. The length tuning of the powered electrode allowed the electromagnetic focus to be varied above the substrate and allowed the control of the discharge shape, size and position. The experiments demonstrated that small changes of a few mm in powered electrode position could change the deposition rate by a factor of two and the optimal deposition position varied as pressure and power varied. Thus, the length tuning provided an important experimental

variable for process control and optimization especially in the high-pressure regime.

Polycrystalline diamond film growth rates ranged from 3-21 μm/hr as the methane concentration was varied from 2-5% when substrate temperature varied within 879-1178° C. The diamond growth rate increased with increasing operating pressure and higher methane concentration. Optical quality films were produced with methane concentrations as high as 4% and at growth rates of 12-14 μm/hr. Thus, high quality films were synthesized 6-7 times faster than the equivalent films grown at 110-130 Torr in the reference reactor.

Single crystal diamond was synthesized at operating pressures of 180 Torr to 250 Torr and growth rates ranged from 8-36 μm/hr without any nitrogen addition into the gas chemistry. The temperature of the substrate during deposition varied between 951° to 1282 °C. In general, higher operating pressures, methane concentrations, and higher substrate temperatures resulted in higher growth rate. In addition to the smooth surface appearance of the grown single crystal diamond, other surface morphologies such as pyramidal square hillocks, round conical hillocks, orange peel/crater like, and dark particles/non epitaxial crystallites were also observed. Raman measurements indicated that the grown single crystal diamond was of good quality.

10.1.2 Microwave plasma assisted combustion

Two applicators and the associated experimental systems were successfully developed i.e., hybrid miniature torch in cylindrical cavity applicator and modified coaxial re-entrant cavity applicator. In both, the steady state low and high power coupling of microwave energy into a combustion flame was experimentally observed. The early experiments utilized the cylindrical cavity applicator that demonstrated the coupling of microwave energy into a combustion flame [152]. As the input microwave power is increased from a few watts to approximately 30 W the impressed electric field and the flame/discharge power density increase dramatically. Between impressed powers of 30 W-40 W the hybrid flame/discharge abruptly jumps in size and the power density decreases. At the highest microwave input power levels of 50-100W the flame/discharge appears to be discharge dominated. The generation of a hybrid plasma flame with 10-30 W of input microwave power produces leaner burning conditions, flame/discharge stability increases and flame extinction is extended. For $P_p > 20$ W the flame discharge can be maintained with no fuel; i.e. a pure atmospheric discharge is formed. This microwave experimental system is very useful for further fundamental experimental investigations of microwave energy interaction with flames. Additional experimental diagnostic spectroscopic measurements, such as spatially resolved species and temperature measurements, will be continued as future PhD thesis research activities.

A second applicator i.e., coaxial re-entrant cavity applicator, also experimentally demonstrated the microwave energy excitation of a premixed flame. In comparison to the cylindrical cavity applicator, the coaxial applicator was more microwave energy efficient and was also more physically compact. The applicator coupled and focused the microwave energy into a small gap region where the flame was positioned. The mechanical tuning of the applicator allowed for the efficient matching of microwave power into the flame and also allowed the optimal positioning of the flame with respect to the impressed electric field. The research activities demonstrated that, by coupling microwave power of less than 10 Watts into the combustion-premixed flame, the flame intensity, length, volume, and temperature are altered, and as the power is increased from 10 W to 20 W, microplasmas were produced in and adjacent to the flame. Microwave energy was continuously coupled into the flame from a few watts to over 30 watts resulting in a range of hybrid flame behaviors. That is, at the very low input power levels microwave energy directly interacts with the flame electron gas and as the input power level is increased further inelastic process become important resulting in the formation of microplasmas. Additional experimental investigations are required to understand the details of these complex microwave energy flame-coupling interactions and also to understand the properties the resulting hybrid flame.

10.2 Recommendation for future research

Based on the current results and findings, there are a number of recommendations that should be investigated further. Listed below are examples of future or follow up work for each application:

10.2.1 Microwave plasma assisted CVD diamond synthesis

1. Further investigate the optimum growth condition of polycrystalline and single crystal diamond synthesis using the modified reactor. This includes growth rates, uniformity and quality.

2. Develop an improved deposition process technology that enables the synthesis of large area and high quality SCD. This could be achieved by redesigning a new cooling stage inner conductor and substrate holder that allow the operation of higher pressure above 260 Torr.

3. Add nitrogen gas from a few parts per million (ppm) to several hundreds of ppm into the gas chemistry. This potentially increases the single crystal diamond growth rates without sacrificing the quality.

10.2.2 Microwave plasma assisted combustion

1. Identification of fuel oxidation or combustion product radicals (CH_3, C_2H_2, etc) and combustion flame concentrations measurements using

Fourier Transform Infra Red (FTIR) absorption and Laser induces fluorescence (LIF).

2. Design a flat flame burner applicator that can couple microwave energy into the combustion flame and synthesize diamond film using hybrid plasma flame combustion chemical vapor deposition.

APPENDICES

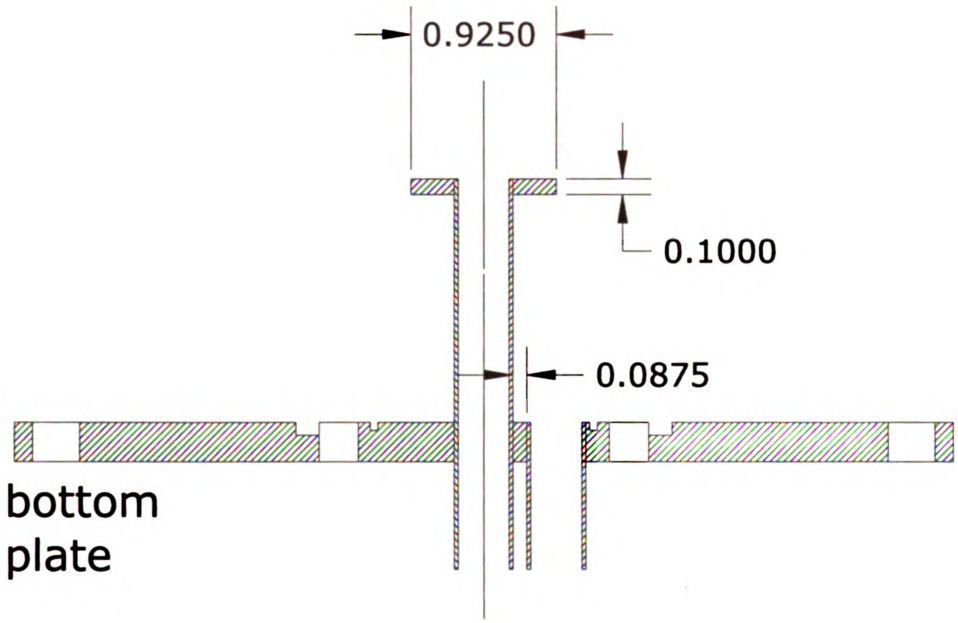

Appendix A.1- Water cooling stage inside the cylinder body cross section.

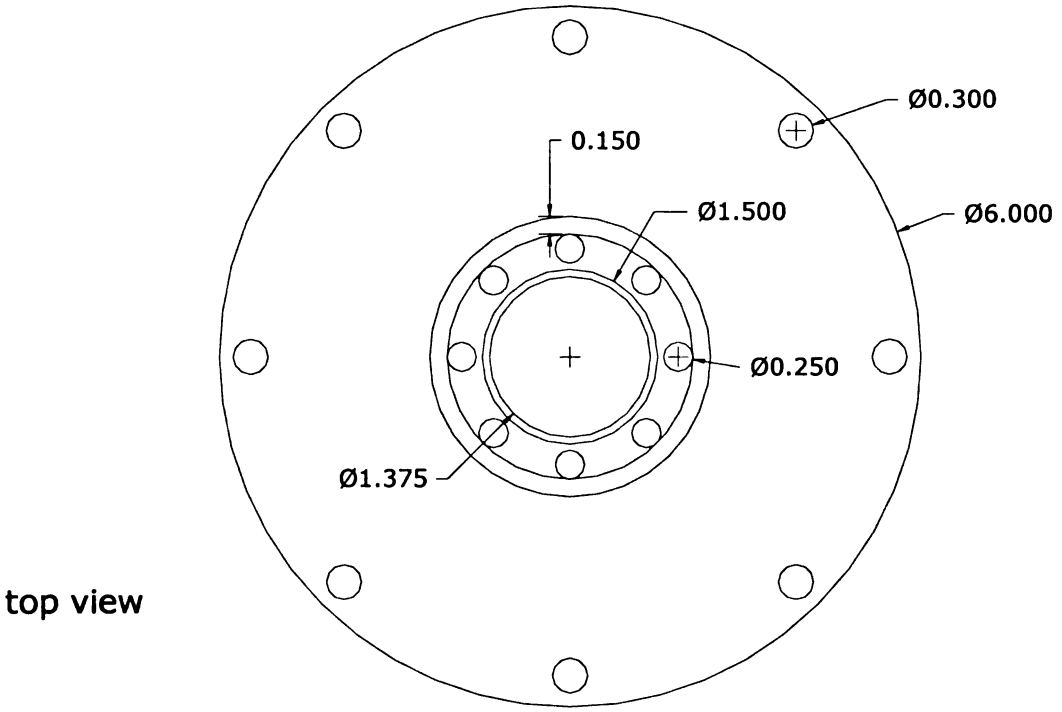

top view

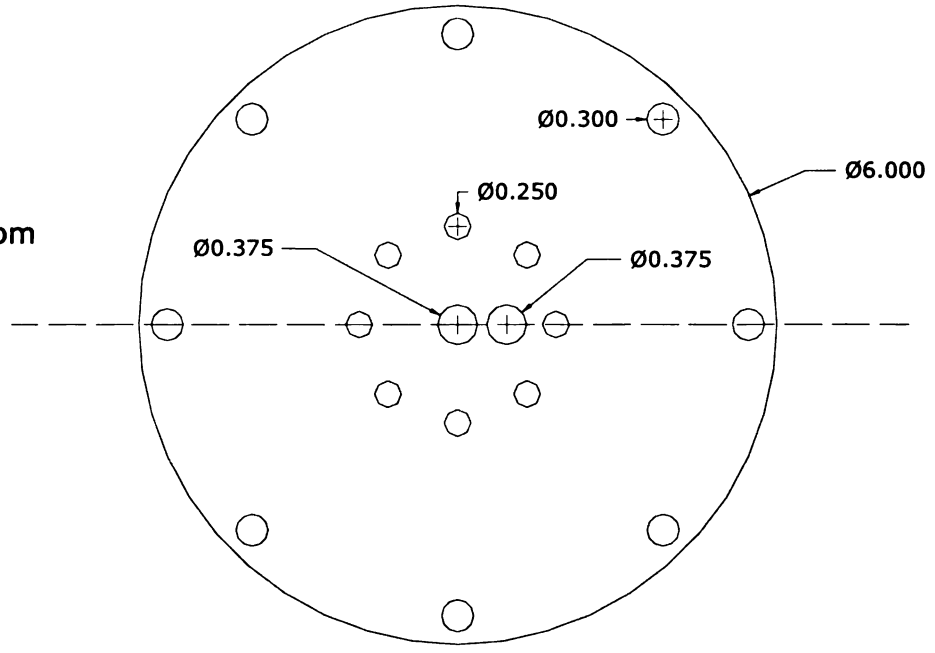

bottom view

Appendix A.2 - Water cooling stage top and bottom view cross sections.

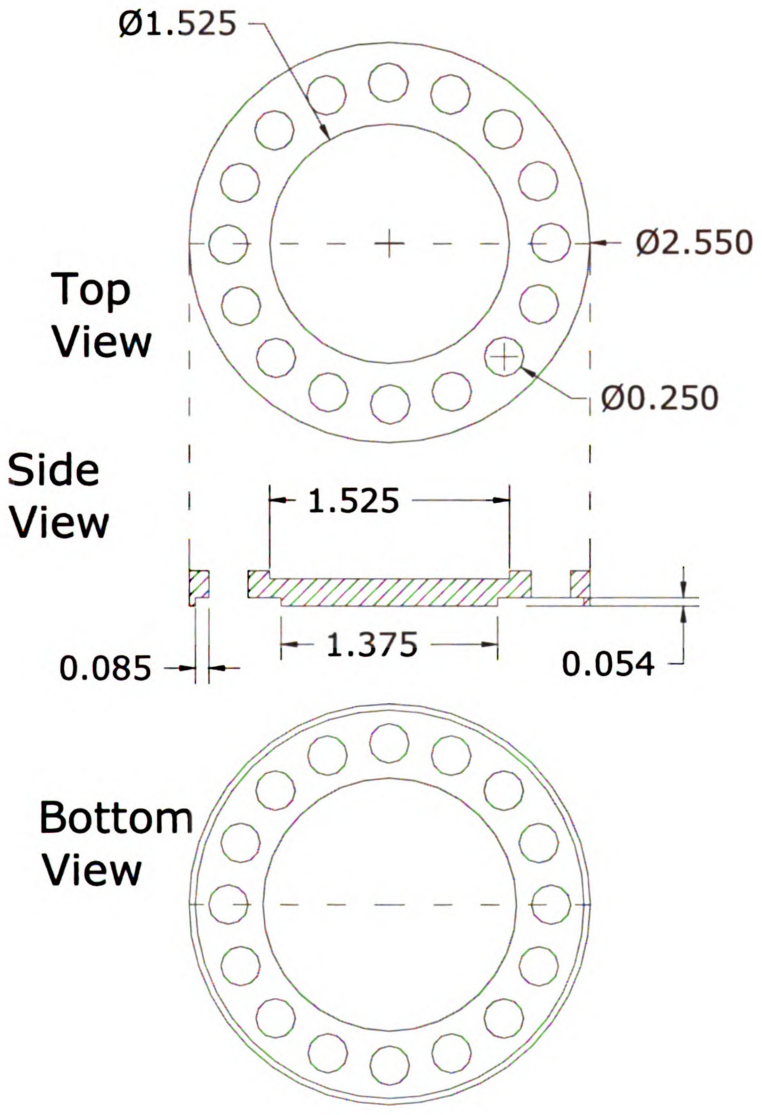

Appendix A.3 - Polycrystalline substrate holder drawings. Units are in inches.

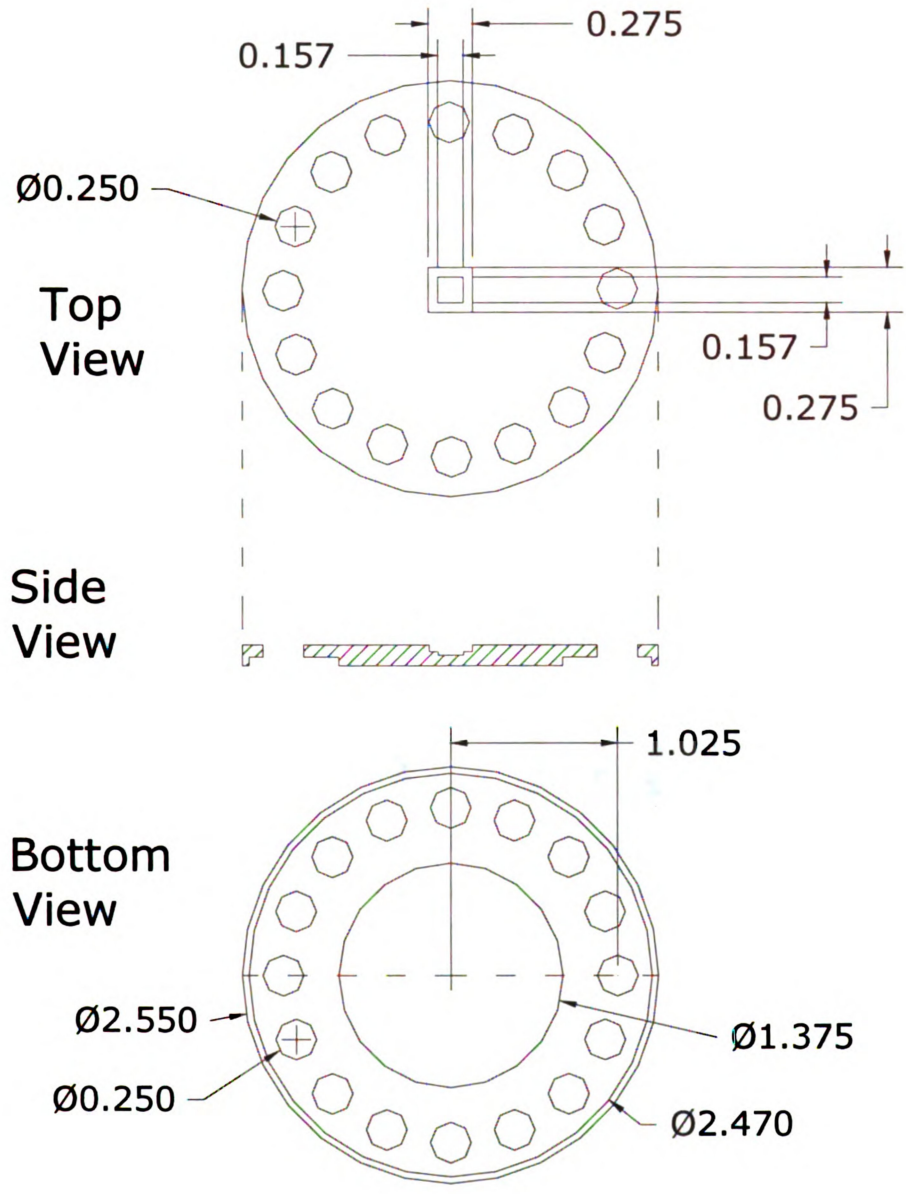

Appendix A.4 - Single crystal diamond substrate holder drawings. Units are in inches.

APPENDIX B Raman Spectra of Polycrystalline Diamond

Table B.1 - Raman spectra for samples grown at 180 Torr operating pressure with 2-5% CH_4/H_2 gas chemistry

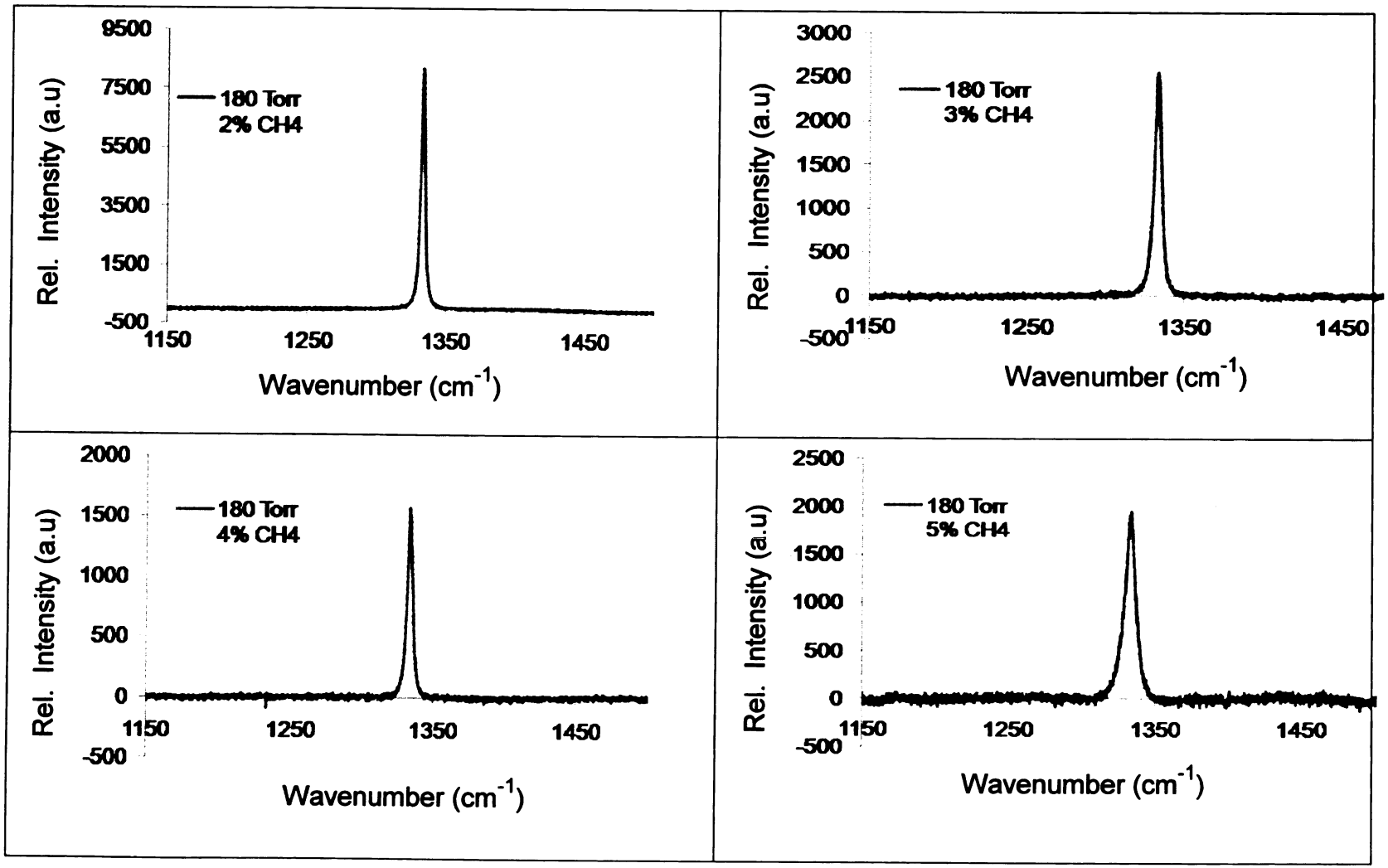

Table B.2 - Raman spectra for samples grown at 200 Torr operating pressure with 2-5% CH_4/H_2 gas chemistry

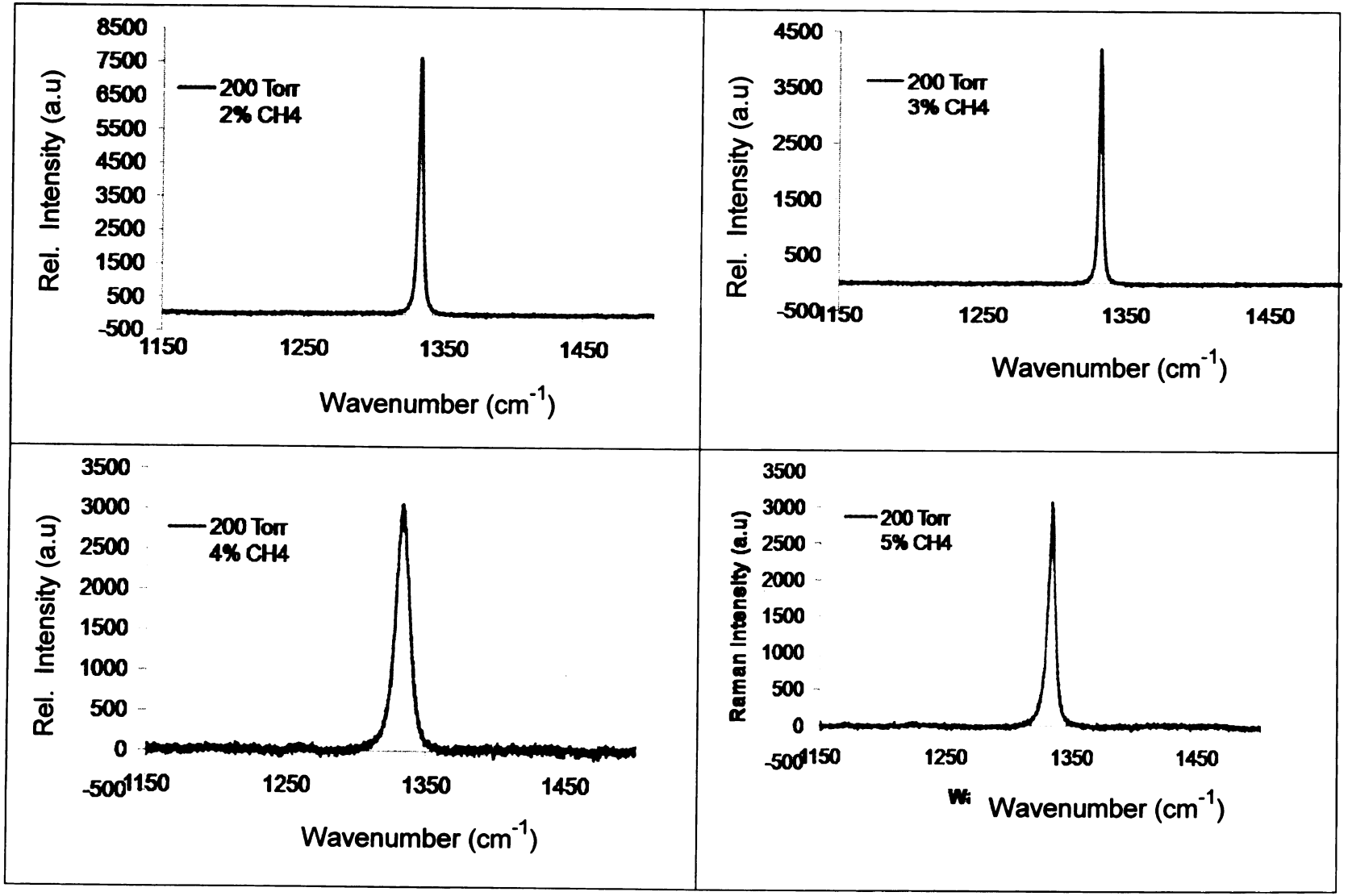

Table B.3 - Raman spectra for samples grown at 220 Torr operating pressure with 2-5% CH_4/H_2 gas chemistry

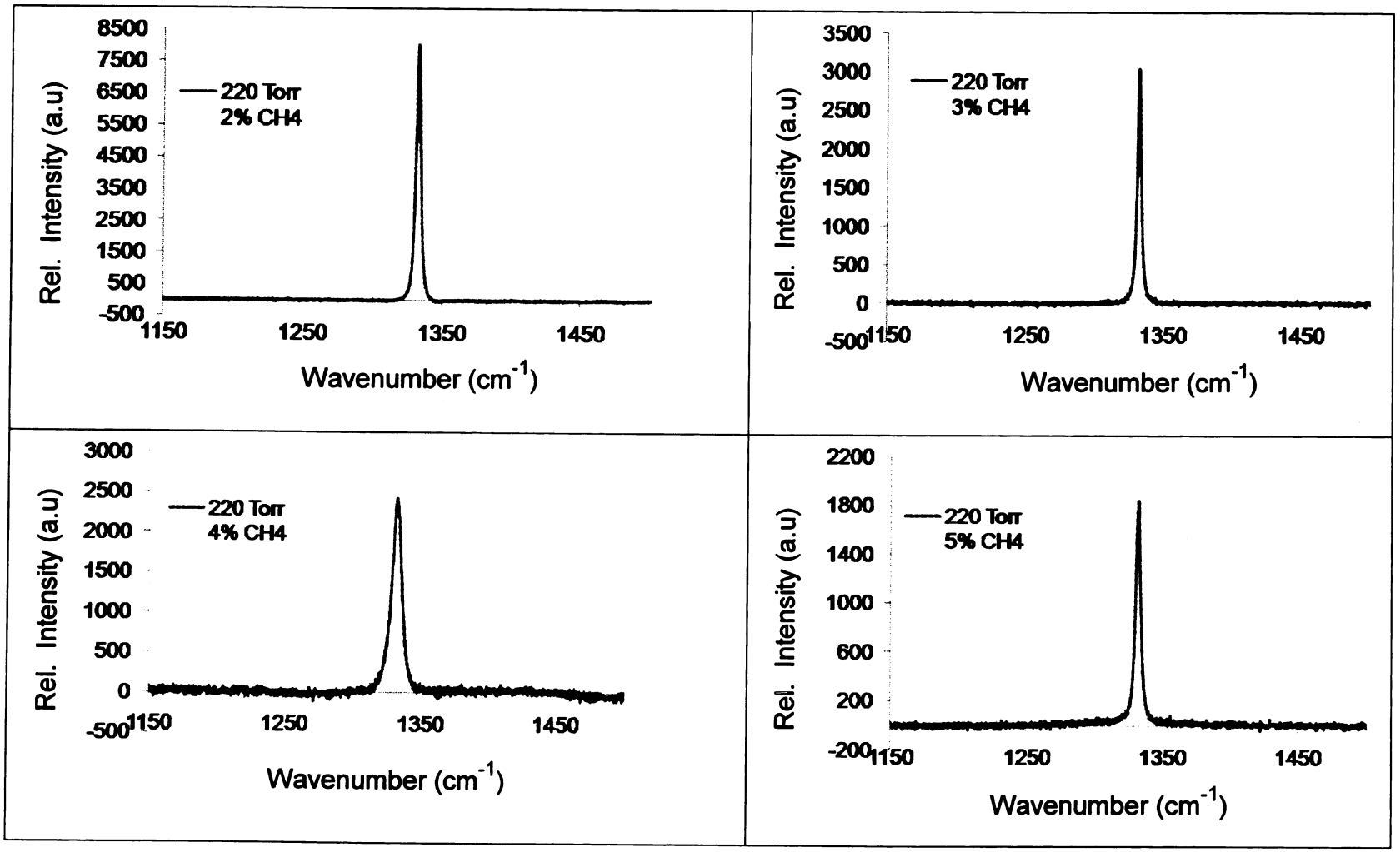

Table B.4 - Raman spectra for samples grown at 240 Torr operating pressure with 2-5% CH_4/H_2 gas chemistry

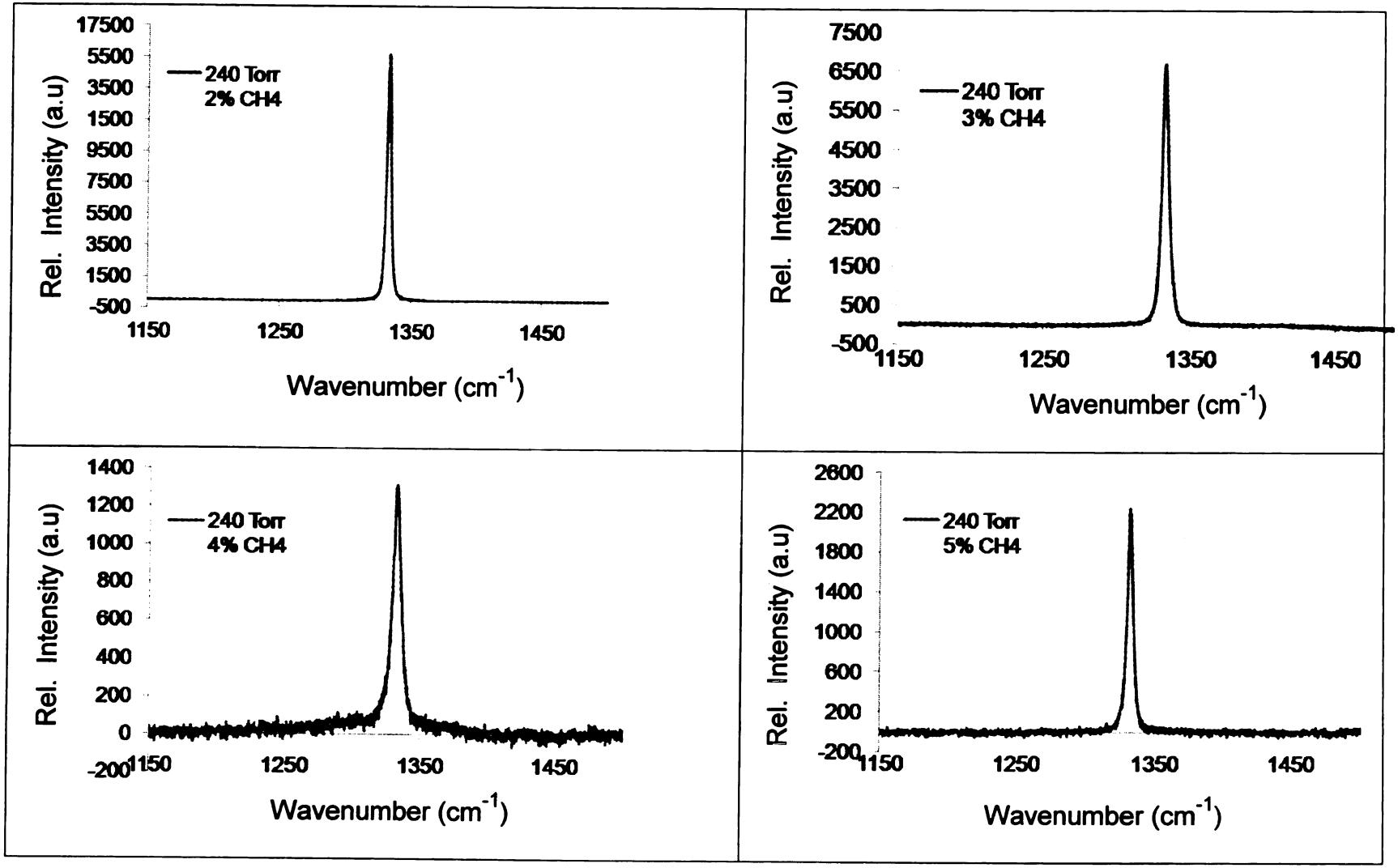

APPENDIX C Experimental Data MPACVD Diamond Synthesis

Table C.1 - Polycrystalline diamond experimental data

Sample	Pressure (Torr)	CH_4/H_2 (%)	Pabs (kW)	Ts (°C)	Weight Gain (gr)	Growth Time (hr)	Growth Rate (μm/hr)	Average Thickness (μm)	ΔZ (mm)
KWH7	180	2	2.62	1054	0.04461	8	3.14	25	-1.4
KWH2	180	3	2.73	1031	0.07107	8	5.0	40	-1.4
KWH20	180	3	2.32	1038	0.04253	4	5.98	24	-4.55
KWH14	180	4	2.70	938	0.05360	3	10.05	30	-3.05
KWH22	180	4	2.42	1099	0.12895	6.5	11.16	73	-1.4
KWH23	180	4	2.44	1082	0.10786	11.5	12.13	133	-1.4
KWH17	180	5	2.39	1058	0.10471	4	14.72	59	-3.05
KWH28A	200	2	2.15	1037	0.05486	10	3.1	31	-2.55
KWH28B	200	2	2.09	1077	0.06122	20	3.44	65	-2.55
KWH28C	200	2	2.14	1090	0.06184	30	3.5	105	-2.55
KWH3	200	3	2.72	1095	0.09615	8	6.8	54	-1.4

KWH27	200	3	2.43	1106	0.18570	14	7.5	105	-2.55
KWH29	200	3	2.11	1061	0.17406	10	9.7	97	-2.55
KWH32	200	3	1.87	1046	0.11510	10	6.5	65	-2.55
KWH12	200	3	2.48	1019	0.11725	8	8.24	66	-3.05
KWH10	200	4	2.69	1158	0.17534	8	12.3	98	-3.05
KWH11	200	5	2.55	1223	0.09226	3.5	14.83	52	-3.05
KWH18	200	5	2.60	1125	0.06572	2.25	16.43	37	-4.55
KWH30	200	5	2.12	1063	0.07282	3.5	11.7	41	-2.55
KWH13	220	2	2.76	1140	0.03010	5	3.39	17	-3.05
KWH38A	220	2	2.13	917	0.07753	10	4.36	44	-2.55
KWH38B	220	2	2.17	926	0.15568	20	4.38	88	-2.55
KWH4	220	3	2.64	1080	0.10800	8	7.6	61	-5.0
KWH25	220	3	2.53	1108	0.05830	5	6.5	33	2.45
KWH26	220	3	2.58	1120	0.01700	1.5	6.4	9.6	0.0
KWH26	220	3	2.50	1086	0.11870	7	9.54	67	-2.55
KWH34	220	3	2.29	1146	0.12401	8	8.72	69	-3.05

KWH15	220	4	2.44	1102	0.06950	3	13.2	40	-3.05
KWH36	220	4	2.44	1093	0.30533	15	11.45	172	-2.55
KWH9	220	5	2.57	1066	0.06883	3	15.88	48	-1.4
KWH21	220	5	2.33	1088	0.05630	2	15.33	32	-1.4
KWH8	240	2	2.54	1166	0.05791	8	4.10	33	-1.4
KWH6	240	3	2.51	1173	0.11868	8	8.34	67	-1.4
KWH33	240	3	2.43	1124	0.1263	8	8.88	71	-2.55
KWH16	240	4	2.61	1180	0.04970	2	13.9	28	-3.05
KWH19	240	5	2.58	1146	0.07560	2	21.26	42	-4.55

Table C.2 – Single crystal diamond experimental data

Sample	Pressure (Torr)	CH_4/H_2 (%)	Pabs (kW)	Ts (°C)	Weight Gain (gr)	Growth Time (hr)	Growth Rate (μm/hr)	Average Thickness (μm)	Delta Z (mm)
KWH101	180	3	1.83	1055	0.00135	4	8	31.35	2.5
KWH111	180	3	2.07	867	0.00177	6	6	36.0	-3.1
KWH202	180	3	2.25	965	0.003542	8	10.3	80.3	-3.1
KWH113	180	5	2.16	1018	0.00515	8	14.95	119.6	-3.1
KWH103	200	3	1.81	1072	0.00335	8	9.73	77.80	0.0
KWH108	200	3	2.41	1162	0.00128	4	5.95	23.8	2.1
KWH203	200	3	2.30	991	0.00588	8	17.1	136.8	-3.1
KWH208	200	5	2.35	1013	0.00209	5	9.7	48.5	-3.1
KWH117	200	5	2.01	1043	0.0055	8	15	124.2	-3.1
KWH106	220	3	1.88	1224	0.06655	4.25	8.77	37.27	2.5
KWH112	220	5	2.29	974	0.00314	7.5	9.75	73.13	-3.1

KWH116	220	5	2.05	1076	0.00484	8	14	112.4	-3.1
KWH105	240	3	1.73	1110	0.00340	8	9.87	78.96	0.0
KWH109	240	5	2.28	1149	0.00735	8	21.4	171.0	-3.1
KWH114	240	5	2.06	1120	0.01041	8	30.5	242.0	-3.1
KWH204	240	5	2.31	1076	0.01678	23	16.95	390.0	-3.1
KWH205	240	5	2.25	1361	0.00733	10	17.5	170.5	-3.1
KWH206	240	5	2.01	1282	0.01538	10	35.8	357.8	-3.1
KWH207	250	3	2.32	1031	0.00478	8	13.9	111.2	2.1
KWH110	250	5	2.13	1124	0.00650	8	19.4	150	-3.1
KWH115	250	5	2.09	1107	0.00516	8	15	120	-3.1

APPENDIX D MPAC Assembly Drawing Components

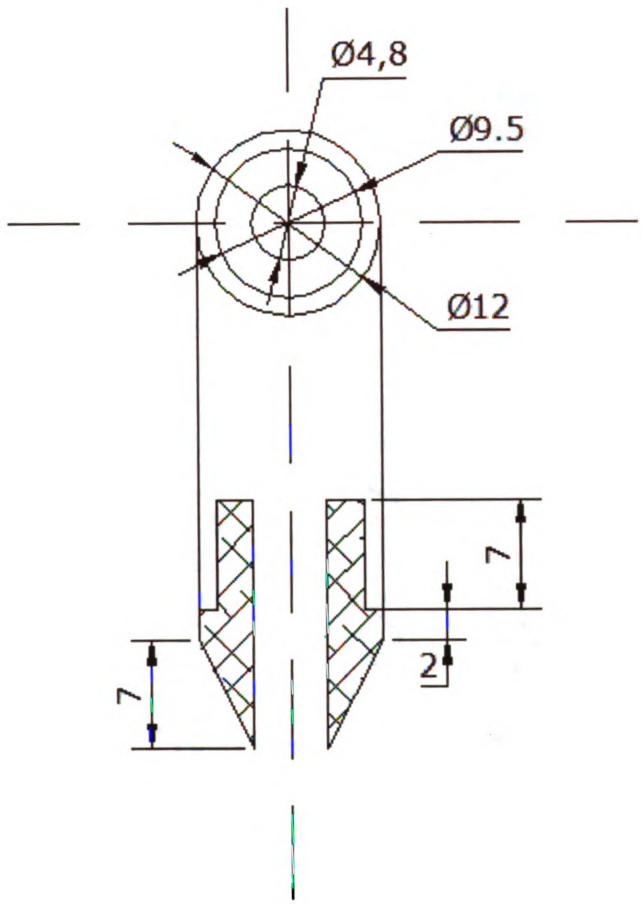

Figure D.1 – Nozzle brass plug design for the re-entrant cavity applicator #2. Units are in mm.

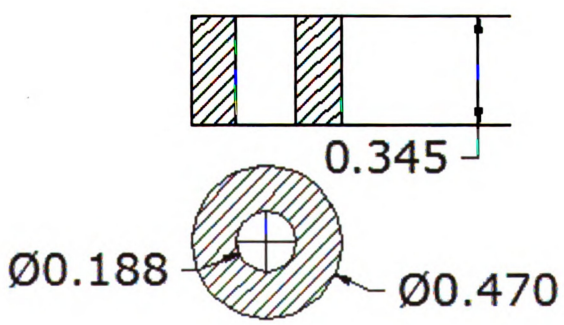

Figure D.2 –Teflon spacer for the re-entrant cavity applicator #2. Units are in inches.

APPENDIX E Experimental Data MPAC

Table E.1 – Tabulated data for the measurements of plasma flame volume in chapter 9

Flow rates (sccm)	MW Power (W)	Length (Pixel)	Diameter (Pixel)	Length (mm)	Diameter (mm)	Volume (mm^3)
150/75: O_2/CH_4	0	294	60	4.9	1	1.28
	2	303	67	5.05	1.11	1.64
	4	310	68	5.16	1.13	1.73
	6	330	72	5.5	1.2	2.07
	8	340	74	5.66	1.23	2.25
	10	418	79	6.96	1.31	3.16
	12	458	104	7.63	1.73	6.00
	14	476	118	7.93	1.96	8.03
	16	536	126	8.93	2.1	10.31
	18	538	128	8.96	2.13	10.68
	20	560	135	9.33	2.25	12.37
	22	576	154	9.6	2.56	16.55
	24	574	160	9.56	2.66	17.81
Flow rates (sccm)	**MW Power (W)**	**Length (Pixel)**	**Diameter (Pixel)**	**Length (mm)**	**Diameter (mm)**	**Volume (mm^3)**
100/50: O_2/CH_4	0	117	54	1.95	0.9	0.41
	2	121	55	2.01	0.91	0.44
	4	120	57	2	0.95	0.47
	6	124	58	2.06	0.96	0.50
	8	151	64	2.51	1.06	0.74
	10	170	77	2.83	1.28	1.22
	12	255	95	4.25	1.58	2.78
	14	280	99	4.66	1.65	3.32
	16	290	100	4.83	1.66	3.51
	18	300	120	5	2	5.23
	20	320	140	5.33	2.33	7.60
	22	355	140	5.91	2.33	8.43
	24	360	144	6	2.4	9.04
Flow rates (sccm)	**MW Power (W)**	**Length (Pixel)**	**Diameter (Pixel)**	**Length (mm)**	**Diameter (mm)**	**Volume (mm^3)**
50/25: O_2/CH_4	0	45	26	0.75	0.43	0.03

	2	53	30	0.88	0.5	0.05
	4	60	40	1	0.66	0.11
	6	63	40	1.05	0.66	0.12
	8	70	46	1.16	0.76	0.17
	10	115	75	1.91	1.25	0.78
	12	128	79	2.13	1.31	0.96
	14	150	104	2.5	1.73	1.96
	16	167	120	2.78	2	2.91
	18	170	144	2.83	2.4	4.27
	20	206	144	3.43	2.4	5.17
	22	221	157	3.68	2.61	6.60
	24	250	167	4.16	2.78	8.45

Table E.2 - Tabulated data for the flame extinction plot for applicator #1

Combustion Only (brass, 0.4)		***Combustion +Microwaves***	
	Blowout	**10 W**	**20-100w**
V_{O2} (sccm)	**V_{CH4} (sccm)**	**V_{CH4} (sccm)**	**V_{CH4} (sccm)**
180	72	64	0
160	56	53	0
140	44	41	0
120	35	32	0
100	26	23	0
80	19	19	0

Combustion Only (brass, 0.4)		***Combustion +10W***		***Combustion +20-100W***	
Equivalence Ratio	**V_{TOT} (sccm)**	**Equivalence Ratio**	**V_{TOT} (sccm)**	**Eq. Ratio**	**V_{TOT} (sccm)**
0.80	252	0.71	244	0.00	180
0.70	216	0.66	213	0.00	160
0.63	184	0.59	181	0.00	140
0.58	155	0.53	152	0.00	120

0.52	126	0.46	123	0.00	100
0.48	99	0.48	99	0.00	80

Table E.3 – Tabulated data for the flame extinction plot for applicator #2

Combustion Only (brass, 0.4)		***Combustion +Microwaves***		
	Blowout	**3W**	**5W**	**6W**
V_{O2} (sccm)	**V_{CH4} (sccm)**	**V_{CH4} (sccm)**	**V_{CH4} (sccm)**	**V_{CH4} (sccm)**
160	67	60	58	0
150	58	54	52	0
120	37	35	34	0
98	26	24	18	0
70	15	14	0	0
50	9	8	0	0
30	5	0	0	0

Combustion Only (brass, 0.4)		***Combustion +3W***		***Combustion +5W***	
Equivalence Ratio	**V_{TOT} (sccm)**	**Eq. Ratio**	**V_{TOT} (sccm)**	**Eq. Ratio**	**V_{TOT} (sccm)**
0.8375	227	0.75	220	0.725	218
0.7733	208	0.72	204	0.693	202
0.6166	157	0.583	155	0.566	154
0.5306	124	0.489	122	0.367	116
0.4286	85	0.4	84	0	70
0.3600	59	0.32	58	0	50
0.3333	35	0	30	0	30

Combustion Only (brass, 0.4)		***Combustion+6W***	
Equivalence Ratio	**V_{TOT} (sccm)**	**Eq. Ratio**	**V_{TOT} (sccm)**
0.8375	227	0.725	218
0.7733	208	0.693	202
0.6166	157	0.566	154
0.5306	124	0.367	116
0.4286	85	0	70
0.3600	59	0	50
0.3333	35	0	30

REFERENCES

[1] M. Kamo, H. Yurimuto, Y. Sato, *"Epitaxial growth of diamond on diamond substrate by plasma assisted CVD,"* Applied Surface Science 33/34, 553-560 (1988).

[2] T. Teraji, *"Chemical vapor deposition of homoepitaxial diamond films,"* Physica Status Solidi (a) 203, 3324 (2006).

[3] T. S. McCauley and Y. K. Vohra, *"Homoepitaxial diamond film deposition on a brilliant cut diamond anvil,"* Applied Physics Letters 66, 1486 (1995).

[4] V. Mortet, A. Kromka, R. Kravets, J. Rosa, V. Vorlicek, J. Zemek, M. Vanecek, *"Investigation of diamond growth at high pressure by microwave plasma chemical vapor deposition,"* Diamond & Related Materials 13, 604–609 (2004).

[5] C. S. Yan, Y. K. Vohra, H. K. Mao, and R. L. Hemley, *"Very High Growth Rate Chemical Vapor Deposition of Single Crystal Diamond,"* Proceedings of the National Academy of Sciences United States of America, 99, 12523 (2002).

[6] O. A. Williams and R. Jackman, *"High growth rate MWPECVD of single crystal diamond,"* Diamond & Related Materials 13, 557 (2004).

[7] K. P. Kuo and J. Asmussen, *"An Experimental Study of High Pressure Synthesis of Diamond Films Using a Microwave Cavity Plasma Reactor,"* Diamond & Related Materials 6, 1097 (1997).

[8] U. Kahler, *"Microwave Plasma Diamond Film Growth,"* Diplomarbeit Thesis, Michigan State University and Gesamthochschule Wuppertal, (1997).

[9] Y. Hirose, First Intern. Conference on the New Diamond Science Technology, New Diamond Forum, Japan, 38 (1988).

[10] L. M. Hanssen, W. A. Carrington, J. E. Buttler, and K. A. Snail, *"Diamond synthesis using an oxygen-acetylene torch,"* Materials Letters, 7:289 (1988).

[11] K. V. Ravi, *"Morphological instabilities in the low pressure synthesis of diamond,"* Journal of Materials Research, 7(2):384-393 (1992).

[12] T. L. Huu, H. Zaidi, D. Paulmier, *"Combustion flame synthesis: a promising technique to obtain diamond single crystal,"* Thin Solid Films, 308-309, 147-153 (1997).

[13] S M. Starikovskaia, *"Plasma assisted ignition and combustion,"* Journal Physics D: Applied Physics 39, R265–R299 (2006).

[14] A. V. Ward, *"Potential uses of microwave to increase internal combustion efficiency and reduce exhaust pollutants,"* Journal of Microwave Power 12, 187-198 (1977).

[15] M. A. V. Ward, *"Interaction of propane-air laminar flame plasmas with the microwave TM010 mode excited in a cylindrical combustion bomb cavity,"* Journal of Microwave Power 14, 241-259 (1979).

[16] C. S. MacLatchy, R. M. Clements, and P. R. Smy, *"An experimental investigation of the effect of microwave radiation on a propane-air flame,"* Combustion and Flame 45, 161-169 (1982).

[17] E. G. Groff, and M. K. Krage, *"Microwave effects on premixed flames,"* Combustion and Flame Vol. 56, 293-306 (1984).

[18] S. F. Mertz, J. Asmussen, and M. C. Hawley, *"An experimental study of reactions of CO and H2 in a continuous flow microwave discharge reactor,"* IEEE Transaction on Plasma Science 2 (11), 297-307 (1974).

[19] A. I. Babaritskii, I. E. Baranov, and M. B. Bibikov, *"Partial hydrocarbon oxidation processes induced by atmospheric pressure microwave discharge plasma," High Energy Chemisty* 38, 407-410 (2004).

[20] H. O. Person, Handbook of Carbon, Graphite, Diamond and Fullerenes, Noyes Publications, park Ridge, New Jersey (1993).

[21] M. A. Prelas, G. Popovici, L. K. Bigelow, eds., Handbook of Industrial Diamonds and Diamond Films, Marcel Dekker, Inc., New York, (1998).

[22] R. F. Davis, Diamond Films and Coatings: Development, Properties, and Applications, Noyes Publications, Park Ridge, New Jersey (1993).

[23] P. K. Bachmann, and R. Messier, *"Emerging technology of diamond thin films,"* C&EN, 67 (20):24-39 (1989).

[24] S. Matsumoto, Y. Sato, M. Kamo, and N. Setaka, *"Vapor deposition of diamond particles from methane,"* Jpn. Journal of Applied Physics Vol. 21. pp. L183-L185 (1982).

[25] C. J. Chu, R. H. Hauge, J. L. Margrave, M. P. D'Evelyn, *"Growth kinetics of (100), (110), and (111) homoepitaxial diamond films,"* Applied Physics Letters Vol. 61. pp. 1393-1395 (1992).

[26] K. Suzuki, A. Sawabe, H. Yasuda, and T. Inuzuka, *"Growth of diamond thin films by dc plasma chemical vapor deposition,"* Applied Physics Letters Vol. 50. pp.728-729 (1987).

[27] S. W. Reeve, W. A. Weimer, and D. S. Dandy, *"On the optimization of a dc arcjet diamond chemical vapor deposition reactor,"* Journal Materials Research Vol. 11, pp. 694-702 (1996).

[28] S. Matsumoto, M. Hino, and T. Kobayashi, *"Synthesis of diamond films in a rf induction thermal plasma,"* Applied Physics Letters 51. pp 737-739 (1987).

[29] R. C. Aldredge and D. G. Goodwin, *"Influence of ambient atmosphere on diamond synthesis using an oxygen-acetylene torch,"* Journal Materials Research Vol. 9, pp. 80-84 (1994).

[30] J. S. Kim and M. A. Cappelli, *"An experimental study of the temperature and stoichiometry dependence of diamond growth in a low pressure flat flames,"* Journal Materials Research Vol. 10, pp. 149-157 (1995).

[31] H. Ling, Z. Q. Xie, Y. Gao, T. Gebre, X. K. Shen, and Y. F. Lu, *"Enhanced chemical vapor deposition of diamond by wavelength-matched vibrational excitations of ethylene molecules using tunable CO_2 laser irradiation,"* Journal of Applied Physics Vol. 105. pp. 064901 (2009).

[32] P. K Bachmann, D. Leers, H Lydtin, *"Towards a general concept of diamond chemical vapor deposition,"* Diamond & Related Materials 1:1-12, (1991).

[33] C. P. Klages, *"Chemical vapor deposition of diamond,"* Applied Physics A, 56:513-526 (1993).

[34] Q. Liang, C. S. Yan, Y. Meng, J. Lai, S. Krasnicki, H. K. Mao, R. J. Hemley, *"Recent advances in high-growth rate single-crystal CVD diamond,"* Diamond & Related Materials 18, 698–703, (2009).

[35] N. G. Glumac, and D. G. Goodwin, *"Diamond synthesis in a low pressure flat flame,"* Thin Solid Films, volume 212 (1-2), 122-126 (1992).

[36] N. G. Glumac, and D. G. Goodwin, *"Large-area diamond film growth in a low pressure flame,"* Materials Letters Volume 18 (3):119-122 (1993).

[37] Q. Liang, C. Y. Chin, J. Lai, C. S. Yan, Y. Meng, H. K. Mao, and R. J. Hemley, *"Enhanced growth of high quality single crystal diamond by microwave plasma assisted chemical vapor deposition at high gas pressures,"* Applied Physics Letters 94, 024103 (2009).

[38] M. Murayama, S. Kojima, and K. Uchida, *"Uniform deposition of diamond films using a flat flame stabilized in the stagnation-point flow,"* Journal of Applied Physics, 69 (11):7924 (1991).

[39] Y. Matsui, A. Yuuki, M. Sahara, and Y. Hirose, *"Flame structure and diamond growth mechanism of acetylene torch,"* Japan Journal Applied Physics 28, 1718-1724 (1989).

[40] J. S. Kim and M. A. Cappelli, *"Temperature measurements in low pressure diamond-forming premixed flame,"* Journal of Applied Physics, Vol 84, 8, (1998).

[41] D. G. Goodwin, *"Scaling laws for diamond chemical vapor deposition diamond surface chemistry,"* Journal Applied Physics 74 (11), 6888 (1993).

[42] F. Silva, J. Achard, O. Brinza, X. Bonnin, K. Hassouni, A. Anthonis, K. De Corte, J. Barjon, *"High quality, large surface area, homoepitaxial MPACVD diamond growth,"* Diamond & Related Materials 18, 683–697 (2009).

[43] P. K. Bachmann, and H. Lydtin, in Diamond and Diamond-like Films and Coatings, edited by R. E. Clausing, L.L. Horton, J. C. Angus, and P. Koidl, Plenum Press, New York, P. 829 (1991).

[44] T. H. Chein, J. Wei, Y. Tzeng, *"Synthesis of diamond in high power-density microwave methane/hydrogen/oxygen plasmas at elevated substrate temperatures,"* Diamond & Related Materials 8, 1686–1696 (1999).

[45] B. Deragin and D. Fedosev, *"Growth of Diamond and Graphite from the Vapor Phase,"* Izd. Nauka, Moscow, USSR (1977).

[46] C. C. Battaile, D. J. Srolovitz, J. E. Butler, *"Morphologies of diamond films from atomic scale simulations of chemical vapor deposition,"* Diamond & Related Materials, 6, 1198-1206 (1997).

[47] T. A. Grotjohn, D. K Reinhard and J. Asmussen, *"Microwave Plasma-Assisted Diamond Film Deposition,"* Diamond Films Handbook, Marcel Dekker, New York, NY, p.211-302 (2002).

[48] Y. A. Mankelevich, P. W. May, *"New insights into the mechanism of CVD diamond growth: Single crystal diamond in MW PECVD reactors,"* Diamond & Related Materials 17, 1021–1028 (2008).

[49] S. S. Zuo, M. K. Yaran, T. A. Grotjohn, D. K. Reinhard, J. Asmussen, *"Investigation of diamond deposition uniformity and quality for freestanding film and substrate applications,"* Diamond & Related Materials 17, 300–305 (2008).

[50] M. Funner, C. Wild, and P. Koidl, *"Novel microwave plasma reactor for diamond synthesis,"* Applied Physics Letters, Vol. 72, No. 10, 9 (1998).

[51] T. P. Mollart and K. L. Lewis, *"Optical-quality diamond growth from CO2-containing gas chemistries,"* Diamond & Related Materials 8, 236 (1999).

[52] V. Ralchenko, I. Sychov, I. Vlasov, A. Vlasov, V. Konov, A. Khomich, S. Voronina, *"Quality of diamond wafers grown by microwave plasma CVD: effects of gas flow rate,"* Diamond & Related Materials 8, 189 (1999).

[53] Y. Ando, T. Tachibana, K. Kobashi, *"Growth of diamond films by a 5-kW microwave plasma CVD Reactor,"* Diamond & Related Materials 10, 312 (2001).

[54] Y. Mokuno, A. Chayahara, Y. Soda, Y. Horino, N. Fujimori, *"Synthesizing single-crystal diamond by repetition of high rate homoepitaxial growth by microwave plasma CVD,"* Diamond & Related Materials 14, p. 1743-1746 (2005).

[55] A. Tallaire, J. Acharda, F. Silvaa, R.S. Sussmanna, A. Gicquel, *"Homoepitaxial deposition of high-quality thick diamond films: effect of growth parameters,"* Diamond & Related Materials 14 p. 249–254 (2005).

[56] H. Sternschulte, T. Bauer, M. Schreck, B. Stritzker, *"Comparison of MWPCVD diamond growth at low and high process gas pressures,"* Diamond & Related Materials 15, 542 (2006).

[57] S. J. Charles, J. E. Butler, B. N. Feygelson, M. E. Newton, D. L. Carroll, J. W. Steeds, H. Darwish, C. S. Yan, H. K. Mao, and R. J. Hemley, *"Characterization of nitrogen doped chemical vapor deposited single crystal diamond before and after high pressure,high temperature annealing,"* physica status solidi (a) 201, No.11, 2473-2485 (2004).

[58] W. L. Mao, H. K. Mao, C. S. Yan, J. Shu, J. Hu, and R. J. Hemley, *"Generation of ultrahigh pressure using single-crystal chemical-vapor-deposition diamond anvils,"* Applied Physics Letters Vol. 83, 25, (2003).

[59] C. S. Yan, H. K. Mao, W. Li, J. Qian, Y. Zhao, and R. J. Hemley, *"Ultrahard diamond single crystals from chemical vapor deposition,"* Physica status solidi (a) 201, No. 4, R25– R27 (2004).

[60] C. S. Yan and Y. K. Vohra, *"Multiple twinning and nitrogen defect center in chemical deposited homoepitaxial diamond,"* Diamond Related Materials 8, 2022-2031 (1999).

[61] R. J. Hemley, H. K. Mao, C. S. Yan, Y. K. Vohra, *"Apparatus and method for diamond production,"* United States Patent # US 6,858,078 B2 (2005).

[62] R. J. Hemley, H. K. Mao, C. S. Yan, *"Ultratough CVD single crystal diamond and three dimensional growth thereof,"* United States Patent # US 7,594,968 B2 (2009).

[63] Y. Meng, C. Yan, J. Lai, S. Krasnicki, H. Shu, T. Yu, Q. Liang, H. Mao, and R. J. Hemley, *"Enhanced optical properties of chemical vapor deposited single crystal diamond by low-pressure/high-temperature annealing,"* Proceedings of the National Academy of Sciences United States of America, vol. 105, no. 46 17620–17625 (2008).

[64] H. Yamada, A. Chayahara, Y. Mokuno, Y. Horino, S. Shikata, *"Simulation of microwave plasmas concentrated on the top surface of a diamond substrate with finite thickness,"* Diamond & Related Materials 15 p. 1383-1388 (2006).

[65] Y. Mokuno, A. Chayahara, Y. Soda, H. Yamada, Y. Horino, N. Fujimori, *"High rate homoepitaxial growth of diamond by microwave plasma CVD with nitrogen addition,"* Diamond & Related Materials 15, p. 455-459 (2006).

[66] A. Chayahara, Y. Mokuno, Y. Horino, Y. Takasu, H. Kato, H. Yoshikawa, N. Fujimori, *"The effect of nitrogen addition during high-rate homoepitaxial growth of diamond by microwave plasma CVD,"* Diamond & Related Materials 13, p. 1954-1958 (2004).

[67] H. Yamada, A. Chayahara, Y. Mokuno, Y. Horino, S. Shikata, *"Numerical analyses of a microwave plasma chemical vapor deposition reactor for thick diamond syntheses,"* Diamond & Related Materials 15 p. 1389 – 1394 (2006).

[68] H. Yamada, A. Chayahara, Y. Mokuno, Y. Soda, Y. Horino, N. Fujimori, *"Modeling and numerical analyses of microwave plasmas for optimizations of a reactor design and its operating conditions,"* Diamond & Related Materials 14 p. 1776 – 1779 (2005).

[69] H. Yamada, Akiyoshi Chayahara, Yoshiaki Mokuno, Yuji Horino, Shinichi Shikata, "Simulation of temperature and gas flow distributions in region close to a diamond substrate with finite thickness", Diamond & Related Materials 15 p. 1738–1742 (2006).

[70] H. Yamada, A. Chayahara, Y. Mokuno, S. Shikata, *"Numerical and experimental studies of high growth-rate over area with 1-inch in diameter under moderate input-power by using MWPCVD,"* Diamond & Related Materials 17, 1062–1066 (2008).

[71] A. Gicquel, K. Hassouni, S. Farhat, Y. Breton, C.D. Scott, M. Lefevbre and M. Pealat., *"Spectroscopic analysis and chemical kinetics modeling of a diamond deposition plasma reactor,"* Diamond Related Materials 3 p. 581-586 (1994).

[72] C. Findeling-Dufour, A. Vignes, A. Gicquel, *"MWPACVD diamond homoepitaxial growth: role of the plasma and the substrate parameters,"* Diamond & Related Materials 4 p. 429-434 (1995).

[73] A. Tallaire, J. Achard, F. Silva, R. S. Sussmann, A. Gicquel, and E. Rzepka, *"Oxygen plasma pre-treatments for high quality homoepitaxial CVD diamond deposition,"* Physica status solidi (a) 201, No. 11, 2419 (2004).

[74] A. Tallaire, A. T. Collins, D. Charles, J. Achard, R. Sussmann, A. Gicquel, M.E. Newton, A. M. Edmonds, R. J. Cruddace, *"Characterisation of high-quality thick single-crystal diamond grown by CVD with a low nitrogen addition,"* Diamond & Related Materials 15, 1700-1707 (2006).

[75] J. Achard, F. Silva, A Tallaire, X. Bonnin, G. Lombardi, K. Hassouni and A. Gicquel, *"High quality MPACVD diamond single crystal growth: high microwave power density regime,"* Journal Physics D: Appl. Phys. 40, 6175–6188 (2007).

[76] J. Asmussen, T. A. Grotjohn, T. Schuelke, M. F. Becker, M. K. Yaran, D. J. King, S. Wicklein, and D. K. Reinhard, *"Multiple substrate microwave plasma-assisted chemical vapor deposition single crystal diamond synthesis,"* Applied Physics Letters, Vol. 93, no. 3 (2008).

[77] J. Asmussen, K. W. Hemawan, J. Lu, T. A. Grotjohn, *"Single Crystal Diamond Synthesis at High Pressures and High Power Densities,"* Materials Research Society Fall 2009 Meeting, Boston, MA, Dec (2009).

[78] K. W. Hemawan, J. Lu, T. A. Grotjohn, D. K. Reinhard, and J. Asmussen, *"High Pressure Single Crystal Diamond Deposition with Nitrogen Addition,"* International Conference on New Diamond and Nano Carbons, Traverse City, MI, June (2009).

[79] K. W. Hemawan, T. A. Grotjohn, D. K. Reinhard, and J. Asmussen, *"High Pressure Microwave Plasma Assisted CVD Synthesis of Diamond,"* International Conference on New Diamond and Nano Carbons, Traverse City, MI, June (2009).

[80] T. A. Grotjohn, K. W. Hemawan, J. Gu, J. Lu, , and J. Asmussen, *"Microwave Plasma Assisted Diamond Synthesis Reactor Design for*

Large Deposition Areas at High Rates," 36th IEEE Int. Conf. on Plasma Science, San Diego, CA, June (2009).

[81] R. Ramamurti, M. Becker, T. Schuelke, T. A. Grotjohn, D. K. Reinhard and J. Asmussen,*"Deposition of thick boron-doped homoepitaxial single crystal diamond by microwave plasma chemical vapor deposition,"* Diamond & Related Materials 18, 704-706 (2008).

[82] J. Asmussen, Keynote paper 11, presented at the 2nd Conference on New Diamond and Nano Carbons, May 26-29th, Taipei, Taiwan, (2008).

[83] F. Silva, K. Hassouni, A. Gicquel, X. Bonnin, invited paper presented at the International Workshop on Strong Microwaves, Aug. (2008).

[84] K. P. Kuo, *"Microwave Assisted Plasma CVD of Diamond Films Using Thermal-Like Plasma Discharge,"* Ph.D. dissertation, Michigan State University (1997).

[85] S. S. Zuo, *"Microwave Plasma-Assisted CVD Polycrystalline Diamond Films Deposition at Higher Pressure Conditions,"* Ph.D. dissertation, Michigan State University (2009).

[86] J. Asmussen, R. Mallavarpu, J. R. Hamann, and H. C. Park, *"The design of a microwave plasma cavity,"* Proceed. IEEE, 62, 109 (1974).

[87] R. Mallavarpu, M.C. Hawley and J. Asmussen, *"Behavior of a microwave cavity discharge over a wide range of pressures and flow rates,"* IEEE Transaction on Plasma Science PS-6, 341 (1978).

[88] P. L. Kapitza, Soviet Physics, Journal of Experimental and Theoretical Physics, 30, 973 (1970).

[89] S. Whitehair, and J. Asmussen, *"Experiments and analysis of a compact electrothermal thruster,"* Journal Propulsion and Power, 3, 136-144 (1987).

[90] S. Offermans, *"Electrodless High-power Microwave Discharges,"* Journal of Applied Physics 67, 115 (1990).

[91] K. D. Diament, B. L. Ziegler, R. B. Cohen, *"Microwave electro-thermal thruster performance,"* Journal of Propulsion and Power, 23, 27-34 (2007).

[92] J. E Brandenburg, J. Kline, D. Sullivan, *"The microwave electro-thermal (MET) thruster using water vapor propellant,"* IEEE Transaction on Plasma Science 33, 2, 776-782 (2005).

[93] David K. Cheng, Field and Wave Electromagnetics, Second Edition, Addison-Wesley Publishing Company, November (1992).

[94] D.M. Pozar, Microwave Engineering, Addison-Wesley Publishing Company, Inc., Reading, Massachusetts (1998).

[95] R. F. Harrington, Time Harmonic Electromagnetic Fields, Wiley-IEEE Press, 2nd edition (2001).

[96] A. Ishimaru, Electromagnetic Wave Propagation, Radiation, and Scattering, Prentice Hall, New Jersey (1991).

[97] V. V. Sarwate, Electromagnetic Fields and Waves, New Age International, New Delhi, India (1993).

[98] N. Marcuvitz, Waveguide Handbook, Institution of Electrical Engineers, New York (1986).

[99] M. K. Yaran, D. King, T. Schuelke, T. Grotjohn, D. Reinhard, and J. Asmussen, *"Homoepitaxial Single Crystal Diamond Grown by Microwave Plasma Chemical Vapor Deposition,"* IEEE Int. Conference on Plasma Science, Traverse City, MI (2006).

[100] J. Asmussen, T, Grotjohn, T. Schuelke, K. W. Hemawan, M. K. Yaran, *"High Pressure Microwave Plasma CVD Reactor,"* Patent Pending, MSU ID 4.1-894, May 2008.

[101] H. Liu and D. S. Dandy, *"Diamond Chemical Vapor Deposition, Nucleation and Early Growth Stages,"* Noyes Publications, New Jersey, (1995).

[102] X. Jiang, K. Schiffmann and C. P. Klages, *"Nucleation and Initial growth Phase of Diamond Thin Films on (100) silicon,"* Physical Review B 50, 8402 (1994).

[103] W. S. Huang, *"Microwave Plasma Assisted Chemical Vapor Deposition of Ultra- Nanocrystalline Diamond Films,"* Ph.D. dissertation, Michigan State University, Department of Electrical and Computer Engineering (2004).

[104] D. T. Tran, *"Synthesis of Thin and Thick Ultra-Nanocrystalline Diamond Films by Microwave Plasma Assisted CVD System,"* M.S. thesis, Michigan State University (2005).

[105] Rutledge and Gleason, *"Characterization Methods,"* in Handbook of Industrial Diamonds and Diamond Films, M. A. Prelas, G. Popovici, and L. K. Begelow eds., pp. 423, Marcel Dekker Inc., New York (2002).

[106] A. M. Zaitsev, *"Optical Properties,"* in Handbook of Industrial Diamond and Diamond Films, M. A. Prelas, G. Popovici, and L. K. Begelow eds., pp. 227, Marcel Dekker Inc., New York (2002).

[107] L. J. Balk and R. Heiderhoff, *"Film Characterization Methods: Structure and Composition,"* in Diamond Films Handbook, J. Asmussen and D.K. Reinhard eds., Chapter 3, Marcel Dekker Inc., New York (2002).

[108] M.J. Ulczynski, B. Wright, D. K. Reinhard, *"Diamond-coated glass substrates,"* Diamond and Related Materials 7, 1639 (1998).

[109] D. K. Reinhard, *"Post Processing and Evaluation of Carbon Materials,"* ICOPS 2006 mini course section 2B, page 4, Traverse City, MI (2006).

[110] R. N. Chakraborty, D. K. Reinhard and P. D. Goldman, *"Etching of Diamond Wafers with Electron Cyclotron Resonance Plasmas,"* Extended Abstracts, Vol. 95-1, The Electrochemical Society, 396 (1995).

[111] R. N. Chakraborty, *"Post Deposition and Processing of Diamond Film Using Electron Cyclotron Resonance Plasmas,"* Ph.D. dissertation, Michigan State University (1995).

[112] D. T. Tran, T. A. Grotjohn, D. K. Reinhard, and J. Asmussen,*"Microwave Plasma Assisted Etching of Diamond,"* Diamond & Related Materials, 17, 717-721 (2008).

[113] Shannon Nicely, Personal communication, August 2009.

[114] T. A. Grotjohn, J. Asmussen, J. Sivagnaname, D. Story, A.L. Vikharev, A. Gorbachev, A, Kolysko, *"Electron density in moderate pressure diamond deposition discharge,"* Diamond & Related Materials 9, 322 (2000).

[115] A. L. Vikharev, A. M. Gorbachev, A. V. Kolysko, D. B. Radishev, and A. B. Muchnikov, *"Microcrystalline diamond growth in presence of argon in millimeter wave plasma assisted CVD reactor,"* Diamond & Related Materials 17, 1055 (2008).

[116] A. L. Vikharev, A. M. Gorbachev, A. V. Kozlov, V. A. Koldanov. A. G . Litvak, N. M. Ovechkin, D. B. Radishev, Yu. V. Bykov, and M. Caplan, *"Diamond films grown by millimeter wave plasma assisted CVD reactor,"* Diamond & Related Materials 15, 502 (2006).

[117] T. Bauer, M. Schreck, H. Sternschulte, B. Strictzker, *"High growth rate homoepitaxial diamond deposition on off-axis substrates,"* Diamond & Related Materials 14, 266 (2005).

[118] S. M. Lee, C. S. Park, M. S. Cha, and S. H. Chung, *"Effects of electric fields on the lift off of nonpremixed turbulent jet flames,"* IEEE Transaction on Plasma Science 33, 1703 (2005).

[119] S. D. T. Axford, J. M. Goodings and A. N. Hayhurst, *"Mass-Spectrometric Sampling of Ions from Flames at Atmospheric Pressure: The Effects of Applied Electric Fields and the Variation of Electric Potential in a Flame,"* Combustion and Flame 114, 294-302 (1998).

[120] N. Chintala, A. Bao, G. Lou, I. V. Adamovich, *"Measurements of combustion efficiency in nonequilibrium RF plasma-ignited flows,"*Combustion and Flame 144, 744-756 (2006).

[121] L. Bromberg, D. R. Cohn, A. Rabinovich, and N. Alexeev, *"Plasma catalytic reforming of methane,"* International Journal Hydrogen Energy 24, 1131-1137 (1999).

[122] L. A. Rosocha, D. M. Coates, D. Platts, and S. Stange, *"Plasma-enhanced combustion of propane using a silent discharge,"* Physics of Plasmas 11, 5 (2004).

[123] S. Stange, Y. Kim, V. Ferreri, L. A. Rosocha, and D. M. Coates, "Flame images indicating combustion enhancement by dielectric barrier discharges," IEEE Transaction on Plasma Science 33 (2), 316-317 (2005).

[124] M. S. Cha, S. M. Lee, K. T. Kim, S.H. Chung, "*Soot suppression by nonthermal plasma in coflow jet diffusion flames using a dielectric barrier discharge*," Combustion and Flame 141, 438-447 (2005).

[125] F. Wang, J. B. Liu, J. Sinibaldi, C. Brophy, A. Kuthi, C. Jiang, P. Ronney, and M. A. Gundersen, *"Transient plasma ignition of quiescent and flowing air/fuel mixture,"* IEEE Transaction on Plasma Science 33, 844 (2005).

[126] B. Ranganath and T. Echekki, "*On the role of heat and mass transport during the mutual annihilation of two premixed propane–air flames,"* International Journal of Heat Mass Transfer, 49, 5075 (2006).

[127] M. A. Lieberman and A. J. Lichtenberg, Principles of Plasma Discharges and Materials Processing, John Wiley and Sons, Inc. pp 339 (1994).

[128] S. B. Leonov and Dmitry A. Yarantsev, *"Plasma induced ignition and plasma assisted combustion in high speed flow,"* Plasma Sources Science and Technology, 16, 132-138 (2007).

[129] S. H. Zaidi, E. Stickman, X. Qin, Z. Zhao, S. Macheret, Y. Ju, R.B. Miles, *"Measurements of Hydrocarbon Flame Speed Enhancement in High Q Microwave Cavity",* AIAA (2006).

[130] K. W. Hemawan, C. L. Romel, S. Zuo, I. S. Wichman, T. A. Grotjohn and J. Asmussen, *"Microwave Plasma Assisted Premixed Flame Combustion,"* Applied Physics Letters 89, 141501 (2006).

[131] E. G. Groff and M. K. Krage, *"Microwave effects on premixed flames,"* Combustion and Flame Vol. 56, 293-306 (1984).

[132] S. J. Whitehair, *"Experimental development of a microwave electro thermal thruster",* Ph.D. Thesis, Michigan State University (1986).

[133] I. I. Esakov, Lev P. Grachev, Kirill V. Khodataev, Viacheslav A. Vinogradov, and David M. Van Wie, *"Propane–Air Mixture Combustion Assisted by MW Discharge in a Speedy Airflow",* IEEE Transactions on Plasma Science, Vol. 34, No. 6 (2006).

[134] J. Asmussen, H. H. Lin, B. Manring, and R. Fritz, *"Single mode or controlled multimode microwave cavity applicators for precision materials processing,"* Review of Scientific Instruments 58, 1477 (1987).

[135] R. M. Fredericks and J. Asmussen, *"Retuning and hysteresis effects of a rf plasma in a variable size microwave cavity,"* Journal of Applied Physics 42, 3647 (1971).

[136] J. Asmussen, T. A. Grotjohn, T. Schuelke, M. Becker, M. Yaran, D. King, S. Wicklein, and D. K. Reinhard, *"Multiple substrate microwave plasma assisted chemical vapor deposition single crystal diamond synthesis,"* Applied Physics Letters 93, 031502-1 (2008).

[137] J. Rogers and J. Asmussen, *"Standing Waves along a Microwave Generated Surface Wave Plasma,"* IEEE Transaction on Plasma Science 10, 11 (1982).

[138] J. Root and J. Asmussen, *"Experimental performance of a microwave cavity plasma disk ion source,"* Review of Scientific Instruments, 56, 1511, (1985).

[139] L. Mahoney, M. Dahimene and J. Asmussen, *"Low power, 3.2-cm, efficient microwave electron cyclotron resonant ion source,"* Review of Scientific Instruments 59, 448, (1998).

[140] A. Kono, T. Sugiyama, T. Goto, H. Furuhashi, and Y. Uchaid, *"Production of CW high density non equilibrium plasma in the atmosphere using microgap discharge excited by microwave,"* Jpn. Journal of Applied Physics 40, L238-L241 (2001).

[141] A. Kono, T. Shibata and A. Aramaki, *"Heat transport simulation for atmospheric pressure high density microgap plasma,"* Jpn. Journal of Applied Physics 45, 940 (2006).

[142] J. Sivagnaname, *"Optical Emission Spectroscopy, Investigation of Microwave Plasmas,"* M.S. Thesis, Michigan State University, (1998).

[143] J. J. Narendra, *"Characteristics and Modeling of Miniature Microwave Plasma Discharge Created with Microstripline Technology,"* M.S. Thesis, Michigan State University, (2004).

[144] G. N. Goyette, J. R. Peck, Y. Matsuda, L. W. Anderson and J. E. Lawler, *"Experimental comparison of rotational and gas kinetic temperatures in N2 and He-N2 discharges"* Journal Physics D: Applied Physics, 31, 1556, (1998).

[145] S. N. Suchard and J. E. Melzer, Spectroscopic Data 2: Homonuclear Diatomic Molecules, IFI/Plenum, New York, (1976).

[146] G. Herzberg, Molecular Spectra and Molecular Structure, I. Spectra of Diatomic Molecules, D. Van Nostrand Co., Inc., Princeton, (1950).

[147] K. W. Hemawan T. Grotjohn, J. Asmussen, *"Plasma-Assisted Combustion in a Miniature Microwave Plasma Torch Applicator,"* 32nd IEEE ICOPS, Monterey, CA, June 18-22, (2005).

[148] K. W. Hemawan, C. L. Romel, I. S. Wichman, T. A. Grotjohn, and J. Asmussen, *"Microwave Plasma-Assisted Premixed Flame Combustion,"* Proceedings of the Central States Section of the Combustion Institute, Cleveland, OH (2006).

[149] K. W. Hemawan, T. A. Grotjohn, and J. Asmussen, *"Microwave Plasma-Assisted Premixed Flame Combustion,"* 3rd International Workshop on Micro plasmas, Greifswald Germany, May 9-11 (2006).

[150] K. W. Hemawan, S. Zuo, C. L. Romel, T. A. Grotjohn, I. Wichman and J. Asmussen, *"Plasma-Assisted Combustion in a Miniature Microwave Plasma Torch Applicator,"* 33rd International Conference on Plasma Science, Traverse City, MI, June 4-8 (2006).

[151] K. W. Hemawan, T. A. Grotjohn, and J. Asmussen, *"Plasma-Assisted Combustion in a Miniature Microwave Plasma Torch Applicator,"* Gordon Research Conference on Plasma Processing Science, Hadley, MA (2006).

[152] K. W. Hemawan, C. Romel, S. Zuo, I. Wichman, T. Grotjohn, J. Asmussen, *"Microwave Plasma Assisted Premixed Flame Combustion,"* Applied Physics Letters, 89,141501 (2006).

[153] T. A. Grotjohn, K. W. Hemawan, S. Zuo and J. Asmussen, *"Miniature atmospheric pressure microwave plasma torch applicators and characteristics,"* 50th International AVS Symposium, Baltimore (2003).

[154] S. Zuo, K. W. Hemawan, J. J. Narendra, T.A. Grotjohn, and J. Asmussen, *"Miniature atmospheric pressure microwave plasma torch,"* 31st International Conference on Plasma Science, Baltimore, June 28-July 1 (2004).

[155] J. Asmussen, T. A. Grotjohn, S. Zuo, and K. Hemawan, *"Miniature microwave plasma torch application and method of use thereof"*, Patent # 7,442,271, October (2008).

[156] S. R. Turns, An Introduction to combustion, McGraw Hill Companies Inc., Boston, (2000).

[157] F. P. Incropera and D. P. Dewitt, Introduction to Heat Transfer, John Wiley and Sons, New York (2002).

[158] C. L. Romel, *"An Experimental Study of Microwave Plasma-Enhanced Combustion,"* M.S. Thesis, Michigan State University (2006).

[159] K. W. Hemawan, T. A. Grotjohn, and J. Asmussen, *"Plasma-Assisted Combustion in a Coaxial Re-entrant Microwave Cavity,"* IEEE Pulsed Power and Plasma Science, Albuquerque, NM, June 17-22 (2007).

[160] K. W. Hemawan, T. Grotjohn, I. Wichman, T. Lee, J. Asmussen, *"Plasma Assisted Combustion in a Coaxial Re-entrant Microwave Cavity,"* Review of Scientific Instruments 80, 053507 (2009).